In vitro models of the human intestinal mucosa to study the interaction of nanoparticle-based drug delivery systems

Dissertation
zur Erlangung des Grades
des Doktors der Naturwissenschaften
der Naturwissenschaftlich-Technischen Fakultäten der
Universität des Saarlandes

von
Olga Hartwig

Saarbrücken
2022

Tag des Kolloquiums:	21.07.2022
Dekan:	Prof. Dr. Jörn Erik Walter
Berichterstatter:	Prof. Dr. Claus-Michael Lehr Prof. Dr. Alexandra K. Kiemer
Vorsitz:	Prof. Dr. Marc Schneider
Akademischer Mitarbeiter:	Dr. Agnes-Valencia Weiss

Die vorliegende Arbeit wurde von Januar 2017 bis November 2020 unter der Leitung von Prof. Dr. Claus-Michael Lehr und Dr. Brigitta Loretz am Institut für Biopharmazie und Pharmazeutische Technologie der Universität des Saarlandes und am Helmholtz-Institut für Pharmazeutische Forschung Saarland (HIPS) angefertigt.

Diese Forschungsarbeit wurde im Rahmen des NEW DEAL Projekts für die Entwicklung einer neuen siRNA-basierten Nanotherapie für chronisch entzündliche Darmerkrankungen durchgeführt und durch das Rahmenprogramm der Europäischen Kommission für Forschung und Innovation HORIZON 2020 unter Grant Agreement Nr. 720905 gefördert.

Table of contents

Table of contents ***1***

Short summary ***3***

Zusammenfassung ***4***

Abbreviations ***5***

1 Introduction ***8***

1.1 Physiology and function of the human gastrointestinal (GI) tract **9**

1.2 Biological barriers of the human intestinal mucosa **12**

1.2.1 Intestinal mucus barrier 13

1.2.2 Intestinal (sub-)epithelial cell barrier and its immune cells 16

1.3 Inflammation of the GI tract – Focus on Inflammatory bowel diseases (IBD) **18**

1.4 Therapeutic strategies for IBD **22**

1.4.1 Classic and novel treatment options for IBD 22

1.4.2 Nanotechnology-based drug delivery systems 23

1.5 Experimental models to investigate drug and DSS interaction **26**

1.5.1 Most common *in vivo* and *ex vivo* models of IBD 26

1.5.2 *In vitro* models of the intestinal mucosa 29

1.6 Aim of the thesis **39**

2 Part I - Interaction studies of nanoparticles with GI mucus ***41***

2.1 Introduction **42**

2.2 Material and Methods **45**

2.2.1 Materials 45

2.2.2 Preparation of biosimilar mucus (BS) 45

2.2.3 Isolation of porcine intestinal mucus (PIM) 46

2.2.4 Cell culture of goblet cells, staining and collection of cell-derived mucus 46

2.2.5 Particle characterization using light scattering 47

2.2.6 Macrorheology of intestinal mucus samples 48

2.2.7 Microrheology of intestinal mucus samples 49

2.2.8 Determination of mucin content by Periodic Acid Schiff (PAS) 50

2.2.9 Morphological analysis of mucus using scanning electron microscopy (SEM) 51

2.2.10 Transport study of particles across intestinal mucus layer 51

2.2.11 Particle interaction within mucin glycoproteins 52

2.2.12 Nanoparticle uptake in cell-based intestinal barrier model 52

2.3 Results **54**

2.3.1 Macrorheological characterization of different intestinal mucus sources 54

2.3.2 Microrheological analysis of intestinal mucus using MPT 59

2.3.3 Quantification of mucin content in native intestinal mucus 64

2.3.4 Analysis of particle mobility through intestinal mucus (macro-scale) 65

2.3.5 Analysis of particle interaction with mucin glycoproteins (micro-scale) 68

2.3.6 Characterization of cell-based intestinal barrier models 70

2.3.7 Particle uptake in cell-based intestinal barrier model cell-derived mucus 74

2.4 Discussion **77**

2.5 Conclusion **85**

3 Part II - Leaky gut model to mimic chronic inflammation of the human intestinal mucosa ***86***

3.1 Introduction 87

3.2 Material and Methods 90

3.2.1 Materials 90
3.2.2 Cell culture 91
3.2.3 Experimental setup of the leaky gut model 93
3.2.4 Transepithelial electrical resistance (TEER) 94
3.2.5 Measurement of cytokine production 95
3.2.6 Staining procedure for confocal microscopic analysis 96
3.2.7 Live/dead cell staining using membrane integrity assay (FDA/PI) 97
3.2.8 Surface area measurements for Caco-2 confluency calculation 97
3.2.9 Dissociation of the co-culture model into single cell suspension 98
3.2.10 Analysis of cell yield and viability after co-culture dissociation 99
3.2.11 Data analysis and statistics 99

3.3 Results 101

3.3.1 Characterization of leaky gut model using confocal microscopy 101
3.3.2 Epithelial barrier integrity of leaky gut model 104
3.3.3 Immune response within leaky gut model after LPS inflammation 105
3.3.4 Dissociation of co-culture model and analysis of single cell suspension 107

3.4 Discussion 112

3.5 Conclusion 116

4 Part III - Leaky gut model as preclinical model to validate JAK inhibitors 117

4.1 Introduction 118

4.2 Material and Methods 120

4.2.1 Materials 120
4.2.2 Cell culture 121
4.2.3 Experimental setup of leaky gut model 121
4.2.4 siRNA-based nanomedicine targeting JAK/STAT pathway 121
4.2.5 Co-culture treatment using JAK inhibitors and controls 122
4.2.6 Localization and uptake study of siRNA-based nanomedicine 123
4.2.7 Quantification of STAT1 phosphorylation using flow cytometry 126
4.2.8 Efficacy testing of JAK/STAT inhibitors in co-culture model 127
4.2.9 Data analysis and statistics 128

4.3 Results 129

4.3.1 Trafficking and localization study of siRNA-based nanomedicine 129
4.3.2 Activation of JAK/STAT pathway using IFN-γ 147
4.3.3 Inhibition of JAK/STAT pathway using Tofacitinib 150
4.3.4 Efficacy testing of JAK/STAT pathway using siRNA-based nanomedicine 154

4.4 Discussion 157

4.5 Conclusion 164

5 Summary and outlook 166

6 References 168

7 Appendix 184

8 Scientific output 188

8.1 Publications 188

8.2 Oral presentations 189

8.3 Poster presentations 189

9 Acknowledgements 190

Short summary

After oral administration, drugs and delivery systems are facing challenging biological barriers throughout the gastrointestinal (GI) tract including pH variations, digestive enzymes, microbiota, mucus, and cellular barriers. The reproduction of intestinal physiology *in vitro* with close resemblance with the native scenario is of high interest in the field of drug development and formulation. The implementation of important features concerning intestinal disorders such as inflammatory bowel diseases (IBD) provides the environment to predict intestinal absorption under diseased conditions. This project aimed to provide different experimental *in vitro* models to investigate the interaction of nanoparticulate systems with the intestinal mucosa including mucus, epithelial barrier and sub-epithelial immune cells. For mucus interaction, different GI mucus sources were characterized by macro- and microrheology and applied for diffusion studies to identify muco-inert or mucoadhesive properties. For cellular interaction, a co-culture model consisting of an epithelial cell layer and underlying immune cells was developed mimicking IBD-related pathophysiological conditions. This so-called leaky gut model holds promise as a human *in vitro* model for combined investigation of intestinal absorption across the (sub-)epithelial barrier and assessment of therapeutic outcome of anti-inflammatory drugs and delivery systems.

The respective *in vitro* testing platforms provide an early set for selection and optimization of anti-inflammatory drugs or delivery systems and as pre-clinical tools may allow for faster translation.

Zusammenfassung

Wirkstoffe bzw. Wirkstoffträger sind nach oraler Applikation im gesamten Magen-Darm-Trakt mit unterschiedlichen biologischen Barrieren konfrontiert, darunter pH-Variationen, Verdauungsenzyme, Mikrobiota sowie der Mukus- und zellulären Barriere. Die *in vitro* Reproduktion der Darmphysiologie ist im Bereich der Arzneimittelentwicklung von hohem Interesse. Hierbei bietet die Implementierung wichtiger Merkmale in Bezug auf Darmerkrankungen wie IBD eine notwendige Voraussetzung, um die Absorption unter Krankheitsbedingungen vorherzusagen.

Das Ziel dieses Projekts war es, verschiedene *in vitro* Modelle bereitzustellen, um die Interaktion nanopartikulärer Systeme mit der Darmschleimhaut, einschließlich der Mukus- und Epithelbarriere sowie den darunterliegenden Immunzellen, zu untersuchen. Für die Analyse der Mukus-Interaktionen wurden Mukusproben aus unterschiedlichen Quellen makro- und mikrorheologisch charakterisiert und in Adhäsions- und Diffusionsstudien verwendet, um deren Eignung in Bezug auf Mukus-Penetration einzuordnen. Für die zelluläre Interaktion wurde ein Ko-Kulturmodell bestehend aus einer Epithelzellschicht und darunterliegender Immunzellen entwickelt, das IBD-bedingte pathophysiologische Zustände nachahmt. Dieses sogenannte ´leaky gut´ Modell ist als humanes *in vitro* Modell vielversprechend, da eine kombinierte Untersuchung der intestinalen Absorption über die epitheliale Barriere, das Erreichen der subepithelialen Immunzellen sowie die Einstufung der anti-entzündlichen Behandlung möglich ist.

Diese *in vitro* Testplattformen können für die Vorauswahl bzw. Optimierung von Wirkstoffen und -trägern genutzt werden und können als präklinische Modelle eine schnellere Translation ermöglichen.

Abbreviations

AB	Blood type group AB
AF	Alexa Fluor
AFM	Atomic Force Microscopy
APC	Allophycocyanin dye
API	Active pharmaceutical ingredient
α-MEM	α-Minimum Essential Medium
ATCC	American Type Culture Collection
BD	Becton Dickinson
BS	Biosimilar Mucus
CACO-2	Human colorectal adenocarcinoma cell line
CBA	Cytometric Bead Array
CD	Crohn´s disease
CD11b	Cluster of differentiation molecule 11b
CD14	Cluster of differentiation molecule 14
CD326	Cluster of differentiation molecule 326 (EpCAM)
CLSM	Confocal Laser Scanning Microscopy
CM	Conditioned media
COOH	Carboxyl group
DCs	Dendritic cells
DDS	Drug delivery system
DiI	1,1′-dioctadecyl-3,3,3′,3′-tetramethylindocarbocyanine
DLS	Dynamic light scattering
DMEM	Dulbecco´s Modified Eagle Medium
DMSO	Dimethyl sulfoxide
DNA	Deoxyribonucleic acid
EpCAM	Epithelial cell adhesion molecule
DSMZ	German Collection of Microorganisms and Cell Cultures
DSS	Dextran Sulfate Sodium
dTHP-1	Macrophage-like cells
ECM	Extracellular matrix
EDTA	Ethylenediamine tetraacetic acid
ELS	Electrophoretic light scattering
EM	Emission
EPR	Enhances permeation and retention
EtOH	Ethanol
EVOM	Epithelial Volt Ohm Meter

EX	Excitation
F-actin	Filamentous actin
FACS	Fluorescence Activated Cell Sorting
FCS	Fetal calf serum
FDA	Fluorescein diacetate
FITC	Fluorescein isothiocyanate
FPS	Frames per second
FRAP	Fluorescence Recovery after Photobleaching
FS	FluoSpheres®
FSC	Forward scatter
G´	Elastic modulus
G´´	Viscous modulus
GI	Gastrointestinal
HBSS	Hank´s Balanced Salt Solution
HEPES	4-(2-hydroxyethyl)-1-piperazineethanesulfonic acid
HMDS	Hexamethyldisilazane
HyD	Hybrid Detector
IBD	Inflammatory bowel diseases
IL	Interleukin
IFN-γ	Interferon gamma
iPSC	Induced pluripotent stem cell
JAK	Janus kinase
Lipo	Lipofectamine
LNPs	Lipid nanoparticles
LPS	Lipopolysaccharides
LVR	Linear viscoelastic region
M cells	Microfold cells
MAP	Mucoadhesive particles
MPP	Mucopenetrating particles
MPT	Multiple Particle Tracking
MSD	Mean squared displacement
MUC	Mucin (glycoprotein)
MUTZ-3	Monocytic cell line (acute myelomonocytic leukemia)
MW	Molecular weight
n.a.	Not analyzed
NA	Numerical aperture
$NaHCO_3$	Sodium bicarbonate
NP	Nanoparticle

NTA	Nanoparticle tracking analysis
NEAA	Non-essential amino acids
ON	Overnight
PAA	Polyacrylic acid
PAS	Periodic Acid Schiff
PBS	Phosphate buffered saline
PC	Phosphatidylcholine
PDI	Poly dispersed index
PE	Phycoerythrin
PEG	Polyethylene glycol
PET	Polyethylene terephthalate (polyester)
PI	Propidium iodide
PIM	Porcine intestinal mucus
PMA	Phorbol 12-myristate 13-acetate
PFA	Paraformaldehyde
PSC	Pluripotent stem cell
RNAi	RNA interference
RPM	Rotations per minute
RPMI	Roswell Park Memorial Institute
RT	Room temperature
SD	Standard deviation
SE	Standard error
SEM	Scanning Electron Microscopy
siRNA	Small interfering ribonucleic acid
siJAK1	siRNA targeting Janus kinase 1
SSC	Side scatter
STAT	Signal transducers and activators of transcription
TEER	Transepithelial electrical resistance
THP-1	Monocytic cell line (acute monocytic leukaemia)
TNBS	Trinitrobenzene sulfonic acid
TOFA	Tofacitinib
TJ	Tight junctions
TNF-α	Tumor necrose factor-*alpha*
TRITC	Tetramethylrhodamine Isothiocyanate
UC	Ulcerative colitis
2D	Two-dimensional
3D	Three-dimensional

1 Introduction

Parts of this chapters have been addressed in the following publications, both published in the peer-review journal of *Advanced Drug Delivery Reviews*:

Hartwig O *, Shetab Boushehri MA *, Shalaby KS, Loretz B, Lamprecht A, Lehr CM. Drug delivery to the inflamed intestinal mucosa - targeting technologies and human cell culture models for better therapies of IBD. *Advanced Drug Delivery Reviews* (2021) Aug; 175:113828. doi: 10.1016/j.addr.2021.113828.
(* contributed equally)

Main contributions to this publication: OH wrote two sections of the manuscript related to "Animal models and their limitations" and "Cell- and tissue-based *in vitro* models", prepared corresponding illustrative figures, and took responsibility for the revision/editing of the manuscript as well as the organization of the collaborative work.

Murgia X, Loretz B**, Hartwig O**, Hittinger M, Lehr CM. The role of mucus on drug transport and its potential to affect therapeutic outcomes. *Advanced Drug Delivery Reviews* 124 (2018) 82–97. https://doi.org/10.1016/j.addr.2017.10.009.

Main contributions to this publication: OH contributed to the section related to "Current attempts to optimize mucosal drug delivery", prepared corresponding illustrative figure, and revised the manuscript.

1.1 Physiology and function of the human gastrointestinal (GI) tract

The human gastrointestinal (GI) tract, starting from the mouth to ending with the anus, is a complex system responsible for the digestion and absorption of food-derived nutrients as well as the elimination of undigested food and waste products [1]. After ingestion, food is first broken down through mastication in the oral cavity and blend with saliva released from the salivary glands for bolus formation, taste perception, or lubrication of mucosa (Fig. 1.1) [2]. The food bolus passes through the esophagus to the stomach where food gets mixed with gastric juices (e.g. pepsin) and afterwards, enters the small intestine, where further digestion and the main nutrient absorption takes place [3]. The digestive process is supported by the liver and pancreas which are responsible for the secretion of bile and pancreatic enzymes (e.g. lipase or protease) and hormones (e.g. insulin), respectively [1]. Undigested food and waste products are passaged to the large intestine (colon) which is responsible to absorb remaining water resulting in stool [1]. The migration of the food bolus along the GI tract is supported by peristalsis within the GI tract which is mediated by muscular contraction and is highly affected by the innervation of the intestine. Furthermore, the GI tact comprises its own independent nervous system, termed enteric nervous system (ENS), which is considered a ´second brain´ responsible for the regulation of the peristaltic motion [4].

To exercise all these functions, the GI tract is made of a series of hollow organs that are joint in a muscular tube with a length of approximately nine meters and variable diameters [3]. Compared to the small intestine and its multiple coils of up to 7 meters in length, the colon is much shorter with around 1.5 meters, however, wider in diameter [5]. Due to the surface enlargement capacity of (micro-)villi structures which protrude into the luminal side, the small intestine has a total surface area of around 32 m^2, whereas the large intestine where villi are absent covers approximately 2 m^2 [6].

The intestinal wall can be divided into four different layers from the outside (lumen) towards the inside: the mucosa which includes epithelium, lamina propria, and

muscularis mucosa, the submucosa, the muscularis externa, and the serosa (Fig. 1.1) [7]. A single layer of columnar epithelial cells composed of several cell types is continuously replenished and shed into the luminal space. The epithelial integrity is maintained with a complete renewal every 3-5 days under normal conditions [8]. Therefore, multipotent cells are migrating from the base of the stem cell niche located in the crypts of Lieberkühn towards the villus tips while differentiating into mature cells possessing specialized functions (Fig.1.1) [9].

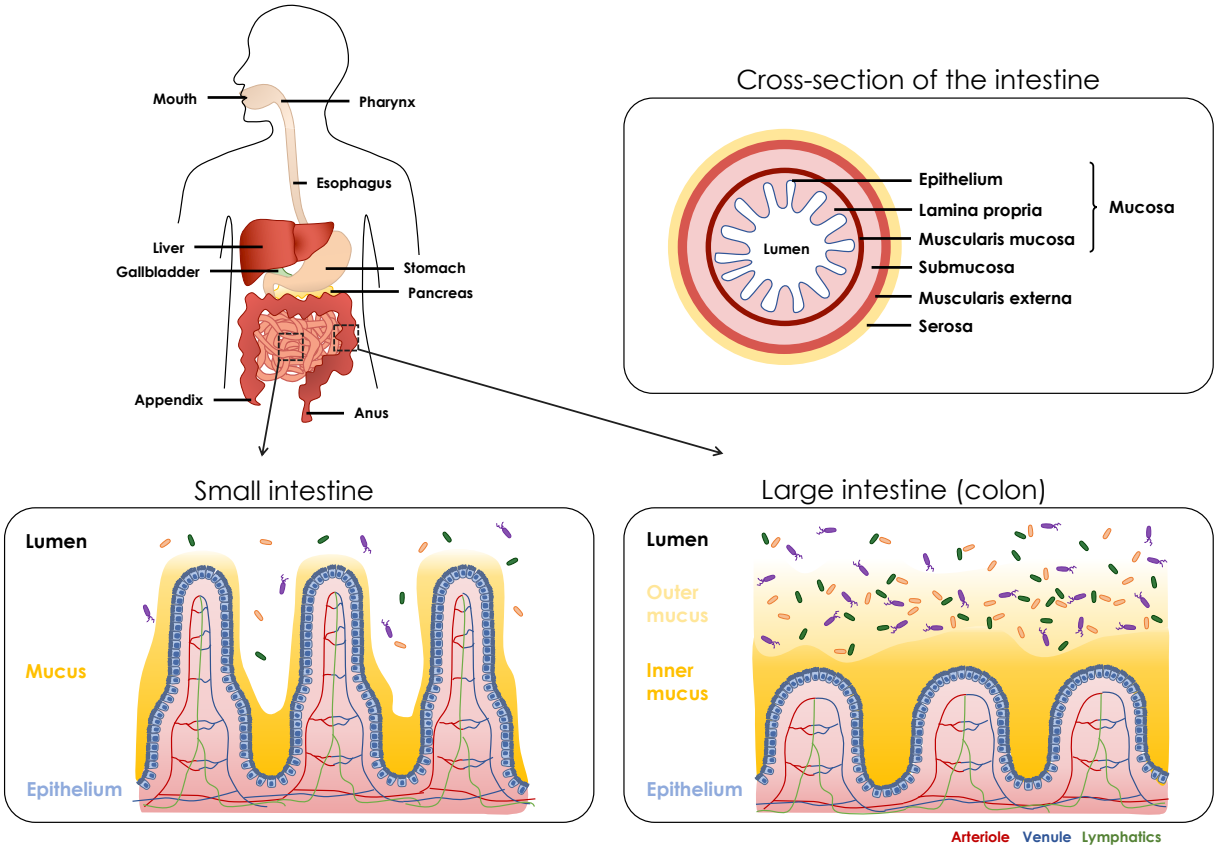


FIGURE 1.1 Schematic illustration of the human gastrointestinal (GI) tract and organization of the intestinal mucosa. The main function of the GI tract involves the digestion and absorption of food components, as well as the elimination of undigested matter. The digestion system starts with the mouth and ends with the anus. Cross-section of the intestine including different layers: mucosa (epithelium, lamina propria, and muscularis mucosa), submucosa, muscularis externa, and serosa. The small intestine is characterized by luminal projections (villi) and invaginations (crypts of Lieberkühn) where the intestinal epithelium is coated by a thin mucus layer. Villi structures are absent in the large intestine (colon) that is covered with a two layered mucus where the outer layer is colonized by symbiotic microorganisms. (Adapted from Refs. [10–12])

Besides absorptive enterocytes that represent the vast majority, the intestinal epithelium is composed of various secretory cells like goblet (mucus secretion), enteroendocrine (hormones), and Paneth cells (antimicrobial factors) [13].

The intestinal mucosa contains an abundant vasculature of arterial and venous blood capillaries which provide the supply of oxygen and circulation of nutrients [14]. The intestinal lymphatic system is responsible for tissue fluid homeostasis, immunosurveillance, and transport of nutrients, with a much higher interconnected lymphatic network the small intestine than in the colon [15].

The intestinal wall is continuously exposed to a wide range of antigens and potential immune stimuli which derive from dietary constituents and commensal enteric bacteria [5]. As a ´supraorganism´ the human body is colonized by 10 to 100 trillion indigenous microbial organisms including bacteria, fungi and viruses which mediate host defense, immune development, and nutritional state [16,17]. The digestive system harbours more than 40 trillion bacteria, termed the intestinal microbiome, that reside at the interface of the mucosal epithelial barrier, with the majority colonizing the large intestine (Fig. 1.1) [13,18]. Each person has its individual composition of gut microbiota that is formed throughout life and can be influenced by various factors such as diet or antibiotics [19].

It is therefore not surprising that the intestine comprises the largest number of immune cells compared to any tissue in the body [20]. For instance, intraepithelial lymphocytes (predominantly T cells) that reside along the entire GI tract are patrolling the intestinal epithelial barrier [21]. Moreover, the connective tissue under the epithelium, the lamina propria, contains the gut-associated lymphoid tissue (GALT) such as Peyer´s Patches (small intestine) or colonic patches (large intestine) [22]. These organized lymph node-like tissues with localized T cells, B cells, and dendritic cells (DCs) are covered with microfold (M-) cells specialized for luminal antigen sampling and the potential induction of the adaptive immune response [22]. In particular, sub-epithelial phagocytes such as macrophages representing the innate immunity are key players for the maintenance of intestinal homeostasis and support the removal of

cellular debris during mucosal regeneration [23]. However, intestinal epithelial cells act as the frontline sensors of microbial components and integrate these signals into antimicrobial and immunoregulatory processes [10]. In addition, immune surveillance is managed by Paneth cells that regulate the composition of the intestinal flora via secretion of antimicrobial peptides (AMPs) and immunomodulatory proteins, and by Tuft cells that monitor intestinal lumen and transmit signals to the underlying immune cells [24,25]. For those purposes, a finely balanced cross-talk between epithelial cells and innate as well as adaptive immune cells via immune-modulatory mediators enables the maintenance of the epithelial barrier and tolerance to the microbiota in homeostasis [26].

1.2 Biological barriers of the human intestinal mucosa

The GI tract is exposed to the environment and hence, constitutes an important barrier against external factors [27,28]. Due to its large surface area, the small intestine is the major site of drug absorption [3]. Despite oral drug delivery being the most simple and convenient route of administration, it remains challenging due to the several biological barriers of the human intestine. This includes the mucus layer as well as the epithelial cell layer which represents both, a physical and chemical barrier against e.g. invading microbes or toxins but also for oral formulations. Besides the presence of gut microbiota and related metabolites, the GI lumen contains a variety of dietary compounds such as fats, carbohydrates or proteins, and cellular debris due to epithelial cell turnover [29]. In addition, gastric juices with acid pH and digestive enzymes including lipases, proteases and nucleases are further barriers to drug and drug delivery systems. Targeting the intestinal mucosa should encompass considerations regarding drug stability and delivery purposes, as well as permeability across these mucosal barriers. Furthermore, additional challenges associated with pathophysiological changes of intestinal inflammation should be contemplated for effective drug delivery.

1.2.1 Intestinal mucus barrier

In the human body, all non-keratinized epithelia including the eyes, the reproductive, respiratory, and GI tract are covered by a thin mucus layer [30]. This complex hydrogel is continuously secreted and shed from mucosal tissues and acts as a protective barrier between the external environment and the epithelium [31]. Moreover, depending on the anatomical site, mucus fulfills different tasks such as lubrication, physical barrier, reservoir matrix for microbial compounds or nutrient source for microbial entities [32]. Mucus is a viscoelastic hydrogel with both, solid-like and liquid-like properties, and irrespective of the mucus source it is mainly composed of water ~95% and to a smaller extent of glycoproteins called mucins (1-5% w/v), non-mucin proteins, lipids, salts and cellular debris [33]. Extracellular DNA is part of the mucus composition and derives from epithelial cells that are shed from the mucosal site due to epithelial cell turnover. DNA has a significant contribution to the barrier function of the small intestinal mucus [34]. Intestinal mucus is continuously secreted by specialized cells, termed goblet cells, and prevents the entry of undesirable luminal contents while, at the same time, preserving the absorption of nutrients [35]. Intestinal goblet cells produce predominantly mucin protein MUC2 and constitute the major structural component that determines the viscoelastic property of mucus [36]. The primary structure of MUC2 consists of multiple domains, including tandem repeats of distinct amino acids, Proline-Threonine-Serine (PTS) domains, that are highly decorated with glycans (up to 80% of the total mucin mass) [37,38] (Fig. 1.2). Accordingly, sugar moieties such as N-acetylgalactosamine (GalNAc), N-acetylglucosamine (GlcNAc), N-acetylneuraminic acid (NeuAc), galactose, and fucose are attached to the PTS domains which support the brush-like structure and results in an overall negative charge [17,39]. The interconnected mesh-like network is resulting from the crosslinking between mucin monomers that form larger-order structures based on disulfide bonds between Cysteine (Cys)-rich domains [17] (Fig. 1.2). In comparison, the non-glycosylated regions of the mucin protein backbone provide in addition hydrophobic domains within the mucus network [17].

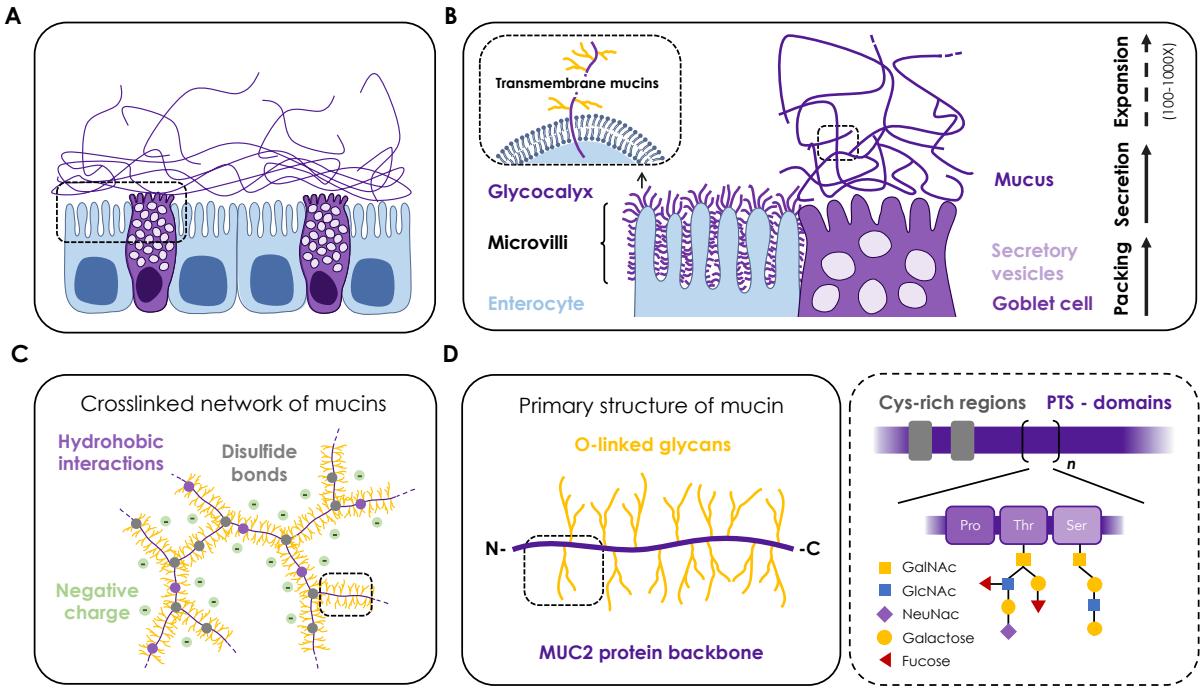


FIGURE 1.2 Schematic overview of mucus production and structural composition. Representation of intestinal epithelium interspersed with mucus-secreting goblet cells (**A**). Gut epithelia with microvilli and transmembrane mucins (glycocalyx), and adjacent goblet cells with secretory vesicles containing mucins. After secretion, mucins form of a net-like structure that expanse 100 – 1000 times in volume (**B**). Crosslinking between mucins to form larger-order structures based on disulfide bonds between Cysteine (Cys)-rich domains providing additional hydrophobic interactions (**C**). The overall negative charge of mucins comes from respective sugar groups attached to the mucin protein core and stabilizes the mucin network via repulsive forces. Primary structure of mucin protein backbone (MUC2) composed of tandem Proline (Pro)-Threonine (Thr)-Serine (Ser) (PTS)-rich domains and various O-glycans linked to Ser and Thr amino acids (**D**). Examples of glycosylation assembly and the addition of elongating branches of sugar residues such as N-acetylgalactosamine (GalNAc), N-acetylglucosamine (GlcNAc), N-acetylneuraminic acid (NeuAc), galactose, and fucose. (Adapted from Refs. [17,27,40].)

In addition to gel-forming mucins, gut epithelia comprise transmembrane mucins located on the microvilli surface of enterocytes, termed glycocalyx, a micrometer thick pericellular mesh-like matrix with heavy glycosylation representing an additional protective barrier [27] (Fig. 1.2).

Mucus composition, pH, thickness, and mucus clearance mechanisms vary according to specific functions required at the physiological location [30]. Besides its protective function for the underlying epithelia against digestive secretions or invading pathogens, GI-secreted mucus lubricates the intestinal wall and facilitates the passage of food, and harbours a huge amount of microbial community [32,41]. The proper

functions of the mucus barrier, however, are related to its dynamic feature which implies a constant renewal and shedding of mucus [30]. Regarding IBD pathophysiology, defects in mucus production or processing were observed with either reduced mucus production for ulcerative colitis (UC) or increased levels for Crohn´s disease (CD) patients, however, with similar results regarding the translocation of bacteria [42–44]. Intestinal mucus is separating the epithelium from gut microbiota including commensal and pathogenic bacteria through entrapment and clearance mechanisms [45]. However, especially colonic outer mucus provides also an attractive habitat for beneficial microflora supporting the symbiotic relationship with the host by the provision of dietary components [46].

The complex biochemical composition of mucus is advantageous to absorb a wide range of molecules and particles, including therapeutic or pathogenic entities such as toxins or microorganisms [30]. Mucus controls the transport by two different mechanisms, the physical- and interaction-filtering [30,47] (Fig. 1.3). In the context of drug and drug delivery systems, the diffusion through intestinal mucus is affected by the mucus mesh-spacing estimated to be approximately 200 nm [29]. Thus, the mobility of particulates bigger than the average pore size of mucus will be limited (Fig. 1.3). However, since mucus displays a highly heterogeneous structure, a broad pore size distribution ranging from a few nanometers to several micrometers was described [48,49]. Next to size filtering mechanism, the mobility of particles smaller than the mesh pore size is governed by their respective surface chemistry [30]. Non-interacting particles with polyethylene glycol (PEG)-coating showed relatively high diffusion rates through mucus compared to positively charged or hydrophobic nanocarriers providing electrostatic or hydrophobic interactions, respectively [50,51] (Fig. 1.3).

Moreover, the intestinal mucus is secreted continuously with approximately 10 L per day [50]. The combination of persistent mucus secretion and peristaltic motion favours on the one side the passage of chyme (lubricative property) and on the other side, removes entrapped material efficiently avoiding the epithelial cell contact [30].

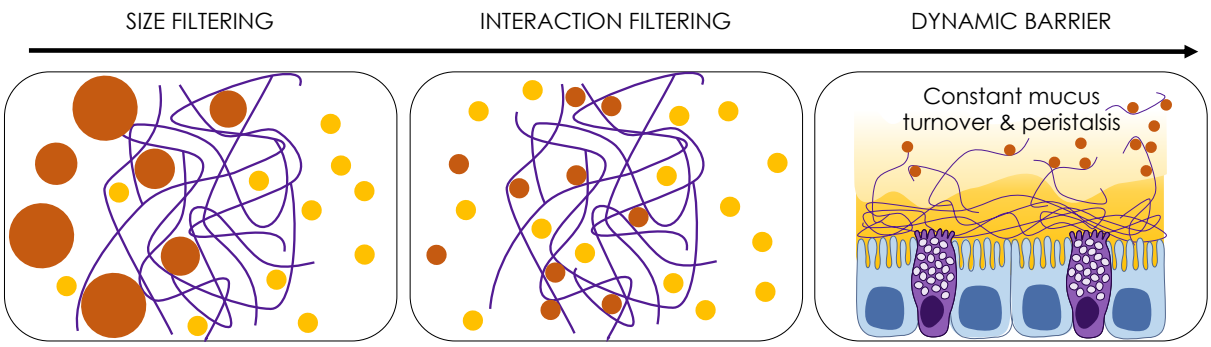


FIGURE 1.3 Schematic illustration of possible mechanisms including size and interaction filtering as well as dynamic feature of the mucus barrier. Size filtering mechanisms allow the passage of particles with dimensions smaller that the mesh spacing (yellow), whereas larger particles (orange) are excluded (left). Particles which interact with mucin glycoproteins via non-covalent binding including electrostatic, hydrophobic interactions, or H-bonds (orange) are subjected to filtering mechanism and show hindered muco-penetration (middle). In contrast, muco-inert particles (yellow) have distinct particle surface properties such as hydrophilicity or neutral charge avoiding these interactions. The dynamic feature of the intestinal mucus barrier with constant mucus turnover (secretion, degradation, and shedding) impedes particle penetration together with peristaltic motion (right). (Adapted from Refs. [30,52].)

Regarding mucoadhesive drug delivery systems (DDS), mucus turnover can be faster than drug release and thus, prevents the drug reaching the intestinal epithelium [30] (Fig. 1.3). For muco-inert particles likewise, the corresponding velocity of muco-penetration can be decisive to overcome the mucus layer before being removed by the constant mucus turnover [30].

1.2.2 Intestinal (sub-)epithelial cell barrier and its immune cells

Underneath the mucus layer, the human intestinal barrier comprises the epithelium and a large amount of sub-epithelial immune cells. The intestinal epithelium is composed of a single layer of different cell types and has two main functions including the provision of a physical barrier and the mediation of immune responses [53]. The dynamic barrier separates the intestinal lumen from the sterile internal environment of the body and provides the controlled absorption of nutrients, electrolytes, and water [54]. Within this context, the selective barrier is maintained through the formation of protein complexes that mechanically connect adjacent cells in order to seal the intercellular space [28]. These junctions are composed of tight junctions (TJ)

as the most important structural component [55]. One of the main functions is to control the movement of fluids and solutes in the paracellular space, creating a selectively permeable barrier within the GI tract [56]. Their assembly is a highly dynamic process and influenced by multiple cytokines such as tumor necrosis alpha (TNF-α) which induces an increased permeability [57]. Intestinal epithelial cells (IECs) are the frontline sensors of luminal contents including food antigens or microbial components, and integrate these signals into immunoregulatory processes [10]. IECs are contributing to intestinal homeostasis via secretion of interleukin (IL)-10 and transforming growth factor-β (TGF-β) [58]. However, to promote the immunomodulatory environment, IECs express on their surface the so-called pattern recognition receptors (PRRs) that recognise conserved microbial-associated molecular patterns (MAMPs) [59]. For instance, toll-like receptors (TLRs) are expressed along the GI tract necessary to identify commensal or pathogenic entities at the close proximity to the epithelium [60]. Moreover, TLR signalling was found to be involved in the regulation of different processes such as epithelial cell proliferation, IgA production, maintenance of TJ formation, and the production of anti-microbial peptides (AMPs) [60]. The latter represents the chemical barrier of the intestine which as chemical agents secreted by Paneth cells at the bottom of the crypts attack invading microorganisms, and thus, enable the segregation of gut bacteria [61].

The sub-epithelial layer of the intestine, termed lamina propria, comprises various kinds of myeloid and lymphoid cell types. Accordingly, a huge number of immune cells resides in the lamina propria including macrophages, dendritic cells (DCs), or regulatory T and B cells which maintain intestinal homeostasis. Innate immunity protagonists are responsible for constant communication with the intestinal microenvironment (immunosurveillance) and, if required, to induce appropriate immune responses involving the adaptive immunity. Besides the presence of dendritic protrusions by myeloid cells, the small intestine contains lymphoid tissues such as Peyer´s Patches that are associated with microfold (M) cells necessary for luminal antigen sampling [22].

1.3 Inflammation of the GI tract – Focus on Inflammatory bowel diseases (IBD)

Inflammatory bowel diseases (IBD) is an umbrella term for GI disorders caused by chronic relapsing inflammation. Especially Western countries record an increase of IBD incidence with an estimated IBD population of more than 10 million worldwide for 2030 [62]. IBD comprises two main disease conditions such as Crohn´s disease (CD) and ulcerative colitis (UC) showing similarities regarding risk factors, but differences in their clinical presentation (Fig. 1.4).

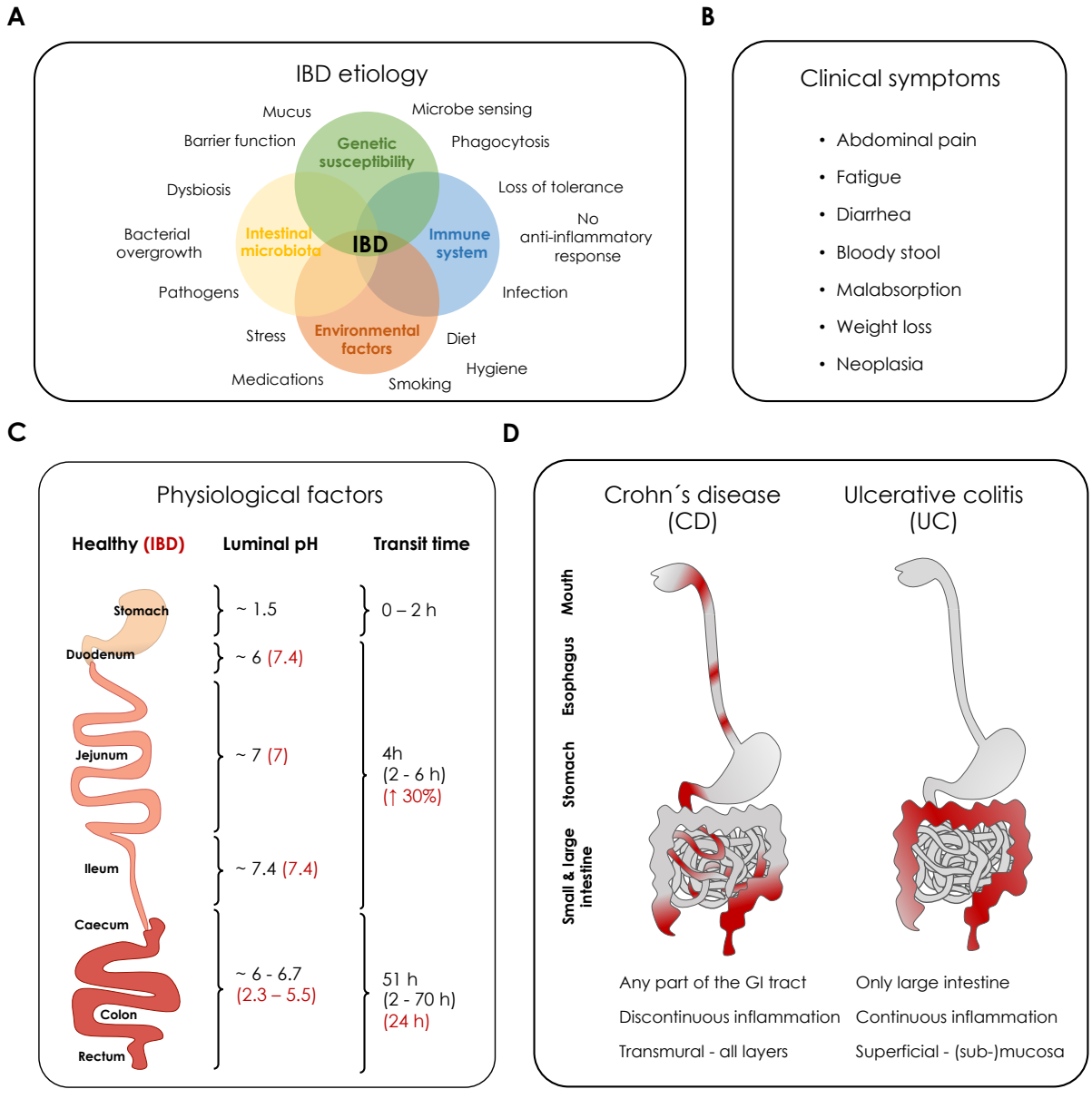


FIGURE 1.4 Inflammatory bowel disease (IBD). Overview of IBD etiology (**A**), corresponding clinical symptoms (**B**), physiological factors of the GI tract including pH and transit time with IBD-related deviations (shown in red) (**C**), and differences between the main entities such as Crohn´s disease (CD) and ulcerative colitis (UC) (**D**). (Adapted from Refs. [3,63–66])

All parts of the GI tract, from the mouth to the anus, can be affected in CD showing a patchy distribution and transmural (various gut layers) inflammation, that may involve granulomas and crypt abscesses [67] (Fig. 1.4). In contrast, UC is often restricted to the large intestine and associated with a continuous but more superficial inflammation of the (sub-)mucosa [68]. IBD etiology is not fully elucidated, however, genetic and environmental factors are triggering its complex pathogenesis including a dysregulated immune system, dysbiosis of the microbiome and dysfunction of the intestinal epithelial barrier [64] (Fig. 1.4). Recent studies confirmed that alterations in the relative abundance of resident microbial population are associated with the pathogenesis of intestinal disorders and extra-intestinal manifestations [69]. Besides microbial changes, differences in physiological factors include gastrointestinal pH and transit time showing minor alterations in the small intestine, but significant decreases of the colonic pH and accelerated motility, respectively [3] (Fig. 1.4). Regardless of type, IBD results in significant morbidity and reduced quality of life for many patients. Common symptoms are abdominal pain, persistent diarrhea, and bloody stool which can lead to severe complications such as fistulas and intestinal strictures in CD or colorectal cancer for both entities [70].

The intestinal epithelial barrier has been identified as a primary contributing factor, therefore IBD is often termed leaky gut diseases [71]. The translocation of bacterial products into the intestinal wall and the lack of anti-inflammatory mechanisms contribute to an aberrant production of pro-inflammatory mediators including cytokines and chemokines, followed by the progressive immune cell infiltration and tissue destruction [72]. In this regard, both IBD phenotypes have shown activated innate and acquired immune responses and the loss of tolerance to enteric commensal bacteria [63].

Figure 1.5 illustrates the differences of the intestinal mucosa under healthy or homeostatic conditions compared to IBD pathophysiological alterations including the chronically inflamed state.

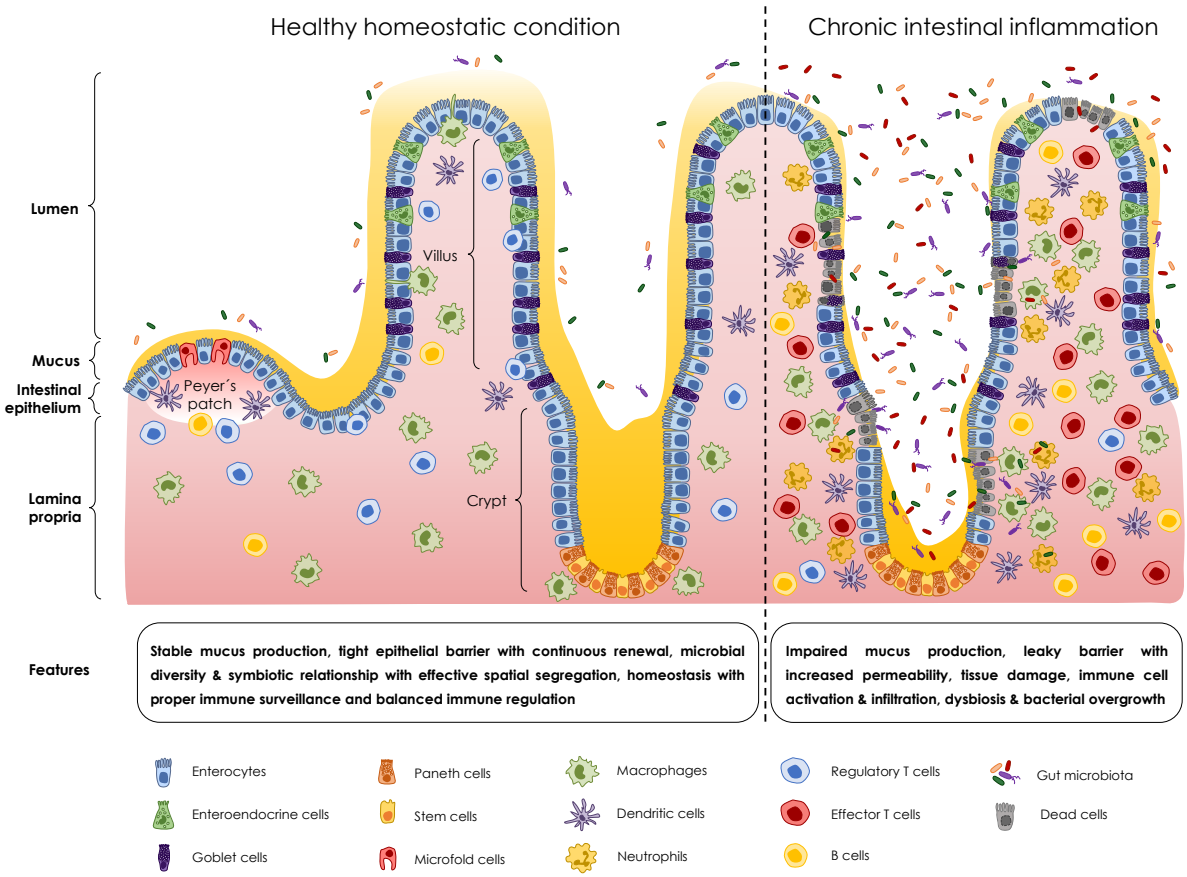


FIGURE 1.5 Schematic illustration of intestinal homeostasis versus IBD conditions and chronic intestinal inflammation. Representation of small intestinal epithelium with villus-crypt structures covered with a protective mucus layer separating the microbial community. The majority of absorptive enterocytes are interspersed with goblet (mucus secretion) and enteroendocrine cells (hormone secretion), whereas at the crypt base Paneth cells (antimicrobial factor secretion) and pluripotent stem cells (epithelium renewal) are localized. Intestinal homeostasis is characterized by steady mucus production, epithelial barrier integrity, and a balanced immune regulation. This tolerogenic environment is maintained by intestinal resident macrophages that sample luminal antigens without perturbing epithelial integrity. Both, innate and adaptive immune cells including naïve T and B cells are found in intestinal lymphoid tissue (Peyer´s Patches) covered with microfold cells necessary for immune surveillance and luminal antigen sampling. Under chronic inflammation, the dysfunction of the mucosal barriers (mucus production and epithelial integrity) together with dysbiosis and bacterial overgrowth lead to the translocation of luminal content (antigens and bacteria) and promotion of aberrant intestinal inflammation. The dysfunctional immune response with the lack of anti-inflammatory mechanisms and uncontrolled immune cell recruitment cannot resolve infection/inflammation and results in persistent tissue injury. (Adapted from Refs. [5,61,73,74].)

Under homeostatic conditions, the intestinal epithelium maintains a balanced immune response during the constant sampling of luminal material and the presence of regulatory immune cells (Fig. 1.5; left side). The symbiotic relationship with commensal microorganisms is related to the effective spatial segregation, supported by the steady secretion of mucus from the goblet cells. Upon various risk factors, intestinal inflammation is induced by defects in the protective mucus layer and the loss of appropriate barrier function (Fig. 1.5; right side). The activation of local immune cells including dendritic cells (DCs), macrophages, granulocytes, and lymphocytes together with enhanced secretion of immunomodulatory factors leads to further immune cell recruitment from the periphery. The lack of proper anti-inflammatory mechanisms results in persistent tissue injury with deleterious damages of the intestinal barrier (Fig. 1.5; right side).

The immunopathogenesis of CD has been associated with a T helper (T_h)1-dominated lymphocyte response, whereas UC with T_h17 and regulatory T cells as the main cellular key players [75]. Accordingly, naïve T_h cells that reside in the lamina propria are primed towards different effector types depending on the inflammatory context and the type of dominant cytokine. DCs representing a major cytokine source contribute to T cell differentiation. Compared to interleukin (IL)-12 and interferon gamma (IFN-γ) that direct T helper cells towards T_h1 subtype differentiation, IL-6 and TGF-β induce and IL-23 expand T_h17 cell population. T_h17 cells maintain inflammation via secretion of several pro-inflammatory cytokines such as IL-17A, IL-17F, IL-21, and IL-22 that interact with multiple cell types including epi- and endothelial cells, fibroblasts, and monocytes/macrophages, and neutrophils [76,77]. Compared to IECs, regulatory T lymphocytes are responsible to balance the inflammatory responses through the secretion of anti-inflammatory mediators such as TGF-β and IL-10.

1.4 Therapeutic strategies for IBD

To date, there is no cure for IBD, and various medications are available to treat the symptoms ranging from broad mechanisms of action of non-specific immunomodulators or immunosuppressive agents to more specific therapeutic strategies. Nevertheless, novel therapeutics are not effective for all IBD patients and are still related to adverse effects.

1.4.1 Classic and novel treatment options for IBD

Classical treatment options include anti-inflammatory drugs and immunosuppressants like aminosalicylates (e.g. 5-AZA) or corticosteroids (e.g. budesonide or prednisone) which are not effective for all IBD patients and related to severe adverse effects [78–80]. Based on the improved knowledge of IBD pathophysiology and related mechanisms, novel therapeutic strategies have been developed aiming for increased specificity. The emergence of biologics including monoclonal antibodies targeting specific overexpressed cytokines such as anti-TNF-α or immune cell homing epitopes like anti-integrins have significantly improved IBD treatment options [81]. However, despite of enhanced specificity, a substantial percentage of IBD patients remain non-responsive, lose their responsiveness or suffer from adverse reactions [82]. Within these "treat to target" approaches to identify novel molecular targets in the treatment of IBD, researchers set the focus on specific signal pathways, including janus kinase/signal transducer and activator of transcription (JAK/STAT) signal cascade. JAK/STAT shared by multiple cytokines is an important therapeutic target in the field of immune-mediated diseases like rheumatoid arthritis (RA), psoriasis and alopecia areata [83,84]. The only so far approved JAK inhibitor for IBD is tofacitinib (TOFA), a small molecule that inhibits JAK1/JAK3 and showed efficacy for UC, but not for CD [83,85]. To date, in the context of IBD research, a localized delivery is of high interest to minimize the systemic exposure and to improve the therapeutic efficacy at the target site of inflammation.

1.4.2 Nanotechnology-based drug delivery systems

Nanoparticle (NP)-based delivery systems are used to ensure the safe arrival to the site of action where the desired therapeutic effect can be achieved. Drug delivery formulations aimed for the GI tract are designed to protect their cargo against the inherent harsh conditions such as acidic pH or enzymatic degradation, and furthermore, to transport their cargo to the site of action. Due to their larger surface-area-to-volume ratio, NPs provide a greater surface area for the interaction with the mucosal surface as well as higher adsorption capacity for surface loading [3]. NP systems targeting the small intestine are applied to improve the oral bioavailability of drugs or biologicals, and exploit its highly absorptive function that is mediated by a variety of specialized cells, and aim for local uptake and systemic absorption [86]. Three pathways are associated with NP uptake including the paracellular (between cellular junctions), transcellular (through the cells followed by exocytosis at the basolateral site), and M cell-mediated transport [3]. Particle uptake in the GI tract showed to a greater extend the accumulation of smaller particles (100 nm) compared to microparticles (1µm) [87]. However, before reaching the intestinal epithelial cells, NPs need to penetrate the intestinal mucus barrier that is continuously renewed with an estimated turnover of 50 - 270 min [88].

Within this context, several strategies have been proposed in order to improve either mucoadhesion or mucopenetration (Fig. 1.6).

For instance, NP surface modification such as cationic charge or decoration with polymers lead to electrostatic interactions and physical chain entanglements with mucus fibers, respectively, increasing the steric hindrance within mucus (Fig. 1.6A). On the other hand, drug delivery systems comprising an anionic surface charge or dense PEG chains reduce mucus interactions via electrostatic repulsion and hydrophilic shielding, respectively (Fig. 1.6B). However, for mucopenetrating particles, a fast penetration below mucus renewal and shedding must be achieved for successful cellular contact with epithelial cells [30].

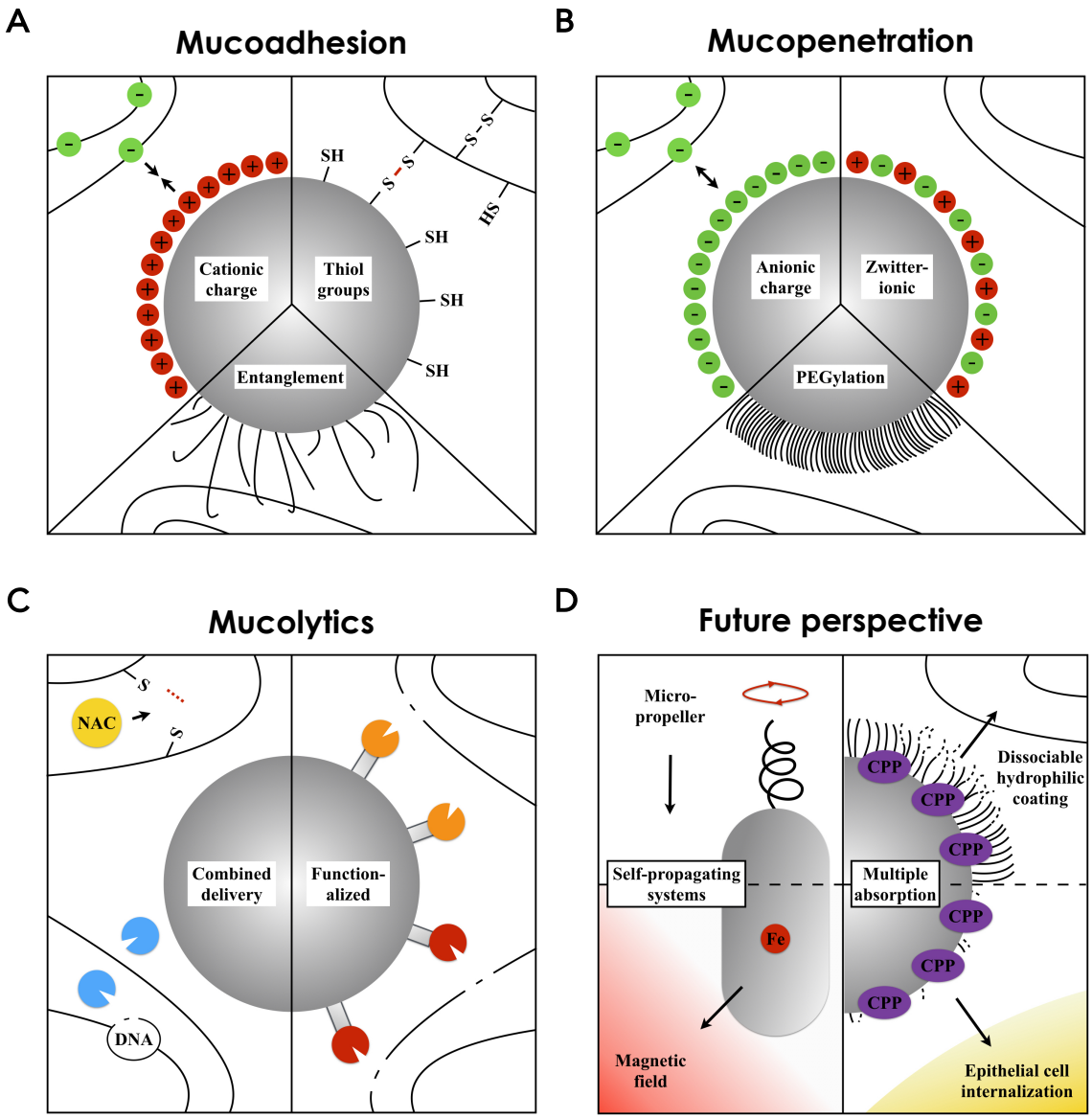


Figure 1.6 Strategies to improve drug delivery to mucosal tissues. Surface modification for mucoadhesive nanocarriers providing an increased interaction with mucus (**A**). This includes positively charged carriers (e.g. chitosan) that bind to anionic mucins based on electrostatic interactions, particles with reactive thiol groups (-SH) that attach to mucus by forming disulfide bonds, and carrier systems decorated with polymers like polyacrylic acid (PAA) that lead to physical chain entanglements with mucus fibers and increase steric hindrance. Mucopenetrative carriers aim to reduce mucus interaction (**B**). For example, highly negatively charged particles avoid mucus interaction due to electrostatic repulsion, zwitterionic carrier systems with a net neutral surface charge that facilitate the diffusion through mucus, or polyethylene glycol (PEG)ylated particles that possess a densely packed polymer chains that form a hydrophilic protective layer for effective mucus penetration. The use of mucolytic agents as adjuvants improves the diffusion of drug delivery systems through mucus by altering its structure and decreasing the overall viscosity (**C**). This includes for instance the combined delivery of *N*-acetylcysteine (NAC) that reduces disulphide bonds (S-S) between cross-linked mucins or nucleases (DNAse) that degrade DNA present in mucus. Particles that are functionalized with proteolytic enzymes (papain or bromelain) that disrupt the mucus gel structure and enhance mucopenetration. Recent advances to overcome the mucus barrier comprise self-propagating drug delivery systems or multiple

absorption strategies (**D**). For example, mirco-propeller structures mimicking flagellated bacteria or particles with incorporated iron (Fe) atoms that are attracted by external magnetic fields improving mucopenetration. Drug delivery systems that combine both mucopenetration and cellular internalization are coated with mucus-inert polymers that will dissociate while mucus permeation and epithelial absorption is subsequently facilitated by cell-penetrating peptides (CPP). (This figure was published in Murgia *et al*. [30] Copyright Elsevier 2018.)

Other strategies involve the use of mucolytics or functionalization with proteolytic enzymes in order to maximize the delivery of NPs (Fig. 1.6C). More recent advances include self-propagating drug delivery systems or multiple absorption strategies combining mucus penetration and epithelial absorption (Fig. 1.6D).

Over the last decades, nanotechnology has significantly advanced the field of IBD management, with the main goal to improve the therapeutic effect to adverse effect ratio. NPs benefit from the epithelial enhanced permeation and retention (EPR) effect which results in the accumulation within the inflamed regions of the GI tract compared to healthy tissue. The EPR effect can be explained by the defective barrier function of the epithelium with increased tissue ulceration and the decrease of the amount of the tight junction proteins [89,90]. In comparison to passive delivery into the inflamed mucosa, targeted or localized delivery is based on various strategies to increase residence time as well as the drug release within the GI tract and thus, to enhance the interaction with mucosal tissue and moreover, with distinct target cells [86]. In this line, targeting of the intestinal macrophages has presented a very efficient technique to target the inflamed sites of the GI tract [91].

In the context of IBD, a study performed in human volunteers has shown contradictory results with enhanced accumulation of microparticles (3 μm) in the inflamed mucosa compared to healthy controls and nanoparticles [92].

However, despite of all promising applications in the field of IBD, NP-based technology remains challenging due to the complex interplay of these advanced carrier systems with mucosal biological barriers.

1.5 Experimental models to investigate drug and DSS interaction

In the field of drug research, the applicability of both, *in vivo* and *in vitro* models of intestinal inflammation, is necessary to evaluate drug-related responses before clinical translation. A variety of models exist that aim for appropriate correlation with distinct human physiology, however, often lack the possibility to achieve complete resemblance as well as to reproduce existing inflammatory processes.

The first part of this section provides an overview of current experimental models that are implemented in IBD research starting first with most common *in vivo* and *ex vivo* models. The second part describes the broad range of very simple to more complex *in vitro* testing systems which are still under development and may not all implement the state of inflammation. These *in vitro* models include the application of intestinal organoids, the integration of microfluidics for dynamic models, and the co-cultivation with intestinal bacteria.

1.5.1 Most common *in vivo* and *ex vivo* models of IBD

An increasing number of IBD animal models are available to investigate specific disease-related pathogenesis including fruit flies, fish, dogs, pigs or non-human primates. Nevertheless, the majority includes mostly well-established rodent models. In contrast, fish and larger species including canine or swine models provide physiologic and immunologic functions with IBD phenotype similar to humans, but non-human primates are considered the most representative model for the study and treatment of acute and chronic intestinal inflammation [93]. To circumvent related ethical issues, the use of rodent colitis models prevails in IBD research and has facilitated the understanding of the disease mechanisms and mucosal immunity, the identification of novel therapeutic strategies, and validation of drug efficacy prior to clinical trial testing. Nevertheless, IBD mouse models provide several limitations in the context of human IBD pathophysiology.

The most common experimental IBD mouse models encompass chemically-induced and genetically engineered models mimicking certain aspects of human CD and UC. Within this context, acute intestinal inflammation can be induced through the administration of different chemicals, such as dextran sulfate sodium (DSS), trinitrobenzene sulfonic acid (TNBS) or oxazolone [94]. These widely used colitis models are useful for the screening of new drugs and share common phenotypes such as non-specific epithelial injury, diarrhea and weight loss with relatively easy setup and rapid onset of inflammation. However, the degree of intestinal inflammation depends for instance on dosage, duration, mouse strain or microbial environment, and can be determined by body weight, endoscopic or histological analysis, or by *in vivo* imaging [95,96]. Despite of immunological and histopathological similarities between chemically induced IBD models and IBD patients' phenotypes, major differences arise from the source of insult as well as from the resulting intestinal immune response [97]. To induce chronic inflammation, repeated and longer administration of the respective chemicals is required, however, the chronic phenotype remains different from humans.

For that purposes, genetically manipulated mouse models with deficiency or overexpression of particular genes showed a better reflection of human IBD including a long-lasting chronic inflammation. For example, knockout mice that lack IL-10, a key cytokine of gut homeostasis, will lead to the induction of spontaneous intestinal inflammation with transmural lesions and inflammatory cell infiltrations [98]. Another example are mucin 1 or 2 knockout mice, in which defective mucus production and epithelial barrier defects with CD-like phenotype in background strains of naïve T cell transferred $CD45RB^{high}$ mice [99], or UC-like colitis in T cell receptor chain alpha ($TCR\alpha$) mice [100]. However, many more IBD models have been established, among which germ-free mice that are colonized with specific microbial communities using human faecal transplantation, or the so called ´humanized mice´ with engrafted human immune cells [94,101].

Overall, both chemically and genetically induced models have been found effective for drug screening. Nevertheless, besides ethical considerations in terms of animal studies, there are distinct confinements related to the application of IBD animal models. Even though animal models are key components in the field of drug development and approval, the recapitulation of *in vivo* conditions similar to humans often impedes clinical translation [94,102,103]. IBD complexity including a multifactorial etiology, heterogenous phenotypic subtypes as well as diverse clinical appearances can certainly not be reflected by one experimental mouse model [96]. In addition, limitations of murine models are related to nutrition or coprophagy, since mice are herbivores and re-ingestion of nutrients affects the dietary balance as well as microbial composition, and in this line, the intestinal health [93]. Moreover, the anatomy and physiology of the mouse GI tract are different from the human counterpart such as a non-glandular forestomach, lower pH gradient from stomach to intestine, and a much larger GI size/body weight [104]. In this context, the small body size of mice requires adapted testing for conventional human dosage forms such as tablets, capsules, or pellets. Furthermore, the qualitative and quantitative measurement of therapeutic outcomes between preclinical animal studies and human clinical trials are classified in different disease remission scores, and thus, pharmacological considerations such as the route of administration, drug dosage, and biodistribution may affect treatment comparison and interpretation [101]. A major bottleneck in pharmaceutical drug testing is the translation of therapeutic outcomes generated within model systems to the human environment [105]. The remaining interspecies differences still interfere with emerging therapeutic approaches targeting distinct pathophysiological conditions of human IBD.

In comparison, *ex vivo* models are based on small amounts of human biopsies, showing good viability and functional stability within the first 24 hours [106]. Mucosal biopsies can be placed in cell culture medium and exposed to different factors triggering inflammation such as cytokines or bacterial components. Or alternatively, whole intestinal tissue samples are applied to Ussing chambers to study the barrier

function and tissue permeability following exposure to various stimuli or drug treatments. The main benefit of such *ex vivo* models is the presence of all cell types of the intestinal mucosa with necessary cellular interactions to build innate and/or adaptive immune responses. Treatment with immune-modulatory agents induced a disruption of epithelial barrier and immune cell homeostasis towards activation of innate/adaptive immune system [107]. Despite intestinal tissue is beneficial regarding its complexity, the main concerns are the limited time window for experiments, maintenance of tissue viability and challenging interpretation of the resultant data due to inter-individual differences.

1.5.2 *In vitro* models of the intestinal mucosa

A broad range of *in vitro* models of the human body are extensively used in different research field, representing a compromise between physiological resemblance and feasibility of experimental setup. One of the most important benefits regarding *in vitro* models is their potential to reduce the need of animal testing. For instance, in the field of drug delivery, toxicology, or nutraceutics there is an increasing interest to reproduce the human intestine *in vitro*. However, the recreation of intestinal physiology and, more importantly, the implementation of important features concerning intestinal disorders remains still challenging.

In the last decades, the advent of a variety of intestinal models made significant contributions to the simulation of the physiology as well as pathophysiology of the human intestinal mucosa (Fig. 1.7). Compared to animal models, *in vitro* studies allow the much higher control of experimental conditions, comprising the choice of cell type and origin, cell growth and incorporation of additional mediators to modulate distinct cellular processes. Apart from this, investigations within multicellular organisms may result in overseen or unrelated experimental outcomes, whereas the simplified context of *in vitro* models provides the precise assignment of pharmacological effects to the cells being used. In this context, the main advantage over *in vivo* models is the

combination of a well-controlled and repeatable setup with a chosen degree of complexity focussing a particular cellular response.

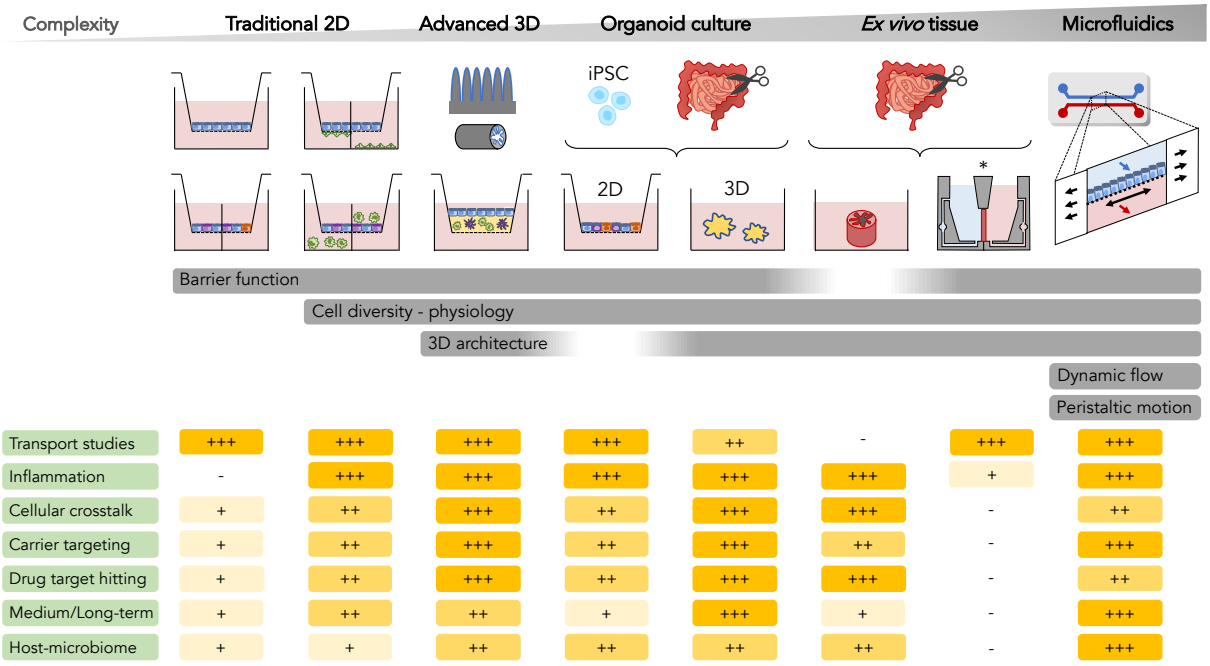


Figure 1.7 Overview of selected IBD *in vitro* models with corresponding characteristics and its applicability or relevance in drug development and delivery analysis. Increasing complexity starts from traditional 2D models based on Transwell® systems with mono-and co-cultures of epithelial and other cell types (e.g. stromal or immune cells). Advanced 3D models including villi/crypt-like structures and scaffold-based co-cultures mimicking intestinal physiology. Organoid-based technology uses induced pluripotent stem cells (iPSCs) or adult stem cells (isolated from intestinal crypts) and creates matrix-supported 3D cultures or 2D alternatives after organoid dissociation. Human biopsies of intestinal tissue that are either cultured as whole tissue explants or applied to Ussing chambers. Microfluidic devices using different cell sources and mechanical cues such as dynamic flow and peristaltic motion. Suitability of the models is classified as low (+), medium (++), high (+++) or not suitable (-). (*) Ussing chamber studies are limited in duration due to tissue viability. (This figure was published in Hartwig *et al*. [109] Copyright Elsevier 2021.)

Overall, the superiority of the *in vitro* models of the human intestinal mucosa is closely related to answering a specific question instead of recapitulating all the essential properties of the *in vivo* scenario.

For the study of orally administered drug and delivery systems non-cellular fluid models represent physiologically relevant GI fluids that mainly originated from pharmaceutical and food safety research. These synthetic fluids are mimicking various

factors in the GI lumen, such as ionic strength, pH, digestive enzymes or food composition [108]. Herewith, the effects on drug or drug carrier stability, dissolution and aggregation can be evaluated.

Regarding cell-based *in vitro* models, the complexity is ranging from simplified 2D intestinal models to complex 3D cell models, an umbrella term for different research test systems including 3D cell culture, organoids or micro-physiological systems [110]. Based on a recently conducted survey by the EU Reference Laboratory for alternatives to animal testing, these models should be properly characterized and validated for the implementation and acceptance for regulatory purposes [110].

2D in vitro models of the intestinal epithelium

The simplified context for intestinal barrier and drug interaction studies is using monolayers of distinct cell types cultured in 2D offering relatively low costs and high throughput analysis. Immortalized cell lines of the human epithelium are frequently used as either mono- or co-culture of different cell types. Along with that, 2D models can be modified by extracellular matrix (ECM)-substrates or mucus samples to improve cellular growth or include a mucus layer, respectively. Caco-2 cells with a small intestine-like signature, have been accepted by the pharmaceutical companies and regulatory authorities as the gold standard to predict intestinal drug absorption and permeation [111–113]. Caco-2 usually differentiate into enterocyte-like cells and adopt features like TJ-mediated barrier function, apical brush border formation and the expression of distinct enzymes and receptors/transporters similar to the *in vivo* phenotype [112]. Conventional approaches to create differentiated polarized epithelial cell monolayers are using Transwell®-based systems mimicking the lumen (apical) to blood orientation (basolateral compartment) of the intestinal wall. This allows the measurement of the barrier function and the intestinal permeability of drugs, toxins or microorganisms, and responsiveness to apical stimulation via release of biochemical key factors. Overall, the application of human cell lines is advantageous due to their cell accessibility throughout other laboratories, a more

standardized experimental setup and the applicability to a human exposure scenario for drug interaction studies. Nevertheless, these cell models have significant shortcomings, since cell lines may represent diverse genetic abnormalities that may not represent healthy cell behaviour. However, primary epithelial cells have very short cultivation time which makes them unsuitable for drug interaction studies [114]. Even though Caco-2 cells are widely used for pharmacological and toxicological studies, the major drawback is the lack to represent the entire diversity of the intestinal epithelium consisting of enterocytes, goblet, Paneth and enteroendocrine cells [115]. Multicellular models including mucus-secreting or microfold (M) cells are highly relevant, as the IBD onset is associated with an altered mucus thickness and composition permitting the translocation of gut microbiota into the intestinal wall [116]. Co-cultures of Caco-2 and HT29 (goblet) cells have thereby improved drug permeation studies by the introduction of a mucus layer [117–119]. Alternatively, mucus surrogate with comparable viscoelastic properties to native intestinal mucus was added on top of the Caco-2 cells representing an additional barrier for the permeation of both hydrophobic and hydrophilic drugs [120]. However, these mucus barrier models are limited due to the magnitude of the mucus layer displaying a thicker mucus layer compared to the *in vivo* scenario [30]. Co-cultures with M-like cells are intended to mimic the epithelial cells that cover gut-associated lymphoid tissues such as Peyer's patches that are necessary for antigen- and bacteria sampling from the gut lumen showing high phagocytotic and transcytotic activity [22,121]. An increased particle uptake and translocation was attributed to the presence of M-like cells [112,122,123]. However, drug delivery strategies aiming for M cell uptake should consider a limited absorption due to the low proportion of M cells in the intestinal epithelium (~1%) and the lack of specificity of many drug carriers such as nanoparticles [124,125].

In vitro co-culture models with immune cells

The cellular composition of an *in vitro* model determines the eventual experimental outcomes and the integration of the mucosal immune cells into the *in vitro* models is of high interest in order to incorporate the modulation of the innate immunity. In the human GI tract, different immune cell types, comprising tissue-resident and recruited monocyte-derived macrophages and DCs, are localized in the sub-epithelial lamina propria, whose numerical and proportional compositions are altered as a result of inflammation [126,127]. Accordingly, various techniques of co-culturing have been proposed that either use scaffold-free or ECM-based systems. The immune response can be incorporated either through direct immune cell co-culture, or else through the addition of media containing various inflammatory mediators, often obtained through previous conditioning [112,128]. This allows the investigation of cell communication mediated by the exchange of inflammatory mediators and the resultant effects on the barrier function. The human monocyte-like cell line THP-1 rather than primary-derived cells from peripheral blood monocytes (PBMCs), is frequently used to model monocytes and macrophages, and to improve the reproducibility of the experimental setup. Recently, an established co-culture of Caco-2 and PMA-differentiated THP-1 cells (dTHP-1) with macrophage-like phenotype simulated the inflamed intestine through pre-stimulation with LPS in combination of IFN-γ [129,130]. As a result of the co-stimulation, an increase of cytokine release and a decrease of the barrier function were observed offering the possibility to investigate i.a. the effects of toxic substances under diseased conditions. However, the indirect cell communication and spatial cell separation limited the physiological resemblance. More realistic reproductions involve 3D cell cultures embedded in an ECM-like substrate (e.g. hydrogels) or shaped into villus- or crypt- and tube-like scaffolds mimicking the complex structural organisation of the intestinal tissue. This provides cell-to-cell and cell-to-ECM interactions, as well as oxygen, nutrient and metabolic waste gradients [131]. These models create biomimetic intestinal interfaces with distinct biochemical gradients and provide along with cell differentiation or migration the cellular crosstalk for the study of gut

inflammation [132,133]. Thus, a complex 3D intestinal model is bridging the gap between 2D cultures and *in vivo* animal models by simulating essential features of the latter such as human-derived cell types within a substratum of ECM and epithelial/immune cell interplay [134]. A co-culture based on Caco-2 cells on top of Matrigel-embedded dTHP-1 cells was stimulated with IL-1β/LPS to mimic IBD and resulted in enhanced cytokine release (IL-6 and IL-8) [135]. Interestingly, the distribution trend and cellular uptake by both, Caco-2 and dTHP-1 cells, was comparable with the experimental TNBS colitis model. This 3D microenvironment of another setup composed of Caco-2/HT29 epithelial cells co-cultured with collagen-embedded fibroblasts/macrophages improved the expression of drug and efflux transporters such as P-glycoprotein with an impact on drug permeation [136]. Compared to 2D Caco-2 mono-cultures, a general higher permeability of low absorbable drugs and decreased permeability of moderately and high-permeable drugs was observed. However, this model represented the healthy intestinal mucosa and drug absorption was performed without disease modelling.

Villus-structured in vitro models

To reproduce intestinal tissue architecture *in vitro*, several attempts focussed on villus-structured intestinal models using different ECM scaffolds covered with an epithelial monolayer [133,137]. The enabled the study of both the paracellular and endocytotic pathways as well as the persorption of nanoparticles that may translocate through epithelial gaps due to enterocyte shedding from the villus tips [138]. For instance, a long-term triple co-culture contained a Caco-2/HT29 (3:1) epithelium and primary human fibroblasts within a tube-like silk scaffold [139]. The presence of fibroblasts supported the production of mucus, epithelial cell growth and differentiation. For the study of inflammatory processes, a long-term *in vitro* model of Caco-2/HT29 (9:1) on L-pNIPAM hydrogel and spontaneous villus-like structures for up to 12 weeks was used to create an inflammatory environment upon challenge with TNF-α/IL-1β [140]. Compared to 2D counterparts, these models offer higher resemblance to the *in vivo*

(patho)physiological condition, however, there are several limiting factors when studying the translocation of drug carrier systems therewith. For instance, the ECM matrix present in the co-culture model may impede the particle diffusion and needs to be evaluated beforehand. Furthermore, particle motility can be affected by the pore size and density of the Transwell® filter [141].

Human intestinal organoid cultures

In the last decade, more complex *in vitro* systems have been established including human organoid cultures that self-organize and recapitulate major features of native tissue and maintain genetic as well as physiological similarities. Organoids are made of a highly folded intestinal epithelium with crypt and villi formation, and a central hollow region composed of ECM substrate [134]. Structural and biochemical cues for maintenance and proliferation are required including a supportive matrix, typically Matrigel™, and several growth factors such as Wnt, R-Spondin, Noggin, and EGF [142,143]. The application of intestinal organoid technology improves the reflection of the epithelial cell complexity and enables co-culturing with other cell types and microbiota. However, the 3D spheroid architecture of human intestinal organoids makes them unsuitable for the apical-basal transport and drug permeation studies [11,144]. To overcome this limitation, organoids are mechanically disrupted and cultured on ECM-free 2D surfaces (Transwell®) which permits the addition of other cell types (immune cells or pathogens) or different stimuli, and allow for the study of inflammatory responses or drug screening [145].

The increased complexity, however, retains some limitations which could potentially impact the inflammatory response and drug interactions studies. Besides ethical aspects and limited access to primary tissue, the main drawback is the relative high variability between individual samples [7]. Moreover, organoids do not represent immune-related responses due to the lack of immune cells or connective tissue. While organoids possess more *in vivo*-like properties, difficulties may arise due to accessing human biopsies as well as their long-term cultivation [146].

Microfluidic systems of the intestine

More recently, microphysiological systems, also known as organ-on-a-chip technology, have been developed to grow cells within microfluidic channels of different shapes. These microfabricated devices combine various cell types of different origins with a microenvironmental context such as dynamic fluid flow and shear stress. Since epithelial cells experience constant mechanical forces during digestive processes, which are indispensable for cell maturation, metabolic activity, mucus production and the formation of villi-like microarchitectures [147]. In comparison to static culture conditions, the provision of dynamic fluid flow favours similar histological appearance observed in vivo (e.g. villus-formation or mucus production) [148]. In addition, a variety of compounds such as toxin or drug candidates can be applied to the microfluidic chambers, and the corresponding effects including the analysis of barrier integrity, or the production of related mediators can be validated. For instance, Caco-2-based intestine-on-a-chip models were challenged by cytokine triggers such as TNF-α, which alone or in combination with other cytokines, such as IL-1β, IL-6, IL-8 [149], IL-1β and IFN-γ [150], or bacterial LPS can promote and inflammatory state [151]. Common readouts of such an inflamed state are a compromised barrier integrity measured by TEER, and cytokine release mediated by activated cells. More recently, different co-culture setups within the OrganoPlate (Mimetas) comprising Caco-2, HT29 separated from two immune cells types, THP-1 and MUTZ-3 were developed [152]. Inflammation induction within the tubular structures by TNF-α and IL-1β, resulting in a decreased barrier function and elevated cytokine production (IL-8). This tetra-culture model based on an OrganoPlate system represents a high throughput approach interesting for pharmaceutical drug screening rather than the application of nanoparticle-mediated delivery systems.

In comparison to static culture conditions, cells placed in microfluidic devices are subjected to continuous perfusion of nutrients and simultaneous removal of waste products mimicking the physiological environment. However, the chip material as well

as ECM used might have an impact on bioassays used for drug response and their mechanisms of action, respectively [153].

In vitro co-culture models with intestinal microbiota

The incorporation of intestinal microbiota into the *in vitro* models can enable investigating their role in the development of intestinal inflammation, or else the discovery of new targets for research in the field of inflammatory and infectious diseases. However, this remains challenging for several reasons. Conventional 2D models are not suitable for the co-culture of aerobic bacteria due to the rapid bacterial overgrowth contaminating the cultures. While microfluidic devices may better reproduce intestinal inflammation and bacterial overgrowth, the integration of obligate anaerobic bacteria still remains hard to achieve [7]. Regarding these challenges, a short-term triple-culture consisting of Caco-2/HT29/stromal cells within a tube-like scaffold, and the anaerobic gut microbiota (pathogenic *Yersinia* or probiotic *Lactobacillus*) provided the investigation of the epithelium with gut-colonizing bacteria [139]. Compared to 2D epithelial cell layers, this model showed lower oxygen tension measurements in the luminal space with aerobic culture conditions. However, to study the luminal exposure of microbial products or microbes within the organoid cultures, micro-injections into the lumen are required, which still remains challenging [154]. Moreover, in the context of gut microbiome diversity and IBD-related dysbiosis, the representation of distinct or individual microbial composition remains hard to achieve *in vitro* due to potential bacterial overgrowth and/or requirements for culture conditions regarding anaerobic bacterial community.

There are only a few studies on nanodrug formulations using 3D co-culture models comprising immune cells. A co-culture model based on PBMC-derived macrophages and DCs embedded in a collagen matrix and covered with Caco-2 cells was developed to study the inflammation process [155,156]. The co-culture was exposed to inflammatory stimuli using IL-1β, thereby generating an inflamed model with IBD

characteristics including decreased epithelial barrier function and enhanced cytokine production. The therapeutic efficacy of anti-inflammatory nano-formulations was compared with the free drug and showed increased deposition of the former in the inflamed model. Later, this model was improved through the exchange of the primary immune cells with cell line-derived macrophage- (dTHP-1) and dendritic-like MUTZ-3 cells in order to enhance the reproducibility and to enable a better assessment of the cytotoxicity of nanomaterials [157].

Taking all the debated factors into consideration, the ideal *in vitro* intestinal model for biomedical research should be robust and comprehensive, reflect the healthy and pathophysiological characteristics of the human intestine, and provide a predictive setup for human responses that are aimed to be studied. Mimicking chronic inflammation during IBD requires longer-term inflammation models. Furthermore, to enable the clinical translation of *in vitro* findings, high standardization and reproducibility of the experimental setups along with high throughput application is required.

1.6 Aim of the thesis

Besides ethical considerations of animal models, interspecies differences still interfere with emerging therapeutic approaches targeting distinct pathophysiological conditions of human IBD. *In vitro* models of the human intestinal mucosa are closely related to answering a specific question instead of recapitulating all the essential properties of the *in vivo* scenario. The simplified context of *in vitro* models allows the combination of a well-controlled and repeatable setup with a chosen degree of complexity mimicking the physiological counterpart. Beyond that, the implementation of important features regarding intestinal disorders provides the precise assignment of pharmacological effects focussing particular interaction sites and cellular responses. This promotes the understanding of underlying mechanisms and responsibility of single factors providing detailed insights that may be overseen in animal models.

The aim of this thesis was the development of suitable *in vitro* equivalents as preclinical testing platforms investigate the capacity of drugs and delivery systems (DDS) to overcome the intestinal barriers for an efficient therapeutic outcome. Guided by the principle of reduced complexity, the assessment of DDS was broken down into three testing steps: i) mucus penetration, ii) uptake or transport through the epithelial cells, and iii) develop a readout for proving biological function (JAK1-knockdown). For that purpose, appropriate samples/models and methods needed to be identified and implemented.

Regarding the intestinal mucus barrier, different *in vitro* models ranging from simple setups to more complex cell-based systems were tested to fulfil important requirements such as reproducibility and physiological resemblance. Within this context, various mucus sources including porcine intestinal mucus, its surrogate, or cell-secreted mucus were investigated in terms of their suitability to access diffusive properties of DDS.

Considering the intestinal (sub-)epithelial barrier, a complex *in vitro* model of the human intestinal interface was used to investigate the barrier crossing in a first

attempt. Pro-inflammatory stimulation of the tight barrier model did not reflect the higher permeability of the inflamed *in vivo* scenario. As a consequence, the model was adapted to the so-called leaky gut model representing more severe epithelial damage and thus, allowing some barrier crossing. This included a proper model characterization and the assessment of intestinal barrier crossing of DDS.

For the provision of a good quantification of target engagement, a functional readout on the molecular target was aimed for rather than the less specific marker of TEER used in earlier studies. In order to determine these effects, co-culture was dissociated, and respective cells were released allowing the measurement of the STAT-phosphorylation as a downstream signal of JAK. Such readout was hypothesized to be more sensitive and specific to measure even moderate drug effects.

The developed *in vitro* test systems were used to test the nanomedicine and DDS of the NEW DEAL consortium, being a JAK1 siRNA targeting the pivotal JAK/STAT signaling pathway and nanostructured lipid particle.

The following chapters will focus on the characterization of respective intestinal barrier models and their application to study the interaction with nanomedicine:

Part I. Characterization of different intestinal mucus sources in terms of reproducibility and physiological resemblance, and investigation of mucus-particle interaction.

Part II. Development of leaky gut model mimicking severe IBD pathophysiology including an impaired epithelial barrier function and responsiveness to inflammatory stimuli.

Part III. Application of leaky gut model mimicking severe IBD pathophysiology and exploration of nanomedicine interaction as well as therapeutic efficacy including the establishment of a functional assay.

2 Part I - Interaction studies of nanoparticles with GI mucus

Parts of this chapter have been addressed in the following original peer-reviewed publication:

Huck BC *, **Hartwig O** *, Biehl A, Schwarzkopf K, Wagner C, Loretz B, Murgia X, Lehr CM. Macro- And Microrheological Properties of Mucus Surrogates in Comparison to Native Intestinal and Pulmonary Mucus. Biomacromolecules, 20(9), pp. 3504–3512. doi: 10.1021/acs.biomac. 9b00780. (* contributed equally)

Main contributions to this publication: OH performed all GI mucus-related experiments, analyzed corresponding data, and wrote/edited the manuscript.

2.1 Introduction

Mucus is a complex biological material that lines all wet epithelial surfaces of the human body, including the eyes, the respiratory, cervicovaginal and GI tract, and prevents the penetration of microorganisms and noxious substances. Its main components include, irrespective of the mucus source, water (90 - 95%), electrolytes (~1%), lipids (1 - 2%), and various proteins such as glycoproteins (mucins; 1 - 5%) and non-mucin proteins, and cellular debris (e.g. DNA or lipids) [36,158]. Mucin glycoproteins are secreted by the mucosal epithelia and constitute the major structural component which determines the viscoelastic property of mucus [36]. However, mucus composition, pH, mucus layer thickness, and mucus clearance mechanisms vary according to specific functions required at the anatomical site [30]. Besides its protective function for the underlying epithelia against digestive secretions or invading pathogens, GI-secreted mucus lubricates the intestinal wall and facilitates the passage of food, and harbours a huge amount of microbial community [32,41]. The proper functions of the mucus barrier, however, are related to its dynamic feature which implies a constant renewal and shedding of mucus in order to support the clearance mechanism [30]. In the context of IBD pathophysiology, defects in mucus production or processing were observed with either reduced mucus production for UC or increased levels for CD patients, however, with similar results regarding the translocation of bacteria [42–44].

In spite of this, a proper knowledge of mucus interactions is highly requested for orally administered drugs and corresponding delivery systems. The heterogeneity of mucus provides multiple interactions sites for drugs and DDS (interaction filtering) and in addition, its mesh-like structure controls their diffusion through the mucus layer (size filtering) [30]. From this perspective, different methods and techniques have been established to investigate the interaction of drugs and drug carrier systems within the mucus network. Several *in vitro* models of the intestinal mucus were proposed with different physiological resemblance ranging from simplified solutions of reconstituted mucins or isolated animal GI mucus to mucus-secreting cell-based models, *ex vivo*

mucosal tissues, and *in vivo* murine models [35,159]. Aside from traditional drug-mucus interaction studies such as diffusion cells experiments with donor-to-acceptor strategy (Ussing chambers, Franz diffusion cells, or Transwell® setups), the mobility of drugs and nanocarriers can be investigated by microrheological analysis such as multiple particle tracking (MPT) [30]. In general, mucus models should ideally recapitulate the native human mucus including the compositional as well as structural features. Nevertheless, *in vitro* intestinal models still require standardized protocols with regard to mucus isolation procedure and storage conditions, and show limitations regarding interindividual variations and reproducibly [160–162]. At the same time, the selected model is limited by the ease of use, experimental variability, as well as the corresponding detection method [159].

This section presents different mucus sources as well as different experimental methods to study the interaction of nanomedicine with the intestinal mucus barrier. Depending on the physicochemical properties of drug carrier as well as cargo, the penetration across the mucus barrier might be compromised. Thus, in the context of mucosal drug delivery, the evaluation of mucoinert or -adhesive properties represent an important step within the drug development and validation process. With this context, native and artificial mucus samples were first characterized in terms of their structural properties by means of macrorheological bulk analysis. Furthermore, the application of tracer particles provided valuable insights in the microrheology of respective mucus samples. Beyond mucus characterization, the diffusion of siRNA-loaded lipid nanoparticles (LNPs) through mucus was evaluated in an in-house manufactured Transwell®-based diffusion setup. In line with that, the use of dynamic light scattering provided another method to quantify the interaction between siRNA-LNPs and mucins. For better understanding of nanomedicine-mucus interaction, the combined effects of cellular and mucus barrier were additionally tested in the intestinal barrier model based on mucus-secreting cells.

In summary, the collection of experimental data derived from various *in vitro* models and techniques provided the possibility to characterize the impact of intestinal mucus on drug and drug carrier diffusion.

2.2 Material and Methods

2.2.1 Materials

4-(2-hydroxyethyl)-1-piperazineethanesulfonic acid (HEPES) and microscope slide were ordered from Carl Roth (Karlsruhe, Germany). Calcium chloride ($CaCl_2$), magnesium sulfate ($MgSO_4$), sodium chloride (NaCl), cholesterol, mucin from porcine stomach (type II), linoleic acid, Alcian blue 8GX, glutaraldehyde (16%), hexamethyldisilazane (HMDS), 4',6-Diamidino-2-Phenylindole Dihydrochloride (DAPI), and bovine serum albumin (BSA), saponin, TRITC-conjugated Phalloidin were from Sigma-Aldrich (Taufkirchen, Germany) and Tween 80 from Cealo (Hilden, Germany). Polyacrylic acid (PAA; Carbopol 974P NF) was purchased from Lubrizol (Brussels, Belgium) and phosphatidylcholine (PC) from Lipoid (Ludwigshafen, Germany). 1.0 × 1.0 cm Gene Frame chambers (25 µL) were ordered from Thermo Fisher Scientific (Waltham, USA). The nylon mesh filter (30 µm mesh size; 20% open surface) was purchased from A. Hartenstein (Würzburg, Germany). HT29-MTX-E12 (12040401) were ordered from European Collection of Authenticated Cell Cultures (ECACC, Salisbury, UK). Human colorectal adenocarcinoma cell line Caco-2 (HTB-37) was obtained from American Type Culture Collection (ATCC, Manassas, USA). Red fluorescent (Ex 580/Em 605), carboxylate-modified (COOH) polystyrene microspheres (FluoSpheres®; tracer particles (FS); stock 2% solids) with a nominal diameter of 100, 200, and 500 nm were ordered from Invitrogen (Carlsbad, USA). Transwell® Permeable Supports (#3460; polyester (PET) membrane with 0.4µm pore size) were purchased from Corning (New York, USA). Paraformaldehyde (PFA) was obtained from Electron Microscopy Sciences (Hatfield, USA). FITC-conjugated wheat-germ agglutinin (WGA) was purchased from Vector Laboratories (Burlingame, USA).

2.2.2 Preparation of biosimilar mucus (BS)

Biosimilar mucus was prepared as mucus surrogate according to the protocol published by Boegh *et al*. [120]. Briefly, two different 10 mM HEPES buffers were

prepared containing 1.3 mM $CaCl_2$, 1.0 mM $MgSO_4$, with and without 137 mM NaCl, termed buffer A and B, respectively. First, 90 mg of PAA was dissolved in buffer B under magnetic stirring at 800 rpm and 500 mg (w/v) porcine gastric mucin type II was added. After complete dissolution, the pH was adjusted to 7.0 by adding NaOH. A lipid mixture was prepared separately in buffer A containing a final concentration of 0.11% (w/v) linoleic acid, 0.36% (w/v) cholesterol, 0.18% (w/v) PC, and 0.16% Tween 80. Finally, the lipid mixture was added to the PAA/mucin solution, followed by addition of 3.1% (w/v) BSA and pH adjusted to 7.4 with NaOH. After preparation, biosimilar mucus was stored overnight (ON) at 4 °C and used the day after for experiment.

2.2.3 Isolation of porcine intestinal mucus (PIM)

Native porcine intestinal mucus was isolated from the small intestine of four different Swabian-Hall swine (body weight 30−40 kg) at the Institute of Clinical and Experimental Surgery (Saarland University Medical Center, Homburg, Germany) based on published protocol [120]. Immediately after euthanasia, the surgeon performed a laparotomy and removed around 1 meter of the proximal jejunum. For the isolation of native mucus, the small intestine was cut into shorter pieces of around 10 cm. Intestinal fragments were opened longitudinally using a scissors and stretched out carefully. The mucosal surface was gently rinsed with isotonic buffer A (2.2.2) and the mucus scraped carefully from the luminal side using a spatula. Aliquoted samples were stored at −20 °C and thawed at 4°C ON prior to experiments.

2.2.4 Cell culture of goblet cells, staining and collection of cell-derived mucus

The goblet cell line HT29-MTX-E12 was cultured in DMEM supplemented with 10% FCS and 1% NEAA. Sub-confluent cells (70-80%) were passaged once a week using trypsin-EDTA. Detached cells were centrifuged at 300 x g for 4 min and passaged with splitting ratio of 1:10. Cell culture medium was replenished every second or third day.

Caco-2 HTB-37 were cultured at the same culture condition and split weekly with a ratio of 1:20. For co-culture experiments in Transwell® systems, HT29-MTX-E12 and Caco-2 HTB-37 cells were mixed prior to seeding to yield a cell ratio of 1:1 with a seeding density of 6 x 10^4 cells/well. Measurement of transepithelial electrical resistance (TEER) of mono- and co-cultures are described in detail below (3.2.4).

Cell-derived mucus was visualized by Alcian blue staining, a positively charged phthalocyanine dye intended to stain anionic sites of mucins (acidic moieties) according to published protocol by Walczak *et al*. [163]. After pre-determined cultivation, cell layer was gently washed with PBS and fixed with 3% (v/v) PFA for 15 min at RT. Cells were incubated with 1% (w/v) Alcian blue solution in 3% (v/v) acetic acid for 15 min, followed by washing steps. Transwell® membrane plus cell layer was cut out from the insert and images were collected using a stereomicroscope (Model SZX7, SZX2-ILLTQ, Olympus Corporation, Tokyo, Japan).

For mucus collection, HT29-MTX-E12 cells were cultured in cell culture dishes with a growth area of 55 cm^2 (5 x 10^6 cells/dish). After 10 day of cultivation, cell-secreted mucus was collected using a cell scraper and gently removed from the cell layer. Aliquoted samples were stored at −20 °C and thawed at 4°C ON prior to experiments.

2.2.5 Particle characterization using light scattering

LNPs with some cationic lipid component and polyethylene glycol (PEG) surfactants as published by Delmas and colleagues [164,165] were used for siRNA delivery and fluorescent label added [166], when indicated. For LNP loading with siRNA, a specific JAK1-targeting siRNA obtained as previously described in Clément *et al*. [167] or a non-targeting control siRNA (siNEG) was used. Both, siRNA duplexes containing 3´-cholesterol modification on the sense strand were synthesized and purified by RNAse-free HPLC at IDT Technologies (Coralville, USA). LNPs and respective siRNA were complexed (termed ´nanoplexes´) by simple mixing. As recommended by NEW DEAL project partners, N/P ratio of 8 (N/P 8) indicating the ratio of positive charge (N: amino

groups of LNPs) to negative charge (P: phosphate groups of siRNA) was selected for the experiments.

Fluorescent tracer particles (FluoSpheres®; FS) and LNPs were characterized for hydrodynamic diameter and zeta potential using dynamic light scattering (DLS) and electrophoretic light scattering (ELS), respectively (ZetaSizer Nano ZSP; Malvern Instruments, Malvern, UK). For measurements, particle dispersion was diluted in PBS (DLS) or MilliQ water (ELS) with a final concentration of 50 µg/mL for FS and 70 µg/mL and 1 mM NaCl for LNPs, respectively (Table 2.1).

Table 2.1 Characterization of fluorescent lipid nanoparticles (blank and siJAK1-loaded LNPs; nanoplexes) and polystyrene tracer particles (FS) of different sizes (mean ± SD)

	Hydrodynamic diameter [nm]	Poly dispersed index (PDI)	Zeta potential [mV]
40 nm LNPs	35.3 ± 0.31	0.176 ± 0.005	+35.4 ± 1.93
Nanoplexes N/P 8	80.2 ± 4.88	0.305 ± 0.045	n.a.
100 nm FS	108.2 ± 0.59	0.026 ± 0.020	n.a.
200 nm FS	214.4 ± 3.40	0.018 ± 0.014	−28.7 ± 2.37
500 nm FS	537.6 ± 15.5	0.046 ± 0.013	−34.0 ± 0.46

2.2.6 Macrorheology of intestinal mucus samples

Bulk rheology was measured using an Anton Paar MCR 702 rheometer (Graz, Austria) equipped with a cone-plate geometry (diameter: 25 mm, cone angle: 2°). A volume of 150 µL of mucus was placed between the measuring units. Potential mucus dehydration during the measurement was prevented using a low viscosity silicon oil. All experiments were performed at 25°C within the linear viscoelastic region (VLR) of the mucus samples determined by amplitude strain sweeps in a range of 0.1 – 10% strain (γ) with a frequency (ω) fixed at 1 Hz (= 6.25 rad/s). Elastic/storage (G') and viscous/loss (G'') moduli were determined by frequency sweep experiments with

increasing oscillation frequency in a range of 0.5 – 50 rad/s at γ = 1%. Complex viscosity (η^*) was computed according to equation (1) for viscoelastic samples:

$$\eta^* = \frac{\sqrt{(G')^2+(G'')^2}}{\omega} \qquad (1)$$

2.2.7 Microrheology of intestinal mucus samples

The Brownian motion of tracer particles was investigated in mucus samples by means of multiple particle tracking (MPT). A volume of 25 µL of either native or biosimilar mucus was mixed with 1 µL of the tracer particles (0.1% w/v) and placed within a 1.0 × 1.0 cm gene frame chamber mounted on a microscope slide. The chamber was sealed with a cover slip and equilibrated for 2 h prior to video microscopy. Measurements were performed using an inverted fluorescence microscope (Eclipse Ti-S; Nikon, Tokyo, Japan) equipped with a Nikon Intensilight 130 W mercury lamp and 40X S-plan Fluor Nikon objective (NA 0.6) or 60X NIR Apo Nikon objective (NA 1.0). Particle movement was captured by short tracking videos of ≥10 s length at a frame rate of 50 frames per second (fps) with an Orca R2 monochrome 1.3 MP CCD camera (Hamamatsu; Hamamatsu City, Japan) at a resolution of 0.135 µm per pixel. To improve the quality and digital readout of the video files, pre-processing was performed by adjusting brightness as well as contrast and by applying a Fast Fourier Transform bandpass filter available at ImageJ as described by Ho *et al*. [168]. 2D particle displacement within the x/y direction at each frame was obtained using *ParticleTracker* from *MOSAIC ToolSuite* (Plugin for ImageJ) developed by Sbalzarini and Koumoutsakos [169]. Individual particle movement (trajectory) was converted to a time-averaged mean squared displacement (MSD or $\Delta r^2(\tau)$) using a custom-developed *Python* script, where (τ) is the time scale (or lag time) over which the particle movement was calculated, and where Δx and Δy are particle displacements in x and y directions, respectively:

$$[\Delta r^2(\tau)] = (\Delta x^2 + \Delta y^2) \qquad (2)$$

Resulting MSD was plotted on a double logarithmic scale and the slope of each individual MSD trajectory (α) was determined as:

$$\alpha = \frac{dlog\Delta r^2(\tau)}{dlog\,(\tau)} \qquad (3)$$

and describes the extent of particle diffusion depending on viscous and elastic proportions of the tracking medium. An α-value equal to 1 describes unrestricted thermally driven Brownian motion, whereas α < 1 indicates hindered or sub-diffusive motion. The effective diffusivity (D_{eff}) for each particle is related to MSD as:

$$\Delta r^2(\tau) = 4D\tau \qquad (4)$$

2.2.8 Determination of mucin content by Periodic Acid Schiff (PAS)

Periodic Acid Schiff (PAS) assay was used to quantify the concentration of mucin glycoproteins (neutral) within native intestinal mucus, according to the protocol of Kilcoyne *et al*. [170]. Porcine gastric mucins were dissolved in PBS to prepare the standard curve in a range of 0.2 – 6.25 mg/mL. 100 µL of standard or mucus sample were placed in a 96-well plate well and oxidized with freshly prepared 0.06% (v/v) periodic acid in 7% (v/v) acetic acid. After periodic acid oxidation for 1.5 h at 37°C, the Schiff Reagent was added and incubated for 40 min at RT. The absorbance was read at 555 nm using a Tecan microplate reader Infinite M200Pro (Tecan, Crailsheim, Germany). Data is represented as mean ± SD of triplicates of three different native mucus isolations.

2.2.9 Morphological analysis of mucus using scanning electron microscopy (SEM)

The ultrastructure of mucus was investigated via scanning electron microscope (SEM) according to published protocol by Murgia *et al*. [171]. Undiluted porcine intestinal and biosimilar mucus were directly placed on a SEM stub and freeze-dried ON (Alpha 2-4 LSC, Christ, Osterrode am Harz, Germany) and stored at -20°C until use. Afterwards, freeze-dried mucus was gold-sputtered (QUORUM Q150R ES, GaLa Instrumente GmbH, Bad Schwalbach, Germany) and images were captured at 5 kV accelerating voltages using SEM (EVO HD15, Zeiss, Oberkochen, Germany).

For the visualization of cell-secreted mucus of goblet cells (HT29-MTX-E12), cells were grown in Transwell® systems (2.2.4) and after pre-determined cultivation, prepared for SEM imaging. After cell culture medium removal, cells were fixed with 3% (v/v) glutaraldehyde in PBS for 2 h at RT. After undergone EtOH series dehydration (30 – 100%) with 10 min for each step, cells were dried ON using hexamethyldisilazane (HMDS). The cell layer plus PET membrane of the Transwell® insert were carefully cut out and mounted on SEM stubs for gold-sputtering and SEM imaging as described above.

2.2.10 Transport study of particles across intestinal mucus layer

The investigation of particle interaction with mucus was performed on a macro-scale transport of nanoparticles across the mucus layer. The time-dependent vertical penetration of nanoparticles was investigated using a modified diffusion setup that combines the plastic frame of a Transwell® insert with a 30µm nylon filter mesh. First, an exact volume of mucus (113 µL) using positive displacement multipipette was placed to the donor compartment resulting in a layer thickness of ~1 mm. 500 µL of nanoparticle dispersion in PBS of defined concentration was placed carefully on top of mucus layer and 1.5 mL of PBS was added to the acceptor compartment. Mucus permeation was studied for incubation at RT in static condition and samples were removed at pre-determined time points (0, 2, 4, 8, and 24 h) from the acceptor

compartment (0.2 mL) and immediately replaced using the same amount of PBS. The collected samples were analyzed for fluorescence with a Tecan microplate reader Infinite M200Pro (Tecan, Crailsheim, Germany) at specific wavelengths (nm). According to the incorporated fluorescent dye, tracer particles (red fluorescent FluoSpheres®; FS) and DiI-labeled lipid nanoparticles (LNPs) were detected at Ex 570/Em 610 and Ex 520/Em 570, respectively. Serial dilutions of nanoparticles were used for the preparation of calibration curves and for the quantification of particle permeation. The cumulative permeation (%) of nanoparticles was calculated by taking the dilution upon sampling into consideration and plotted versus time.

2.2.11 Particle interaction within mucin glycoproteins

The investigation of particles interaction with mucin glycoproteins was investigated by means of Nanoparticle Tracking Analysis (NTA; Nanosight LM-10; Malvern Instruments, Malvern, UK) equipped with a 532 nm laser as published recently by Ho and Christmann *et al.* [172]. In brief, DiI-labelled blank LNPs or nanoplexes (complexed with siRNA at N/P ratio of 8 using either siJAK1 or siNEG; 94 nM) and red fluorescent tracer particles (FS) (Table 2.1) were mixed with 0.1% (w/v) gastric mucin solution in PBS (final concentration: 62.5 µg/mL LNPs and 50 µg/mL FS) and particle movement (Brownian motion) was measured in fluorescence mode without (PBS only) or in presence of mucin fibres. A mucin control (without particles) was performed at both, scatter light mode and fluorescence mode, in order to show the complete reduction of background fluorescence upon the application of the fluorescence mode. Videos were recorded with a duration of 30 s and analyzed by NanoSight Software NTA 3.3. Data is represented as mean ± SE.

2.2.12 Nanoparticle uptake in cell-based intestinal barrier model

For particle interaction studies with cell-derived mucus and cellular uptake, co-culture of HT29-MTX-E12 and Caco-2 HTB-37 cells were mixed prior to seeding to yield a cell ratio of 1:1 with a seeding density of 6 x 10^4 cells/well. After pre-determined

cultivation, 100 nm and 500 nm fluorescent tracer particles (FS) or 40 nm blank LNPs (Table 2.1) were applied from the apical site and incubated for 4 h (100 µg/mL). Particle suspension was removed, and cells were washed with PBS. Before fixation, cells were stained with FITC-WGA for 10 min at 37°C at a final concentration of 10µg/mL which binds to the cell membrane as well as to mucins [34]. Afterwards, cells were fixed with 3% PFA (v/v) in PBS for 15 min at RT, stained for cell nuclei (DAPI; 0.5 µg/mL). For additional cytoskeleton staining, cells were first permeabilized with 1% (w/v) BSA 0.05% (w/v) saponin in PBS for 20 min at RT and afterwards stained with TRITC-conjugated Phalloidin for 30 min at RT. Cell were mounted and analyzed with confocal laser scanning microscopy (CLSM; Leica TCS SP8; Leica, Mannheim, Germany).

Particle fluorescence was detected using HyD detectors with emission filters between 570-600 nm (561 nm laser) and 660-685 nm (633 nm laser) for red fluorescent tracer particles and DiD-LNPs, respectively. DAPI, FITC-WGA, and TRITC-Phalloidin were detected with emission filters between 440-500 nm (405 nm laser), 520-550 nm (488 nm laser), and 570-600 nm (561 nm laser), respectively. Untreated co-culture (without particles) served as a control for CLSM settings to avoid unspecific background signal. Recorded z-stacks are represented in top or side view with merged fluorescence signals for particles (red), cell membrane/mucins (green) and cell nuclei (blue). Images were acquired at 1024×1024 resolution using a 25x water immersion objective (Fluotar VISIR 25x/0.95). Confocal imaging was performed by collecting images from multiple optical planes in the z-dimension (z-stacks) with a thickness of around 100 µm and 0.57 µm z-step size.

Image analysis was performed using software Leica Application Suite X (LAS X; Leica, Mannheim, Germany). Image sequences acquired from z-stack scans were merged to create a 3D reconstruction of the specimen and adjusted in terms of fluorescence intensity, rotation in all dimensions, such as top (xy-) or side (xz/yz-dimension) view of 3D volume projections and exported as tiff files.

2.3 Results

2.3.1 Macrorheological characterization of different intestinal mucus sources

Mucus samples from different sources were characterized in terms of their rheological properties in order to identify the most suitable model in terms of physiological resemblance and reproducibility necessary for the interaction study of drug and drug delivery systems. Figure 2.1 points out the chosen mucus samples as alternatives to human intestinal mucus and related isolation or preparation procedures.

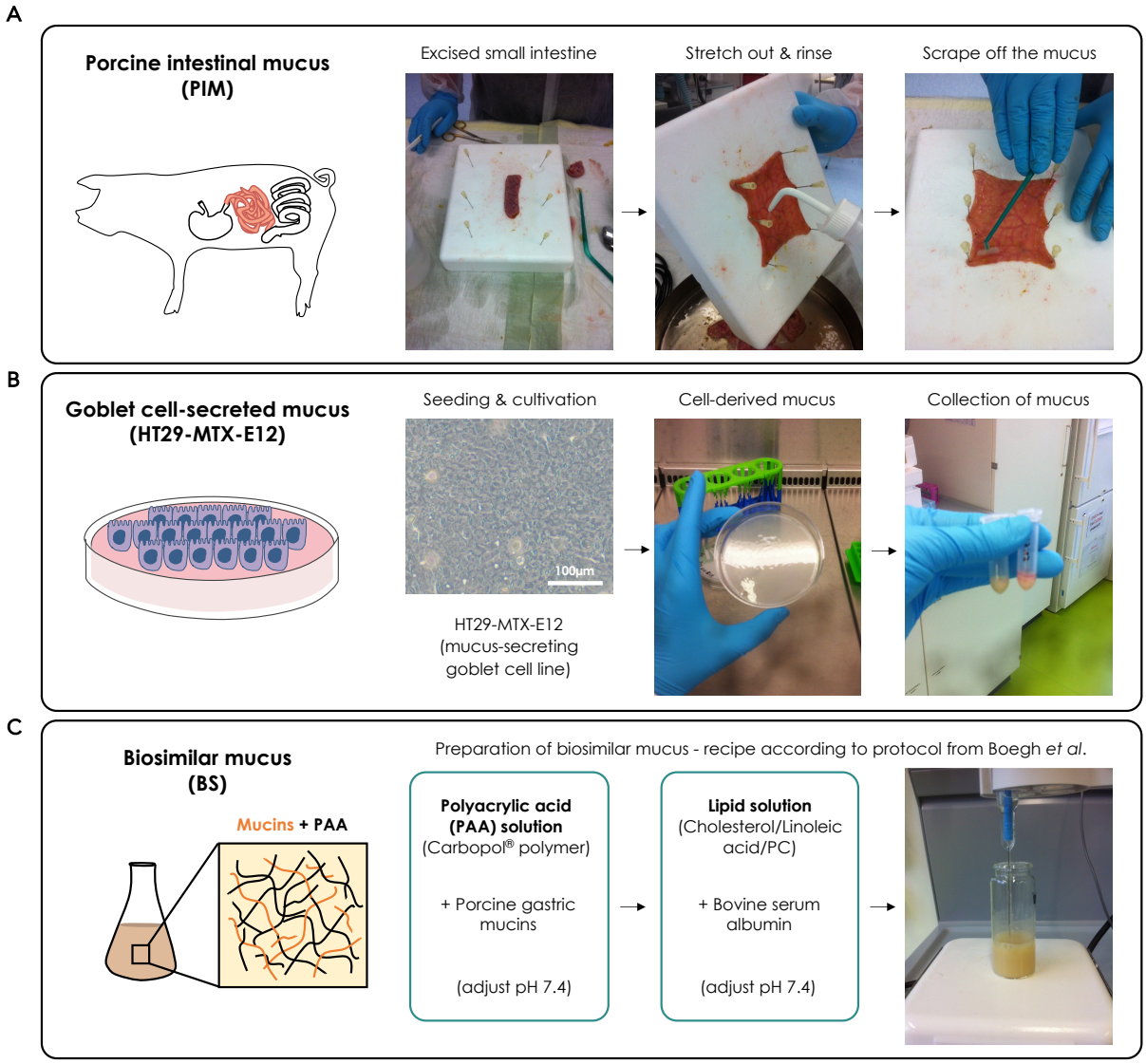


Figure 2.1 Different sources of mucus as alternatives of human intestinal mucus. Native intestinal mucus was isolated from adult pigs (porcine intestinal mucus; PIM) by scraping of the mucus layer from the luminal wall (**A**). Cell-derived mucus was collected from the mucus-secreting cell line HT29-MTX-E12 after cultivation (**B**). Mucus surrogate (biosimilar mucus; BS) was prepared according to the published recipe of Boegh *et al.* [120], a mixture of mucins, polyacrylic acid, lipids, and bovine serum albumin (**C**).

Native intestinal mucus was collected from excised non-fasted porcine intestines and gently scraped off from the mucosal surface resulting in several millilitres from one meter of small intestine (Fig. 2.1A). Cell-secreted mucus was produced *in vitro* by the goblet cell line HT29-MTX-E12 and collected after distinct cultivation time (Fig. 2.1B). However, the collection procedure was difficult and very low yield of cell-derived mucus (approximately 100mL/dish) were obtained. Motivated by the inaccessibility to native intestinal mucus, Boegh and co-workers developed a so called biosimilar mucus (BS) composed of mucins, polyacrylic acid (PAA), lipids and non-mucin proteins such as bovine serum albumin (BSA) representing a rheological profile close to porcine intestinal mucus (PIM) [120,173] (Fig. 2.1C). Compared to the other mucus sources, BS was prepared in a volume of 10 mL per batch one day before analysis which represented the highest amount of mucus yield.

For quality control, the macrorheological behaviour of all three mucus samples was investigated. Using a cone-plate rheometer, an exogeneous stress (oscillation) was applied to mucus samples in order to characterize mucus on the bulk rheological level (Fig. 2.2A). Oscillatory shear experiments provided information about the storage (G´) and loss (G´´) moduli describing the elastic and viscous portion of the viscoelastic mucus, respectively.

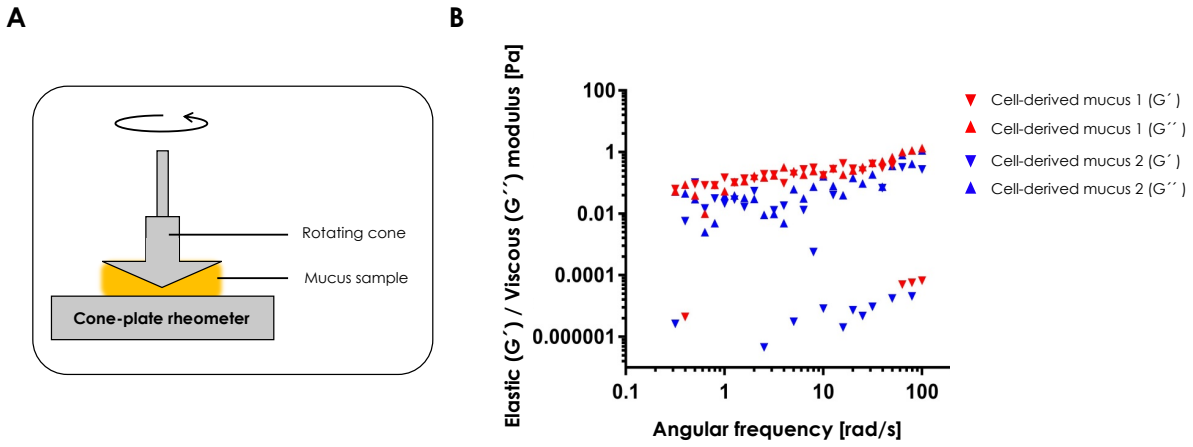


Figure 2.2 Rheological profiling of cell-secreted mucus derived from HT29-MTX-E12 cells. Scheme of macrorheological measurements of mucus samples using a cone-plate rheometer (**A**). Elastic (G´) and viscous (G´´) moduli in a frequency range of 0.3 – 100 rad/s (**B**). The corresponding results show the measurements from two independently collected mucus samples.

First investigations revealed that HT29-MTX-E12-secreted mucus collected from goblet cells lacked the typical viscoelastic properties of mucus and showed partially viscous dominant behaviour (Fig. 2.2B). Hence, this cell-derived mucus source was excluded from subsequent studies.

All subsequent rheological measurements were performed within the linear viscoelastic region (LVR) that determines the range in which the mucus sample remains unaffected by the macroscopic shear deformation. Figure 2.3 displays strain sweep experiments with storage (G´) and loss (G´´) moduli as a function of strain (0.1 – 10%) and constant frequency (1 Hz) for native intestinal mucus in comparison to its surrogate. For native mucus, G´ and G´´ moduli were independent of the applied strain and showed a constant plateau value for 0.1% to approximately 5% strain (Fig. 2.3A). Compared to that, LVR of artificial mucus displayed an earlier deformation and changes for both measured moduli at ~3% strain (Fig. 2.3B).

In this context, subsequent frequency sweep experiments determining G´ and G´´ moduli were performed at constant strain rate of 1%.

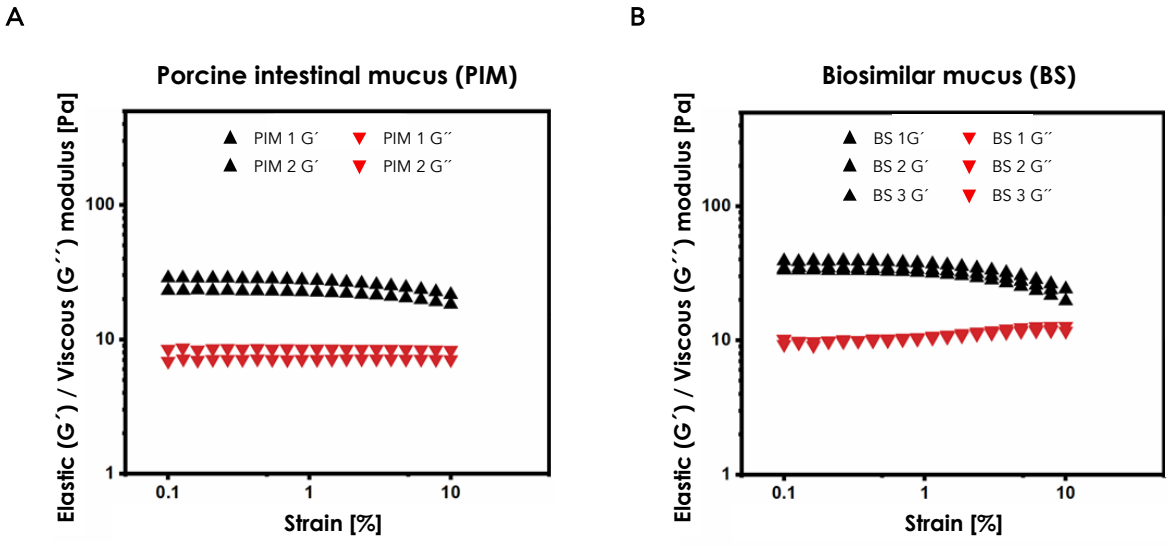


Figure 2.3 Determination of the linear viscoelastic region (LVR) of native mucus and its surrogate. Amplitude strain sweep measurements of porcine intestinal mucus (PIM) (**A**) and biosimilar mucus (BS) (**B**) showing elastic (G´) and viscous (G´´) moduli at a strain amplitude sweep of 0.1 – 10% with a constant angular frequency at 6.28 rad/s (= 1 Hz). Within the LVR, G´ and G´´ are constant indicating the range where the structure of the mucus sample is maintained.

Accordingly, mucus was exposed to an angular frequency ranging from 0.3 – 100 rad/s at constant strain of 1% (Fig. 2.4). As a result, both mucus samples showed an elastic dominant behaviour indicated by G´ > G´´ in the range of frequency measured and represented a gel-like structure related to viscoelastic solid material (Fig. 2.4A). In comparison to the mucus surrogate with reduced batch-to batch deviation, intrasample variations were observed for PIM samples (Supplementary Information; SI Fig. 1). For both, native mucus and surrogate, elastic (G´) and viscous (G´´) moduli were frequency-dependent in a frequency range of 0.3 – 50 rad/s (Fig. 2.4A). Fig. 2.4B displays very similar progressive shear-thinning and solid-like behaviour of both mucus samples in the frequency range of 0.3 – 100 rad/s.

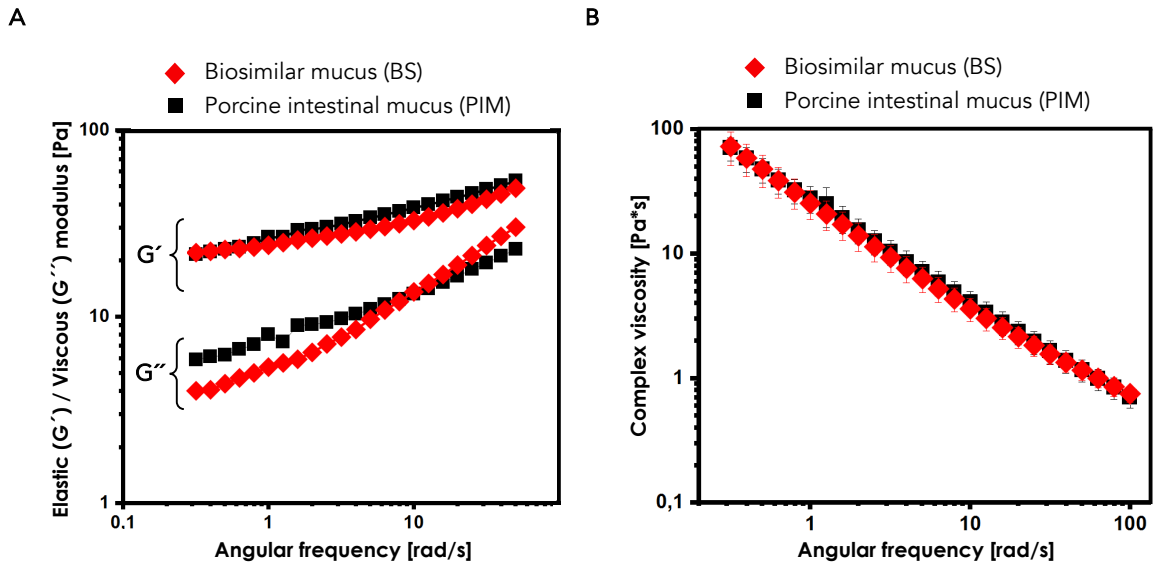


Figure 2.4 Rheological profiling and complex viscosity of native mucus and its surrogate. Frequency sweep of porcine intestinal mucus (PIM) and biosimilar mucus (BS) showing elastic (G´) and viscous (G´´) moduli in a frequency range of 0.3 – 50 rad/s (**A**). Complex viscosity as a function of angular frequency in the range of 0.3 – 100 rad/s (**B**). Measurements were performed at a strain amplitude of 1% within the non-destructive deformation range (LVR). The results show the mean of at least four measurements from three independent samples. (Adapted with permission from [174]. Copyright 2019 American Chemical Society.)

Table 2.2 summarizes several macrorheological properties at relative low shear and angular frequency of 1 rad/s. The ratio of viscous to elastic response is described by the loss tangent value or phase angle (δ) defined as tan(δ) = G″/G′ which characterizes mucus for an ideally elastic deformation behaviour (δ = 0°), for ideally viscous flow behaviour (δ = 90°), and with δ < 45° for a viscoelastic solids and δ > 45° for a viscoelastic liquids [175]. Accordingly, PIM and BS showed viscoelasticity and comparable phase angles with ~16.0° and ~18.7°, respectively (Table 2.2). Regarding the elastic and viscous moduli at 1 rad/s, storage modulus (G´) displayed 26.7 ± 6.3 Pa (PIM) compared to 24.2 ± 6.5 Pa (BS), and loss modulus (G´´) 8.1 ± 3.1 Pa (PIM) compared to 5.4 ± 0.7 Pa (BS) (Table 2.2). The average complex viscosity was similar for both mucus samples with 27.9 ± 6.8 and 25.5 ± 6.7 for PIM and BS, respectively (Table 2.2).

Table 2.2 Macrorheological properties of native intestinal mucus and its surrogate

Mucus sample	Phase angle [°]	Moduli		Complex viscosity [Pa*s]
		Elastic/storage (G´)	Viscous/loss (G´´)	
PIM	18.7 ± 3.4	26.7 ± 6.3	8.1 ± 3.1	27.9 ± 6.8
BS	16.0 ± 3.2	24.2 ± 6.5	5.4 ± 0.7	25.5 ± 6.7

PIM: Porcine intestinal mucus; BS: Biosimilar mucus according to protocol from Boegh *et al*. [120]. Data is shown for angular frequency of 1 rad/s. (Adapted with permission from [174]. Copyright 2019 American Chemical Society.)

In summary, bulk rheological analysis of isolated porcine intestinal mucus and biosimilar mucus revealed for both a Non-Newtonian viscosity with shear-thinning behaviour. Moreover, at the macroscopic level, the mucus samples were identified as viscoelastic gels comprising flow (viscosity) and deformation (elasticity) properties.

2.3.2 Microrheological analysis of intestinal mucus using MPT

The viscoelastic mucus layer covering the intestinal epithelium is an important barrier to mucosal drug delivery that can affect the transmucosal absorption of drug and delivery systems. Regarding mucus heterogeneity, the design of nanoparticle-based delivery systems requires detailed information about viscous and elastic properties. Compared to macrorheological analysis which provides the macroscale characterization of mucus, the degree of physical microheterogeneity was investigated via multiple particle tracking (MPT) analysis. This offered an improved mucus characterization with a spatial resolution and insights in the local viscous and elastic contributions from the mucus mesh architecture. In this context, the distribution of individual particle diffusion allowed the quantification of particle dynamics as well as the assessment of mucus barrier property including qualitative information on their local environment.

To this end, red fluorescent polystyrene microspheres of 0.2 and 0.5 µm particle diameter were used as tracer particles to explore the microrheological properties of native intestinal mucus and its surrogate. Accordingly, a mixture of particles and mucus sample was prepared and transferred to a sealed chamber for video microscopic analysis (Fig, 2.5A). The diffusion of individual particles was tracked, and corresponding trajectories were used to calculate the time-averaged mean squared displacement (MSD) which can be converted to diffusion coefficients. Figure 2.5B/C displays the Brownian trajectories for 200 nm and 500 nm FS tracer particles showing 5 s of particle motion with the mucus samples (left panel) and corresponding MSD as a function of time (middle) with frequencies of α-values (right). Particle transport in water is described as pure Brownian motion in a viscous liquid with α equal to 1 (slope of MSD), whereas ´active diffusion´ and ´restricted diffusion´ correspond to $\alpha > 1$ and $\alpha < 1$, respectively [176,177].

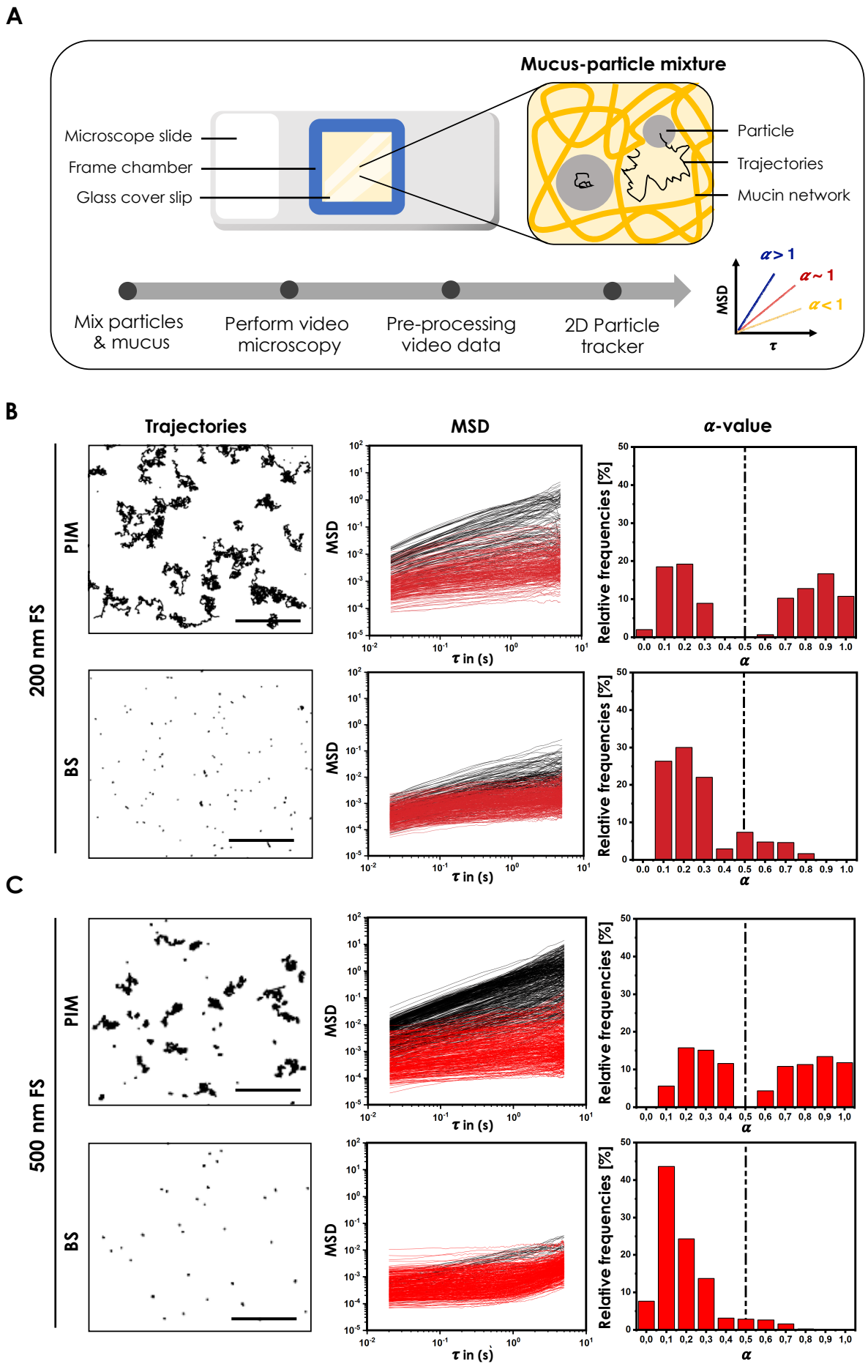

A
Mucus-particle mixture
Microscope slide
Frame chamber
Glass cover slip
Particle
Trajectories
Mucin network
α > 1
α ~ 1
α < 1
MSD
τ
Mix particles & mucus
Perform video microscopy
Pre-processing video data
2D Particle tracker
B
Trajectories
MSD
α-value
200 nm FS
PIM
BS
τ in (s)
Relative frequencies [%]
α
C
500 nm FS
PIM
BS
τ in (s)
Relative frequencies [%]
α

Figure 2.5 Multiple particle tracking (MPT) analysis of polystyrene tracer particles (FluoSpheres®; FS) dispersed in native intestinal mucus and its surrogate. Scheme of MPT setup based on a sealed chamber constructed on a microscope slide that contains the mucus-particle mixture for video microscopic analysis (**A**). The diffusion of 200 nm (**B**) and 500 nm (**C**) FS was studied in porcine intestinal mucus (PIM) and biosimilar mucus (BS). Depicted trajectories show 5 s of particle motion within PIM and BS (left panel). MSD as a function of time scale of FS dispersed in mucus (middle panel) with black lines that correspond to particles in a viscous environment ($\alpha > 0.5$) and red lines to particles in an elastic environment ($\alpha < 0.5$). The α-value plots show the distribution of particles in elastic and viscous environment (right panel). Data is represented as mean of 3-4 mucus samples with a minimum of 350 particles/plot. (Scale bar = 10 µm) (Adapted with permission from [174]. Copyright 2019 American Chemical Society.)

As expected, the movement of particles within mucus gels was hindered for both tracer particle sizes and showed sub-diffusive motion with an MSD growing slower ($\alpha < 1$) compared to the linear MSD with a constant diffusion coefficient typical for Newtonian fluids such as water ($\alpha = 1$). This sub-diffusive motion indicated by an MSD slope of $\alpha < 1$ was further subdivided with an arbitrary cut-off of 0.5 of each MSD trajectory to classify the particles as diffusive ($\alpha > 0.5$) and non-diffusive ($\alpha < 0.5$). Accordingly, the slopes of the MSDs are represented in black and red lines corresponding to particles in an elastic environment ($\alpha < 0.5$) and viscous environment ($\alpha > 0.5$), respectively (Fig. 2.5). With respect to this criterion, 200 nm and 500 nm particles appeared immobilized in porcine intestinal mucus (PIM) with 44.7% and 42.8% of the particles in an elastic environment, respectively (Table 2.3). The remaining particles showed a diffusive behaviour with 55.3% (200 nm) and 57.2% (500 nm) corresponding to local viscous environment (Table 2.3). In contrast, the characterization of individual particle transport modes in biosimilar mucus (BS) revealed a very low percentage of diffusive particles which is also recognizable from the trajectories with reduced extent of displacement (Fig. 2.5B/C; left panel). Only low percentages of mobile particle fractions were detected with around 18.6% and 7.4% of the total number of 200 nm and 500 nm FS particles, respectively (Table 2.3). The majority of FS particles were limited in particle motion when dispersed in BS displaying 81.4% (200 nm) and 92.6% (500 nm) of sub-diffusion (Table 2.3).

D_{eff} is related to the particle´s effective diffusivity, whereas the ratio of D_{water}/D_{eff} indicates the immobilization factor by which the particle transport in mucus is slowed down compared to their theoretical diffusivities in water. Corresponding 200 nm and 500 nm carboxylate-modified polystyrene particles with a hydrophobic and anionic surface were slowed 11- and 20-fold in PIM, respectively, compared to their theoretical speed in water (Table 2.3). In comparison, 500 nm dispersed in water showed an immobilization factor of 1 with 99.8% of mobile particle fraction (Table 2.3) and classical random walks reflecting the purely viscous liquid (Fig. 2.6).

Table 2.3 Microrheological properties of native intestinal mucus and its surrogate

		Transport modes (mobility)		Immobilization factor
		Immobile particle fraction ($\alpha < 0.5$)	Mobile particle fraction ($\alpha > 0.5$)	(D_{water}/D_{eff})
200 nm FS	PIM	44.7 %	55.3%	11
	BS	81.4 %	18.6%	2385
500 nm FS	PIM	42.8%	57.2%	20
	BS	92.6%	7.4%	2570
	Water	0.2%	99.8%	1

(Adapted with permission from [174]. Copyright 2019 American Chemical Society.)

Whereas the motion of both particle sizes was obstructed to a higher extent by the mucus surrogate displaying an immobilization 2400- to 2600-fold compared to water (Table 2.3).

In summary, smaller tracer particles with 200 nm size below the mean pore size of intestinal mucus showed a slightly higher percentage of mobility in both mucus samples compared to the bigger particles. The motion of 500 nm particles seemed to be more restricted due to its comparable dimension of the averaged mucus pore size.

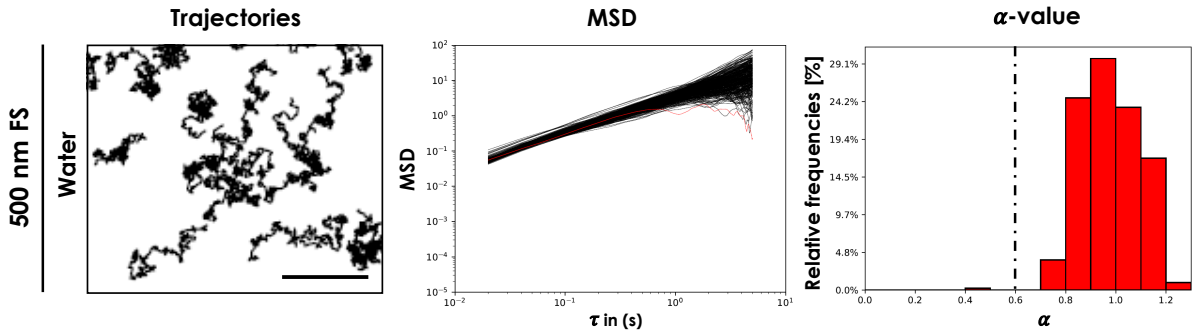
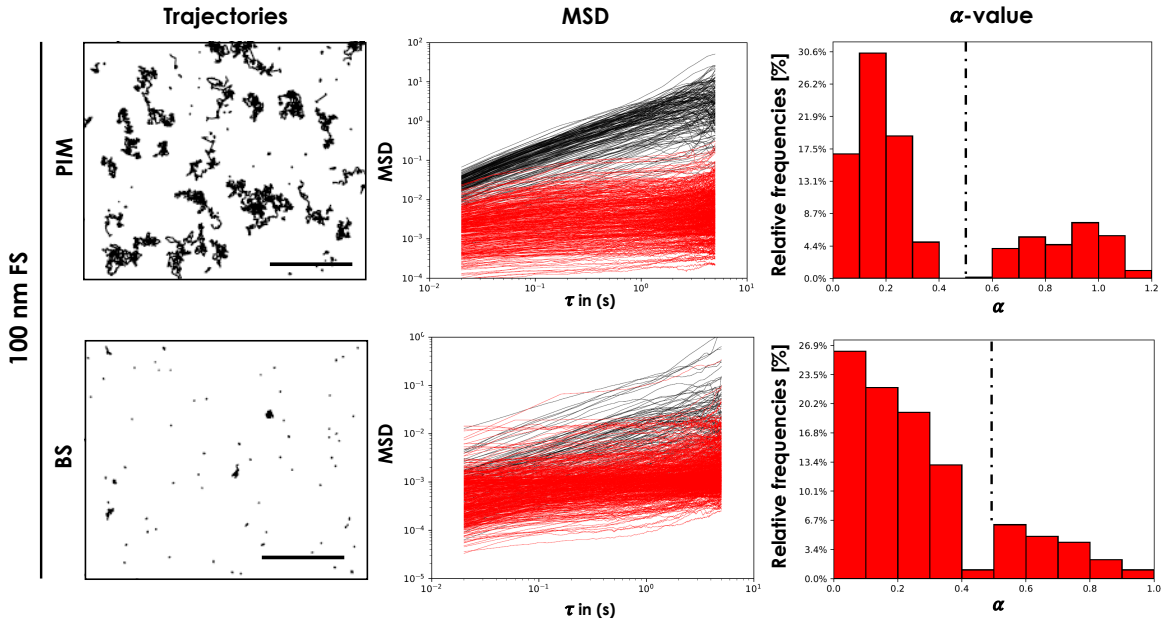


Figure 2.6 MPT analysis of 500 nm FS in water (control). Depicted trajectories show 5 s of particle motion in water. MSD as a function of time scale of FS with black (viscous environment; $\alpha > 0.5$) and red lines (elastic environment; $\alpha < 0.5$). The α-value plots show the distribution of particles in elastic and viscous environment. (Scale bar = 10 µm)

In addition, native intestinal mucus and its surrogate were investigated using carboxylated FS tracer particles of smaller diameter. Figure 2.7 summarizes the microrheological measurements obtained for 100 nm FS particles. In comparison to observations made before for 200 nm and 500 nm FS particles, increased diffusion was observed for 100 nm FS in PIM (Fig. 2.7A). Accordingly, less particles appeared immobilized in PIM, showing an increased mobile fraction of 66.6% that corresponds to a viscous environment (Fig. 2.7B). Nevertheless, a particle fraction of 33.4% was immobilized within PIM (Fig. 2.7B), as visible in some reduced trajectories (Fig. 2.7A; left panel). In contrast, a similar particle immobilization occurred in the mucus surrogate with 18.5% of diffusive and 81.5% of non-diffusive particles, as observed for 200 nm FS (Fig. 2.7B). Regarding the immobilization factor and effective diffusivities compared to water, anionic 100 nm FS were slowed 43-fold in PIM and 3600-fold BS (Fig. 2.7B).

In summary, the smallest particle diameter of 100 nm showed the highest mobile fraction in PIM compared to the other particle sizes, however, one third was obstructed in native mucus. In contrast, 100 nm particles were immobilized in the mucus surrogate with frequencies comparable to 200 nm FS particles suggesting interaction filtering rather than physical filtering mechanisms.

A



B

	Mucus	Transport modes (mobility)		Immobilization factor
		Immobile particle fraction ($\alpha < 0.5$)	Mobile particle fraction ($\alpha > 0.5$)	(D_{water}/D_{eff})
100 nm	PIM	33.4 %	66.6%	43
	BS	81.5 %	18.5 %	3600

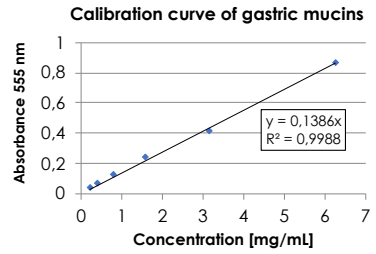
Figure 2.7 MPT analysis of 100 nm FS dispersed in native intestinal mucus and its surrogate. The diffusion of 100 nm was studied in porcine intestinal mucus (PIM) and biosimilar mucus (BS) (**A**). Depicted trajectories show 5 s of particle motion within PIM and BS (left). MSD as a function of time scale of FS (middle) with black (viscous environment; $\alpha > 0.5$) and red lines (elastic environment; $\alpha < 0.5$). The α-value plots show the distribution of particles in elastic and viscous environment (right). Data is represented as mean of 3 mucus samples with a minimum of 350 particles/plot. (Scale bar = 10 µm). Summary of related microrheological properties (**B**).

2.3.3 Quantification of mucin content in native intestinal mucus

Since mucin glycoproteins are the major component of mucus and responsible for the viscous and elastic gel-like properties, a quantification of mucin concentration was determined in collected intestinal mucus by the quantitative Periodic Acid Schiff (PAS) assay that detects carbohydrate moieties of mucin glycoproteins. Figure 2.8 shows the values of the mucin content in porcine intestinal mucus (PIM) obtained from three

different mucus samples. A calibration curve of porcine gastric mucins was prepared for mucin quantification and indicated a linear range from 0.2 to 6.25 mg/mL of mucin concentration (Fig. 2.8A). Mucin concentration in PIM samples was ranging between 31.8 mg/mL and 73.4 mg/mL or 3.18% and 7.34%, respectively (Fig. 2.8B). Accordingly, the average of mucin content in native intestinal mucus was determined with 52.9 ± 20.8 mg/mL and 5.29 ± 2.1% (Fig. 2.8B).

A



B

	Porcine intestinal mucus (PIM) samples			
	1	2	3	**Mean**
Mucin concentration [mg/mL]	31.8 ± 0,4	53.5 ± 4,7	73.4 ± 10,6	**52.9 ± 20.8**
Percentage of mucins [%]	3.18	5.35	7.34	**5.29 ± 2.1**

Figure 2.8 Quantification of mucin content in native mucus (porcine intestinal mucus; PIM) analyzed by Periodic acid Schiff (PAS) assay. Standard curve of porcine gastric mucins after PAS assay (**A**). Quantification of mucin content in native mucus samples isolated from porcine intestine (**B**). Standard and mucus sample were oxidated in 0.06% (v/v) periodic acid in 7% (v/v) acetic acid at 37°C for 1.5 h and incubated with Schiff Reagent for 40 min at RT. Data is shown as mean ± SD of triplicates. (Adapted with permission from [174]. Copyright 2019 American Chemical Society.)

In summary, the resulting mucin content in native intestinal mucus was comparable with the recipe of the biosimilar mucus (BS) which contained 5% (w/v) of porcine gastric mucins.

2.3.4 Analysis of particle mobility through intestinal mucus (macro-scale)

In order to understand how the physicochemical properties of LNPs as well as upon siRNA complexation influence the diffusion through mucus, a Transwell®-based *in vitro* permeation assay was developed. A self-made diffusion setup was modified by a 30 µm nylon mesh filter (in exchange to the existing 0.4 µm PET membrane) which

separated two fluid compartments such as the apical or donor and basolateral or acceptor compartment (Fig. 2.9A). Accordingly, the permeation of drug delivery systems across native intestinal mucus and its surrogate was investigated within this diffusion setup. The chosen filter mesh with respective cuff-off size allowed the passage of nanoparticles. As a result, respective drug delivery carriers were detected in the acceptor compartment (Fig. 2.9C; control without mucus). At the same time, corresponding filter mesh retained the mucus sample with minimized loss during the experiment.

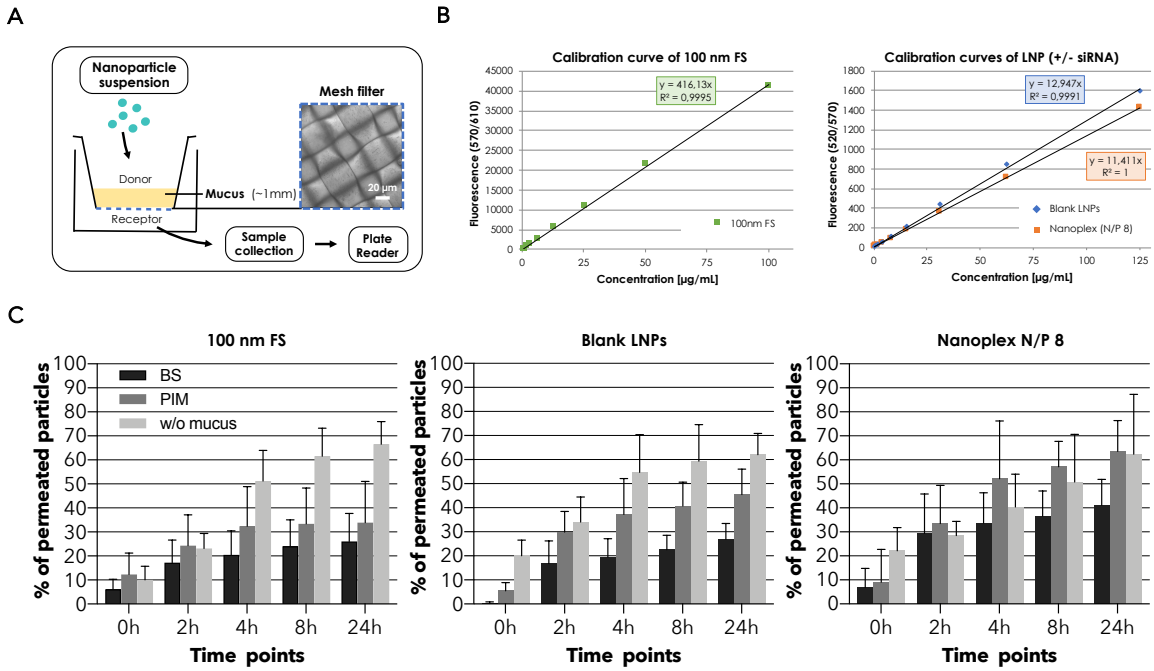


Figure 2.9 Transport study of different nanoparticle systems through native and biosimilar mucus. Scheme of the experimental setup using a modified diffusion setup based on a combination of Transwell® insert and a 30 µm mesh filter (CLSM image) (**A**). Standard calibration curves of 100 nm tracer particles (red fluorescent FluoSpheres®; FS), blank and siRNA-loaded (DiI-labeled) LNPs (nanoplexes; N/P 8) with linear relationship between particle concentration and fluorescence detection (**C**). Cumulative permeation (%) of 100 nm FS (50 µg/well), blank (62.5 µg LNPs/well) and nanoplexes (N/P 8; 62.5 µg LNPs and 188 nM siJAK1 per well) across native mucus (porcine intestinal mucus; PIM) and its surrogate (biosimilar mucus; BS) compared to the empty Transwell® insert without (w/o) mucus sample (**B**). Data is represented as mean ± SD of triplicates of 2 - 3 individual experiments.

Accordingly, a total volume of 113 µL of the mucus sample was placed to the donor compartment onto the filter mesh to ensure the complete coverage of the filter mesh

and resulted in a mucus layer thickness of approximately 1 mm. Translocated particles were quantified in the basolateral compartment by fluorescence-based detection method using a microplate reader. Figure 2.9B depicts the serial dilutions of different fluorescent nanoparticle systems and a linear relationship between particle concentration and fluorescence detection. Corresponding calibration curves were fitted by linear equation and showed a coefficient of determination $R^2 \geq 0.999$ within 10 to 125 µg/mL particle concentrations (Fig. 2.9B).

Particle diffusion across native and artificial mucus was compared to the permeation behaviour in absence of mucus (empty insert) and monitored over time and within 24 h after nanoparticle application (Fig. 2.9C). Carboxylate-modified tracer particles (FluoSpheres®; FS) with a diameter of 100 nm were used as model particles and displayed a cumulative permeation with 67 ± 9% after 24 h in the absence of mucus (Fig. 2.9C; left). As expected, a reduction in particle permeability was observed for both mucus samples, with 26 ± 12% and 34 ± 17% for BS and PIM, respectively (Fig. 2.9C; left). Compare to that, positively charged lipid nanoparticles (LNPs) of 40 nm size had a similar trend for all conditions, showing 62 ± 9% of permeated particles in the absence mucus, with a slight increase for BS with 27 ± 7% and much higher permeated fraction for PIM with 45 ± 11% (Fig. 2.9C; middle). For siRNA-loaded LNPs (nanoplexes; N/P ratio of 8), the cumulative permeation achieved after 24 h comparable numbers without mucus (62 ± 25%), whereas for both mucus samples displaying 41 ± 11% and 64 ± 13% for BS and PIM, respectively (Fig. 2.9C; right).

To confirm the presence and arrival of particles to the basolateral compartment, samples removed after 24 h from the receiver compartment were analyzed by dynamic light scattering (DLS) (SI Fig. 2). DLS measurements revealed comparable sizes for all particle types before and after 24 h of experiment duration, only for blank LNPs a slight increase in polydispersity was observed (SI Fig. 2B). However, DLS measurement was only possible for the control setup and in absence of the mucus (SI Fig. 2D). While particle characterization could not be performed in the presence of the mucus layer (SI Fig. 2D).

In summary, particles showed an enhanced permeation across native intestinal mucus than its surrogate. By comparing the results obtained from the transport study across PIM, the diffusion capacity of nanocarriers can be ranked from low to high: 100 nm FS < LNPs < Nanoplexes.

2.3.5 Analysis of particle interaction with mucin glycoproteins (micro-scale)

The interaction study of nanoparticles with mucin glycoproteins, as the main component of mucus, was performed by dynamic light scattering (DLS) using Nanoparticle Tracking Analysis (NTA) technology. This method enabled particle visualization and determination of particle size distribution based on the analysis of Brownian motion. Moreover, for the analysis of particles dispersed in a 0.1% (w/v) mucin solution NTA provided valuable insights into particle affinities to bind or aggregate within mucin fibres. Based on previous observations, non-interacting or interacting particles were identified upon incubation with low-viscosity gastric mucins by displaying either the same size distribution (for unhindered motion) or an increase towards higher particle size distribution (for hindered motion), respectively [172]. Compared to the light scatter mode measuring the total number of particles regardless of the incorporated fluorescence label, NTA analysis was performed with the application of the fluorescence mode. Accordingly, only fluorescently labelled nanoparticles within the excitation spectra of the laser source (532 nm) were detected. The standard long-pass filter (565 nm) that transmitted all wavelengths longer than 565 nm included the emission maxima of all tested fluorescent nanoparticles.
Figure 2.10 summarizes the motion of fluorescently labelled nanoparticles recorded in fluorescence mode without (PBS; grey line) or in the presence of mucins (0.1% (w/v) mucin aqueous solution; red line).

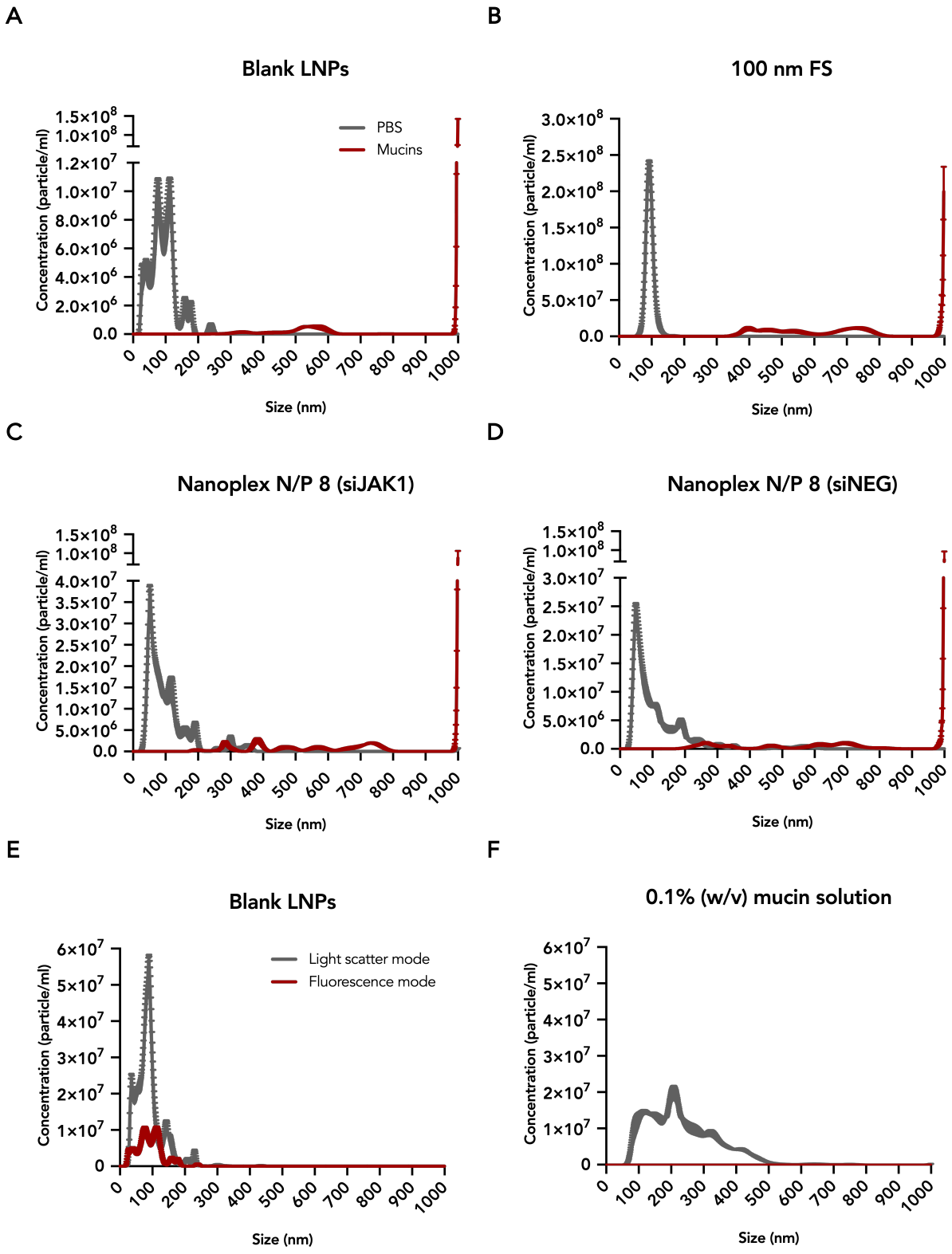


Figure 2.10 Interaction of nanoparticles with reconstituted mucin glycoproteins analyzed by Nanoparticle Tracking analysis (NTA). Particle-mucin interactions were measured in fluorescence mode without (PBS; grey line) or in presence of mucins (0.1% (w/v) mucin solution; red line) for 40 nm blank LNPs (DiI-labeled) (**A**), 100 nm red fluorescent FS tracer particles (**B**), and nanoplexes (siJAK1- (**C**) or siNEG-loaded LNPs (**D**) at N/P ratio of 8). Control measurements of blank LNPs in PBS (**E**) and 0.1% (w/v) mucin solution (**F**) performed in scatter light mode (grey) and fluorescence mode (red). Data is represented as mean ± SE.

The size distribution of cationic DiI-labeled LNPs of 40 nm size shifted to larger particle diameters from ~90 nm to ~910 nm (mean of number-weighted distribution) which indicated strong interactions with present mucins (Fig. 2.10A). Mucin interaction was observed also for red fluorescent control particles of a diameter of 100 nm and anionic surface charge with a size distribution shifted from ~100 nm to ~400 nm (Fig. 2.10B). Nanoplexes with either siJAK1- or siNEG-loading (N/P ratio of 8) and reduced overall charge compared to blank LNPs showed similar, but less pronounced interactions with mucin fibres with size shifts from ~100 nm to ~710 nm and ~730 nm, respectively (Fig. 2.10C/D). Control measurements of blank LNPs dispersed in PBS (Fig. 2.10E) or 0.1% (w/v) mucin solution (Fig. 2.10F) pointed out the effects of the fluorescence mode in comparison to the scattered light mode. Consequently, the application of the fluorescence mode allowed the specific detection of LNP fluorescence (DiI-label) and complete reduction of mucin auto-fluorescence and potential background signal, respectively (Fig. 2.10E/F).

In summary, all particle systems showed affinity for mucus interaction, however, related size increase can be graded from low to high: 100 nm FS < Nanoplex < LNPs.

2.3.6 Characterization of cell-based intestinal barrier models

For combined investigations of mucus and cellular barrier regarding drug and drug delivery interaction, an *in vitro* mucosal model consisting of a co-culture of enterocytes (Caco-2 HTB-37) and goblet cells (HT29-MTX-E12) was chosen to improve *in vivo* correlation.

Within this contest, both cell types of the intestinal epithelium were seeded together a 1:1 cell ratio and cultivated in a Transwell®-based system for two to three weeks under submerged conditions (Fig. 2.11A). Respective co-culture was investigated in terms of epithelial barrier function and the presence of a mucus layer. The obtained results defined the optimal time point to perform subsequent particle uptake

experiments. Figure 2.11B displays the transepithelial electrical resistance (TEER) measurements of the co-culture (1:1) compared to separated cell cultures (mono-cultures) that monitored corresponding tight junction integrity over 30 days.

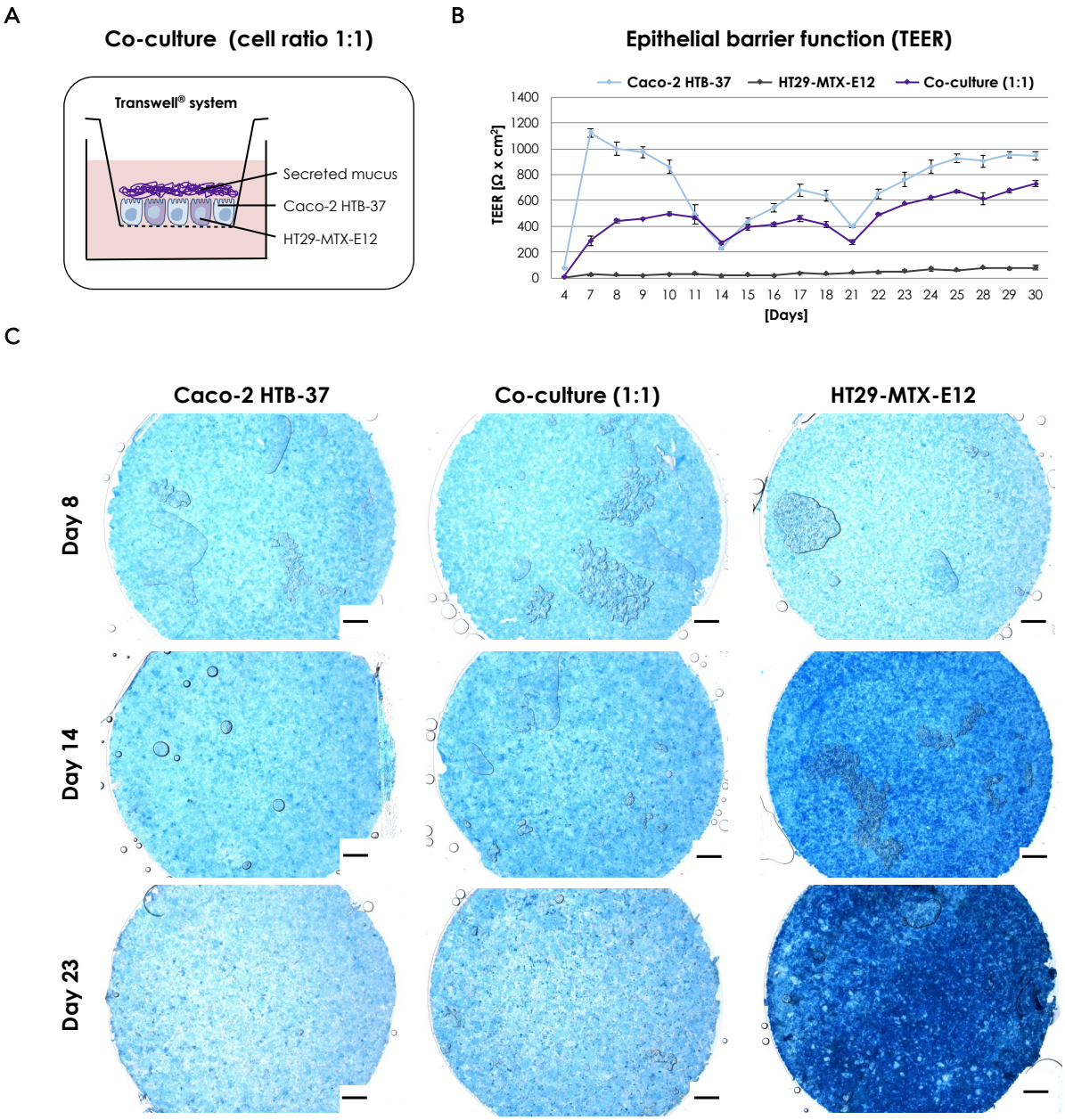


Figure 2.11 Co-culture of Caco-2 HTB-37 and HT29-MTX-E12 as a model of intestinal barrier. Scheme of co-culture setup based on Transwell® system and composed of Caco-2 HTB-37 (enterocytes) and HT29-MTX-E12 (goblet cells) in a cell ratio of 1:1 (**A**). Epithelial barrier function and transepithelial electrical resistance (TEER) measurements of mono- or co-cultures (**C**). Stereomicroscopic images of excised Transwell® inserts for the visualization of cell-secreted mucus after Alcian blue staining after pre-determined cultivation time points (**B**). Scale bar = 1mm.

Both, Caco-2 HTB-37 cells and co-culture with HT29-MTX-E12 cells showed barrier properties with TEER values ranging between 600 – 900 Ω*cm^2 and 400 – 700 Ω*cm^2 after 2 – 3 weeks, respectively (Fig. 2.11B). Compared to that, the mono-culture of HT29-MTX-E12 cells displayed TEER values below 120 Ω*cm^2 throughout the cultivation and hence, indicating the lack of an epithelial barrier function (Fig. 2.11B). Cell-secreted mucus was visualized by Alcian blue, a cationic dye that binds to acidic mucin glycoproteins indicated by a deep blue colour (Fig. 2.11C). From the stereomicroscopic images, only the mono-culture of HT29-MTX-E12 cells produced a confluent mucus blanket after 14 days with increased presence of mucins and Alcian blue staining after ~3 weeks of cultivation (Fig. 2.11C). In comparison to that, the co-culture (1:1) did not produce a sufficient amount of mucus and showed similar to Caco-2 HTB-37 mono-culture only a light blue colouring for all time points tested (Fig. 2.11C). Closeup views highlight mucin secretion by HT29-MTX-E12 cells and merely a background signal for both, Caco-2 HTB-37 as well as co-culture (SI Fig. 3).

Beyond that, co-culture was investigated in terms of cell growth behaviour as well as spatial organization. Based on pre-staining of one respective cell line before co-culturing, proliferating cells were visualized via incorporated fluorescent dye (CellTrace™). HT29-MTX-E12 cells had the tendency to grow as colonies that were surrounded by Caco-2 HTB-37 cells (SI Fig. 3A). Upon reaching confluency, co-culture exhibited a homogeneous cell distribution of both cell types (SI Fig. 3B).

In addition, the presence and morphology of intestinal mucus secreted by the goblet cell line (HT29-MTX-E12) was investigated in mono-and co-culture setups using scanning electron microscopy (SEM). Figure 2.12 shows the representative SEM images of cell-secreted mucus of post-confluent cultures (14 days). Caco-2 HTB-37 cells showed a typical brush border with densely packed and well-organized microvilli structures on their apical surfaces whereas only few microvilli were found for HT29-MTX-E12 cells (Fig. 2.12A). In contrast to Caco-2 HTB-37 cells, co-culture (1:1) as well as HT29-MTX-E12 cells cultured alone showed the accumulation of apical fibre-like structures with distinct entanglements on top of the cell layer (Fig. 2.12A).

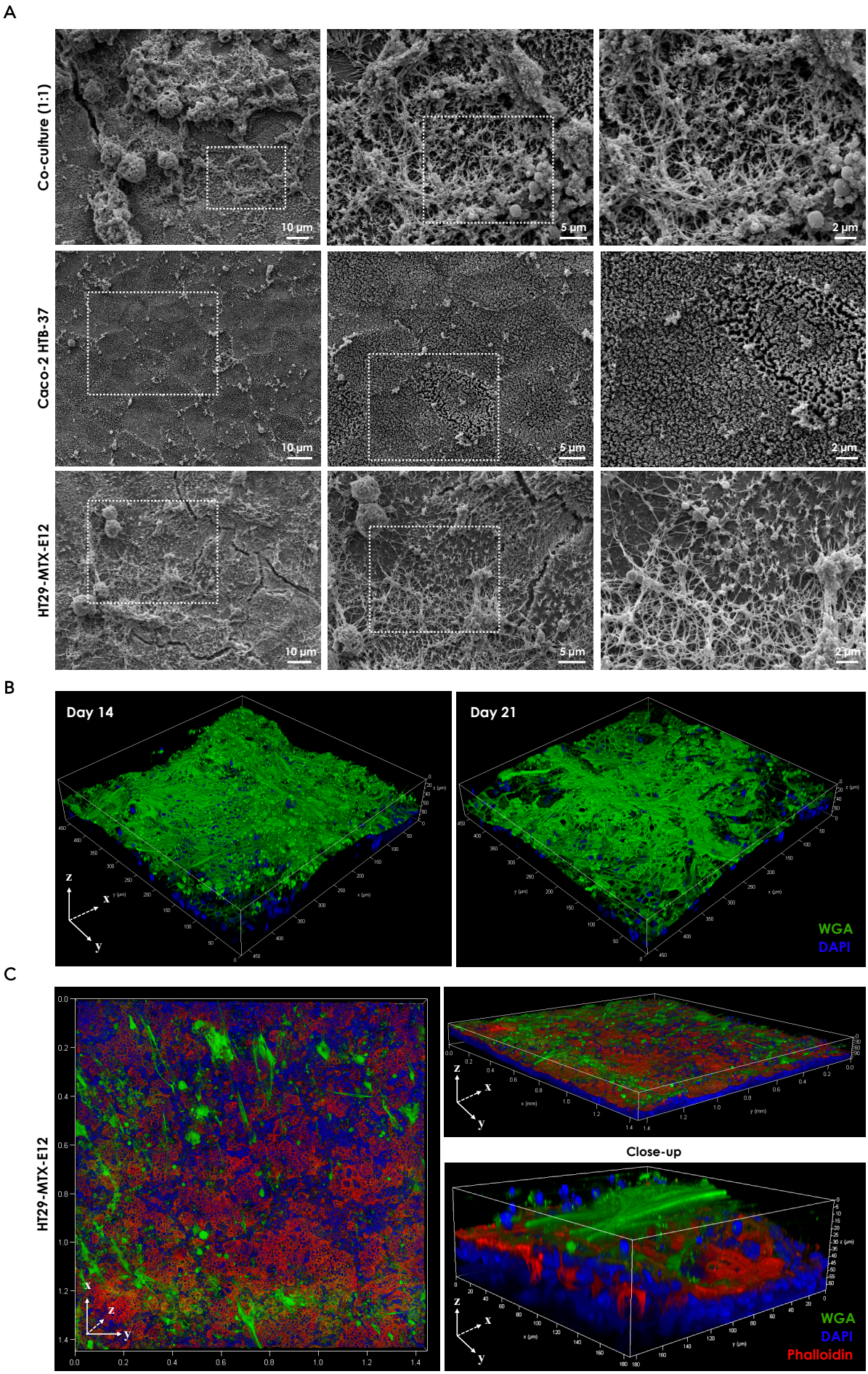

A
Co-culture (1:1)
Caco-2 HTB-37
HT29-MTX-E12
10 µm
5 µm
2 µm
B
Day 14
Day 21
WGA
DAPI
C
HT29-MTX-E12
Close-up
WGA
DAPI
Phalloidin

Figure 2.12 Morphological analysis of cell-derived mucus using scanning electron microscopy (SEM) and confocal laser scanning microscopy (CLSM). SEM pictures of co-culture (day 14) of Caco-2 HTB-37 and HT29-MTX-E12 cells (ratio of 1:1) compared to mono-cultures with close-up views (**A**). Confocal images of HT29-MTX-E12 (day 14 *versus* 21) stained with FITC-conjugated WGA for secreted mucins (green) and DAPI for cell nuclei (blue) (**B**). Microscopic images of HT29-MTX-E12 (day 10) with additional TRITC-conjugated Phalloidin staining (cytoskeleton; red) for discrimination of cells (red cell membrane) and cell-secreted mucus (green filaments) (**C**). Recorded z-stacks are represented in top or lateral view with overlaid fluorescence signal. (axis unit = µm)

Furthermore, cell-secreted mucus was analysed via confocal microscopy including the preceded staining with FITC-conjugated wheat germ agglutinin (WGA) and DAPI for the visualization of carbohydrate residues of mucins and cell nuclei, respectively (Fig. 2.12B). After 14 days of cultivation, the mono-culture of HT29-MTX-E12 cells displayed numerous bundles of fibre-like strands (green) distributed on top of the cells and partial staining of the cell membrane (green) without changes after extended cultivation time (21 days) (Fig. 2.12B). Additional staining of cytoskeleton (filamentous (F)-actin) in HT29-MTX-E12 cells using rhodamine-conjugated phalloidin revealed that respective fibre strands (green) can be distinguished from the cell membrane as well as cytoskeleton staining (red) (Fig. 2.12C).

In summary, the cell-based intestinal barrier model composed of enterocyte- and goblet-like cells with chosen cell ratio of 1:1 presented epithelial barrier function, but low mucus production. For mono-cultures of HT29-MTX-E12 cells, the presence of negatively charged mucins 14 days after post-confluency was confirmed.

2.3.7 Particle uptake in cell-based intestinal barrier model cell-derived mucus

Based on previous results, the evaluation of particle interaction with cell-secreted mucus including the cellular uptake was performed with mono-cultured goblet cells (HT29-MTX-E12). This selection ensured a sufficient amount of mucus production and a more continuous mucus layer mimicking physiological condition. Particle-mucus interaction as well as cellular uptake was compared to Caco-2 HTB-37 cells that lack mucus production.

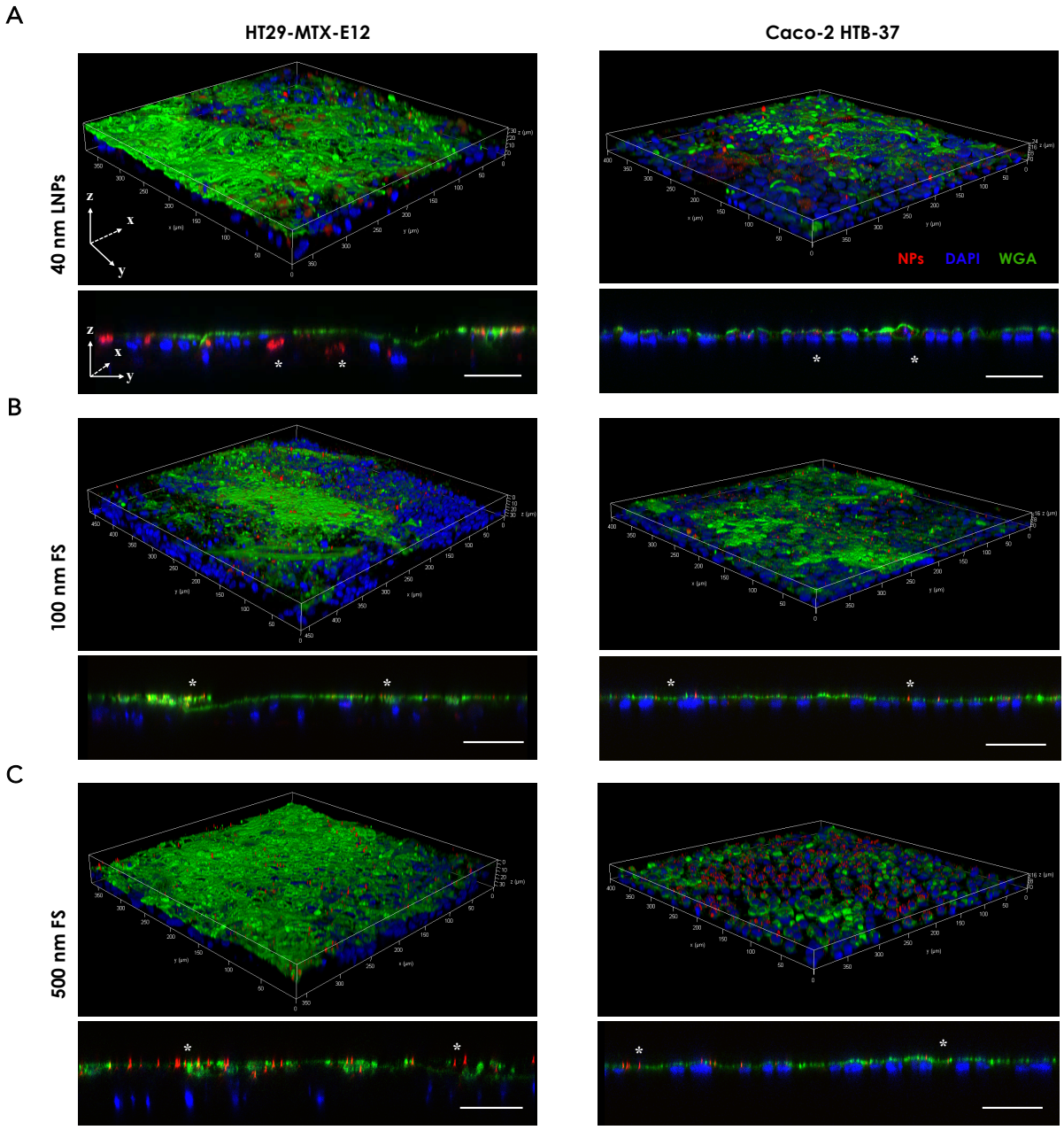


Figure 2.13 Representative confocal microscopic images of cellular uptake of fluorescent nanoparticles in HT29-MTX-E12 and Caco-2 HTB-37 cells (day 14). Blank LNPs (40 nm) and control particles (100 nm and 500 nm FS) were incubated with mono-cultures of HT29-MTX-E12 or Caco-2 HTB-37 cells and cellular uptake was analyzed by CLSM. Recorded z-stacks are represented in lateral view with corresponding cross-section with merged fluorescence signals for cell nuclei (DAPI, blue), cytoskeleton (WGA, green), and nanoparticles (NPs; red). (*) indicates internalized *versus* non-internalized NPs. Scale bar represents 50 µm.

Figure 2.13 displays representative microscopic images of the cellular uptake of blank LNPs (40 nm) and control particles of different sizes (100 nm/500 nm FS) in mono-cultures of HT29-MTX-E12 *versus* Caco-2 HTB-37 cells. Cationic LNPs were

successfully internalized after 4 h of incubation in both cell types and were localized below the cell membrane in close proximity to the cell nuclei (Fig. 2.13A). In contrast to that, the majority of anionic control particles of 100 nm size were co-localized within the cell membrane and the mucus layer in Caco-2 HTB-37 and HT29-MTX-E12 cells, respectively (Fig. 2.13B). The same observations were made for bigger nanoparticles of 500 nm size where particles remained attached to the cellular surface, without being internalized by enterocyte- and goblet-like cells (Fig. 2.13C).

Overall, positively charged LNPs with a diameter of 40 nm were taken up by both cell types irrespective of the produced mucus layer. In contrast, negatively charged tracer particles of bigger sizes were not internalized by the cells, however, adhered to fiber-like structures localized on the cellular surface as well as on the apical cell membrane.

2.4 Discussion

Mucus is a heterogenous biological hydrogel lining all wet epithelia in our body and represents a substantial barrier to nanoparticle (NP)-based drug delivery systems. In line with that, formulations for mucosal drug delivery require the evaluation of mucus barrier interaction to improve the therapeutic efficacy of respective drugs. This will lead to a better selection of drug candidates as well as optimization of corresponding delivery platform design. *In vitro* models representing the biological structure and function of the intestinal mucus are of high importance in the context drug development because new drugs against intestinal inflammatory diseases have shown a high rate of failure with approximately 85% [35].

The limited availability of human GI mucus has stimulated scientific interest in artificial mucus surrogates that ideally should reproduce both composition and structural properties of its natural paradigm, providing a robust experimental model for drug permeation studies [162]. Under these circumstances, different mucus sources were chosen to represent the human GI mucus and proved for physiological resemblance and reproducibility. Accordingly, three mucus samples were investigated including native mucus that was isolated from the small intestine of pigs, an artificial mucus based on published recipe, and a cell culture-derived mucus from mucus-secreting goblet cells. Native mucus collected from the porcine intestine represented the highest physiological resemblance including the composition and structure of human GI mucus. However, native mucus is often related to difficult interpretation of experimental results due to its complex, highly variable, and undetermined composition [162]. A recent study revealed more inter-animal than intra-animal variations with 25-fold variability of the bulk rheology between PIM samples with the highest and lowest viscosity [120]. These variations may be related to the isolation process where mucus is scraped from the mucosal surface and may result in a variable contamination of chyme or epithelial tissue components. Furthermore, intestinal mucus is continuously altered due to food or water content and digestive activity.

Fasted animals would have been beneficial to exclude potential deviations, however, food intake recapitulates the *in vivo* situation better. Moreover, the dehydration state of the animals suffering stress situations (e.g. surgical interventions in this case) may affect the composition of intestinal mucus prior to isolation. Overall, these inter- and intra-animal variations might play an important role in the colloidal transport of particles through the mucus layer. Thus, the evaluation of potential interactions occurring between diffusing entities of interest and the mucus hydrogel was investigated including an artificial mucus with known components and increased reproducibility. Both, native and artificial mucus showed a dominant elastic modulus ($G' > G''$) which is a characteristic rheological signature of cross-linked biopolymers and correspond to previous characterizations of native mucus samples [120,178]. In accordance with native mucus, the so-called biosimilar mucus consisted of purified mucins, lipids, polyacrylic acid (PAA), and non-mucin proteins. Mucin glycoproteins are the major polymeric component of mucus and responsible for its viscoelastic character [34]. However, commercially available gastric mucins lack the possibility to form cross-linked networks between individual mucin polypeptides after reconstitution [179]. This is related to the purification procedure of mucin glycoproteins where potential degradation may impact their gel-forming capacity and hence, the crosslinking. Thus, the matching rheological profile of native intestinal and biosimilar mucus is related to the high viscosity anionic polymer PAA that has distinct resemblance to mucins [120].

As anticipated, microrheological analysis provided valuable insights in the nanoscopically heterogeneous environment within the mucus hydrogel. Hereby, analyzing the diffusion of hundreds of individual particles, the quantification of their diffusive behavior enables to draw conclusions on the surrounding microenvironment in which the particles are moving including viscosity and elasticity [180,181]. Particle mobility within the mucus hydrogel is governed by two mechanisms: interaction filtering or size filtering [39,52]. Beyond that, mucus is a dynamic barrier which

comprises steady mucus turnover and clearance as an additional dimension inhibiting particle penetration [30].

To gain insights into the microstructure of both native and artificial mucus, MPT analysis were performed using carboxylate-modified tracer particles with a diameter of 100 nm, 200 nm, and 500 nm. For respiratory mucus, the latter particle size was found to be sterically immobilized by native porcine tracheal mucus with ~94% [49]. Previous reports stated that surface functionalization with polyethylene glycol (PEG) enabled particle diffusion through mucus at a rate similar to the diffusion in water [182,183]. Although PEGylated, the majority of 500 nm particles were sterically immobilized in native human airway mucus, similar to uncoated particles [184]. A comparable MPT study showed that only 0.6% of carboxylated 500 nm particles were identified as mobile in porcine intestinal mucus [34]. Hereby, electrostatic repulsion between negatively charged particles and negatively charged mucin fibres increased the particle transport through mucus [185]. In contrast, cationic nanodelivery strategies are related to mucoadhesive properties with low MSDs due to increased interactions with mucin fibres [185]. Based on these findings, a cut off size of 500 nm was defined for therapeutic nanoparticles with the aim to cross the mucus layer.

Within this context, the biggest particle type was used to verify the presence of pores within the mucus network, irrespective of its surface functionalization. Compared to the mucus surrogate, native intestinal mucus was found to be extremely heterogenous with both, viscous and elastic regions corresponding to the presence of mucus pores and dense polymeric network, respectively. In contrast to previous studies, more than the half of 500 nm showed unhindered diffusion in porcine intestinal mucus which indicated a viscous environment and the presence of mucus pores bigger than 500 nm. Because intestinal mucus was collected from non-fasted pigs, the increased permeability might be related to its heterogeneous composition which is highly affected by the digestive activity. As stated previously, mucus-particle interaction is driven by food ingestion with an impact on particle diffusion due to increased lipid concentration or pH-induced changes [186]. A very recent study proved the similarity

of porcine jejunal and human small intestinal in terms of their microstructural organization and showed comparable particle mobility of carboxylated 500 nm tracer particles and corresponding diffusive fraction (α: 0.8 - 1) of around 60% [187].

A comparable, but slight increase in mobility was observed for 200 nm particles which reflected the structural heterogeneity of native mucus. A recent study revealed comparable diffusion of carboxylate-modified 200 nm in porcine intestinal mucus and improved mobility of PEG-coated particles, however, particle motion was categorized in immobile (α: 0 - 0.2), sub-diffusive (α: 0.2 - 0.8), and diffusive (α: 0.8 - 1) [51].

The pore diameter of porcine jejunal mucus was estimated to be approximately 200 nm [188]. Consequently, for particulates smaller than the average of inter-fiber spacing will not encounter steric hindrance, thus assuming unlimited diffusion though the mucus gel. For the smallest particle size tested (100 nm), one third of the particles was still trapped within the native mucus which indicated besides size filtering mechanisms also chemically-driven particle-mucus interactions. Lipids and non-mucin proteins are important mucus components that have been identified to affect the diffusion of several lipophilic drugs [179]. Due to the hydrophobic nature of polystyrene, even 100 nm particles still adhered to native mucus via hydrophobic interactions [50]. Nevertheless, these observations are in line with previous studies where particle transport across intestinal mucus was depending on particle size with a decrease of particle mobility with increasing particle size (20 to 500 nm) [189]. In line with that, an 10-fold difference in MSD and the diffusion coefficient was observed for anionic 100 and 500 nm particles in porcine intestinal mucus [29].

Even though biosimilar mucus (BS) precisely reproduced the macroscale rheology of native intestinal mucus, it immobilized almost all particles with ~90% of 500 nm and ~80% both, 100 and 200 nm, suggesting a higher cross-linking density and a lower pore-size range. Accordingly, BS represented an overestimated barrier to these particles. Regarding the mucin content, BS matched well with the concentration found in native intestinal samples. Since mucin density ranging between 1 and 5% (w/v) governs the mesh-pore size of mucus hydrogels, a reconstituted mucin hydrogel of

1% mucin concentration already reduced particle mobility by a factor 2500 compared to the free diffusion [52]. However, also increased concentrations of purified mucins up to 20% will increase viscosity but not lead to cross-linking nor elastic-dominant structure [190]. The addition of synthetic polymer PAA that formed hydrogen bonds with sugar residues present in the mucin carbohydrate backbone which has contributed to the interaction filtering mechanisms. As previously shown, particle diffusion of ~450 nm particles was increased in biosimilar mucus where PAA was omitted, and even more for PAA polymer alone indicating larger mesh spacing [178]. Thus, the discrepancy between macro- and microrheology may be attributed to the differences in cross-linking density between native mucus and its surrogate with a high impact on particle transport and mobility.

Regarding the lipid nanoparticles (LNPs) which were used for nucleic acid delivery, the combination of particle size below 50 nm and the observed photobleaching of the incorporated fluorescence dye did not allow tracking analysis. Besides high resolution tracking videos required for the detection of fast particle movement, the evaluation of particle diffusion by MPT necessitates the incorporation of a strong and photostable fluorescent dye with high contrast to the sample autofluorescence [181]. Nevertheless, an *in vitro* permeation assay was used to investigate the diffusion through mucus of blank LNPs of 40 nm diameter as well as upon siRNA complexation.

Overall, all nanocarriers were able to permeate through both mucus layers after 24 h of incubation, and similar to MPT analysis, displayed an enhanced permeation across native intestinal mucus compared to its surrogate. As anticipated, for particle below the estimated mucus mesh pore size, the particle mobility largely depends on their surface chemistry [30]. Nanoplexes diffused better through both mucus samples compared to blank LNPs and 100 nm control particles and showed an increased diffusion for native mucus with similar permeation observed without mucus. This might be related to the reduced positive overall charge of siRNA-loaded LNPs and the lower electrostatic interaction with mucin fiber. Accordingly, it has been shown that

hydrophilic particles with a neutral surface charge comprising muco-inert properties exhibited limited interactions with mucus [191].

The self-made diffusion setup exhibited a mucus thickness of ~1 mm which was necessary to cover the mesh filter completely. However, this represented a higher magnitude compared to human intestinal mucus which ranges between ~100 µm and ~800 µm for small intestine and colon, respectively [32]. Based on *ex vivo* human colonic biopsy, mucus was found to be approximately 600 µm thick [192]. Nevertheless, the mucus layer in the small intestine depends to a large extend on the food intake and digestive activity which represents high variations [50]. Moreover, the thickness of the intestinal mucus determined by the rate of secretion and degradation as well as shedding [50]. Furthermore, variable and somewhat conflicting information derived from the different techniques as well as species used for the calculation of mucus thickness [162]. Most data on mucus thickness were obtained from animal tissue of different species, and thus, may not represent the human scenario. As mentioned above, mucus layer thickness showed considerable fluctuations between the fasting and the fed states of an animal [193]. In the context of IBD, there are contradictory reports on either decreased (UC) or accelerated mucus production (CD) as well as related to altered mucin concentration [194]. In conclusion, modelling the macro-scale penetration of particles across such a thick mucus layer provided the possibility to study particle diffusion in the presence of an increased mucus secretion. In addition, using a more reductionist approach, particle interaction was evaluated with only mucin glycoproteins that should unravel particle affinity for mucin binding. Based on NTA analysis, the interactions between nanocarriers and negatively charged mucin fibers were detected by a shift in size distribution to bigger sizes. As a result, the hindrance of particle motion showed the following rank order from low to high: 100 nm FS < nanoplexes < blank LNPs. Despite the muco-inert properties of LNPs such as their nanoscale size and a dense PEG-coating which could potentially shield the inherent hydrophobicity, their net positive surface charge (+34mV) resulted in high mucin interaction. Upon complexation with negatively charged siRNA, nanoplexes

exhibited a less cationic values (+15 mV) that might have influenced the reduced interaction with mucin. In contrast to the transport study using undiluted native mucus, negatively charged particles (100 nm) displayed less strong interactions with mucins. However, partial interaction could be attributed to the hydrophobic nature of these particles that might interact better with the more exposed hydrophobic regions of the mucin fibres due to the lack of mucin cross-linking. Regarding cationic LNPs, their hydrophilic shell might have reduced mucin interaction due to their dense PEG-coating shielding the hydrophobic lipid core [195,196]. In accordance with previous findings, surface complexation with anionic nucleic acids resulted in a decrease of the overall positive surface charge [197].

Particle interaction was further investigated in a cell-based model mimicking the intestinal mucosal surface comprising a mucus layer using the combined culture of two common intestinal cell types, Caco-2 HTB37 and HT29-MTX-E12. This *in vitro* cell model with enhanced physiological resemblance allowed a more relevant assessment of respective drug delivery systems [198]. Compared to previous cell lines, the HT29-MTX-E12 sub-clone was identified as a suitable *in vitro* model to investigate drug or drug carrier absorption due to monolayer growth, production of functional tight junctions and increased secretion of a continuous mucus layer [199]. Transepithelial resistance of this sub-clone was around 150 Ω*cm^2 which is in line with previous observations, although the estimated mucus thickness of post-confluent cultures (3 weeks) varied between ~5 and ~190 µm [199,200]. In comparison to previous reports that used different cell ratios with higher Caco-2 cell proportion and a more physiologically relevant composition such as 9:1 or 3:1, the increased TEER value of the co-culture, however, led to decreased mucus production [118,128]. Although secretory goblet cells comprise around 16% of the small intestine *in vivo* [201], the selected 1:1 cell ratio represented a compromise between barrier function and mucus secretion. Alcian blue which stained acidic components of mucus indicated that mono-cultures of HT29-MTX-E12 cells consisted of mature goblet cells and the presence of a mucus layer. Despite of the increased barrier function, co-culture with

an equal cell ratio of 1:1 showed no Alcian blue staining which was comparable with Caco-2 HTB-37 cells cultured alone. This might be related to the less confluent and thus, more loosen mucus layer on top of the co-culture which might have been lost during staining procedure, even though washing was done very carefully. Moreover, both cell lines did not mix very well and tended to grow in colonies which might have affected the lack of sufficient mucus within the co-culture model [119,202]. Similar to SEM imaging, mucus staining using FITC-conjugated wheat germ agglutinin (WGA), which targets mucin sugar moieties such as N-acetyl-D-glucosamine and sialic acid [203], indicated fiber-like structures with some entanglement. In general, the visualization of mucus remains difficult since dehydration or fixation induce the collapse/removal of mucin network and do not represent the native state of the mucus structure [162].

Within this context, the impact of the mucus layer on drug carrier diffusion was studied in HT29-MTX-E12 mono-cultures and compared to Caco-2 cells where mucus was omitted. According to the desirable therapeutic effect of the siRNA, LNP formulations should support the local delivery and release to the target cells including a protective shielding of the drug cargo towards extra- and intracellular environment [204]. Intracellular localization was observed for both, LNPs and nanoplexes, whereas anionic particles were not taken up by the cells and remained attached to the cell membrane. This is in line with previous reports where negatively charged polystyrene particles of 50 nm and 200 nm diameter remained attached to the extracellular surface of Caco-2 cells and co-culture (7:3) [123]. Similar to that, HT29-MTX-E12 cells demonstrated to inhibit the diffusion of 200 nm polystyrene particles with a 2-fold increase for mucolytic pre-treated cells [205]. PEG surface functionalization has been reported to improve particle diffusion through mucus [182,183], however, PEGylation has a negative outcome for the endocytosis which is related to the negative charge of the cell membrane [206]. Nevertheless, the net positive charge of LNPs was beneficial for cellular uptake in intestinal epithelial cells due to the presence of anionic glycoproteins on cell surfaces, which is in accordance with previous findings [207,208].

2.5 Conclusion

Local delivery of fragile drugs such as nucleic acids to mucosal tissues is limited due to the presence of a protective mucus layer that covers the epithelial surfaces. Drug delivery systems aiming for mucopenentration must be formulated for maximal delivery to the cellular compartments. Within this context, the evaluation of mucus barrier interaction provides appropriate requirements for a successful drug delivery. Physicochemical properties of nanoparticle (NP)-based drug delivery such as the size, shape, and surface charge or modification affect muco-penetration and -adhesion.

Mucopenetration with enhanced local drug concentrations and efficient cellular uptake require a particle size below the mesh spacing of intestinal mucus and muco-inert particle surface to reduce the entrapment within the mucin fibres. Drug delivery systems, however, need to cope with both, mucus and cellular barriers, that may represent conflicting requirements. In other words, NP properties facilitating cellular uptake (e.g. positive surface charge) could be disadvantageous for mucopenetration, or mucoinert features (e.g. PEGylation) reduces at the same time the cellular uptake with respect to unPEGylated NPs.

To ensure reliable investigations of NP-based mucosal drug delivery systems important considerations should be made regarding the thorough characterization of the mucus model chosen for the respective study. Each of the presented techniques for the evaluation of mucus-particle interaction provided valuable results which can be weight up against each other. Bulk rheological analysis allowed for mucus characterization and understanding of its biophysical property, including viscosity and elasticity. The powerful technique of MPT provided relevant information about particle diffusion within the highly heterogenous microenvironment, whereas transport studies using diffusion cells enabled particle permeation through the mucus barrier at larger spatial distances and timescales.

In conclusion, investigations regarding mucus-particle interactions will lead to the development of more-efficient drug delivery systems targeting the intestinal mucosa.

3 Part II - Leaky gut model to mimic chronic inflammation of the human intestinal mucosa

Parts of this chapter are subjects of a forthcoming publication entitled "Leaky gut model of the human intestinal mucosa for testing siRNA-based nanomedicine targeting JAK1", co-authored by **Olga Hartwig**, Brigitta Loretz, Adrien Nougarede, Dorothée Jary, Eric Sulpice, Xavier Gidrol, Fabrice Navarro, and Claus-Michael Lehr.

Main contributions to this publication: OH performed all cell-related experiments, analyzed corresponding data and wrote/edited the manuscript.

3.1 Introduction

Inflammatory bowel disease (IBD) is an umbrella term for gastrointestinal (GI) disorders caused by chronic relapsing inflammation with still unclear etiology and mainly used for two disease conditions such as Crohn´s disease (CD) and Ulcerative colitis (UC). Especially industrialized countries show an increase IBD incidence with an estimated IBD population of more than 10 millions worldwide for 2030 [62]. The complex pathogenesis of IBD is triggered by genetic and environmental factors and includes a dysregulated immune system, dysbiosis of the gut microbiome and dysfunction of the intestinal epithelial barrier [64]. The translocation of bacterial products into the intestinal wall and the lack of anti-inflammatory mechanisms contribute to an aberrant production of pro-inflammatory mediators including cytokines and chemokines, followed by the progressive immune cell infiltration and tissue destruction [72].

As IBD is a multifactorial disease with divergent pathology, no single model can capture all aspects of disease complexity. Despite numerous experimental models of acute and chronic inflammation exist, mainly using rodent models such as chemically-induced (e.g. dextran sulphate sodium; DSS) or genetically engineered (e.g. IL-10 deficiency) mice [101]. The commonly used DSS-induced colitis, however, may not be representative for the immunohistopathology of human IBD [97]. Despite the understanding of immunopathogenic mechanisms of IBD was supported by a variety of genetic manipulations in mice, current *in vivo* models failed to fully capture the various aspects of human immunity, GI-tract anatomy as well as gut microbiota composition [97,102,209].

In vitro intestinal models are representing an important pre-clinical tool for drug development and act as a complementary system to animal testing. While investigations within multicellular organisms may result in overseen or unrelated experimental outcomes, the simplified context of *in vitro* cell models provides a more precise assignment of pharmacological effects. The choice of the right model system and relevant experimental setup should demonstrate robust readouts for safety and efficacy which affects drug development as well as clinical translation. In this context,

the main advantage over *in vivo* models is the combination of a well-controlled setup with a chosen degree of complexity focussing a particular scientific question. Current *in vitro* intestinal models are ranging from simplified 2D cultures representing the epithelial barrier (e.g. Caco-2 colon carcinoma cells) to more advanced 3D co-culture models with increased physiological resemblance including scaffold-based systems and multiple (preferentially human-derived) cell types providing cellular interplay [134]. Besides that, an ideal *in vitro* intestinal model should moreover capture specific disease-related features to investigate the genuine interplay of drug delivery systems. In this context, previously established *in vitro* models of the human intestinal mucosa were composed of three different cell types arranged in a physiologically relevant environment and placed in a Transwell® filter support [155,157]. Macrophages and dendritic cells of primary origin [155] or derived from human cell lines [157] were co-cultured together with epithelial cells to investigate the effects of pro-inflammatory cytokines (IL-1β) or exposure to lipopolysaccharides (LPS) on barrier function (transepithelial resistance changes) and nanoparticle absorption. Within these studies, elevated cytokine release (IL-8 and TNF-α) together with increased permeability were observed upon inflammation. Moreover, particle uptake was increased under inflamed conditions and revealed a co-localization within primary immune cells [155]. The replacement of primary cells by immune cell lines improved reproducibility without impact on the immune cell response, however, particle uptake was limited to the epithelial cell layer without reaching the underlying sub-epithelial tissue, inclusive immune cells, even under inflamed conditions [157].

In light of these studies and in order to improve the translocation of drug delivery systems across the epithelium followed by the immune cell uptake, it was hypothesized that including a more compromised epithelial barrier would provide *in vivo* IBD resemblance. Chronic intestinal inflammation with aberrant epithelial damage and apoptosis leads to harmful tissue destruction and partial loss of epithelial barrier integrity driven by tight junctions (TJ) openings and epithelial breaches [210,211].

The so-called leaky gut model was developed by the introduction of an impaired epithelium composed of sub-confluent regions that together with the presence of immunocompetent cells should better reproduce severe IBD conditions *in vitro*.

The following section summarizes the advanced features of the leaky gut model with IBD-related pathophysiology. This includes for instance a higher pro-inflammatory cytokine production compared to the previous tight barrier model. Furthermore, this section presents an improved applicability of the co-culture model with new possibilities for single-cell analysis. The dissociation of the co-culture model into singular cells opens novel insights into cell viability and proportion using flow cytometric and Cell counter analysis, respectively.

3.2 Material and Methods

3.2.1 Materials

Human colorectal adenocarcinoma cell line Caco-2 (HTB-37) was obtained from American Type Culture Collection (ATCC, Manassas, USA). THP-1, derived from acute monocytic leukaemia (ACC 16), MUTZ-3 cells, a monocytic cell line with dendritic-like phenotype (ACC 295), and urinary bladder cell line 5637 (ACC 35) were purchased from German Collection of Microorganisms and Cell Cultures GmbH (DSMZ; Braunschweig, Germany). Dulbecco´s Modified Eagle Medium (DMEM), Roswell Park Memorial Institute (RPMI), a-Minimum Essential Medium (a-MEM), fetal calf serum (FCS) and non-essential amino acids (NEAA), 0.05% trypsin-EDTA, sodium bicarbonate ($NaHCO_3$), penicillin/streptomycin (Pen/Strep), Alexa Fluor (AF)488-conjugated Phalloidin, Calcein AM, and Hank´s Balanced Salt Solution (HBSS) were obtained from Invitrogen (Carlsbad, USA). Phorbol 12-myristate 13-acetate (PMA), accutase, human AB serum, lipopolysaccharides (LPS) from Escherichia coli O111:B4, bovine serum albumin (BSA), saponin, collagenase type II, 4',6-Diamidino-2-Phenylindole Dihydrochloride (DAPI), fluorescein diacetate (FDA), propidium iodide (PI), and Phosphate Buffered Saline (PBS) were purchased from Sigma-Aldrich (Taufkirchen, Germany). Collagen type I solution (PureCol; 3mg/mL) was obtained from Advanced Biomatrix (Tucson, USA). Transwell® Permeable Supports (#3460; polyester (PET) membrane with 0.4µm pore size) were purchased from Corning (New York, USA). Paraformaldehyde (PFA) was obtained from Electron Microscopy Sciences (Hatfield, USA). Double-faced adhesive tape was ordered from Coroplast (Wuppertal, Germany). Fluorescence mounting medium was obtained from Agilent Technologies (Santa Clara, USA). CBA Human soluble Protein Flex Set for tumor necrosis factor-alpha (TNF-α) and interleukin-8 (IL-8) were purchased from BD Biosciences (Heidelberg, Germany). FITC-conjugated mouse anti-CD14 and CD11b were purchased from Biolegend (San Diego, USA).

3.2.2 Cell culture

All cell lines, used for this study, were maintained in a stable physico-chemical culture environment. Cells were cultured in humidified incubators (Binder GmbH, Tuttlingen, Germany) with controlled temperature of 37°C, 5% CO_2 atmosphere and a relative humidity of 95%. Cell cultivation and cell-based experiments were performed under aseptic conditions in a laminar flow culture hood (Safe 2020 Class II Biological Safety Cabinet, Thermo Fisher Scientific, Waltham, US). All cell lines were routinely tested for mycoplasma by enzymatic activity method using MycoAlert™ (Lonza, Basel, Switzerland).

Table 3.1 Composition of cell culture medium and culture vessels for each cell line and co-culture model

Cell line	Medium	Supplements	Antibiotics	Vessel
Caco-2 HTB-37	DMEM	10% FCS 1% NEAA	-	T75 flask
THP-1	RPMI 1640	10% FCS	-	T75 flask
MUTZ-3	α-MEM	20% FCS 20% CM	-	12well plate
Co-culture (apical)	DMEM	10% FCS 1% NEAA	1% Pen/Strep	Transwell®
Co-culture (basolateral)	RPMI 1640	10% FCS	1% Pen/Strep	Transwell®

Caco-2 HTB-37 cells were cultured in DMEM supplemented with 10% FCS and 1% NEAA (Table 3.1). Sub-confluent Caco-2 HTB-37 cultures (70-80%) were passaged once a week using trypsin-EDTA (Fig. 3.1). Detached cells were centrifuged at 300 x g (1400 rpm) for 4 min and passaged with splitting ratio of 1:20. Cell culture medium was replenished every second or third day.

THP-1 cells were grown in suspension in RPMI supplemented with 10% FCS and sub-cultured every 3 or 4 days with a splitting ratio of 1:4 or 1:6, respectively (Fig. 3.1). Cell culture medium was not replenished for THP-1 cells. MUTZ-3 cells were cultured in suspension in a-MEM supplemented with 20% FCS and 20% conditioned medium (CM) and split weekly with a ratio of 1:3 (Fig. 3.1). CM was prepared by growing the

5637 in RPMI supplemented with 10% FCS where medium was collected every second day. After sterile-filtering, CM was kept at -20°C until further use.

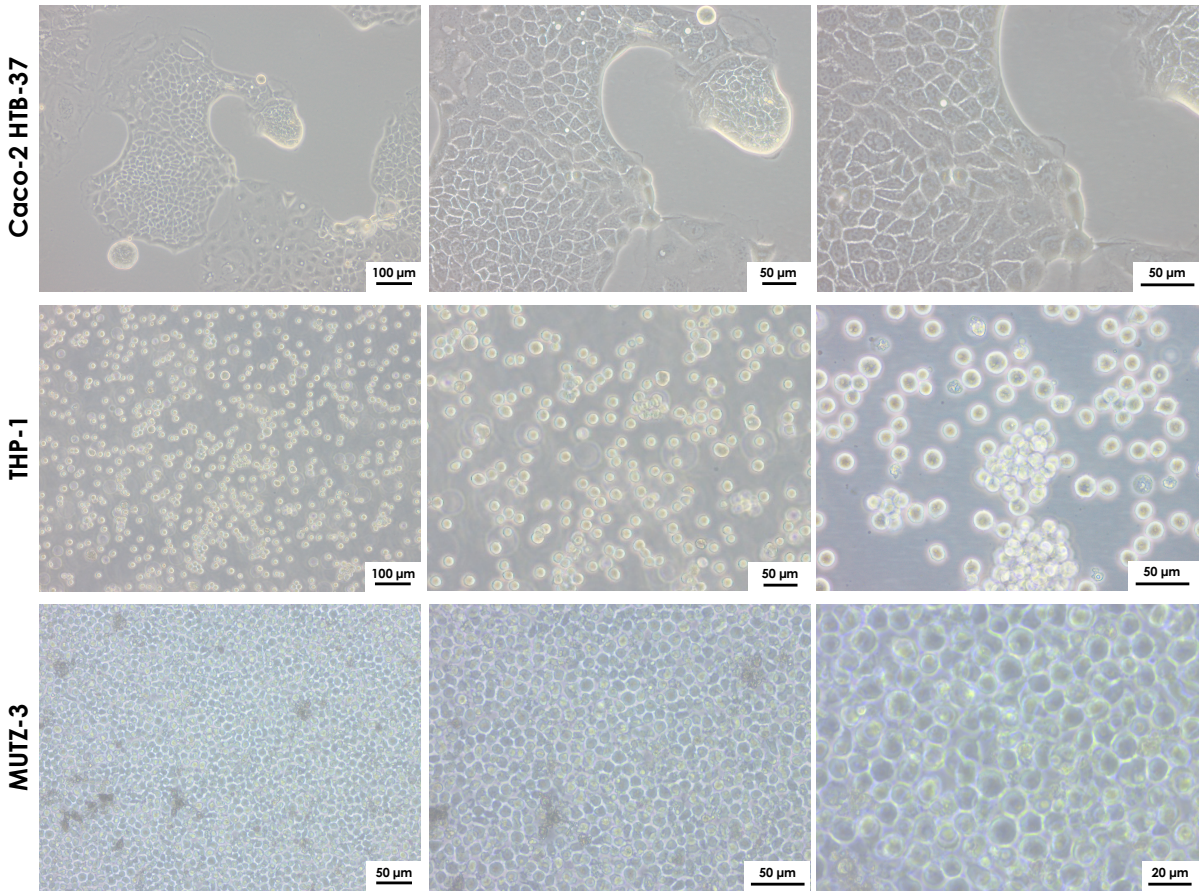
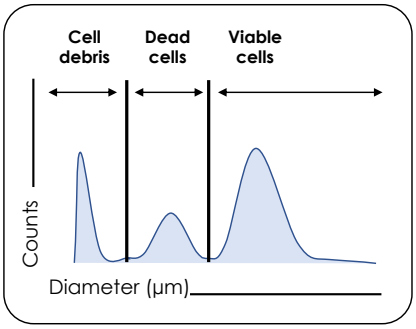


Figure 3.1 Light microscopic images of all three cell types used for the co-culture model of the human intestinal mucosa. Adherent (Caco-2 HTB-37) and suspension cells (THP-1/MUTZ-3) were imaged during cultivation and are shown with increasing magnification.

For sub-culturing, cell density and viability were determined using an automated Cell Counter (Casy® Model TT, Roche Innovatis AG, Reutlingen, Germany), equipped with an 150 µm capillary with a physical measurement range of 3.2 – 120 µm (Fig. 3.2).

A



B

Cell line	Dead cells	Viable cells
Caco-2 HTB-37	7.88 – 12.00	12.01 – 50
THP-1	6.88 – 11.54	11.55 – 50
MUTZ-3	5.00 – 7.87	7.88 – 50

C

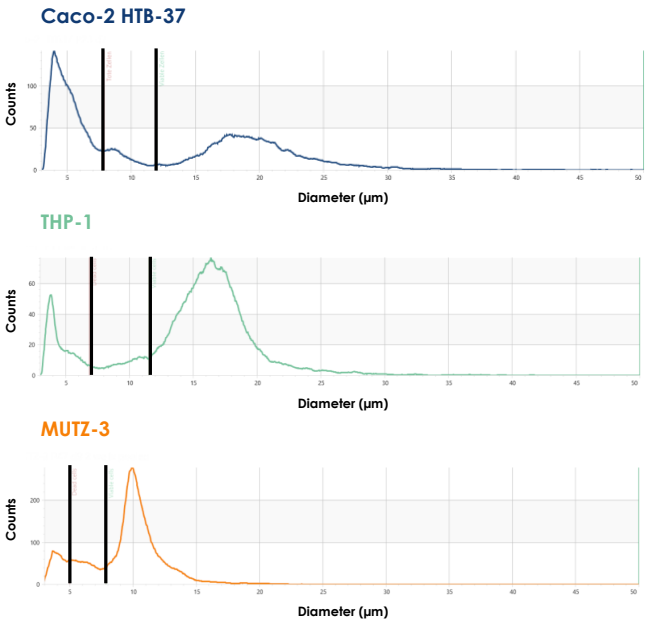


Figure 3.2 Determination of total cell number and percentage viability using an automated Cell Counter (CASY® Model TT). Schematic graph with annotated ranges for cell debris, dead or dying cells and viable cell fraction (**A**). Summary of cell-specific templates with pre-set size ranges (unit: µm) for each individual cell line in order to discriminate between dead and living cell factions (**B**). Representative graphs of cell size distribution for Caco-2 HTB-37, MUTZ-3, and THP-1 cells (**C**).

3.2.3 Experimental setup of the leaky gut model

The starting point of the leaky gut model was a previously published tight barrier model of the human intestinal mucosa to study the effect of acute inflammation [157]. To mimic impaired barrier properties ("leaky gut") like in chronic inflammation, the model was already used after 6 days of cultivation representing a sub-confluent epithelial cell monolayer compared to previous cultivation period of 11 days with a tight epithelium ("tight barrier"), as illustrated in Figure 3.3. Before co-culture start, monocytic THP-1 cells were differentiated into macrophage-like cells (dTHP-1) for 72 hours in the presence of 50 mM PMA. After pre-incubation with accutase for 15 min at RT, dTHP-1 cells were harvested using a cell scraper. Cells were centrifuged at 300 x g for 4 min and pellet was resuspended in human AB serum. 20.000 dTHP-1 cells were embedded together with 10.000 MUTZ-3 cells in 80% (v/v) collagen type I solution containing 10% 10X RPMI + 20 mg/mL $NaHCO_3$ and 10% human AB serum. A total volume of 150 µL was placed into the apical chamber of the Transwell® insert.

After 1 hour of solidification at 37°C and 5% CO_2, Caco-2 cells (100.000/well) were seeded on top of the collagen surface, in a total volume of 0.5 mL of Caco-2 medium containing 1% Pen/Strep. Subsequently, 1.5 mL of THP-1 medium plus 1% Pen/Strep were added to the basolateral side and cells were cultured under submerged conditions with media exchange every 2 to 3 days.

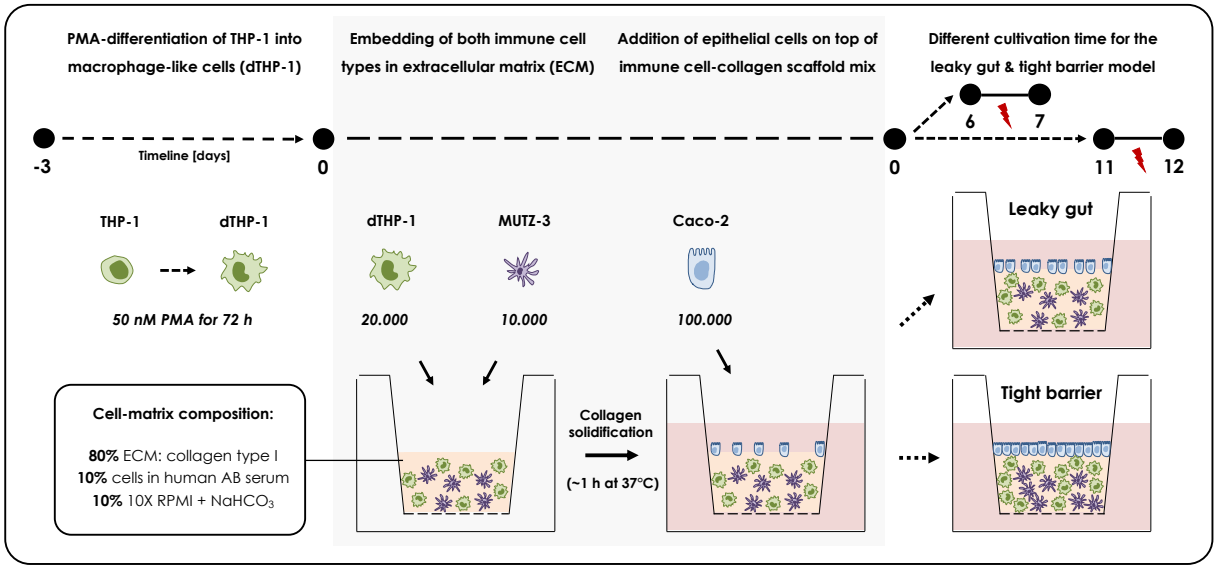


Figure 3.3 Experimental setup of the co-culture model of the human intestinal mucosa mimicking IBD conditions. Three different cell types are arranged in a physiologically relevant microenvironment and placed in a Transwell® system. Monocytic THP-1 cells were first differentiated into macrophage-like cells (dTHP-1) using PMA (50 nM for 72 h). Afterwards, dTHP-1 cells were embedded together with dendritic-like cells (MUTZ-3) in an extracellular matrix (ECM) of collagen type I with a cell ratio of 2:1. After solidification, epithelial cells (Caco-2) were seeded on top and the co-culture was cultivated for 6 days to represent the leaky gut model with a sub-confluent epithelial barrier instead of previously reported 11 days and resulting tight epithelial barrier. For inflammation induction (e.g. responsiveness to *E.coli* LPS), co-cultures were treated on day 6 or day 11 (indicated by red flash).

3.2.4 Transepithelial electrical resistance (TEER)

TEER was determined with an Epithelial Volt Ohm Meter (EVOM2; World Precision Instruments, Sarasota, USA) equipped with STX2 chopstick manual electrodes (Fig. 3.4). To minimize the factors affecting TEER, all measurements were performed before medium replenishment at controlled temperature, placing the Transwell® plate on a pre-warmed heating plate at 37°C. Final TEER values, represented in units of $\Omega*cm^2$,

were calculated by subtracting the blank value (R_{blank}, resistance of the filter support without cells, ~95 Ω) from the sample value (R_{total}) and multiplying it by the effective growth area (*A*) of the Transwell® insert (1.12 cm^2):

$$TEER\ [\Omega\ x\ cm^2\ ] = (R_{total} - R_{blank})\ x\ A$$

Co-cultures with TEER values above 300 Ω*cm^2 were considered having an established epithelial barrier property. For barrier integrity changes upon inflammation with LPS, TEER was measured before and after 6 and 24 h after inflammation induction. TEER values are represented as percentage, normalized to the initial TEER value (before the addition of LPS).

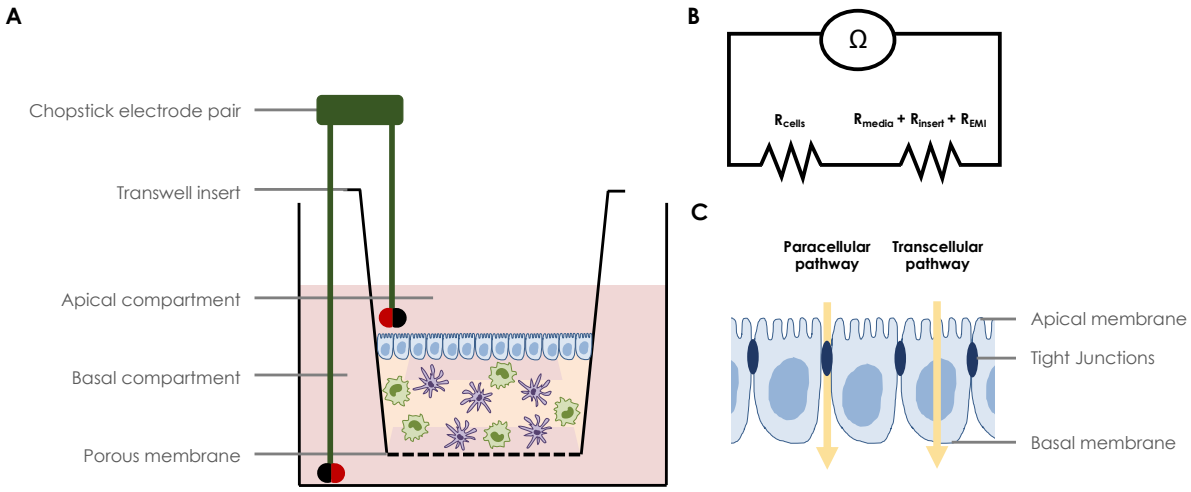


Figure 3.4 Schematic setup of Transepithelial Electrical Resistance (TEER) measurements of co-culture model cultured in Transwell® permeable supports (**A**). An alternating current signal at a frequency of 12.5 Hz is applied across the electrodes that are placed on both sides of the Transwell® system. Each chopstick electrode contains a silver/silver chloride pellet (inner pair, red) to measure voltage and silver pads for passing current (outer pair, black). The total electrical resistance comprises the resistance of the cell layer (R_{cells}), the cell culture medium (R_{media}), the insert membrane (R_{insert}) and the electrode medium interface (R_{EMI}) (**B**). TEER is the sum of two conduction pathways, the trans- and paracellular resistance (**C**). Lower TEER values indicate a lower paracellular resistance in comparison to the transcellular one, whereas higher TEER values represent equal para- and transcellular resistances.

3.2.5 Measurement of cytokine production

The presence of cell-secreted cytokines in co-culture supernatants was determined using BD™ Cytometric Bead Array (CBA) and a fluorescence activated cell sorter

(FACS; LSR II Fortessa, BD Biosciences). Aliquots of cell culture supernatant from both, apical and basolateral compartment of the Transwell® system (with a minimum volume of 55 µL) were collected before and after 6 and 24 h of inflammation with LPS (10 µg/mL). Experiments were performed in triplicates and supernatants were stored at -80°C before analysis. Cytokine quantification was performed using CBA Human soluble Protein Flex Set for TNF-α and IL-8 in accordance with the manufacturer´s protocol. Analysis was performed using FCAP Array™ Software Version 3.0.1 (BD Biosciences) and final cytokine concentration is represented in units of pg/mL.

3.2.6 Staining procedure for confocal microscopic analysis

For confocal microscopic analysis, co-culture was fixed with 4% (v/v) PFA for 30 min at RT and washed twice with PBS. Cells were first permeabilized with 1% (w/v) BSA 0.05% (w/v) saponin in PBS for 20 min at RT and afterwards stained for F-actin (cytoskeleton) with AF488-conjugated Phalloidin for 30 min at RT. Afterwards, cell nuclei were stained with 5 µg/mL DAPI for 30 min at RT. Fluorescence imaging of co-cultures grown in Transwell® systems required the removal of the whole collagen-cell matrix plus supporting PET membrane from the insert. After two washing steps, remaining PBS was removed, and the insert flipped upside down. Using a scalpel, the edges around the PET membrane were carefully cut and the collagen-cell matrix plus membrane transferred to a microscope slide with the cells facing up. After drying, cells were surrounded by a 0.5 µm thick double-faced adhesive tape to prevent deformation of the collagen-cell matrix. Finally, cells were covered with fluorescence mounting medium and sealed with coverslips. Mounted co-cultures were stored in the dark at 4°C until analysis with confocal laser scanning microscopy (CLSM; Leica TCS SP8; Leica, Mannheim, Germany). Fluorescence of DAPI and AF488-phalloidin was detected using HyD detectors with emission filters between 440-500 nm (405 nm laser) and 520-550 nm (488 nm laser), respectively. Images were acquired at 1024×1024 resolution using a 25x water immersion objective (Fluotar VISIR 25x/0.95). Confocal imaging was performed by collecting images from multiple optical planes in

the z-dimension (z-stacks) with a thickness of around 300 µm and 0.57 µm z-step size. Image analysis was performed using software Leica Application Suite X (LAS X; Leica, Mannheim, Germany). Image sequences acquired from z-stack scans were merged to create a 3D reconstruction of the specimen and adjusted in terms of fluorescence intensity, rotation in all dimensions, such as top (xy-) or side (xz/yz-dimension) view of 3D volume projections and exported as tiff files.

3.2.7 Live/dead cell staining using membrane integrity assay (FDA/PI)

The Live/dead staining of the co-culture was performed using fluorescein diacetate (FDA) and propidium iodide (PI) to identify living and dead or dying cells, respectively, according to published protocol [171]. In brief, co-culture was washed with pre-warmed PBS and afterwards incubated for 5 min in the dark at RT with the staining solution containing 20 µg/mL FDA in PBS (stock: 5 mg/mL FDA in acetone) and 40 µg/mL PI (stock: 1 mg/mL in PBS). After removal of staining solution, co-culture was washed with cold PBS and immediately analyzed by CLSM (3.2.6).

3.2.8 Surface area measurements for Caco-2 confluency calculation

Surface area of sub-confluent regions within the leaky gut model was calculated by ImageJ (version 1.52, NIH, Bethesda, USA). Confocal images of the leaky gut model in top view (xy-dimension) and overlaid fluorescence channels for cell nuclei and cytoskeleton (3.2.6) were used to calculate Caco-2 HTB-37 confluency.

Accordingly, cell-free areas within the Caco-2 HTB-37 cell layer were marked by ´free hand´ selection and respective regions were measured using ´Analyze > Measure´ (Fig. 3.5). The sum of resulting areas was divided by the total area of the image and represented as percentage of confluency. Values of sub-confluency were collected from ten different co-cultures derived from six independent experiments with a minimum number of 2 fields per co-culture.

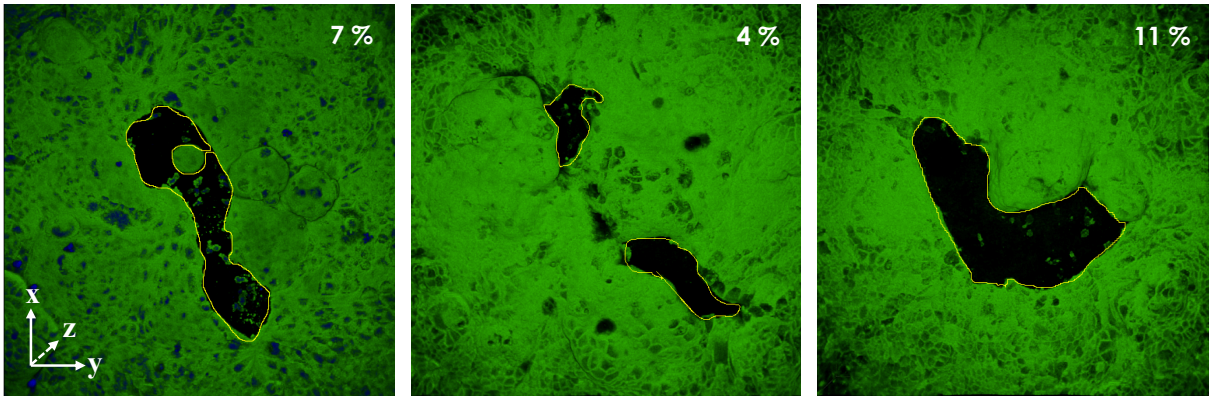


Figure 3.5 Surface area measurements for Caco-2 confluence calculation. Representative confocal images with sub-confluent regions within the leaky gut model in top view (xy-dimension) and overlaid fluorescence channels. Caco-2 confluency of the leaky gut model counterstained for cell nuclei (DAPI; blue) and cytoskeleton (AF488 phalloidin; green) was calculated after 6/7 days of cultivation by ImageJ. After ´free hand´ selection of Caco-2 cell-free areas (yellow line), respective regions were measured using ´Analyze > Measure´ and the resulting area divided by the total area of the image (represented as percentage of confluency).

3.2.9 Dissociation of the co-culture model into single cell suspension

Cells were released form the co-culture model by enzymatic and mechanical digestion in order to apply the resulting single cells for downstream analysis. To ensure sufficient cell yield after dissociation procedure, three wells were pooled together during single-cell preparation. First, Caco-2 HTB-37 cell layer was pre-incubated with trypsin-EDTA, applied to the apical site, and incubated for 10 min at 37°C. Detached cells were collected by several flushing steps using HBSS and placed in Caco-2 culture medium on ice. Afterwards, co-culture was incubated with collagenase type II solution (12.5 U/mL in HBSS) for 20 min at 37°C to release the embedded immune cells from the collagen matrix. Enzymatic degradation was supported by mechanical agitation and repeated pipetting up and down (every 7 min) using a 1 mL pipette tip with ~3 mm cut-off. Cells were collected and added to the previous cell collection on ice. Afterwards, the insert was rinsed twice with PBS to collect all remaining cells from the Transwell®. Resulting single-cell suspension was applied to a cell strainer (100 µm) placed on a 50 mL tube. Cells were centrifuged at 300 x g (1400 rpm) for 4 min, supernatant discarded, and cell pellet resuspended in PBS for subsequent analysis.

3.2.10 Analysis of cell yield and viability after co-culture dissociation

For cell count, an aliquot was analyzed by an automated cell counter (Casy® Model TT) with a pre-set of distinct size ranges to separate for MUTZ-3 with a size range of 8-13 µm and the other two bigger cell types, Caco-2 HTB-37 and dTHP-1 within 13-50 µm. After sample measurement, size distribution of both size ranges was adjusted to the total volume of cell suspension and represented as total cell yield of 3 wells pooled together.

Cell viability was determined by Live/dead cell staining using Calcein AM and DAPI, identifying viable and dead cell fractions, respectively. After incubation with Calcein AM (10 ng/mL in PBS) for 30 min at RT, cells were washed twice with 2% FCS in PBS and resuspended in DAPI solution (0.1 µg/mL in PBS) prior to analysis by FACS. At least 10.000 single cell events were collected and obtained data was analyzed using FlowJo™ software (Version 10.6.0; FlowJo LLC, Ashland, USA). Cells were visualized in granularity vs. size (SSC-A/FSC-A) and fluorescence (FITC-A/Pacific blue-A) flow plots or histograms with separated fluorescence channels for living (Calcein AM or FITC-positive) and for dying/dead (DAPI or Pacific blue-positive) cells. Unstained samples or dead cell control (heat-treated; 30 min at 65°C) were included for the setting of appropriate gating to determine autofluorescence or background and positive control for dead cells, respectively. Respective cell fractions of living (Q1), dead or dying cells (Q2+Q3), and unstained cell population (Q4) are represented as percentage of total cell count.

3.2.11 Data analysis and statistics

Data is represented as mean ± standard deviation (SD) and data collected or exported in Microsoft Excel. The graphs are plotted using GraphPad Prism software (Version 9.0.0). If not stated otherwise, all procedures were conducted at least in three independent experiments (N) and measured in technical triplicate (n). Statistical analysis was performed by unpaired Student´s t-test or one-way analysis of variance

(ANOVA) with post-hoc Tukey´s test for multiple comparison. Differences were considered as significant for $p < 0.05$ (*), $p < 0.01$ (**), $p < 0.001$ (***), and $p < 0.0001$ (****) and not significant for $p \geq 0.05$ (ns).

3.3 Results

3.3.1 Characterization of leaky gut model using confocal microscopy

The leaky gut model is based on a co-culture of human epithelial and immune cells that are arranged in a physiologically relevant microenvironment. This model aims to mimic human IBD pathophysiology of the intestinal mucosa *in vitro*. Accordingly, two immune cell types (macrophage- and dendritic-like cells) were embedded in an extracellular matrix (ECM; collagen type I), placed in a Transwell® system and with subsequently covered with epithelial-like cells (Fig. 3.3). This *in vivo*-like composition including a leaky barrier of the epithelium and inflammatory response mediated by sub-epithelial immune cells provided two essential characteristics of IBD pathophysiology.

Previously published co-culture systems were used as a starting point, representing a confluent epithelium where acute inflammation resulted in a tight junctions (TJ)-mediated permeability increase after pro-inflammatory stimulation [155,157]. The leaky gut model was developed to reproduce pronounced epithelial damage as a consequence of chronic inflammation of IBD and integrated a leaky epithelium that was associated with an increased loss of barrier integrity beyond TJ openings. Resulting co-culture model was investigated in terms cell morphology and spatial features using confocal microscopy (Fig. 3.6). Staining of cell nuclei and cytoskeleton using DAPI and AF488-conjugated phalloidin supported the visualization of the cells within the co-culture model. Figure 3.6A shows the differences between leaky gut (day 7) and previous tight barrier model (day 12). The shortening of the cultivation time resulted in a sub-confluent layer of epithelial cells (leaky regions indicated by white arrows). Moreover, the cell density of proliferative-active immune cells in the sub-epithelial layer was discernible reduced (Fig. 3.6A; side view). The morphology of immune cells embedded in the collagen-matrix varied according to the cell type and showed either small and round shapes of monocytic cells (THP-1) or the development

of podosome-like structures and cell protrusions assigned to dendritic- and macrophage-like cells (MUTZ-3 & dTHP-1) (Fig. 3.6B/C).

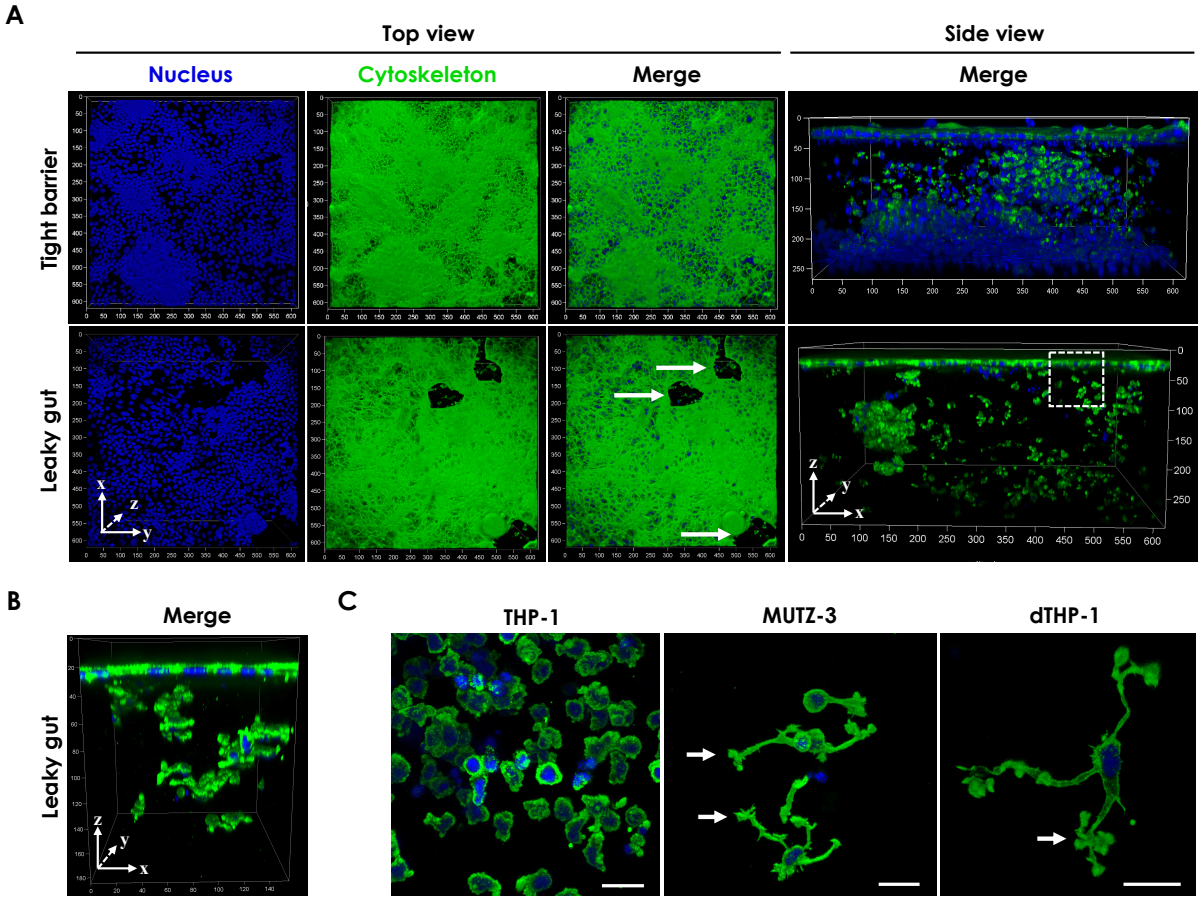


Figure 3.6 Microscopic investigations of tight barrier vs. leaky gut model. Confocal images of co-cultures representing a confluent (day 12; tight barrier model) or sub-confluent epithelium (day 7; leaky gut model) with leaky regions indicated by white arrows (**A**). Cells were stained stained for cell nuclei (DAPI; blue) and cytoskeleton (AF488-phalloidin; green). Recorded z-stacks of ~250 µm depth are represented in top (xy-) or side (xz/yz-dimension) view separated or overlaid (merge) fluorescence channels (axis unit = µm). Close-up of leaky gut model (dashed rectangle) with sub-epithelial immune cells in close proximity to the Caco-2 cell layer (**B**). Morphology of immune cells embedded in collagen-matrix (leaky gut model; day 7) with round shapes (THP-1) or podosomal cell protrusions (MUTZ-3 and dTHP-1) indicated by white arrows (**C**). Images of 3D cells are projections of 20-30 µm z-sections (scale bar = 20 µm) repesented in top-view.

The intestinal *in vitro* model was further improved regarding the cell ratio of immune cells as well as differentiation protocol for the macrophage-like phenotype. Compared to previous co-culture model, the double amount of dTHP-1 cells was embedded together with MUTZ-3 cells resulting in an immune cell ratio of 2:1 (dTHP-1:MUTZ-3). In addition, THP-1 differentiation into macrophage-like cells was performed at higher

PMA concentration (50nM) as well as longer incubation time (72 h). Morphological changes were observed during THP-1 differentiation as cellular adhesion and spreading of dTHP-1 cells during PMA incubation (Fig. 3.7A).

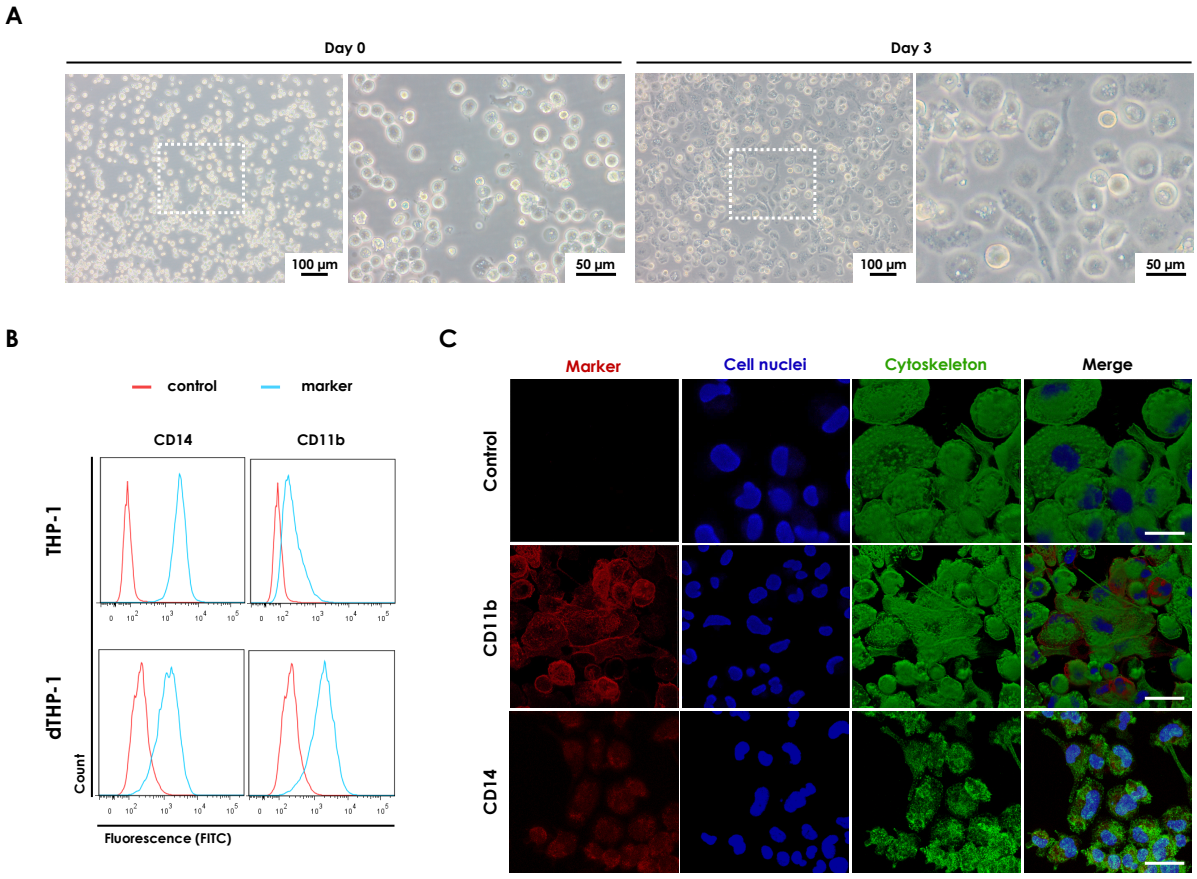


Figure 3.7 Macrophage-like phenotype of dTHP-1 after PMA-differentiation and expression of different cell markers determined by flow cytometry and confocal microscopy. Representative light microscopic images of THP-1 cells diffentated for 3 days in the presence of 50 nM PMA (**A**). CD11b (β2 integrin; macrophage marker) and CD14 (monocyte marker) was estimated by flow cytometry in monocytic (THP-1) and PMA-differentiated (dTHP-1) cells (**B**). THP-1 cells were seeded with or without PMA (50 nM; 72 hours) and harvested for flow cytometric analysis. Histogram overay displays FITC-positive (antibody) cells compared to unstained (control). Confocal microscopic images of dTHP-1 cells (seeded on µslides) stained with mouse anti-CD14 (FITC) or anti-CD11b (AF647) antibodies (**C**). Cells were stained for cytoskeleton (Rhodamine or AF488-phalloidin; green) and cell nuclei (DAPI; blue). Recorded images are represented in split channels or overlaid (merged) fluorescence signal with both cell markers shown in red. (Scale bar = 50 µm)

Immunofluorescence staining either analysed by flow cytometry or confocal microscopy underlined the activation state of dTHP-1 cells. Flow cytometric data revealed an up-regulated expression of macrophage (CD11b) and reduced monocyte

(CD14) marker within PMA-differentiated THP-1 cells in comparison to monocytic THP-1 cells (Fig. 3.7B). Furthermore, the presence of both markers was evaluated by confocal microscopic images using 2D-cultured dTHP-1 cells (Fig. 3.7C).

3.3.2 Epithelial barrier integrity of leaky gut model

Cell confluency and integrity of Caco-2 HTB-37 cell layer within the co-culture model were determined over time by microscopic analysis and transepithelial electrical resistance (TEER) measurements (Fig. 3.8).

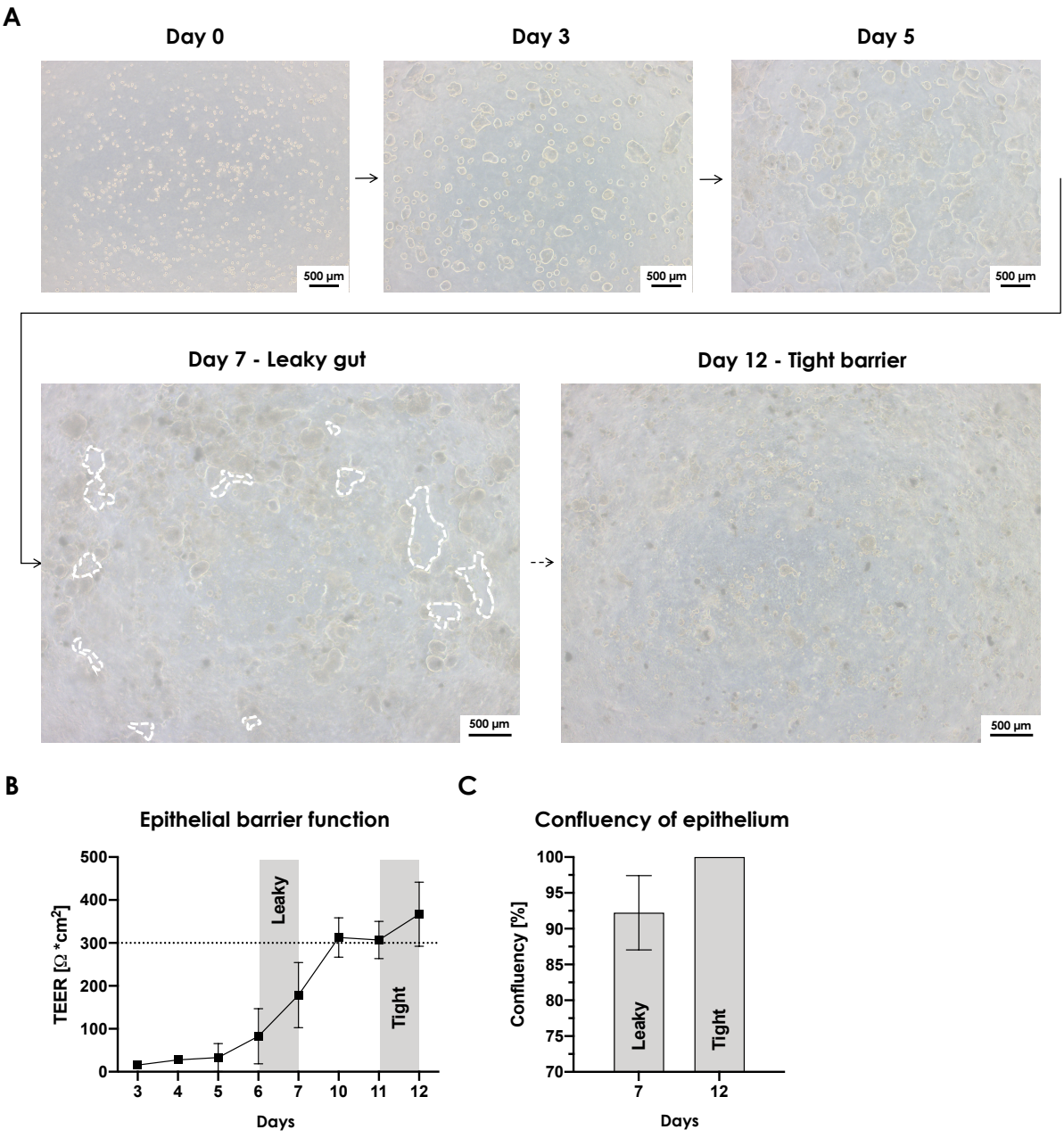


Figure 3.8 Characterization of leaky *versus* tight epithelial barrier of the co-culture model. Light microscopic images of epithelial layer growth depicted from co-culture start (day 0) and on following time points (day 3/5) to leaky gut (day 7) and tight barrier (day 12) model (**A**). Leaky areas are highlighted with a white dashed line. Measurements of epithelial barrier function monitored by TEER over time (intact barrier with 300 Ω*cm^2; dashed line) (n=6-15; N=4) (**B**). Confluency measurements of leaky gut model by area calculation of cell-free regions compared to tight epithelium (100% confluency) with ≥ 2 positions of ten leaky models from 6 independent preparations (n=21; N=6) (**C**). Data is represented as mean ± SD.

After co-culture start and Caco-2 HTB-37 seeding, cells attached to the collagen surface and grew by steady proliferation until representing a leaky or tight epithelium on day 7 or day 12, respectively (Fig. 3.8A). The leaky gut model showed resistance values between 83 ± 64 and 179 ± 76 Ω*cm^2 for day 6 and 7 after seeding, whereas the densely grown Caco-2 HTB-37 cell monolayer of the tight barrier model generated values above 300 Ω*cm^2 (Fig. 3.8B). In addition, sub-confluency of the leaky gut model was calculated by surface area measurements of epithelial cell-free areas resulting in a confluency of 87-97% compared to the 100% confluent epithelium of the tight barrier model (Fig. 3.8C).

3.3.3 Immune response within leaky gut model after LPS inflammation

The leaky gut model was further characterized in terms of the responsiveness to bacterial-derived lipopolysaccharides (LPS; 10 µg/mL) as pro-inflammatory agent. For the tight barrier model, LPS stimulation led to a significant decrease of TEER to about 80% ± 7% and 88% ± 14% after 24 h and 48 h compared to unstimulated control, respectively (Fig. 3.9B). The release of pro-inflammatory mediators, such as interleukin-8 (IL-8) and tumor necrosis factor-alpha (TNF-α), was monitored after 6 and 24 h after apical LPS stimulation. In general, both co-cultures showed an increased cytokine production including IL-8 and TNF-α, however, differences in immune response were observed merely after 24 hours of stimulation. Similar amounts of IL-8 were released after 6 h to the basolateral site (BL), with 980 ± 750 pg/mL and 620 ± 350 pg/mL for leaky gut and tight barrier model, respectively (Fig. 3.9C). The same was observed for the apical compartment (AP), with 720 ± 500 pg/mL and 60 ± 10

pg/mL. After 24h, besides a comparable release of IL-8 for BL, a significantly higher secretion was found for AP with 6800 ± 2500 pg/mL for the leaky gut compared to only 300 ± 140 pg/mL for the tight barrier model. A general higher production of TNF-α within the leaky gut model for both time points and compartments. A significantly higher immune response was observed after 24 h after LPS stimulation with 300 ± 140 pg/mL (AP) and 460 ± 80 pg/mL (BL) compared to very low amounts detected for the tight barrier model with the highest production of 70 ± 50 pg/mL (BL) (Fig. 3.9C).

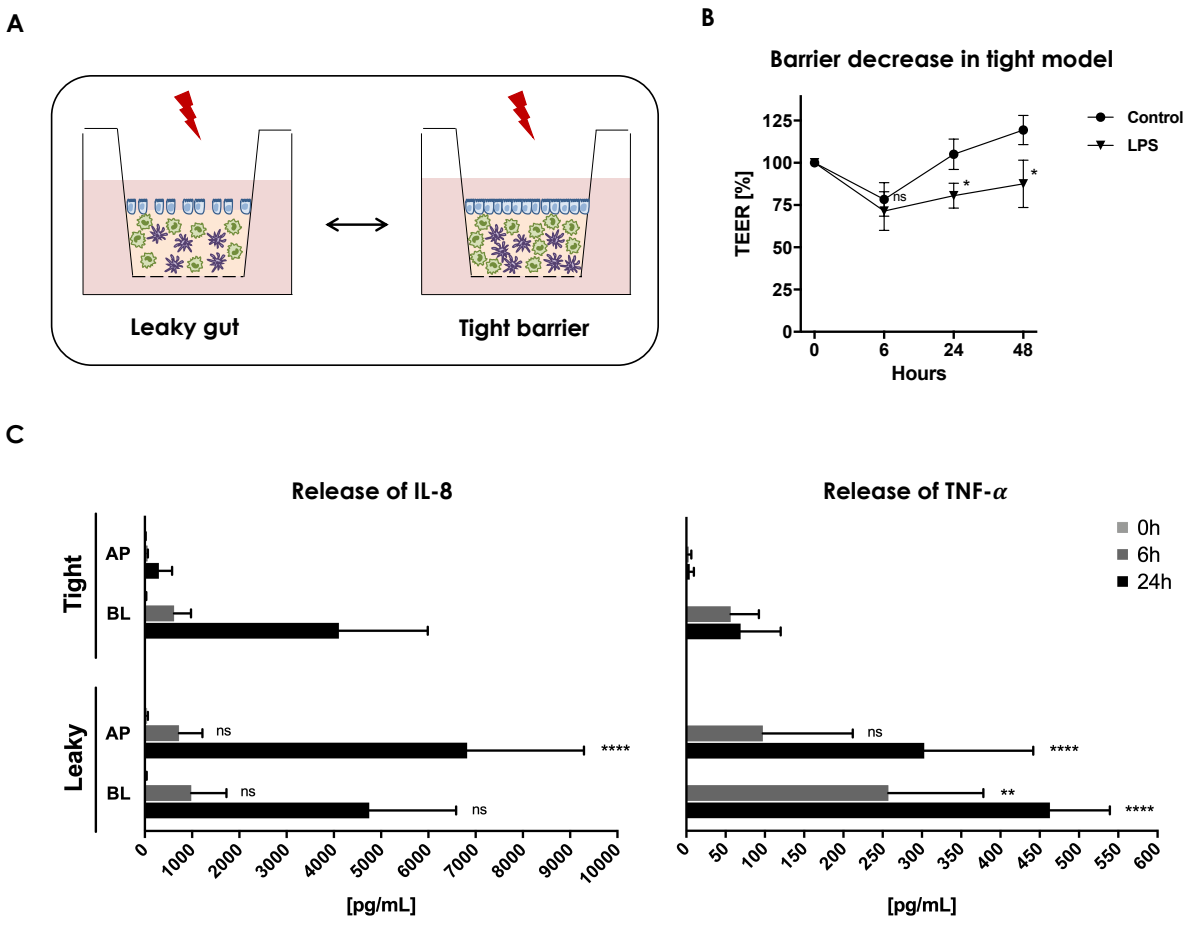


Figure 3.9 Characterization of leaky gut *and* tight barrier model regarding responsiveness to LPS. Scheme of apical stimulation using LPS (10 µg/mL) and monitoring ongoing inflammation within leaky gut compared to tight barrier model (**A**). Barrier function decrease of tight barrier model after LPS inflammation (10 µg/mL) compared to unstimulated control. TEER represented as percentage, normalized to the initial TEER value (*denotes $p< 0.05$ according to Student´s test); (n=9; N=3) (**B**). Cytokine production in leaky gut and tight barrier model including interleukin 8 (IL-8) and tumor necrosis factor alpha (TNF-α) released to the apical (AP) and basolateral (BL) compartment after 6 and 24 hours post LPS stimulation (** $p< 0.01$ and **** $p< 0.0001$ according to ANOVA); (n=6; N=2) (**C**). Data is represented as mean ± SD.

3.3.4 Dissociation of co-culture model and analysis of single cell suspension

The Live/dead cell staining of the intact model was performed on day 14 to identify the viable cell population within the co-culture model using microscopic analysis. Double staining of FDA/PI revealed that the number of dead cells within the Caco-2 HTB-37 cell layer as well as immune cells was negligible and showed good viability after two weeks of cultivation within the ECM (Fig. 3.10).

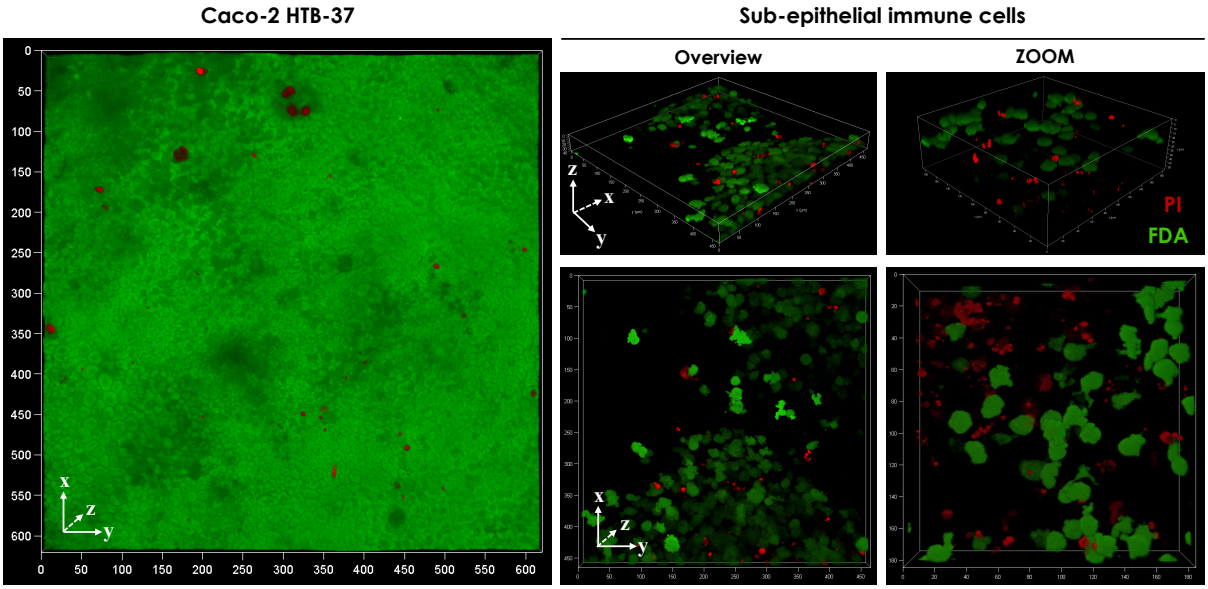


Figure 3.10 Characterization of co-culture model regarding cell viability using FDA/PI staining. Live/dead cell staining to identify viable (FDA; green) and dead or dying (PI; red) cell population within the co-culture model at day 14. Representative images of epithelial cell layer (Caco-2 HTB-37; top view) and sub-epithelial immune cells (lateral/top view) with additional close-up. (axis unit = µm)

In order to provide better insights into cell number and viability as well as the feasibility of downstream analysis, the disintegration of the co-culture into singular cells was performed. Accordingly, the co-culture model was dissociated after pre-determined cultivation by a combination of enzymatic digestion and mechanic disruption as frequently realized for isolation of primary cells from tissue samples. The resulting single-cell suspension was investigated in terms of total cell yield using an automated cell counter with pre-set size ranges to discriminate between cell debris and living cells as well as their cell type. Figure 3.11 shows the related flow cytometric

data of the Live/dead staining using Calcein AM and DAPI for living (FITC-positive; Q1) and dead/dying cell population (Pacific blue-positive; Q2+3), respectively. The staining method was optimized for both, leaky gut (Fig. 3.11A) and tight barrier model (Fig. 3.11B), using appropriate controls to setup the gating strategy including unstained cells to determine autofluorescence and (heat-induced) dead cells as positive control.

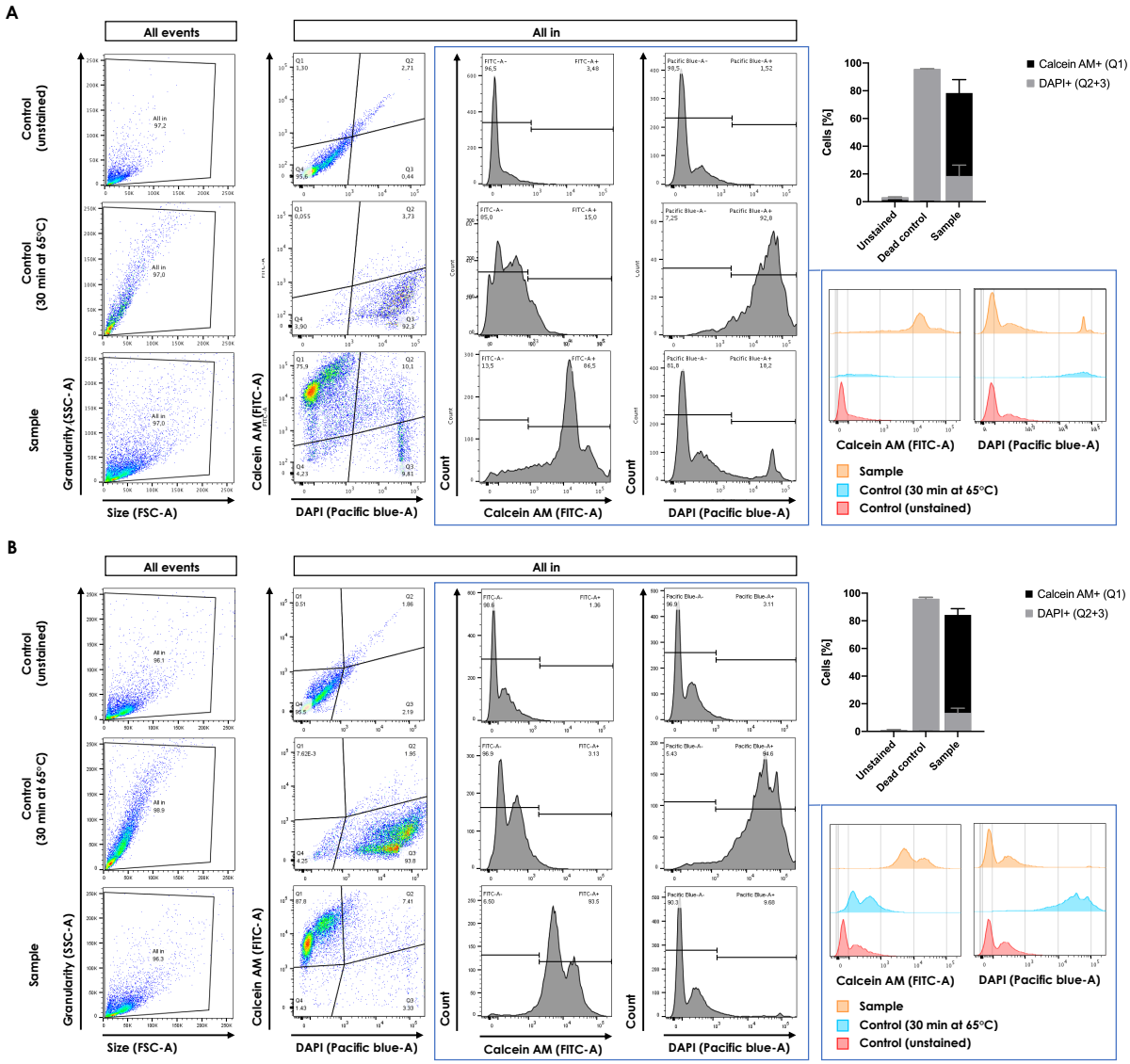


Figure 3.11 Live/dead cell staining of cell suspension after dissociation of leaky gut (A) and tight barrier (B) model using flow cytometry. Resulting single cell suspension was stained for viable (Calcein AM; 10 ng/mL) and dying/dead (DAPI; 0.1 µg/mL) cells and analyzed by FACS. Representative flow cytometric data with gating strategy to identify living (FITC-positive) and dead cell fraction (Pacific blue-positive). Obtained cell populations are visualized in granularity *vs.* size (SSC-A/FSC-A) and fluorescence (FITC-A/Pacific blue-A) density plots or histograms with separated fluorescence channels with positive-cell fractions. Upper panel shows control of unstained cells (without addition of Calcein AM/DAPI) and a

double-negative cell population (dot plot; Q4). The middle panel displays the stained heat-treated dead cell control (65°C for 30 min) and the lower panel shows the stained cell suspension (Sample). Overlaid histograms are highlighted in the blue box. Calcein AM- and DAPI-positive cell population are summarized as percentages of positive cells (mean ± SD).

The volume-based cell size distribution was analyzed by an automated cell counter (Casy® TT) and provided detailed information about cell size, the level of cellular homogeneity, the degree of cell aggregation as well as the percentage of viable cells. Figure 3.12 summarises the cell count measurements performed for each individual cell type in order to identify potential cell size-related differences in the viable cell fraction (IIIa) and for the single-cell suspension resulting from leaky gut and tight barrier model dissociation. Caco-2 HTB-37 cells showed a more heterogeneous cell population with a broad peak ranging between 15 – 25 µm and a mean diameter of around 20 µm (Fig. 3.12A; first plot). In contrast, MUTZ-3 cells were about 11 µm in diameter with a narrow size distribution indicating a more homogeneous cell population (Fig. 3.12A; second plot). The mean diameter of monocytic THP-1 cells was about 17 µm with cell size ranging between 13 – 20 µm, whereas macrophage-like (dTHP-1) cells showed increase in cell size with around 24 µm and represented the broader size distribution (Fig. 3.12A; both last plots). Accordingly, the corresponding cell size can be ranked from small to big as follows: MUTZ-3 << THP-1 << Caco-2 HTB-37 < dTHP-1 (Fig. 3.12B).

Based on the cell count templates of the individual cell types, Caco-2, THP-1, and dTHP-1 displayed broad size ranges with distinct overlapping regions in comparison to MUTZ-3 cells that was distinguished below 13 µm (Fig. 3.12C; dashed line). Accordingly, single-cell suspensions resulting from co-culture dissociations were measured with adapted size ranges. MUTZ-3 cells, the smallest cell type within the co-culture model, were expected within the size range of 8 - 13 µm (IIb) and the other cell types, (d)THP-1 and Caco-2 HTB-37, with similar size ranges between 13 - 30 µm (IIIb) (Fig. 3.12D).

However, cell counting of single-cell suspensions was limited to display the cell size distribution for each specific cell type. In addition, dead or dying cells from bigger cell

types (IIa) could overlap with the MUTZ-3 viable cell range (IIIa). Consequently, the cell proportion of the co-culture models could only be estimated instead of providing absolute cell numbers.

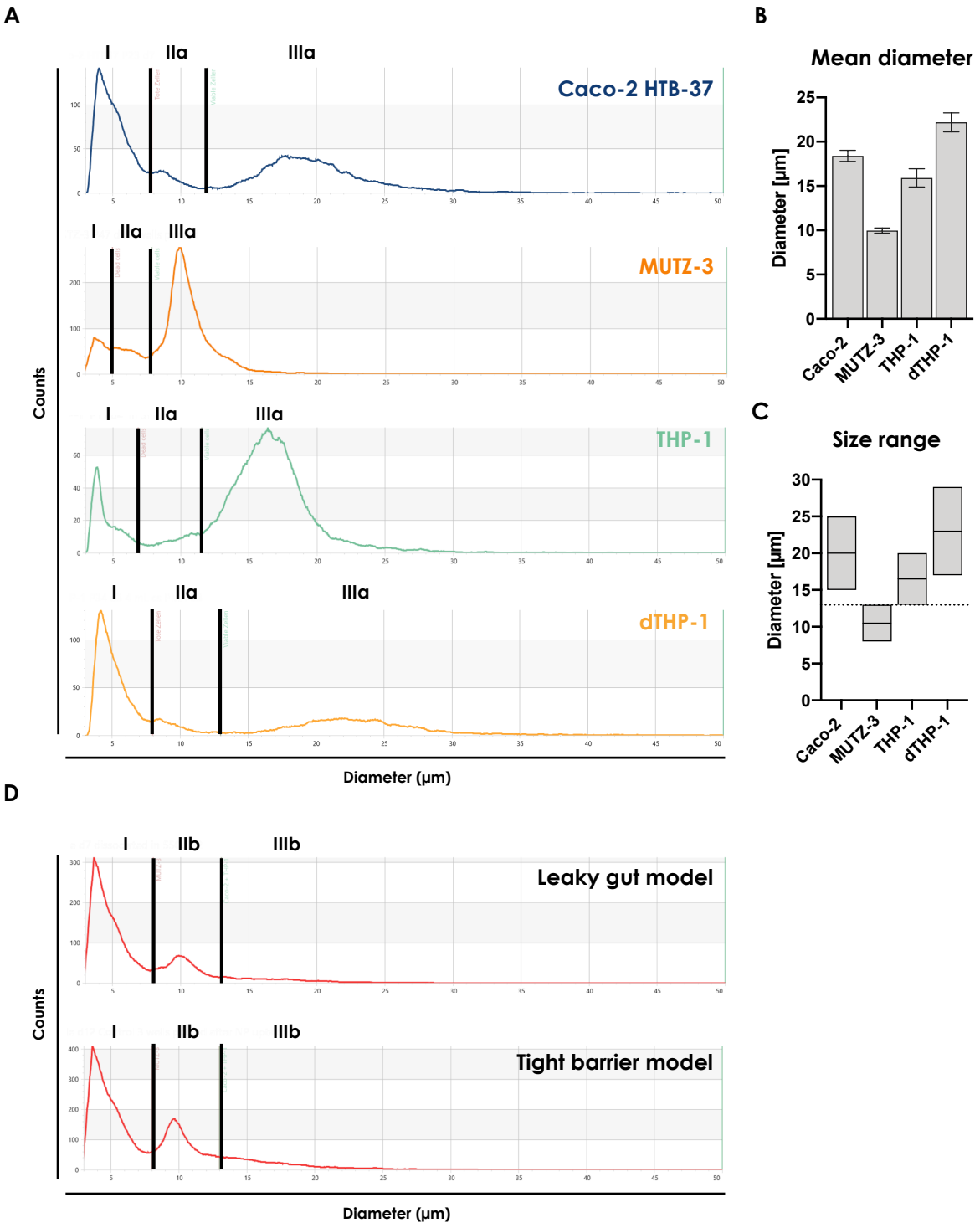


Figure 3.12 Determination of total cell number obtained after co-culture dissociation using an automated cell counter (CASY® TT). Representative size distribution plots of Caco-2 HTB-37, MUTZ-3, THP-1, and dTHP-1 cells (**A**). Cell number and percentage viability was determined by different size ranges pre-set for each individual cell line in order to differentiate between cell debris (< 8 µm; **I**), dead or dying cells (**IIa**), and viable cell population (**IIIa**). Mean diameter (**B**) and size ranges (**C**) of viable cell

population represented as mean ± SD of 9 individual cell counts for each cell type (Floating bars (min to max) with mean value). Representative graphs of resulting single-cell suspension after dissociation of leaky gut and tight barrier model (**D**). Appropriate size ranges were determined to separate for dendritic-like cells (MUTZ-3) with a range of 8-13 µm (**IIb**) and the other two cell types, epithelial (Caco-2 HTB-37) and macrophage-like cells (dTHP-1), with similar size ranges between 13-50 µm (**IIIb**).

After dissociation, the majority of cells showed good viability for both co-culture models, displaying 78.4 ± 9.6% for the leaky gut and 84.3 ± 4.5% for the tight barrier model (Fig. 3.13A). As mentioned before, a lower number of cells was collected from the leaky gut (day 7) compared to the tight barrier model (day 12).

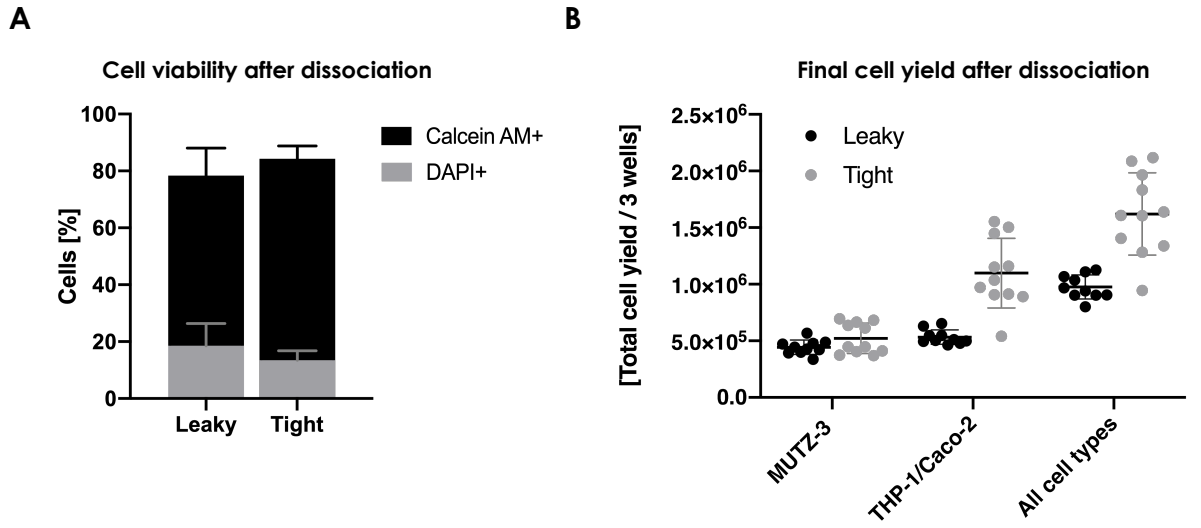


Figure 3.13 Cell yield and viability of single cell suspension after dissociation of co-culture model. Comparison of cell yield of the resulting single-cell suspensions from leaky gut and tight barrier model using an automated cell counter (3 wells pooled together). Cell size distribution of dendritic-like cells (MUTZ-3; 8-13µm) and the other two cell types, epithelial (Caco-2 HTB-37) and macrophage-like cells (dTHP-1), within 13-50µm, were adjusted to the total volume of cell suspension and represented as total cell yield of 3 wells; (n= 8-12; N= 4) (**A**). Resulting single cells suspension was stained for living (Calcein AM-positive) and dying/dead cells (DAPI-positive) and analyzed by FACS (tight barrier: n=6; N=2 and leaky gut model: n=9; N=3) (**B**).

The single-cell suspension from the leaky gut model contained a total amount of approximately 1 x 10^6 cells (three wells pooled) consisting of an equal amount of MUTZ-3 and THP-1/Caco-2 cells (Fig. 3.13B). In comparison to that, the tight barrier model showed a higher cell yield after dissociation with around 1.7 x 10^6 cells with a similar proportion of MUTZ-3 cells, but more than a double amount of the other cell types (Fig. 3.13B).

3.4 Discussion

Recent advances in complex *in vitro* models are challenged by physiological resemblance focusing on intestinal organoids, microfluidic systems with dynamic flow or contractile forces, and co-culture models comprising gut microbiome [110,142]. Nevertheless, the increased complexity of these *in vitro* models retains some confinements regarding drug interactions studies. Besides ethical considerations and limited access to human primary tissue, drawbacks are related to the lack of immune-related responses or high variability between individual samples [7,144]. In addition, there is an unmet need for appropriate *in vitro* models to investigate drug interaction within the human intestinal mucosa under diseased conditions. Intestinal *in vitro* models reproducing IBD pathophysiology could complement animal testing in biomedical research and as preclinical testing platform validate the therapeutic outcomes of drug formulations.

The here presented leaky gut model mimics the intestinal interface comprising an epithelial barrier as well as sub-epithelial immunocompetent cells and incorporates advanced features similar to IBD disease manifestation. The model is based on cell lines of human origin that maximises the model´s applicability to a human exposure scenario. Besides that, it allows for better standardization and validation, as well as for ease of access to cells throughout the laboratories. The reproduction of IBD diseased state including a dysfunctional epithelial barrier and inflammatory processes is necessary to perform drug absorption studies under diseased conditions and to evaluate related therapeutic outcomes.

Intestinal barrier dysfunction plays a central role in IBD pathogenesis and is associated with increased intestinal permeability and local inflamed microenvironment including the elevated concentration of cytokines and continuous immune cell recruitment to the inflammation site [212]. However, a ´leaky gut´ is often referred to an altered permeability with enhanced paracellular diffusion of luminal contents and, moreover, related to epithelial gaps or breaches as a result of an impaired epithelial cell turnover

and cellular damage or apoptosis [213–216]. On the contrary, the leaky gut model is supported by endoscopic observation in IBD patients that showed structural defects termed microerosions that evolve during aberrant epithelial damage and apoptosis and correlate with mucosal wound healing [9,217,218]. IBD is often associated with the lack of resolving mucosal damage [78]. Modelling these excessive epithelial damages of the GI tract were realized by the introduction of a sub-confluent Caco-2 HTB-37 cell layer. The corresponding leakiness or sub-confluency reflecting chronic inflammation of the intestine was ranging between 3 and 13%. This guaranteed the presence of an almost confluent enterocyte-like layer containing small openings. Electrophysiological quantification of epithelial barrier tightness that is indicative for the presence of differentiated cells as well as the expression of TJ regulating paracellular permeability and integrity [219]. TEER measurements of the leaky gut model displayed resistance values below 200 $\Omega*cm^2$ representing a not fully established but partial epithelial barrier. Compared to previous observations, GI epithelial barrier is considered ´tight´ with resistance around 2000 $\Omega*cm^2$, ´intermediate´ with values between 300-400 $\Omega*cm^2$, and ´leaky´ ranging from 50-100 $\Omega*cm^2$ [220]. However, TEER depends on the respective Caco-2 cell clone as well as cell culture conditions such as seeding density or serum content that may result in cell growth-related variations affecting the development of the epithelial barrier. Based on the former studies, Caco-2 cell clone HTB-37 displayed faster cell growth and higher TEER compared to previously used C2BBe1 cell clone [221]. In addition, Caco-2 cell growth is influenced by the passage number showing increased proliferation rate as well as TEER towards higher passages [222]. In line with previous reports, Caco-2 cells displayed slower growth when seeded on top of the collagen matrix gel compared to cells directly seeded on Transwell® porous membranes [133,136]. In consideration of all these variabilities, consistent culture conditions were performed including the use of the same passage numbers excluding late passages in order to achieve a comparable degree of epithelial sub-confluency in the leaky gut model.

Compared to previous co-culture setup, the leaky gut model contained the double amount of macrophage-like cells as well as used an optimized THP-1 differentiation protocol with increased PMA concentration (up to 4-fold) and extended incubation time [157]. The morphology of immune cells embedded in the collagen matrix was characterized by confocal microscopy and revealed distinct phenotypes that are related to (un-)differentiated cells. Similar podosome-like structures with matrix-degrading adhesive properties were identified for macrophages and dendritic cells necessary to enable migration through tissue [223]. According to accepted criteria to recognize fully differentiated THP-1 cells, dTHP-1 cells showed macrophage-like properties with elevated CD11b expression necessary for cell adhesion and motility, and reduced monocyte marker CD14 expression that is usually downregulated during PMA-differentiation [224,225]. For additional characterization of differentiation, cell-specific markers could be extended for collagen-embedded immune cells.

LPS-responsiveness is related to activated immune cells and pro-inflammatory response mediated by the production of cytokines. Despite the reduced total cell number, a significantly higher immune response to LPS stimulation was observed for the leaky gut model with increased cytokine production of both, IL-8 and TNF- α. In earlier studies, macrophage-like cells (dTHP-1) were the main contributors for cytokine production within the co-culture, however, TNF-α expression was quantified only on the transcriptional level [155]. The detection of ongoing inflammation was realized with comparable values observed within other co-culture models, despite of the possible effect that secreted cytokines may have been entrapped within the collagen matrix [129]. Enhanced secretion of pro-inflammatory cytokines within the leaky gut model could be explained with the a more activated macrophage phenotype due to higher and longer exposure to PMA, which concurs with previous reports [226]. Moreover, doubling the number of mature macrophages (dTHP-1) in the leaky gut model turned out to be advantageous for studying LPS-stimulated immune response compared to the previous tight barrier model. Additionally, the shorter cultivation time of the leaky gut model provides more active and differentiated dTHP-1 cells

within the collagen matrix. Previous studies have shown that an extended culture of dTHP-1 cells in the absence of PMA will lead to de-differentiation and recovery of proliferative activity generating monocytic THP-1 cells [225]. As a consequence, the presence of undifferentiated THP-1 cells with a doubling time of ~35 - 50 hours will affect the cell ratio within the model and reduce the responsiveness to pro-inflammatory stimuli [227]. Another reason for the increased cytokine production could be related to the increased permeation of LPS to the sub-epithelial layer and thus, a better access for immune cells stimulation. Based on several previous data, bacterial endotoxins increase paracellular permeability, however, LPS passage through paracellular spaces is hindered for intact epithelial barriers [228].

Co-culture dissociation was performed to release the incorporated cells from the co-culture model and to provide novel insights into cell number and viability as well as the feasibility of downstream analysis. Live/dead cell staining revealed that the cell viability of all cell types remained high throughout the co-culture period, however, cell survival after co-culture disaggregation has an important impact on subsequent cell analysis. Despite not all cells were fully recovered from dissociation procedure, a sufficient number of viable cells were collected from the leaky gut model.

As anticipated, cell counter analysis of resulting single-cell suspensions provided an estimation of the total cell yield instead of cell type-specific cell distribution. As mentioned above, differentiated macrophages (dTHP-1) do not proliferate within the co-culture, but the potential presence of de-differentiated THP-1 cells may contribute to the cell ratio. Regarding the doubling time of each cell type present in the co-culture, MUTZ-3 cells are the slowest proliferating cells (100 - 120 h), THP-1 the fastest (~35 - 50 h) and Caco-2 cells in the middle range (~60 h) (DMSZ/ATCC data sheets). Taking into account that collagen embedding and co-culture could alter the cell proliferation and function, information about the doubling time for each cell line are indicative and may not represent cell growth under 3D conditions [229]. Furthermore, cell size distribution may not be a specific determinant for cell number evaluation of this heterogenous cell suspension as dead or dying cells may fall in the sized range of

smaller cell types and cell aggregates may be identified as cells with a bigger shape. Based on clinical observations, where intestinal inflammation is altering the numerical and proportional composition of intestinal immune cells, comprising tissue-resident and recruited monocyte-derived macrophages or dendritic cells, the present co-culture model is reproducing these changes [126,127]. However, to improve the resolution into cell proportion and cell-related viability, FACS-based analysis could be combined with cell-type specific markers for epithelial and immune cells.

Further applications of the leaky gut model could be performed for GI safety assessment including drug-induced or environmental toxicity studies. Furthermore, as wound healing and inflammation are highly connected biological processes [212], the leaky gut model provides a still growing epithelial layer could lead to further investigations of epithelial healing factors and novel targets supporting barrier restoration.

3.5 Conclusion

The leaky gut model was developed to mimic the intestinal interface comprising an epithelial barrier and sub-epithelial immunocompetent cells with advanced features similar to IBD disease manifestation. Both, the leaky barrier of the epithelium and increased inflammatory response mediated by sub-epithelial immune cells provided two essential characteristics of IBD pathophysiology. The model based on cell lines of human origin to maximise the model´s applicability to a human exposure scenario. This allows for better standardization and validation, as well as access to cells throughout the laboratories. The application of human-derived co-cultures provides the engagement of human target sites and compared to animal testing and interspecies differences, an improvement towards clinical translation.

4 Part III - Leaky gut model as preclinical model to validate JAK inhibitors

Parts of this chapter are subjects of a forthcoming publication entitled "Leaky gut model of the human intestinal mucosa for testing siRNA-based nanomedicine targeting JAK1", co-authored by **Olga Hartwig**, Brigitta Loretz, Adrien Nougarede, Dorothée Jary, Eric Sulpice, Xavier Gidrol, Fabrice Navarro, and Claus-Michael Lehr.

Main contributions to this publication: OH performed all cell-related experiments, analyzed corresponding data and wrote/edited the manuscript.

4.1 Introduction

Inflammatory bowel disease (IBD) encompasses gastrointestinal (GI) disease states caused by chronic relapsing inflammation without known etiology including two main entities such as Crohn´s disease (CD) and Ulcerative colitis (UC). The complex pathogenesis of IBD is related to genetic and environmental factors and includes a dysregulated immune system, dysbiosis of gut microbiome and an impaired intestinal epithelial barrier [64]. The loss of intestinal homeostasis is triggered by the translocation of bacterial products into the intestinal wall and together with the lack of anti-inflammatory mechanisms are favouring an aberrant pro-inflammatory reaction including progressive immune cell infiltration and potential tissue destruction [72].

Classical treatment options include anti-inflammatory drugs and immunosuppressants like aminosalicylates, corticosteroids, or thiopurines, which are not effective for all IBD patients and related to severe adverse effects [78–80]. Newer therapeutic strategies for IBD are biologics including monoclonal antibodies targeting specific overexpressed cytokines such as anti-TNF-α or immune cell homing epitopes like anti-integrins [81]. However, despite increased specificity of antibody treatment, a substantial percentage of IBD patients remain non-responsive, lose their responsiveness or suffer from adverse reactions [82]. Within these "treat to target" approaches for the identification of novel molecular targets in the treatment of IBD, researchers set the focus on specific signal pathways, including janus kinase/signal transducer and activator of transcription (JAK/STAT) signal cascade. JAK/STAT is shared by multiple cytokines and represents an important therapeutic target in the field of immune-mediated diseases like rheumatoid arthritis (RA), psoriasis and alopecia areata [83,84]. The only so far approved JAK inhibitor for IBD is TOFA, a selective inhibitor of the JAK family with efficacy in UC [83,85]. TOFA entered clinical trials for UC and CD because of successful use in RA, without any preclinical evaluation in experimental animal models, which only were used in retrospective [94]. RA animal models represent the disease more faithfully than so far possible with IBD experimental animal models [101]. Therefore, most immunomodulators investigated

in IBD are expanded from other inflammatory diseases and fail to a significant percentage in IBD [209].

The above-mentioned leaky gut model with advanced features to mimic severe IBD conditions in vitro including a dysfunctional epithelial barrier and the presence of immunocompetent cells and investigated two different pharmaceutical approaches targeting JAK/STAT pathway. On the one hand, a small molecule with high permeability and broad mechanism of action, and on the other side, an alternative compound with high specificity using small interfering ribonucleic acid (siRNA)-based therapeutic approach. In contrast to pan-JAKi TOFA, siRNA was used to specifically target human JAK1 (siJAK1) via RNA interference, a natural cellular process regulating gene expression. For local delivery in IBD context and efficient cellular uptake, siJAK1 duplexes were complexed with a protective delivery system such as cationic lipid nanoparticles (LNPs) with a diameter of 40 nm by electrostatic interactions to form siRNA-loaded nanoplexes.

The following section presents a complex *in vitro* model of the human intestinal interface mimicking IBD pathophysiology that allows the combined investigation of intestinal barrier crossing capability of drug/DDS and measuring the target engagement on JAK1 by the inhibition of STAT1 phosphorylation.

4.2 Material and Methods

4.2.1 Materials

Human colorectal adenocarcinoma cell line Caco-2 (HTB-37) was obtained from American Type Culture Collection (ATCC, Manassas, USA). THP-1, derived from acute monocytic leukaemia (ACC 16), MUTZ-3 cells, a monocytic cell line with dendritic-like phenotype (ACC 295), and urinary bladder cell line 5637 (ACC 35) were purchased from German Collection of Microorganisms and Cell Cultures GmbH (DSMZ; Braunschweig, Germany). Dulbecco´s Modified Eagle Medium (DMEM), Roswell Park Memorial Institute (RPMI), a-Minimum Essential Medium (a-MEM), fetal calf serum (FCS) and non-essential amino acids (NEAA), trypsin-EDTA, sodium bicarbonate ($NaHCO_3$), penicillin/streptomycin (Pen/Strep), Alexa Fluor (AF)488-conjugated Phalloidin, Calcein AM, and transfection reagent lipofectamine RNAiMAX (Lipo) were obtained from Invitrogen (Carlsbad, USA). Phorbol 12-myristate 13-acetate (PMA), accutase, human AB serum, bovine serum albumin (BSA), saponin, collagenase type II, and 4',6-Diamidino-2-Phenylindole Dihydrochloride (DAPI) were purchased from Sigma-Aldrich (Taufkirchen, Germany). Collagen type I solution (PureCol; 3mg/mL) was obtained from Advanced Biomatrix (Tucson, USA). Transwell® Permeable Supports (#3460; polyester (PET) membrane with 0.4µm pore size) were purchased from Corning (New York, USA). Paraformaldehyde (PFA) was obtained from Electron Microscopy Sciences (Hatfield, USA). Double-faced adhesive tape was ordered from Coroplast (Wuppertal, Germany). Fluorescence mounting medium was obtained from Agilent Technologies (Santa Clara, USA). AF647 mouse anti-STAT1 (pY701) antibody and AF647 mouse IgG 2a, κ isotype control, Perm Buffer III were purchased from BD Biosciences (Heidelberg, Germany). Recombinant human interferon gamma (IFN-γ) was purchased from Miltenyi Biotec (Bergisch Gladbach, Germany). Tofacitinib citrate (TOFA; CP-690550) was obtained from Selleckchem (Houston, USA).

4.2.2 Cell culture

Cells were maintained as described in section 3.2.2.

4.2.3 Experimental setup of leaky gut model

Co-culture model was setup as described in section 3.2.3.

4.2.4 siRNA-based nanomedicine targeting JAK/STAT pathway

siRNA targeting human JAK1 (siJAK1) was designed for optimal efficacy and safety as previously described [167]. Respective siJAK1 duplexes containing 3´-cholesterol modification on the sense strand were synthesized and purified by RNAse-free HPLC at IDT Technologies (Coralville, USA). The 3´ end of the anti-sense strand was additionally modified with an AF647-fluorescence label in order to track the siRNA regarding uptake studies.

For siRNA delivery, lipid nanoparticles (LNPs) containing some cationic lipid component and polyethylene glycol (PEG) surfactants (Figure 4.1) as published by Delmas and colleagues [164,165] and fluorescent label (DiI dye) added [166], when indicated.

LNPs were characterized for hydrodynamic diameter and zeta potential using dynamic light scattering (DLS) and electrophoretic light scattering (ELS), respectively (ZetaSizer Nano ZSP; Malvern Instruments, Malvern, UK). For measurements, LNP dispersion was diluted in PBS (DLS) or MilliQ water (ELS) with a final concentration of 70 µg/mL LNPs and 1 mM NaCl (Table 4.1).

Table 4.1 Characterization of lipid nanoparticles (LNPs)

	LNP concentration [mg/mL]	DiI concentration [mM]	Hydrodynamic diameter [nm]	Poly dispersed index (PDI)	Zeta potential [mV]
Label-free	238	-	34.7 ± 0.16	0.154 ± 0.014	+27.1 ± 2.3
DiI-labeled	227	0.188	35.3 ± 0.31	0.176 ± 0.005	+35.4 ± 1.9

siRNA-based nanomedicine consisting of LNPs loaded with siRNA targeting human JAK1 was prepared by simple mixing, as illustrated in Figure 4.1. The collaboration partner (CEA Leti, Grenobe, France) optimized the complexation as well as transfection protocol for Caco-2 cells. Accordingly, optimal condition was found for N/P ratio of 8 which defines the loading (siRNA molecule number per nanoparticle) with positively charged lipid content (N = nitrogen) of LNPs and negatively charged nucleic acid (P = phosphate) of siRNA.

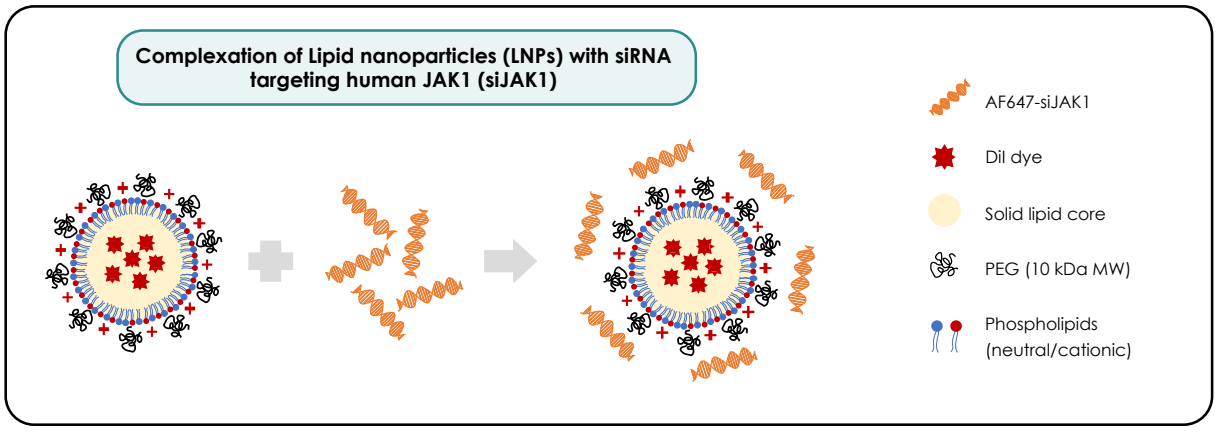


Figure 4.1 Schematic representation of siRNA-based nanomedicine. Respective formulation of siJAK1-loaded lipid nanoparticles (LNPs) termed nanoplexes was prepared by complexation of positively charged 40 nm LNPs with siRNA targeting human JAK1 (siJAK1). During simple mixing, siJAK1 duplexes were loaded on the surface of the nanocarriers via electrostatic interactions. Fluorescent nanoplexes, consisting of AF647-labeled siJAK1 and DiI-labeled LNPs, or label-free nanoplexes were used for localization and uptake studies or efficacy testing, respectively.

4.2.5 Co-culture treatment using JAK inhibitors and controls

Treatment with JAK inhibitors and appropriate controls was performed twice for 6 h on two subsequent days, for the leaky gut model on day 6/7, and for tight barrier model on day 11/12, as illustrated in Figure 4.2. siRNA-loaded LNPs termed ´nanoplexes´ were used at N/P ratio of 8 and at two different concentrations with LNPs at 45 µg/well or 90 µg/well containing siJAK1 at 135 nM (Low) or 270 nM (High), respectively. Nanoplexes were applied apically dispersed in Caco-2 cell culture medium (3.2.3) with reduced serum supplementation (DMEM 3% FCS 1% NEAA). TOFA was applied to both compartments of the co-culture at 5 µM concentration (20

mM DMSO stock). Control treatments included blank LNPs (90 µg/well) or naked siJAK1 (270 nM), LNPs loaded with non-targeting siRNA (siNEG; 270 nM), and commercially available transfection reagent lipofectamine RNAiMAX (Lipo) without or with siJAK1 (270 nM).

4.2.6 Localization and uptake study of siRNA-based nanomedicine

For localization and uptake studies, fluorescent nanoplexes with DiI-labeled nanocarriers (DiI-LNPs) and AF647-labeled siJAK1 (AF647-siJAK1) were used for CLSM and FACS analysis.

For microscopic analysis of nanoplex uptake in mono-cultures, cells were seeded onto 24 well plates containing a glass coverslip (100.000/well Caco-2 HTB-37 or 200.000/well dTHP-1 at 50 nM PMA; day 3) and exposed to blank LNPs or nanoplexes at different N/P ratios (12, 24, and 48) with 48, 64, and 129 µg LNPs per well and 10 nM siJAK1 final concentration, respectively. Cells were fixed, counterstained for cytoskeleton and cell nuclei, and mounted prior to CLSM analysis (3.2.6).

For microscopic analysis of co-cultures and cells were fixed following repetitive treatment with fluorescent nanoplexes (4.2.5), as illustrated in Figure 4.2A, and counterstained for cytoskeleton and cell nuclei (3.2.6). Untreated co-culture control (without the presence of nanoplexes) was used for CLSM settings and to exclude unspecific background signal. Fluorescence of LNPs and siJAK1 was detected using HyD detectors with emission filters between 570-600 nm (561 nm laser) and 660-685 nm (633 nm laser), respectively. Recorded z-stacks are represented in top (xy-) or side (xz/yz-dimension) with merged fluorescence signals or in split channels for DiI-LNPs (red) and AF647-siJAK1 (cyan).

For flow cytometric analysis of nanoplex uptake in mono-cultures, cells were seeded onto 24 well plates (100.000/well Caco-2 HTB-37 or 200.000/well dTHP-1 at 50 nM PMA; day 3) and exposed to blank LNPs or nanoplexes at different N/P ratios (12, 24, and 48) with 48, 64, and 129 µg LNPs per well and 10 nM siJAK1 final concentration, respectively. Carboxylated polystyrene tracer particles (FluoSpheres®; FS) were used

as a control (15 µg/well). LNPs, nanoplexes, or control particles were applied apically dispersed in complete cell culture medium (3.2.3) of respective cell line. After washing steps, cells were detached using appropriate enzymes (3.2.2), resuspended in 2% FCS in PBS (pooling of three wells), and directly analyzed by FACS (10.000 cell counts) without cell fixation.

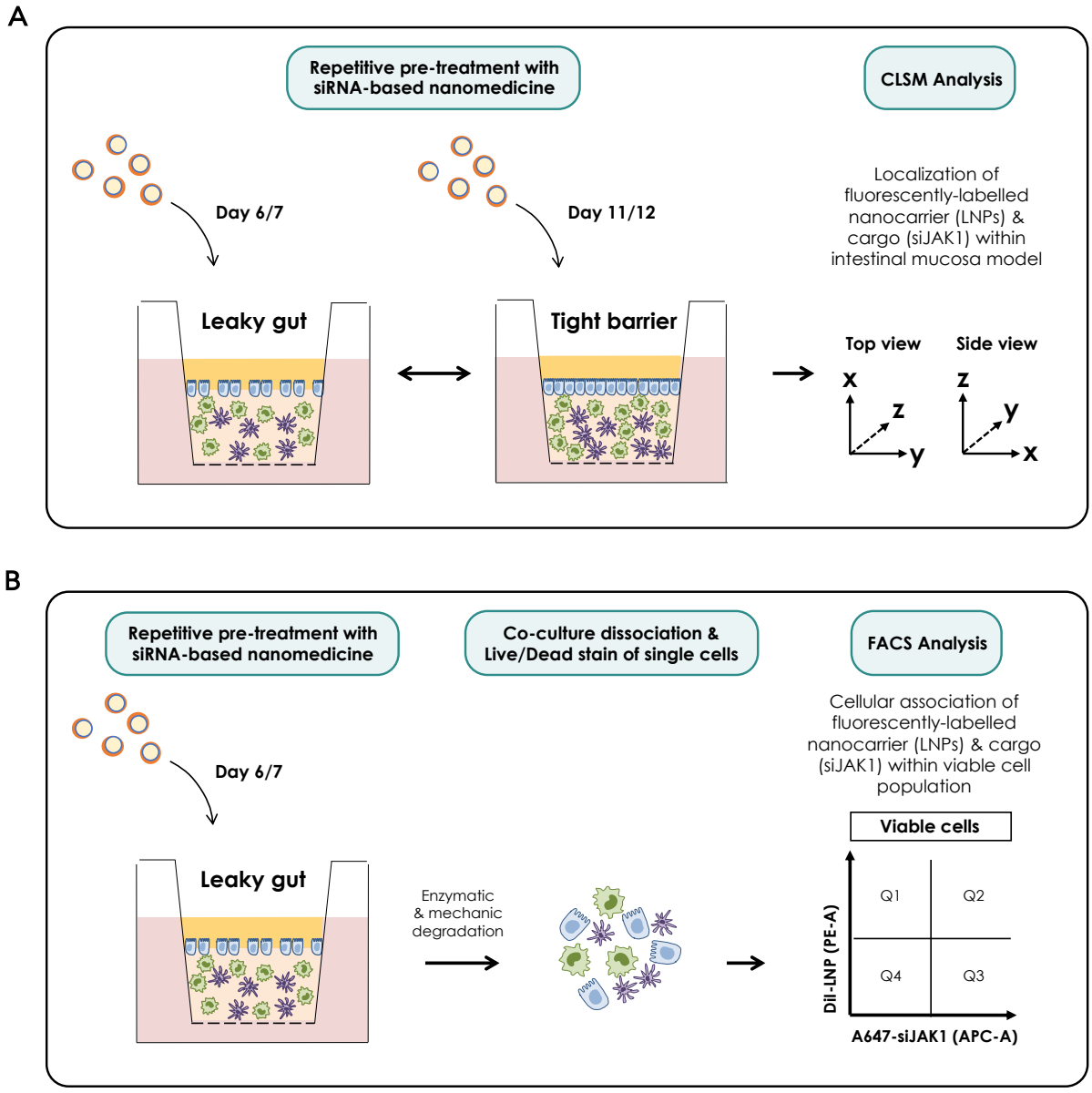


Figure 4.2 Schematic illustration of trafficking and uptake of siRNA-based nanomedicine within co-culture models. For localization studies of siRNA-loaded nanomedicine, co-culture was treated with fluorescently-labeled nanocarriers (DiI-LNPs) and siRNA (AF647-siJAK1) and analyzed by confocal laser scanning microscopy (CLSM) (**A**). Leaky gut model was treated with fluorescently-labeled nanocarrier (DiI-LNPs) and siRNA (AF647-siJAK1) Cellular association of siRNA-loaded LNPs was investigated and analyzed by flow cytometry (FACS) (**B**).

After cell debris and doublet exclusion, cells were visualized in two-parameter density plots or single-parameter histograms with fluorescence intensity distribution of DiI-LNPs (PE-A) and AF647-siJAK1 (APC-A) within the single cell population (Fig. 4.3). Nanoplex quantification is represented as the mean fluorescence intensity (MFI) for DiI and AF647 signal compared to untreated cells (control).

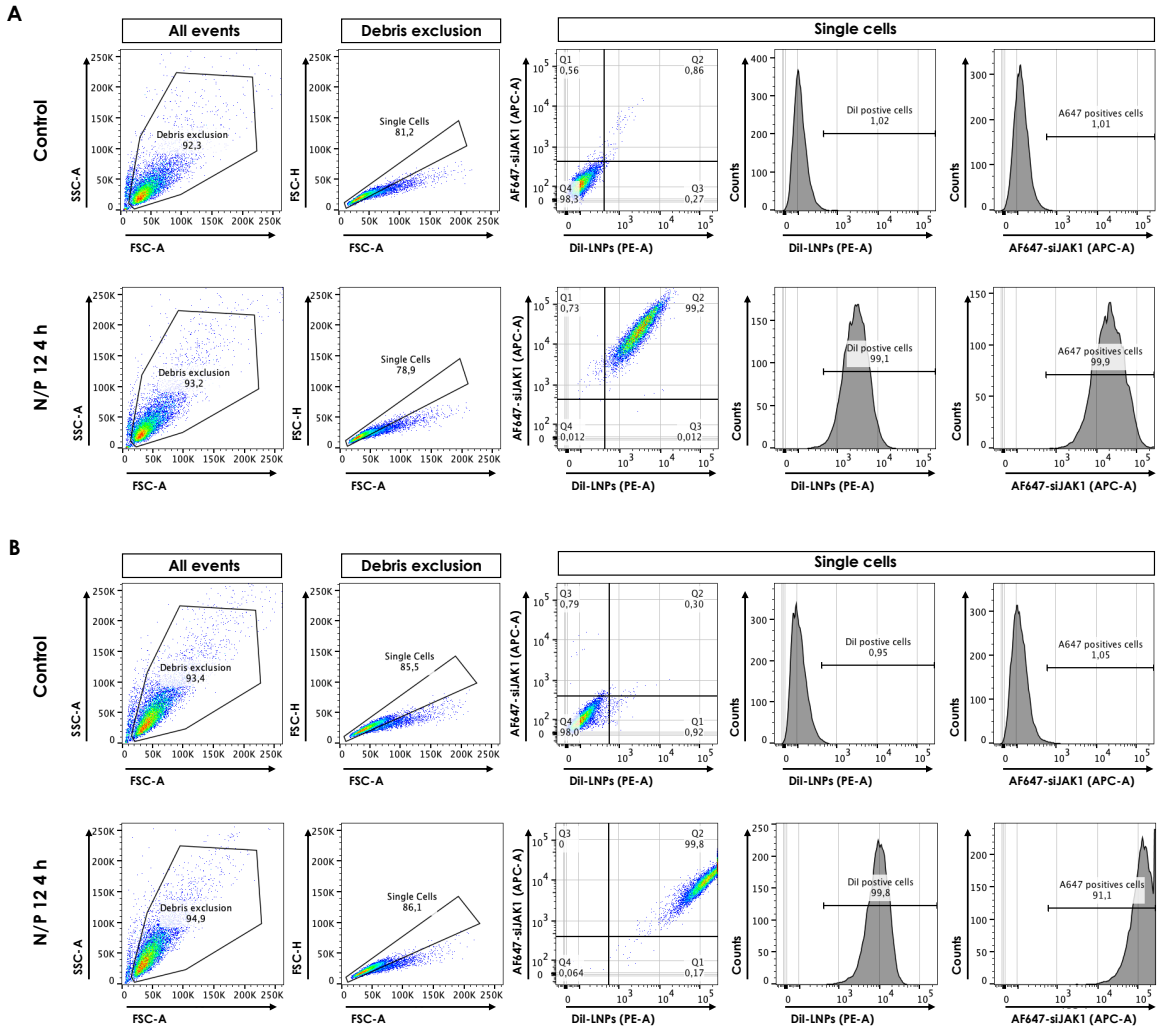


Figure 4.3 Gating strategy for flow cytometric analysis of cellular uptake of nanoplexes in mono-cultures. Representative flow cytometric data of untreated (control) and nanoplex-treated (N/P 12) cells after 4 h of incubation to identify DiI- and AF647-positive cells in Caco-2 HTB-37 (**A**) and macrophage-like (dTHP-1) cells (**B**). Cells were visualized in density plots of granularity (SSC) vs. size (FSC-A) and after debris removal plotted for doublet exclusion FSC-Height vs. -Area (FSC-H/FSC-A). Single cells were shown in two-parameter density plots or single-parameter histograms with positive cell fractions for DiI-LNP- (PE-A) and AF647-siJAK1-positive (APC-A) cells, respectively. Upon nanoplex association, cells exhibited much higher fluorescence intensity indicated by the shift towards higher values.

Quantification of nanoplex uptake/association was investigated after co-culture dissociation (3.2.9) and resulting cell suspension was stained for living and dying/dead cells (3.2.10) prior to FACS analysis (10.000 cell counts). Cells are represented in granularity vs. size (SSC-A/FSC-A) and fluorescence flow plots identifying viable cells (FITC-A/Pacific blue-A) and nanoplex association within the viable cell population (PE-A/APC-A). Percentage of cells associated with LNPs and/or siRNA are displayed as Q1 (LNP positive; $LNP^{+}siJAK1^{-}$), Q2 (double positive; $LNP^{+}siJAK1^{+}$), Q3 (siJAK1-positive; $LNP^{-}siJAK1^{+}$), and Q4 (double negative; $LNP^{-}siJAK1^{-}$) cell fractions (Figure 4.2B).

4.2.7 Quantification of STAT1 phosphorylation using flow cytometry

The efficacy of JAK/STAT inhibition was quantified downstream by the phosphorylation state of STAT1 (pSTAT1) after IFN-γ stimulation and analyzed by intracellular flow cytometry. Assay performance including STAT1 activation and inhibition was first tested on the level of mono-cultures to optimize IFN-γ and TOFA concentration, respectively.

Accordingly, Caco-2 HTB-37 (100.000/well; day 3), dTHP-1 (200.000/well at 50 nM PMA; day 3), and MUTZ-3 (100.000/well) were stimulated for 1 h with IFN-γ ranging from 3 to 25 ng/well. TOFA pre-treatment was performed ranging from 0.5 to 5 µM concentration followed by 25 ng/well IFN-γ stimulation (50 ng/mL).

After pre-treatment or/and IFN-γ stimulation, cells were detached using appropriate enzymes (3.2.2) and resulting cell pellet was directly resuspended in 4% (v/v) PFA in PBS and fixed for 20 min at 4°C. After the washing step with PBS, cells were permeabilized with Perm Buffer III for 30 min at 4°C before intracellular staining with AF647 mouse anti-phospho-STAT1 (pY701) antibody or corresponding isotype control (AF647 mouse IgG 2a, κ) according to manufacturer´s specification.

Cells were washed with PBS and resuspended in 2% FCS in PBS prior to FACS analysis (10.000 cell counts). Cell population was first identified based on its granularity and

relative size (SSC-A/FSC-A). Cell aggregates were excluded on the basis of FSC-Height vs. -Area (FSC-H/FSC-A) and the single cell gate. Phosphorylation profile of STAT1 (pSTAT1) was represented as histogram with AF647 emission collected at APC instrument setting and summarized in both percentage and the mean fluorescence intensity (MFI) of pSTAT1-positive cells.

4.2.8 Efficacy testing of JAK/STAT inhibitors in co-culture model

Co-culture model was treated with JAK1 inhibitors including nanoplexes (without fluorescent labels), TOFA and respective controls (4.2.5), as illustrated in Figure 4.4. Pre-treatment was followed by IFN-γ stimulation (50 ng/mL for 1 h) applied to both compartments of the Transwell® system by partial medium exchange of 100 µL (apical) and 500 µL (basolateral). After pre-treatment and subsequent IFN-γ stimulation, co-culture was dissociated (3.2.9), and cells were immediately fixed in 4% (v/v) PFA in PBS and stained as described above (4.2.7).

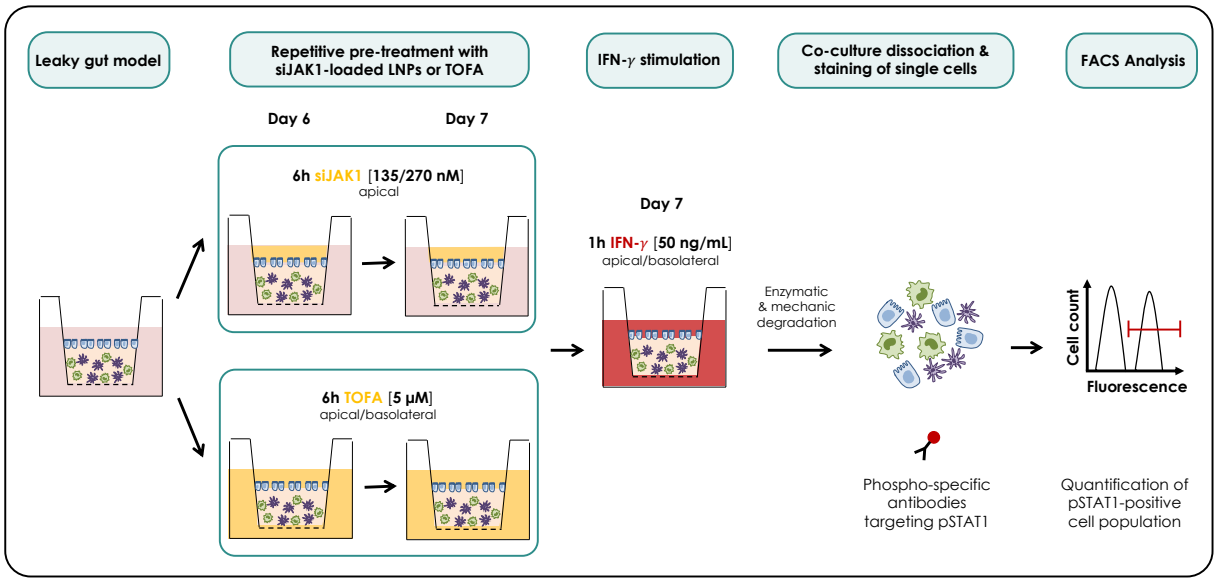


Figure 4.4 Schematic illustration of downstream analysis of JAK/STAT pathway inhibition after leaky gut model treatment using siRNA-based nanomedicine or TOFA. For JAK/STAT pathway inhibition, co-culture was pre-treated with siJAK1-loaded LNPs or TOFA and subsequently stimulated with IFN-γ. After co-culture dissociation, the downregulation of JAK/STAT signaling was evaluated by downstream analysis of STAT1 protein phosphorylation using phospho-specific antibody staining and flow cytometric analysis.

For comparison of different treatment options, pSTAT1-positive cells are represented as percentage, normalized to the IFN-γ stimulated untreated control (100%).

4.2.9 Data analysis and statistics

Data is represented as mean ± standard deviation (SD) and data collected or exported in Microsoft Excel. The graphs are plotted using GraphPad Prism software (Version 9.0.0). If not stated otherwise, all procedures were conducted at least in three independent experiments (N) and measured in technical triplicate (n). Statistical analysis was performed by one-way analysis of variance (ANOVA) with post-hoc Tukey´s test for multiple comparison. Differences were considered as significant for $p < 0.05$ (*), $p < 0.01$ (**), $p < 0.001$ (***), and $p < 0.0001$ (****) and not significant for $p \geq 0.05$ (ns).

4.3 Results

4.3.1 Trafficking and localization study of siRNA-based nanomedicine

The complexation of LNPs with siRNA targeting JAK1 (siJAK1) was performed to produce so called nanoplexes that aim to protect and deliver siRNA in the inflamed tissue and release its cargo inside the target immune cells. For the *in vitro* investigation of nanoplex delivery and trafficking into the human intestinal mucosa, fluorescent nanoplexes were used consisting of DiI-labeled LNPs and AF647-labeled siJAK1. siRNA-based nanomedicine was applied to the apical site of the co-culture model which provided valuable information regarding the localization of nanoplex components (nanocarrier and cargo) after oral administration. The interaction with the intestinal epithelium as the first cellular barrier and the potential permeation into sub-epithelial layer comprising target immune cells was evaluated regarding the effect of epithelial confluency and disease-related barrier dysfunction.

For improved microscopic analysis and visualization of the cellular interaction, co-cultures were counterstained for cytoskeleton (F-actin) and cell nuclei. Side or orthogonal views of the co-culture model provided a better comparison to validate the depth of particle penetration into the intestinal tissue. In addition, the corresponding top views provided an overview of particle absorption to the epithelial surface. Moreover, the use of split fluorescence channels was suitable to identify co-localization of nanoplex components as well as to assign their distribution without any background coming from the counterstaining signal.

Figure 4.5 shows the trafficking of blank LNPs of 40 nm size in the tight barrier model after 4 h *versus* 24 h incubation. Confocal microscopic analysis revealed that nanocarriers were co-localized for both time points within the epithelial cell layer and resulted in an increased amount associated within the Caco-2 cell layer (Fig. 4.5A/B).

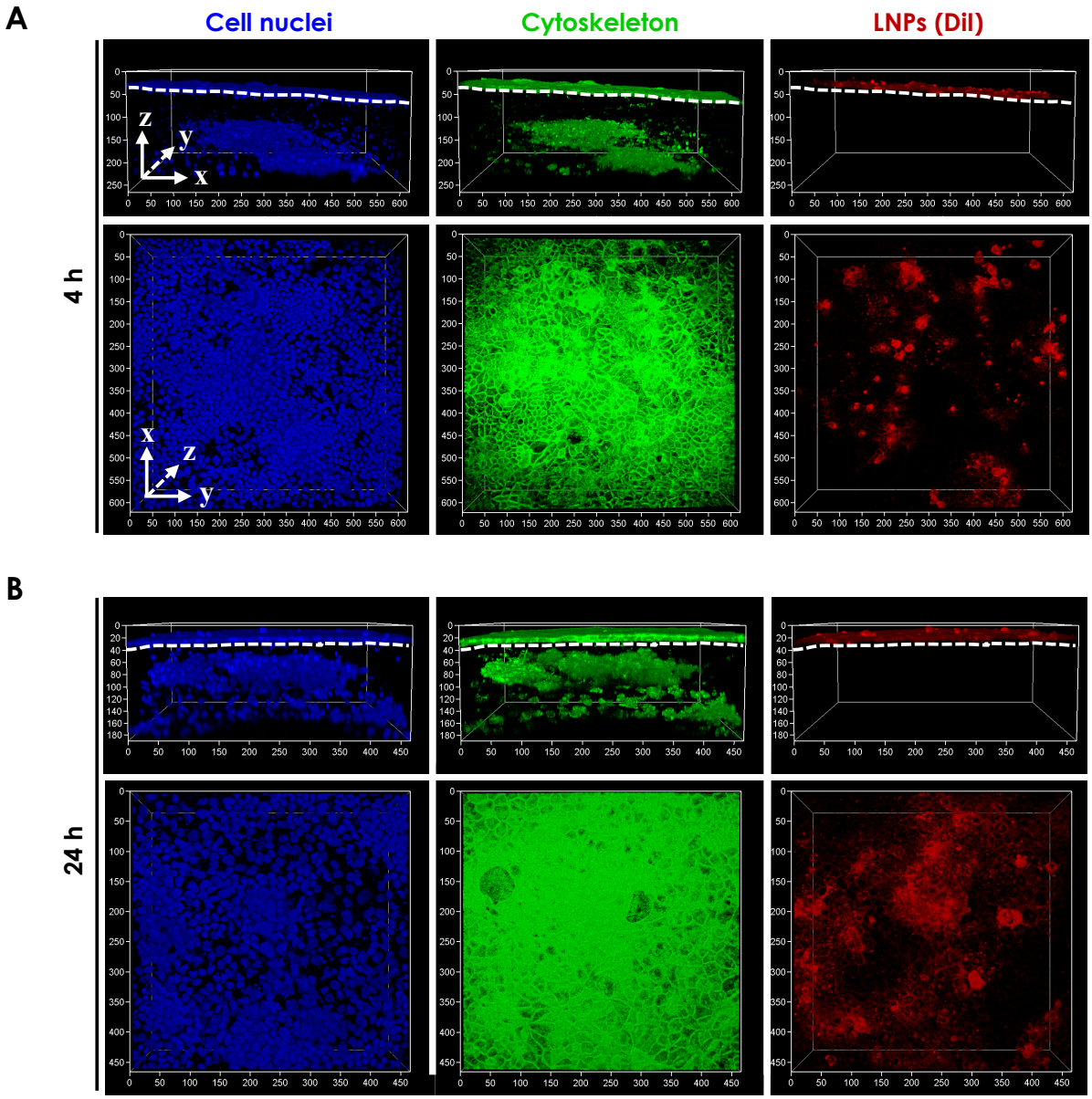


Figure 4.5 Localization study of blank LNPs in tight barrier model under healthy conditions. Nanocarriers (40 nm DiI-LNPs) were applied apically (90 µg/well) to the tight barrier model comprising a confluent epithelium and incubated for either 4 h (**A**) or 24 h (**B**). Recorded z-stacks of around 200 - 250 µm depth (axis unit = µm) are represented in side (xz/yz-) or top (xy-dimension) view and split fluorescence channels for cytoskeleton (AF488-phalloidin; green), cell nuclei (DAPI; blue), and nanocarrier (DiI-LNPs; red). Basal site of epithelial cell layer attached to the collagen matrix is marked by a dashed line to identify the localization of nanocarrier.

LPS-inflammation and resulting barrier function decrease of around 20% (3.3.3) displayed comparable results with limited access of nanocarriers to the immune cell compartment, even for the extended incubation time of 24 h (Fig. 4.6).

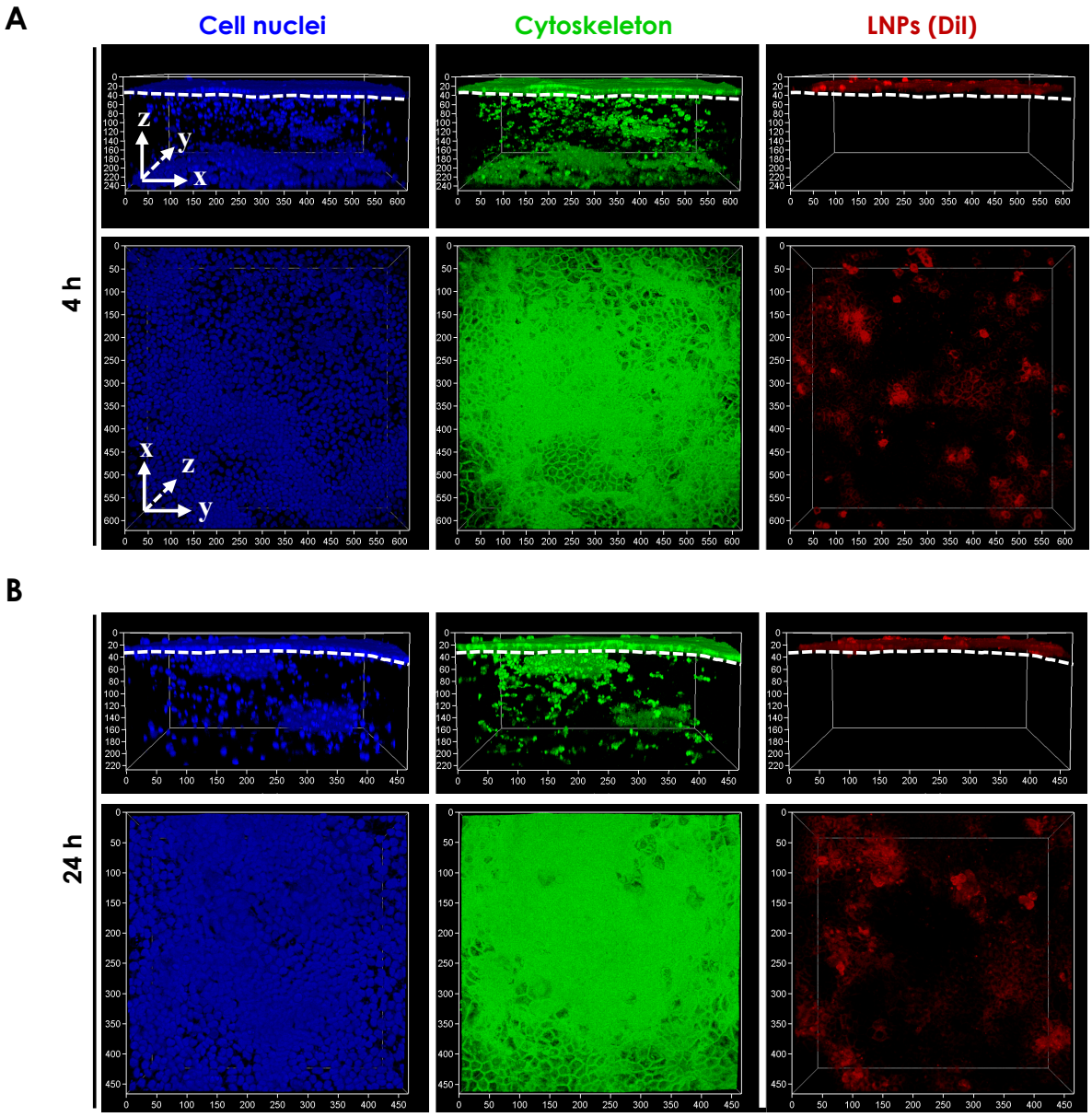


Figure 4.6 Localization study of blank LNPs in tight barrier model after LPS-inflammation. Nanocarriers (40 nm DiI-LNPs) were applied apically (90 µg/well) to the LPS-stimulated tight barrier model and incubated for either 4 h (**A**) or 24 h (**B**). Recorded z-stacks of around 200 - 250 µm depth (axis unit = µm) are represented in side (xz/yz-) or top (xy-dimension) view and split fluorescence channels for cytoskeleton (AF488-phalloidin; green), cell nuclei (DAPI; blue), and nanocarrier (DiI-LNPs; red). Basal site of epithelial cell layer attached to the collagen matrix is marked by a dashed line to identify the localization of nanocarrier.

In summary, blank LNPs were not able to cross the epithelial cell layer and reach the immune cell compartment in the tight barrier model under all mentioned conditions.

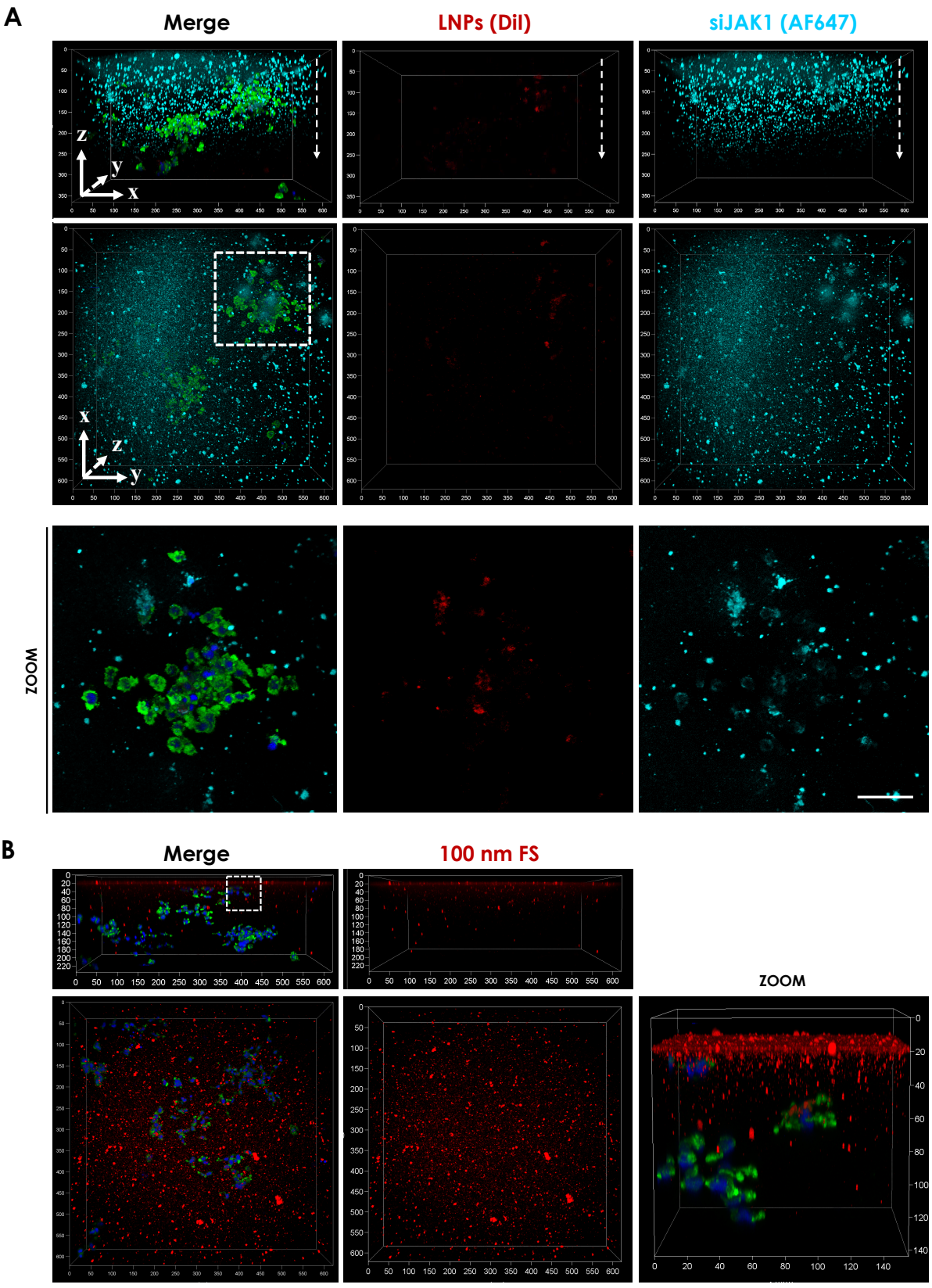


Figure 4.7 Uptake study of siRNA-loaded LNPs (nanoplexes) and control particles in co-culture model without the presence of an epithelial cell layer. Co-culture model without Caco-2 HTB-37 cells on top was used to verify the particle penetration through collagen matrix. Fluorescent nanocarriers (DiI-LNPs; 90 µg/well) complexed with siRNA (AF647-siJAK1; 450 nM) were applied apically for 6 h (**A**). Dashed

arrow indicates the diffusion direction (apical to basolateral). Closeup of chosen area (white dashed line box) of nanoplexes taken up by immune cells localized within the collagen matrix (top view). Images of 3D cells are projections of 30 µm z-sections (scale bar = 50µm). In comparison, diffusion of control particles (FluoSpheres®; FS) of 100 nm size (50 µg/well) after 6 h of incubation (**B**). Cells were stained for cytoskeleton (AF488-phalloidin; green) and cell nuclei (DAPI; blue). Recorded z-stacks of around 350 µm depth (axis unit = µm) are represented in top (xy-) or side (xz/yz-dimension) view with overlaid (merged) fluorescence signal or split channels for DiI-LNPs and FS (red) and AF647-siJAK1 (cyan).

To exclude the possible effect that the ECM layer may impede particle diffusion towards the sub-epithelial space, siRNA-loaded LNPs and 100 nm polystyrene tracer particles (FluoSpheres®; FS) were applied to co-cultures without the presence of the Caco-2 HTB37 cell layer (Fig. 4.7).

The diffusion through the collagen matrix with embedded immune cells was possible for both, nanocarrier and cargo, and showed an advanced penetration after 6 h of incubation with up to 300 µm depth in the z-dimension (estimated distance from the collagen surface) (Fig. 4.7A).

The magnified top view of collagen-embedded immune cells with co-localized nanoplex components and succeeded cellular internalization of siRNA-based nanomedicine after 6 h of incubation (Fig. 4.7A; ZOOM). Furthermore, the application of bigger control particles of 100 nm size displayed comparable diffusion behaviour through collagen, however, the majority of particles remained attached to the surface of collagen matrix (Fig. 4.7B).

As anticipated, the treatment of siRNA-based nanomedicine was optimized to a repetitive incubation time on two subsequent days. To this end, leaky gut model was treated twice with nanoplexes for six hours, starting from day 6, and in comparison, tight barrier model from day 11.

Figure 4.8 shows representative confocal microscopic images of tight barrier *versus* the leaky gut model after application of fluorescent nanoplexes at high concentration (90 µg LNPs and 270 nM siJAK1 per well; N/P 8 High).

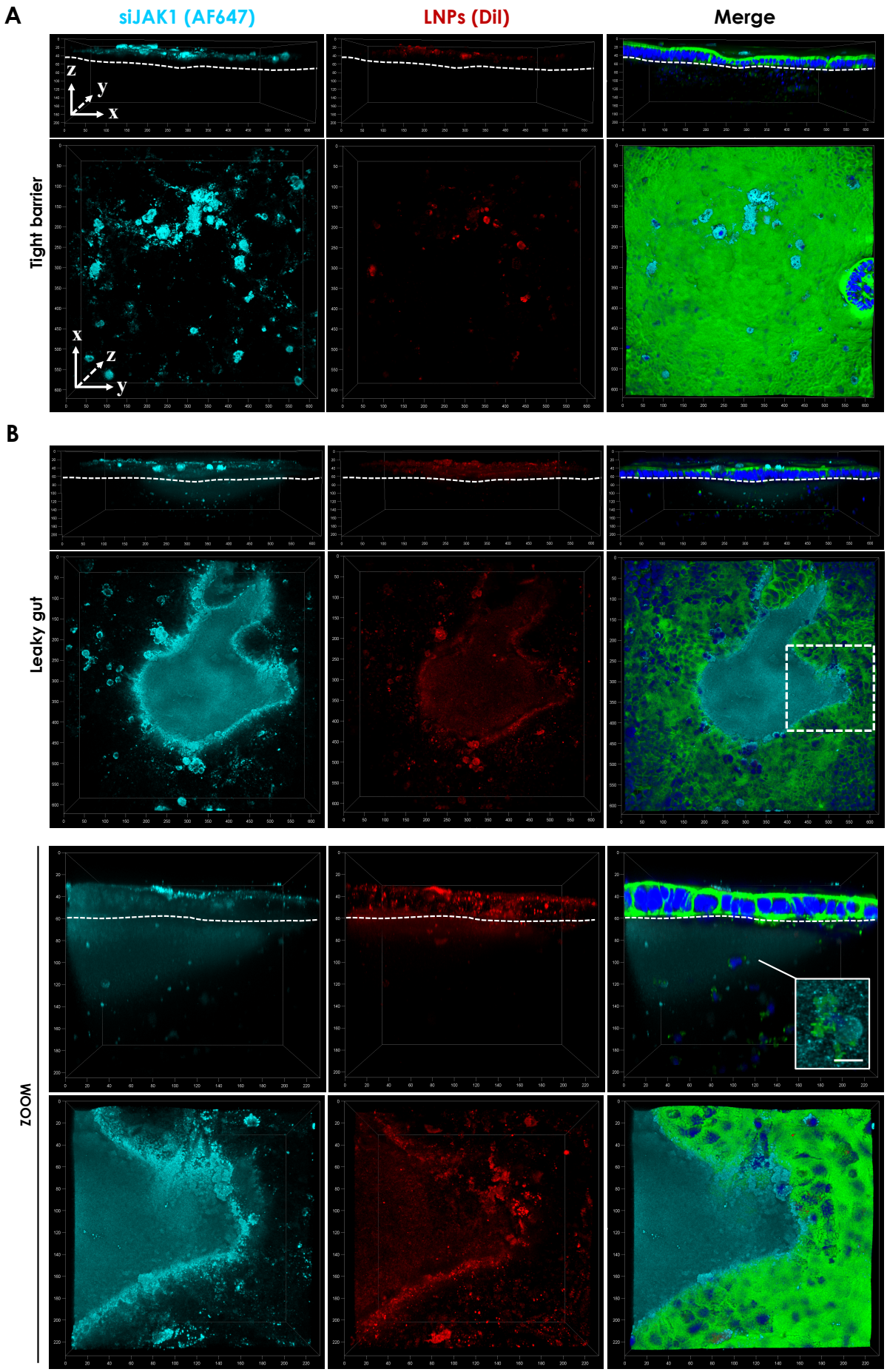

A
siJAK1 (AF647)
LNPs (DiI)
Merge
Tight barrier
B
Leaky gut
ZOOM

Figure 4.8 Confocal microscopic images of nanoplex localization in tight barrier (A) and leaky gut model (B). Nanoplexes from fluorescently-labeled LNPs (DiI-label) and JAK1-siRNA (AF647-label) were used. Co-culture was incubated twice apically for 6 h with nanoplexes (N/P ratio of 8) at 90 µg LNP and 270 nM siRNA per well (N/P 8 High). Closeup of chosen area (white dashed line box) shows detailed nanoplex localization within (sub-)epithelial region in magnified view (ZOOM) and detailed view on immune cell (white box; scale bar = 10 µm). Cells are stained for cytoskeleton (AF488-phalloidin; green) and cell nuclei (DAPI; blue). Recorded z-stacks of around 200 µm depth (axis unit = µm) are represented in top (xy-) or side (xz/yz-dimension) view with overlaid fluorescence signal (merge) or split channels for DiI-LNPs (red) and AF647-siJAK1 (cyan). For side views, the basal site of epithelial cell layer (attached to the collagen matrix) is marked by a dashed line to identify the localization of nanocarrier and/or its cargo.

Similar to the previous results using blank LNPs (Fig. 4.5 and 4.6), nanoplex-treated tight barrier model displayed a co-localization of LNPs as well as cargo (siJAK1) within the epithelial cell layer (Fig. 4.8A; side view). Higher fluorescence signal of both nanoplexes components was observed mostly on the surface of the Caco-2 cell layer with increased uptake or aggregation within apoptotic cells which were identified due to the lack of positive cytoskeleton stain (Fig. 4.8A; top view). However, nanoplexes did not cross the epithelial cell layer, thus, did not encounter the underlying immune cells. Comparable observations were made for low nanoplex concentration (45 µg LNPs and 135 nM siJAK1 per well; N/P 8 Low) as well as control treatments using blank LNPs (Fig. 4.10A/B).

In contrast to that, nanoplexes were accumulated with the sub-confluent regions of the leaky gut model and penetrated into the sub-epithelial layer (Fig. 4.8B). Similar to the tight barrier model, nanoplexes were also located on the surface of the Caco-2 cell layer within apoptotic cells. The closeup view of corresponding leaky region revealed that both, nanocarrier and cargo, were internalized by epithelial cells, and moreover, started to diffuse through the leaky areas resulting in a direct contact with underlying immune cells (Fig. 4.8B; side view). LNPs and to a higher extent siJAK1 were localized with a depth of around 300 µm compared to the reduced concentration of nanoplexes (N/P 8 Low) with a less pronounced penetration into the sub-epithelial space with around 100 µm (Fig. 4.11A).

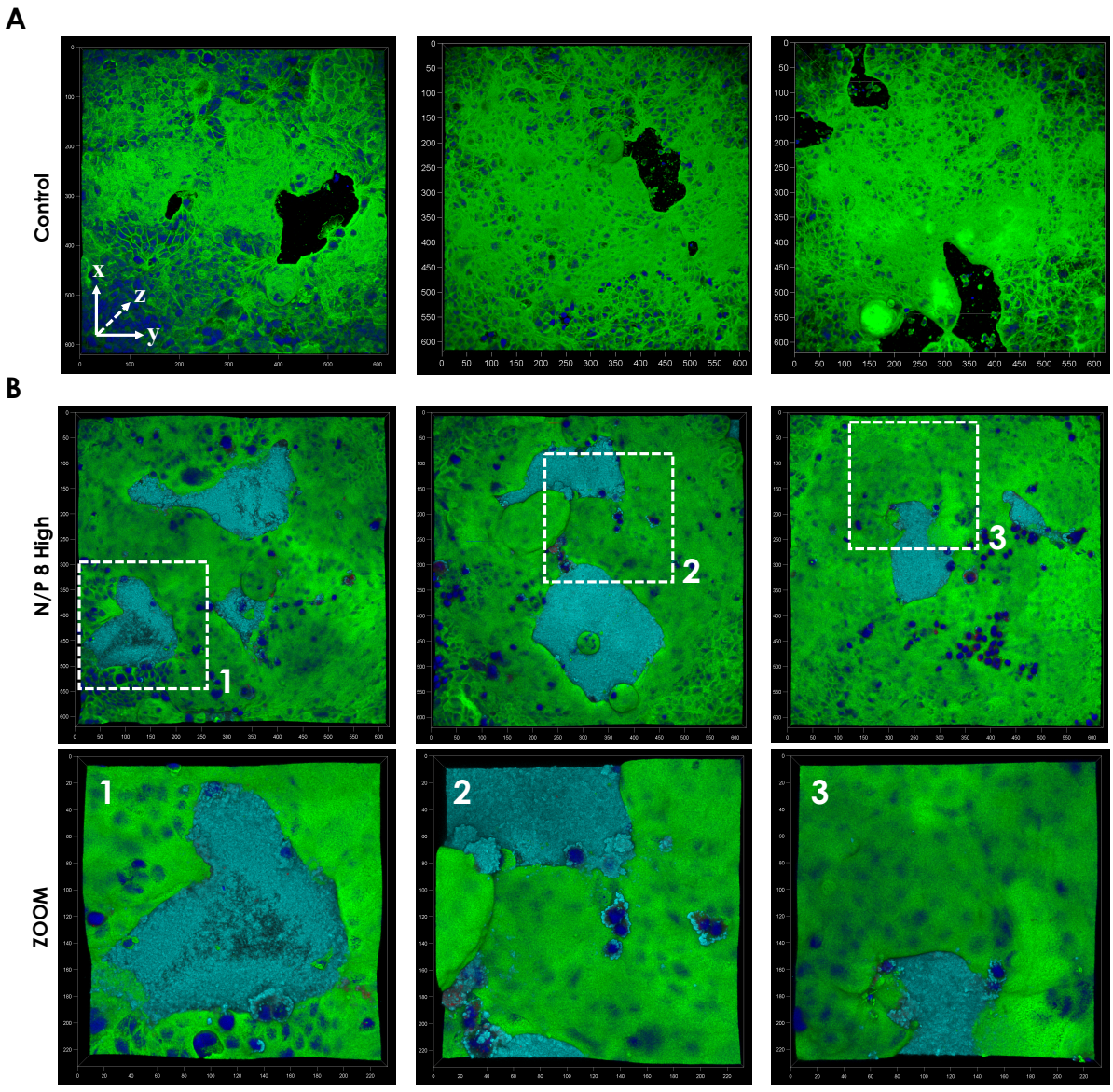


Figure 4.9 Accumulation effect of nanoplexes in sub-confluent regions of the leaky gut model. Leaky regions of the co-culture model without nanoplex treatment (control) (**A**) compared to repetitive treatment with fluorescent nanoplexes (N/P ratio of 8) at 90 µg LNP and 270 nM siRNA per well (N/P 8 High) (**B**). Recorded z-stacks of around 200 µm depth (axis unit = µm) are represented in top (xy-dimension) view with overlaid fluorescence signal (merge) for cytoskeleton (AF488-phalloidin; green), cell nuclei (DAPI; blue), DiI-LNPs (red) and AF647-siJAK1 (cyan).

Figure 4.9 depicts several regions from different co-culture treatments with the same accumulation effect of nanoplexes (N/P 8 High) within the sub-confluent regions of the leaky gut model. Co-culture without nanoplex treatment served to define CLSM settings for optimal fluorescence detection and avoiding unspecific background signal within the respective emission filters (Fig. 4.9A).

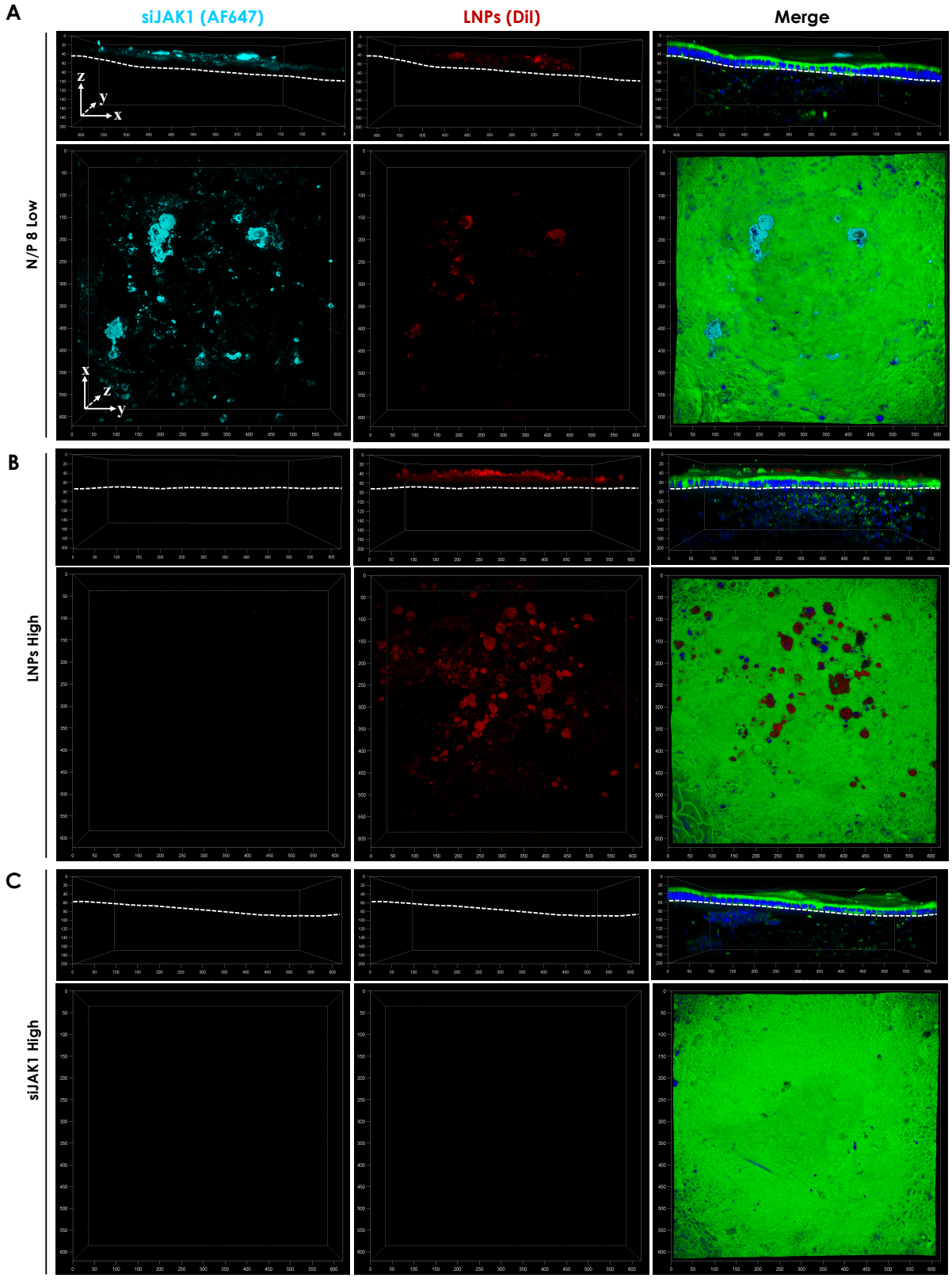


Figure 4.10 **Tight barrier model after nanoplex incubation using fluorescently-labeled nanocarrier (DiI-LNPs) and siRNA (AF647-siJAK1).** Nanoplexes with N/P ratio of 8 (45 µg LNPs and 135 nM siJAK1; N/P 8 Low) (**A**), and control treatments were incubated twice for 6 h including blank LNPs (90 µg per well; LNPs High) (**B**), and naked siJAK1 (270 nM; siJAK1 High) (**C**). Cells were fixed and stained for cytoskeleton (AF488-phalloidin; green) and cell nuclei (DAPI; blue). Recorded z-stacks of around 200 µm depth (axis unit = µm) are represented in top (xy-) or side (xz/yz-dimension) view with overlaid

fluorescence signal (merge) or split channels for DiI-LNPs (red) and AF647-siJAK1 (cyan). Basal site of epithelial cell layer (attached to the collagen matrix) is marked by a dashed line to identify the localization of nanocarrier and/or its cargo.

Blank LNPs that have a more cationic charge in comparison to siJAK1-loaded LNPs, showed similar penetration into the leaky regions and facilitated cellular interactions and as expected, did not show any fluorescence signal for the emission filters set for AF647-siRNA (Fig. 4.11B). After the application of naked siJAK1 at high concentration (270 nM; siJAK1 High) and without the support of the drug delivery vehicle, only very low siRNA signal was detected for both co-culture models indicating poor cellular interactions (Fig. 4.10C and 4.11C).

Microscopic investigations described above allowed the qualitative analysis of nanoplex trafficking and localization within the co-culture model. In addition, flow cytometric analysis were performed to quantify the cellular uptake of siRNA-based nanomedicine. Accordingly, cells associated with fluorescently labeled LNPs and/or siJAK1 were identified by the fluorescence intensity shift to higher values in comparison to the untreated cells showing a low background signal (defined as control or negative cells) (see 4.2.6; Fig. 4.2).

Figure 4.12 and 4.13 display the obtained flow cytometric data that were initially performed in mono-cultures of epithelial- and macrophage-like cells after direct exposure of siRNA-loaded LNPs. Cells were incubated for 1 h and 4 h with either blank LNPs or nanoplexes that were applied at different N/P ratios (12, 24, and 48) corresponding to 48, 64, and 129 µg LNPs per well and 10 nM siJAK1 final concentration, respectively. The increase of N/P ratio correlated with the increase LNP concentration but decrease of siRNA-loading. Preliminary results showed for each cell type a concentration- and time-dependent increase of cellular association for blank LNPs (Fig. 4.12A and 4.13A) and nanoplexes (Fig. 4.12B and 4.13B).

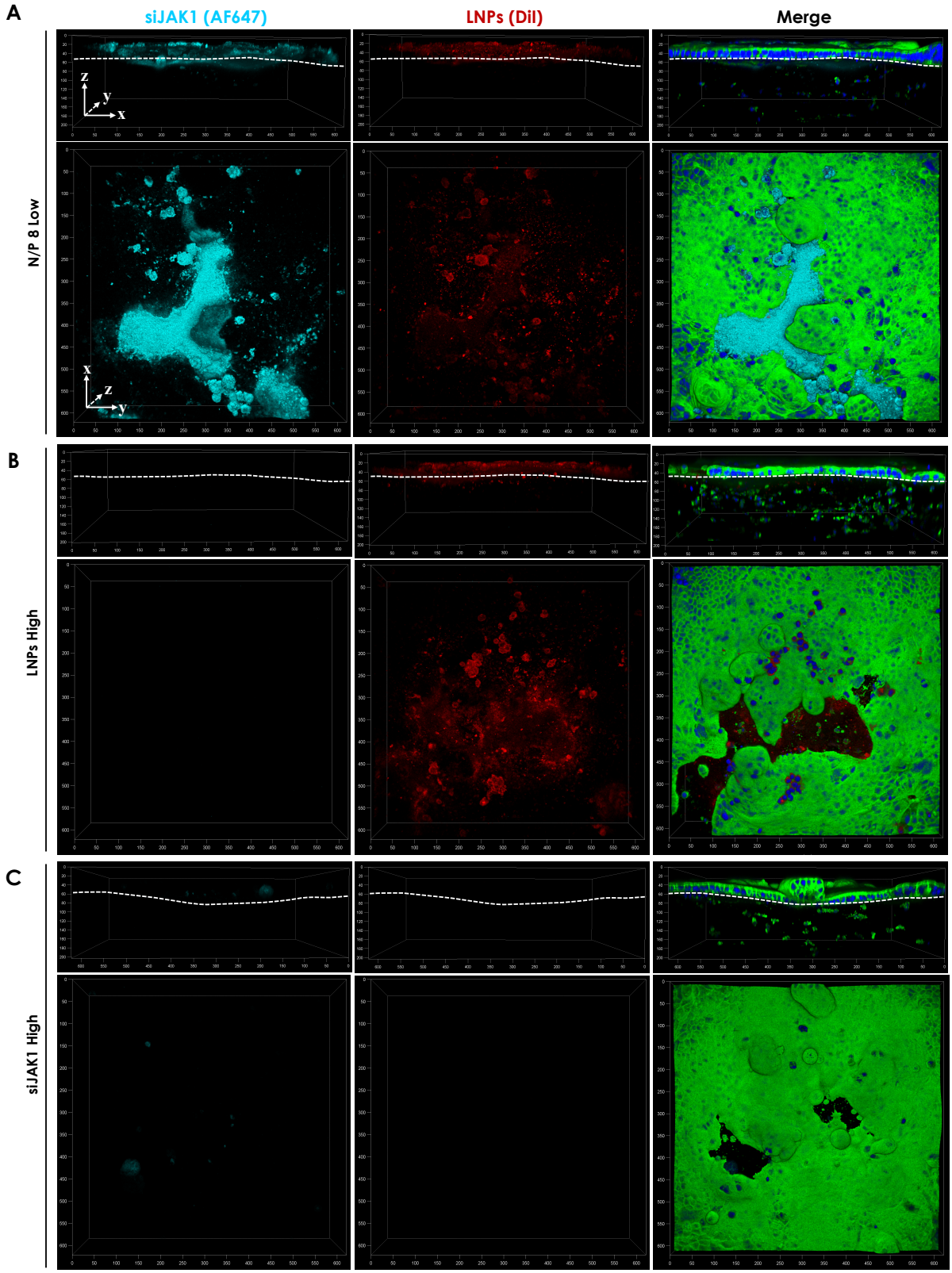


Figure 4.11 Leaky gut model after nanoplex incubation using fluorescently-labeled nanocarrier (DiI-LNPs) and siRNA (AF647-siJAK1). Nanoplexes with N/P ratio of 8 (45 µg LNPs and 135 nM siJAK1; N/P 8 Low) (**A**), and control treatments were incubated twice for 6 h including blank LNPs (90 µg per well; LNPs High) (**B**), and naked siJAK1 (270 nM; siJAK1 High) (**C**). Cells were fixed and stained for cytoskeleton (AF488-phalloidin; green) and cell nuclei (DAPI; blue). Recorded z-stacks of around 200 µm depth (axis unit = µm) are represented in side (xz/yz-dimension; upper panel) or top (xy-dimension; lower panel) view with overlaid fluorescence signal (merge) or split channels for DiI-LNPs (red) and

AF647-siJAK1 (cyan). Basal site of epithelial cell layer (attached to the collagen matrix) is marked by a dashed line to identify the localization of nanocarrier and/or its cargo.

Compared to untreated cells (control), even the lowest LNP amount (48 µg/well) or siRNA-load (N/P 48) and incubation for 1 h displayed 100% of LNP- and siJAK1-positive cells indicating nanoplex association within the investigated cell population. Despite of the general high uptake percentage for both cell types, nanoplexes were taken up to a higher extent by macrophage-like cells (dTHP-1). For instance, after 4 h exposure of blank LNPs (129 µg/well), the mean fluorescence intensity (MFI) of DiI shifted from ~150 MFI (control) towards higher values with ~6.000 MFI for Caco-2 and ~17.000 MFI for dTHP-2 cells, respectively (Fig. 4.12A and 4.13A). In comparison, for nanoplexes with the highest siRNA-load (N/P 12), MFI shifted towards higher values with ~3.000 MFI (DiI) and ~31.000 MFI (AF647) for Caco-2 and ~10.000 MFI (DiI) and ~136.000 MFI (AF647) for dTHP-2 cells, respectively (Fig. 4.12B and 4.13B). Even for the lowest siRNA-load (N/P 48) and incubation for 4h, the fluorescence intensity of siJAK1 reached the maximum of detection for dTHP-1 cells (Fig. 4.13B; APC-A channel).

Complementary to this, microscopic images of N/P 12 supported the observations made by flow cytometry indicating the majority of both cell types positive for nanoplex components, and an increased uptake in macrophages over epithelial cells (Fig. 4.12C and 4.13C). Fluorescence of both, LNPs and siJAK1, are shown in split fluorescence channels and monochrome images (grey) with corresponding overlaid fluorescence signal including counterstaining of cell nuclei and cytoskeleton (merge).

The Caco-2 cell layer displayed a homogeneous distribution of LNPs as well as siJAK1 signal and nanoplex co-localization within the cell membrane (merge) (Fig. 4.12C). In contrast, dTHP-1 cells with very flat and extended cell morphology showed a densely accumulation of LNPs close to the cell nucleus but a more homogeneous distribution of siJAK1 within the cytosolic compartment (Fig. 4.13C; magnified view).

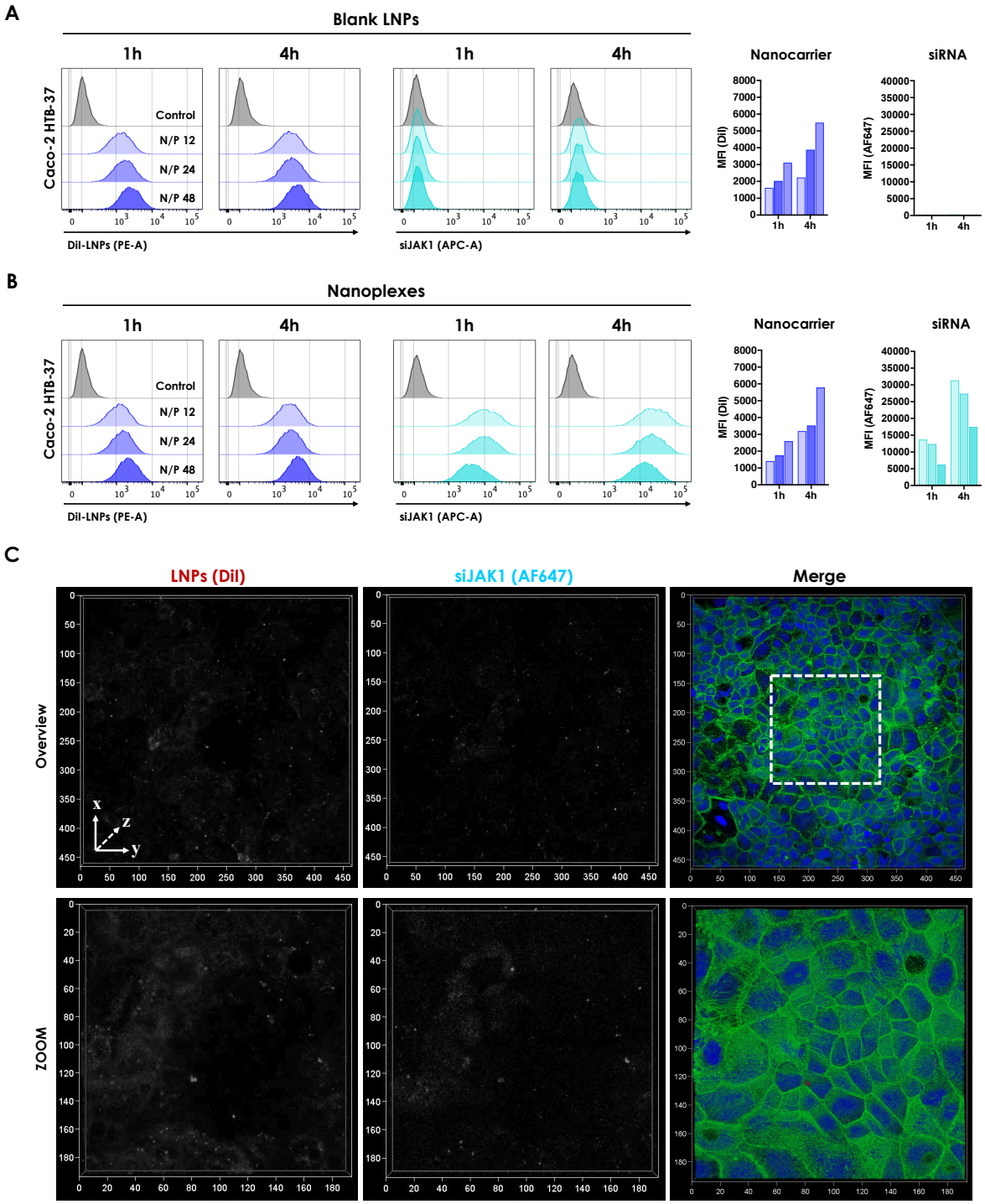


Figure 4.12 Cellular uptake of nanoplexes in epithelial-like cells (Caco-2 HTB-37) analyzed by flow cytometry and confocal microscopy. Caco-2 cells were exposed to fluorescent nanocarrier (DiI-LNPs) and siRNA (AF647-siJAK1) for 1 h and 4 h using either blank LNPs (**A**) or nanoplexes (**B**) at N/P ratio of 12, 24, and 48 (with 48, 64, and 129 µg LNPs per well and 10 nM siJAK1, respectively). After exposure, cells were harvested and directly analyzed by FACS. Overlaid histograms show fluorescence intensity of DiI-LNPs (PE-A) and AF647-siJAK1 (APC-A) within the single cell population compared to untreated cells (control). Adjacent graphs summarize the corresponding mean fluorescence intensity (MFI) of nanoplex components. Representative microscopic images of nanoplex (N/P 12; 4 h) uptake in Caco-2 cells with magnified view of chosen area (dashed line box) (**C**). Cells were counterstained for

cytoskeleton (AF488-phalloidin; green) and cell nuclei (DAPI; blue). Recorded z-stacks of around 50 µm depth (axis unit = µm) are represented in top (xy-dimension) view with overlaid fluorescence signal (merge) or split channels for DiI-LNPs and AF647-siJAK1 (monochrome).

Cellular association of nanoplexes in epithelial- and macrophage-like cells was compared with the cellular uptake of control polystyrene nanoparticles of 100 nm size (FluoSpheres®; FS). Figure 4.14 displays the corresponding results obtained for FS control particles after incubation for either 1h or 4h at 15 µg/well. Flow cytometric data revealed similar uptake for both cell types as observed for nanoplexes. For both time points, all cells were FS-positive with an increased cellular uptake with MFI (Red) shifted to higher values with ~10.000 MFI and ~34.000 MFI for Caco-2 and ~52.000 MFI and ~151.000 MFI for dTHP-2 cells for 1 h and 4 h of exposure, respectively (Fig. 4.14A). The fluorescence intensity of FS reached its maximum of detection for dTHP-1 cells after 1 h of incubation, whereas longer exposure resulted in a fluorescence shift FS-positive cells laying outside the respective fluorescence channel (Fig. 4.14A; PE-A channel).

Besides similar time-dependency, FS showed comparable distribution for Caco-2 and dTHP-1 cells compared to the nanoplex uptake study, indicated by a homogenous cytosolic localization and more densely accumulation with close proximity to the cell nucleus, respectively (Fig. 4.14B).

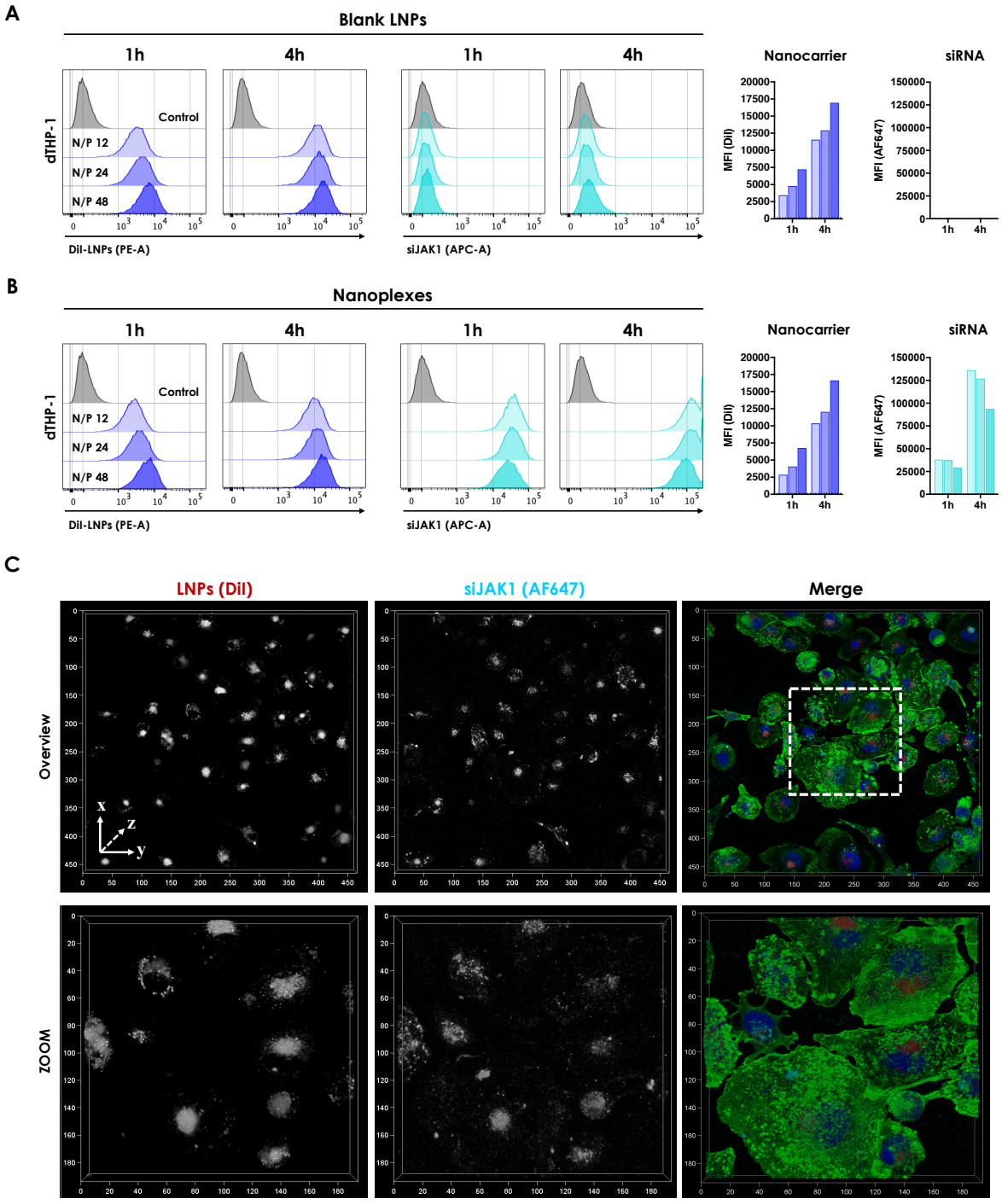


Figure 4.13 Cellular uptake of nanoplexes in macrophage-like cells (dTHP-1) analyzed by flow cytometry and confocal microscopy. dTHP-1 cells were exposed to fluorescent nanocarrier (DiI-LNPs) and siRNA (AF647-siJAK1) for 1 h and 4 h using either blank LNPs (**A**) or nanoplexes (**B**) at N/P ratio of 12, 24, and 48 (with 48, 64, and 129 µg LNPs per well and 10 nM siJAK1, respectively). After exposure, cells were harvested and directly analyzed by FACS. Overlaid histograms show fluorescence intensity of DiI-LNPs (PE-A) and AF647-siJAK1 (APC-A) within the single cell population compared to untreated cells (control). Adjacent graphs summarize the corresponding mean fluorescence intensity (MFI) of nanoplex components. Representative microscopic images of nanoplex (N/P 12; 4 h) uptake in dTHP-1 cells with magnified view of chosen area (dashed line box) (**C**). Cells were counterstained for cytoskeleton (AF488-phalloidin; green) and cell nuclei (DAPI; blue). Recorded z-stacks of around 50 µm

depth (axis unit = µm) are represented in top (xy-dimension) view with overlaid fluorescence signal (merge) or split channels for DiI-LNPs and AF647-siJAK1 (monochrome).

Following the quantitative analysis of cellular uptake of siRNA-based nanomedicine in mono-cultures, nanoplex association was investigated in the co-culture model. Figure 4.15 shows preliminary flow cytometric results of the cellular association after repetitive treatment including controls and subsequent co-culture dissociation.

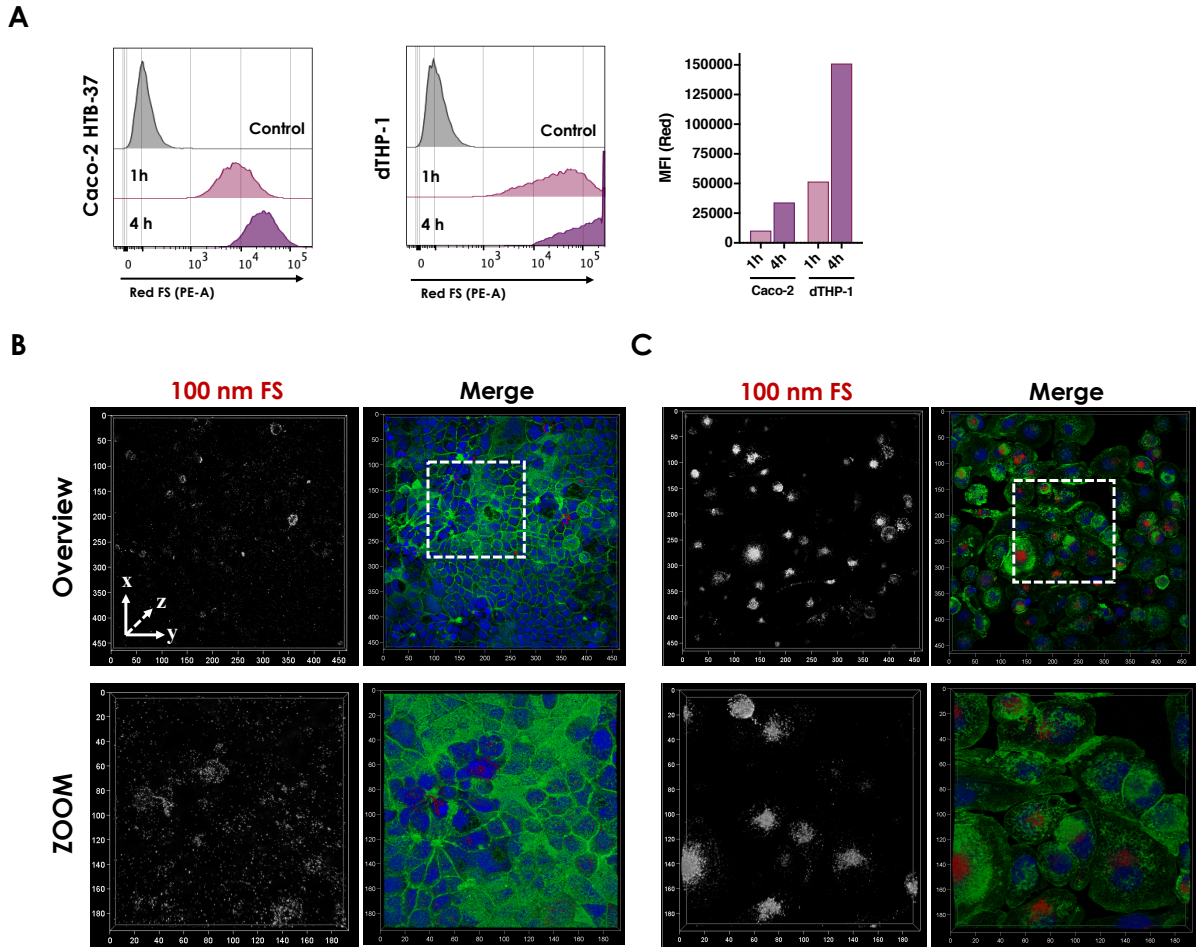


Figure 4.14 Cellular uptake of control particles in Caco-2 HTB-37 and macrophage-like (dTHP-1) cells analyzed by flow cytometry and confocal microscopy. Caco-2 and dTHP-1 cells were exposed to red fluorescent 100 nm polystyrene control nanoparticles (FluoSpheres®; FS) for 1 h or 4 h of incubation at 15 µg per well (**A**). After exposure, cells were harvested, and unfixed cells were directly analyzed by FACS. Overlaid histograms show fluorescence intensity distribution of red FS (PE-A) within the single cell population compared to untreated cells (control) and adjacent graph summarizes the corresponding mean fluorescence intensity (MFI). Representative microscopic images of FS uptake after 4 h in Caco-2 HTB-37 (**B**) and dTHP-1 cells (**C**). Cells were counterstained for cytoskeleton (AF488-phalloidin; green) and cell nuclei (DAPI; blue). Recorded z-stacks of around 50 µm depth (axis unit = µm) are represented in top view (xy-dimension) with overlaid (merge) or split fluorescence channel for red FS (monochrome).

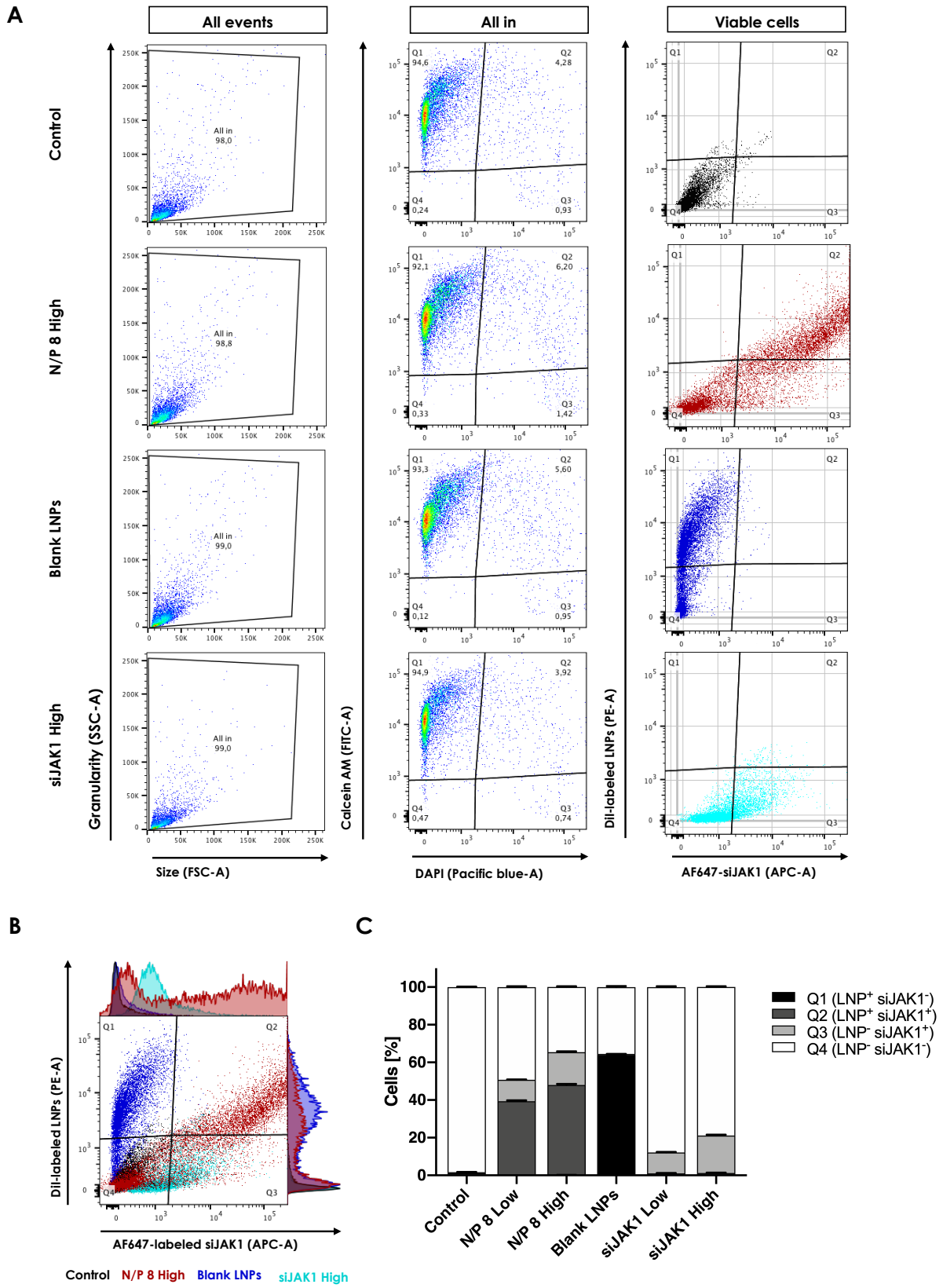


Figure 4.15 Cellular association of nanoplexes in leaky gut model detected by flow cytometry. Leaky gut model was treated with fluorescent nanocarrier (DiI-LNPs) and siRNA (AF647-siJAK1). Co-culture was incubated twice for 6 h with nanoplexes (N/P ratio of 8) at two different concentrations (Low/high) with LNPs at 45 µg or 90 µg per well and siJAK1 at 135 nM or 270 nM, respectively. Control treatments included co-cultures in the absence of nanoplexes (Control), blank LNPs (90 µg/mL) or naked siJAK1

(Low/High). After co-culture dissociation, the resulting cell suspension was stained for living (Calcein AM; 10 ng/mL) and dying/dead cells (DAPI; 0.1 µg/mL). Cells are represented in granularity *vs.* size (SSC-A/FSC-A; left column) and fluorescence density plots identifying viable cells (FITC-A/Pacific blue-A, middle column) and nanoplex association within the viable cell population (PE-A/APC-A; right column) (**A**). Density plot overlay shows cellular nanoplex association represented as quadrant gate frequencies of the viable cell population (PE-A/APC-A) (**B**). Percentage of cells containing LNPs and/or siRNA are displayed as quadrant Q1 (LNP-positive; $LNP^{+}siJAK1^{-}$), Q2 (double-positive; $LNP^{+}siJAK1^{+}$), Q3 (siJAK1-positive; $LNP^{-}siJAK1^{+}$), and Q4 (double-negative; $LNP^{-}siJAK1^{-}$) cell fractions, summarized in a stacked graph (**C**). Data is shown as mean ± SD of triplicates of one experiment (n = 3; N = 1).

In addition, the resulting single cell suspension was stained for viable cells using Calcein AM/DAPI stain. Cellular association of nanocarriers and cargo was represented by two-parameter density plots and gate frequencies of positive cells (quadrants; Q1 - Q4) of the viable cell population with a total frequency of 100% (Fig. 4.15A; right panel). Accordingly, quadrant Q1, Q2, and Q3 included the frequency of LNP-positive, double-positive (both nanoplex components), and siJAK1-positive cells, respectively (Fig. 4.15B). Whereas Q4 covered the cell frequency without any fluorescence detected for LNPs or siJAK1 (double-negative cells).

Compared to untreated control (Q4 > 98%), nanoplex treatment displayed a concentration dependent increase of cellular association with ~39% (Q2) of double- and ~11% (Q3) of siJAK1-positive cells for the low and ~48% (Q2) of double- and ~17% (Q3) of siJAK1-positive cells for the high dose (Fig. 4.15C). The application of blank LNPs at high concentration (90 µg/well) showed the highest number of LNP-positive cells with ~64% (Q1) and no unspecific signal for siRNA (Q2 and Q3 < 1%) (Fig. 4.15C). Regarding the treatment with naked siJAK1, cells displayed a concentration-dependent increase of siJAK1-positive cells with ~11% for low dose (135 nM) and almost the double amount for the high dose (270 nM), with ~20% (Q3) (Fig. 4.15C).

4.3.2 Activation of JAK/STAT pathway using IFN-γ

In the previous section, the cellular uptake of siRNA-based nanomedicine was investigated via microscopy (qualitative) and flow cytometry (quantitative) analysis. However, the information about drug and drug delivery system internalization does not provide the respective correlation with the therapeutic efficacy related to the active ingredient used. To this end, the downregulation of JAK/STAT signaling was evaluated by the phosphorylation profile of STAT1 (pSTAT1) after JAK/STAT pathway activation using IFN-γ. Downstream transcriptional effects of JAK1 inhibition were quantified via intracellular flow cytometric analysis using phospho-specific antibody staining for pSTAT1. As protein phosphorylation is a transient and highly dynamic process, its detection required appropriate stimulation time points and immediate fixation in order to maintain the phosphoepitopes.

In this context, cells were first investigated in terms of JAK/STAT pathway activation and responses to IFN-γ stimulation. Assay performance was validated for mono- and co-culture setups by the use of appropriate controls such as unstained and unstimulated cells, as well as isotype controls. Figure 4.16 summarizes the different pSTAT1 activation profiles of Caco-2 HTB-37, dTHP-1, MUTZ-3 cells, and co-culture model with different degrees of pSTAT1-positive cells after IFN-γ stimulation (50 ng/mL for 1 h). The quantification of STAT1 phosphorylation was detected by the APC fluorescence shift after single cell selection compared to unstimulated control (Fig. 4.16B). Epithelial cells showed a reduced activation of JAK/STAT signal pathway with approximately 30% of pSTAT1-positive cells, whereas both immune cell types were highly responsive to IFN-γ displaying ~60% (dTHP-1) and ~90% (MUTZ-3) of STAT1 phosphorylation (Fig. 4.16C). In summary, phospho-specific antibody staining showed for mono- and co-culture specificity without any background signal within the APC-channel related to auto-fluorescence of unstained or unstimulated cells (Fig. 4.16C).

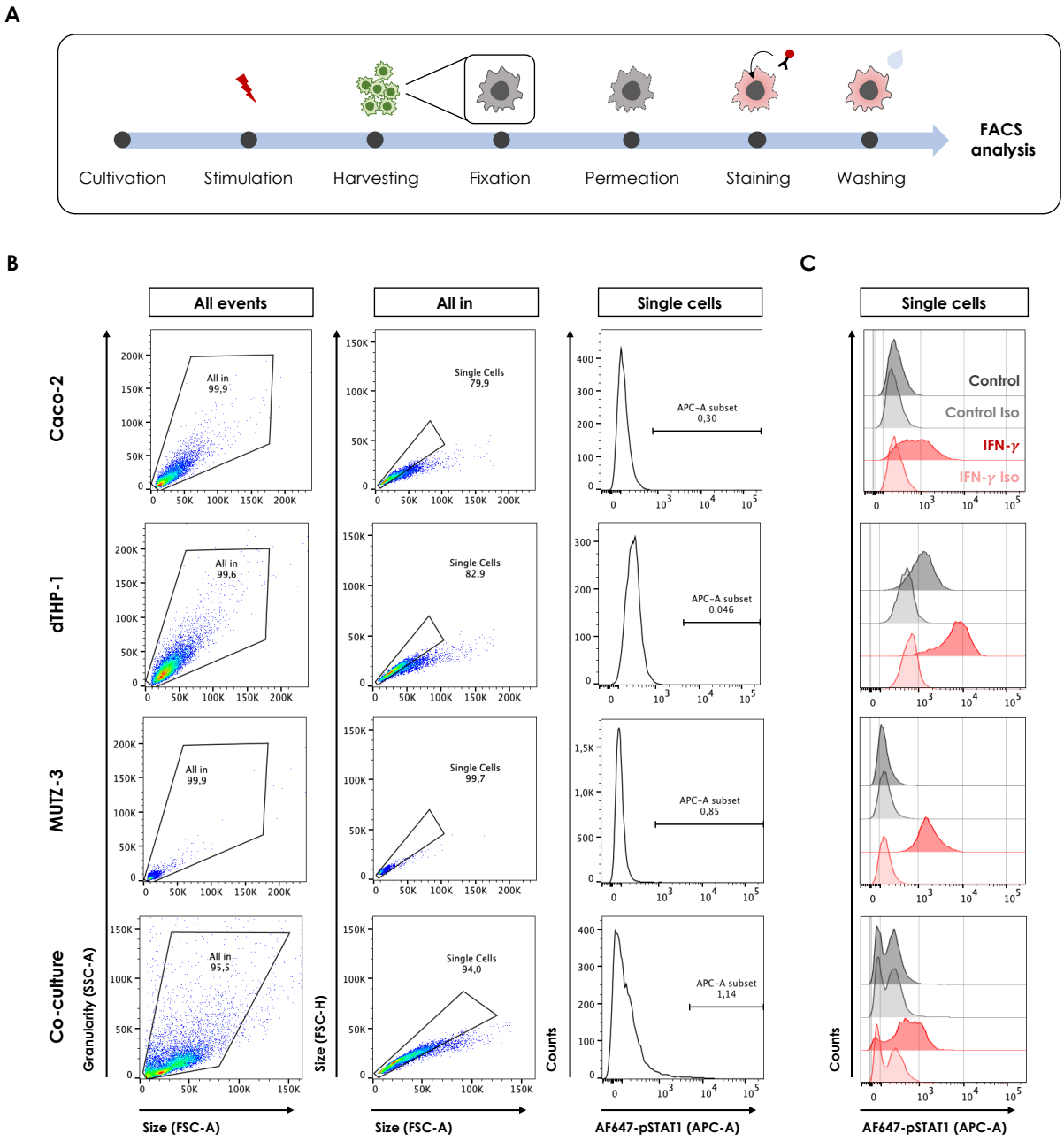


Figure 4.16 Flow cytometric analysis to determine the level of STAT1 phosphorylation in different cell types and co-culture model. Scheme of working procedure for activation and detection of protein phosphorylation via intracellular staining (**A**). Representative flow plots show gating strategy of unstimulated unstained control for each cell line and co-culture model (**B**). Mono-cultures of Caco-2, dTHP-1, and MUTZ-3 cells or co-culture were either left unstimulated or IFN-γ-stimulated (50 ng/mL) for 1 h (**C**). Cells were detached (mono-cultures) or dissociated (co-culture), fixed and permeabilized for intracellular staining with AF647 mouse anti-phospho-STAT1 (pY701) antibody or corresponding isotype control (AF647 mouse IgG 2a, κ). Phosphorylation of STAT1 is represented as histogram with AF647 emission collected at APC instrument setting (APC- A) and provides both, percentage of pSTAT1-positive cells (%) and mean fluorescence intensity (MFI). Histogram overlay summarizes unstimulated controls (grey) or IFN-γ-stimulated cells (red) stained either with specific pSTAT1 antibody (dark color) or isotype control (light color; Iso).

Figure 4.17 depicts the flow cytometric results obtained for each cell line after stimulation with different concentrations of IFN-γ used to modulate STAT1 phosphorylation.

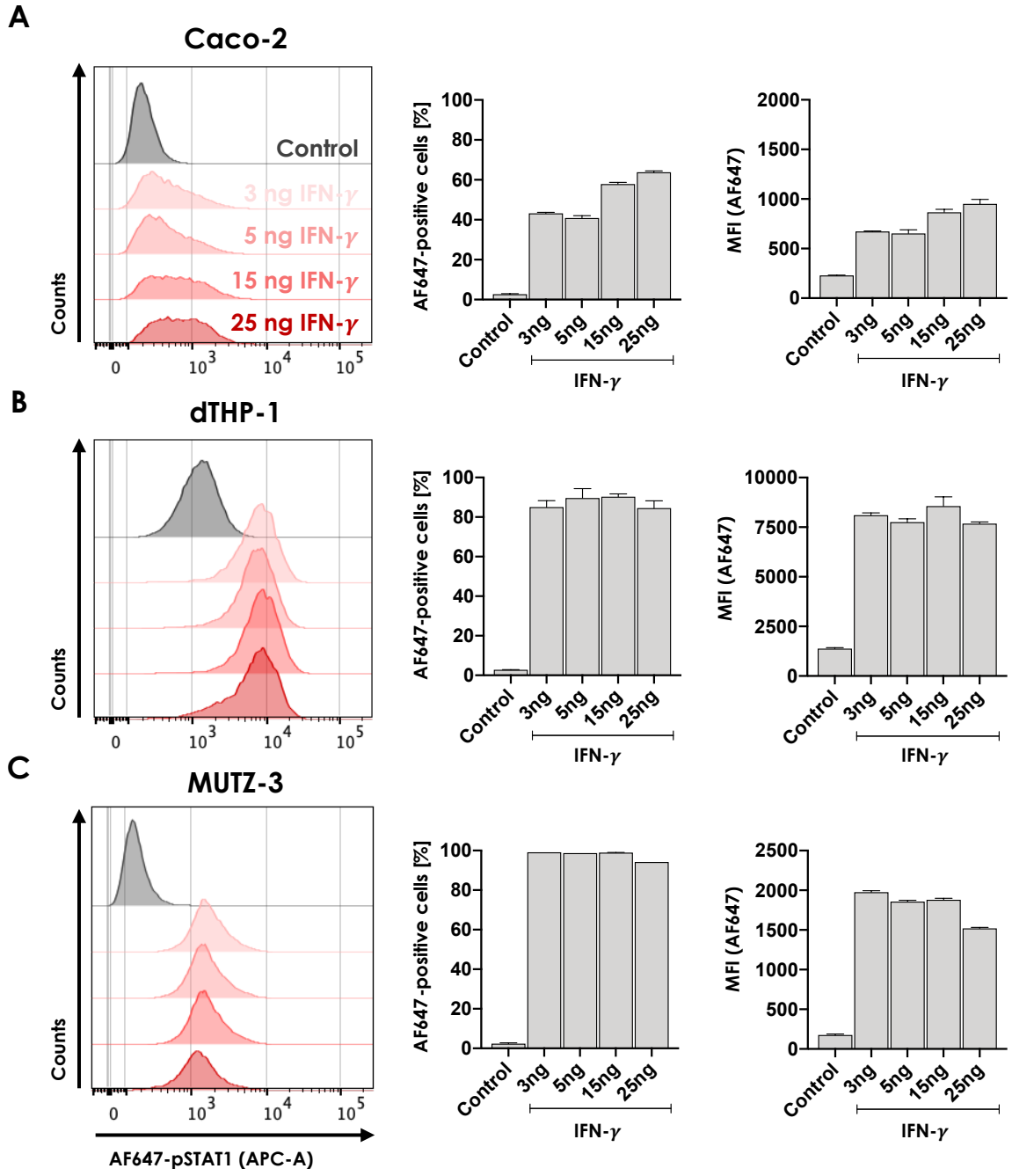


Figure 4.17 Flow cytometric analysis of STAT1 phosphorylation in different cell types of the co-culture model after JAK/STAT pathway activation. STAT1 activation was tested in different mono-cultures of Caco-2 HTB-37 (**A**), dTHP-1 (**B**) and MUTZ-3 (**C**) stimulated with IFN-γ for 1 h ranging from 3 to 25 ng/well. After IFN-γ stimulation, cells were harvested for phospho-specific STAT1 staining and FACS analysis. pSTAT1-positive cells are compared to unstimulated (control; grey). Phosphorylation of STAT1 is represented as histogram overlay with AF647 emission collected at APC instrument setting (APC- A)

and summarized in both percentage of pSTAT1-positive cells (%) and mean fluorescence intensity (MFI). Data represented as means ± SD (n=3; N=1).

Cells showed different steady-state levels of phosphorylation which are represented by the unstimulated cells (Fig. 4.17; control). Caco-2 HTB-37 cells showed a concentration-dependent response to IFN-γ with 43% to 64% pSTAT1-positive cells for the lowest and highest IFN-γ stimulation, respectively (Fig. 4.17A). In contrast, both immune cell types, dTHP-1 and MUTZ-3 cells, displayed already for the lowest IFN-γ concentration a comparable high percentage of pSTAT1-positive cells (>85%), but without any changes in relation to IFN-γ increase (Fig. 4.17B/C). Macrophage-like cells had the highest basal phosphorylation level (~ MFI) compared to the other cell lines (Fig. 4.17B). After validation of IFN-γ stimulation in 2D mono-cultures, the highest concentration of 50 ng/mL (25 ng/well) was chosen to ensure the activation of JAK/STAT pathway and STAT1 signaling for both, mono- as well as co-culture setups.

4.3.3 Inhibition of JAK/STAT pathway using Tofacitinib

With the knowledge from the previous section, all cell types of the co-culture model were responsive to IFN-γ stimulation and showed JAK/STAT signal pathway activation with a clear induction of downstream STAT1 protein phosphorylation. As a next step, the downregulation of JAK/STAT signaling was investigated by the application of the small molecule tofacitinib (TOFA), a pan-JAK inhibitor preferentially inhibiting JAK1 and JAK3, that was used as a positive control.

Figure 4.18 summarises the flow cytometric results obtained for each cell line after pre-treatment with TOFA for 6 h at different concentrations (0.5 - 5 µM) and subsequent IFN-γ stimulation (50 ng/well; 1 h). Therapeutic efficacy (TOFA; orange) was compared to IFN-γ stimulated untreated control (untreated; red), whereas the unstimulated and untreated control showed the basal phosphorylation level of STAT1 (control; grey) (Fig. 4.18; flow plots). All cell types showed dose-dependent inhibition of JAK/STAT signaling after TOFA pre-treatment. Epithelial cells displayed a 50% and

almost complete downregulation of JAK/STAT signaling for the lowest (0.5 µM) and highest (5 µM) TOFA concentration, respectively (Fig. 4.18A). Macrophage-like cells showed comparable inhibition efficacy, despite the highest TOFA dose did not induce pSTAT1 back to the basal phosphorylation level (Fig. 4.18B).

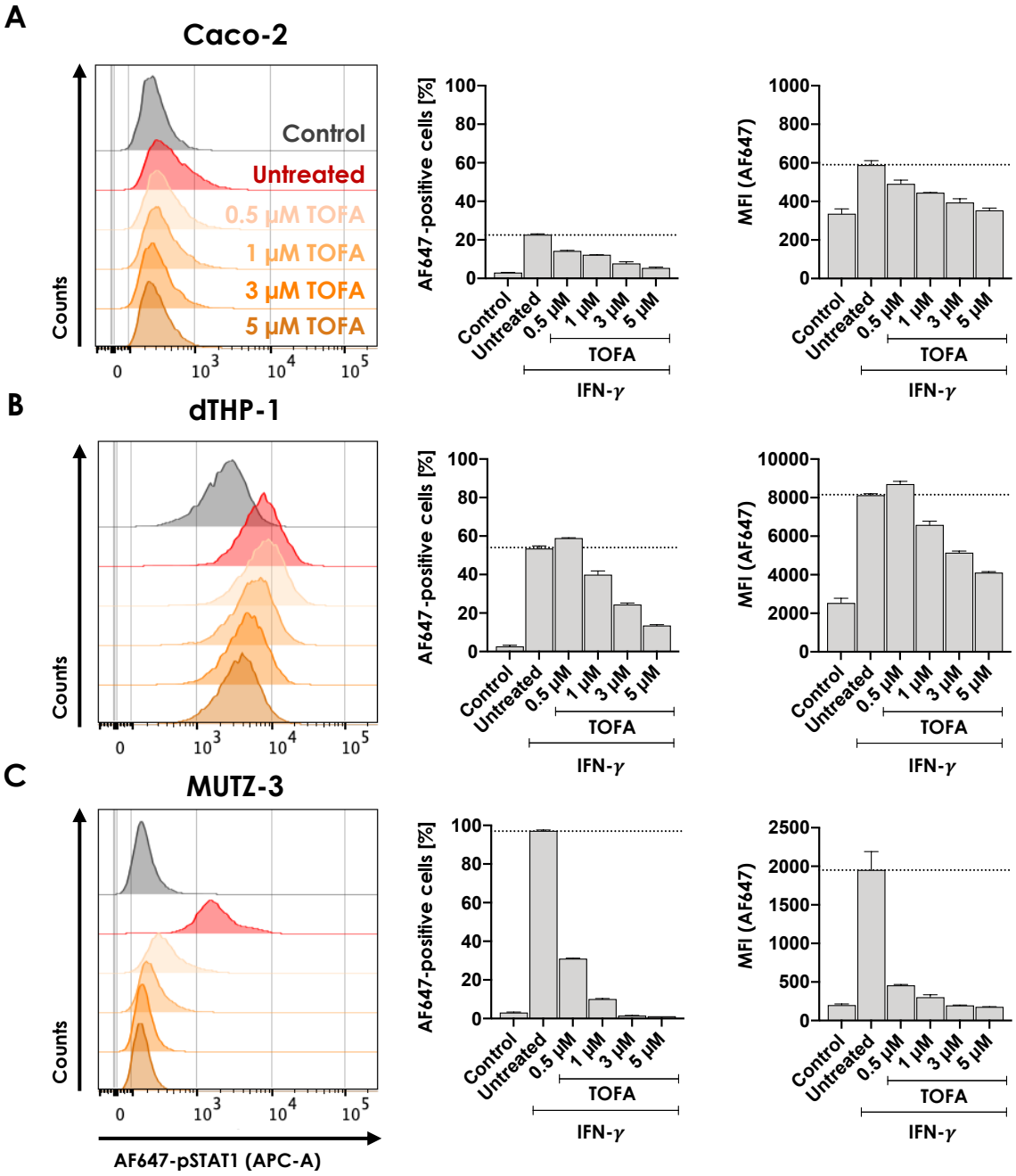


Figure 4.18 Flow cytometric analysis of STAT1 phosphorylation in different cell types of the co-culture after JAK/STAT downregulation using TOFA. Caco-2 HTB-37 (**A**), dTHP-1 (**B**), and MUTZ-3 (**C**) were pre-treated twice with TOFA ranging from 0.5 to 5 µM for 6 h on two subsequent days and afterwards stimulated with 25 ng/well IFN-γ (50 ng/mL) for 1 h. pSTAT1-positive cells are compared to unstimulated (control; grey) and untreated cells (red). Phosphorylation of STAT1 is represented as

histogram overlay with AF647 emission collected at APC instrument setting (APC- A) and summarized in both percentage of pSTAT1-positive cells (%) and mean fluorescence intensity (MFI). Data represented as means ± SD (n=3; N=1).

Compared to the other two cell types, pre-treatment with 3 µM TOFA induced in dendritic-like cells the complete inhibition of JAK/STAT comparable with unstimulated control (Fig. 4.18C).

Figure 4.19 shows the phosphorylation level of STAT1 for both co-culture models, a mixture of all three cell types collected after dissociation, that were pre-treated with TOFA. In contrast to the mono-culture experiments, TOFA (5 µM) was applied twice for 6 h on two subsequent days to both compartments of the co-culture. Compared to the unstimulated control (2.7 ± 0.5%), approximately one third of pSTAT1-positive cells (31.6 ± 1.1%) were identified upon IFN-γ stimulation for the leaky gut model (Fig. 4.19B; dashed line). However, the pre-treatment with TOFA followed by subsequent IFN-γ stimulation showed almost complete JAK/STAT signal inhibition (4.4 ± 0.7%), as observed for unstimulated control (Fig. 4.19B; orange).

Concerning the tight barrier model, less pSTAT1-positive cells (11.0 ± 1.8%) were identified after IFN-γ-stimulation compared to the leaky gut model (Fig. 4.19C; dashed line). TOFA pre-treatment was applied either to the apical or basolateral compartment, however, a similar and effective JAK/STAT inhibition was observed for both TOFA applications (AP: 2.0 ± 0.8%; BL: 2.2 ± 0.8%) compared to control (1.8 ± 0.9%) (Fig. 4.19C).

In conclusion, both co-culture models showed JAK/STAT activation after IFN-γ-stimulation with better detection of induced STAT1 phosphorlyation for the leaky gut model. The repetitive pre-treatment with TOFA was effective for both co-cultures and displayed JAK/STAT signal inhibition with pSTAT1-positive cells similar to the unstimulated control.

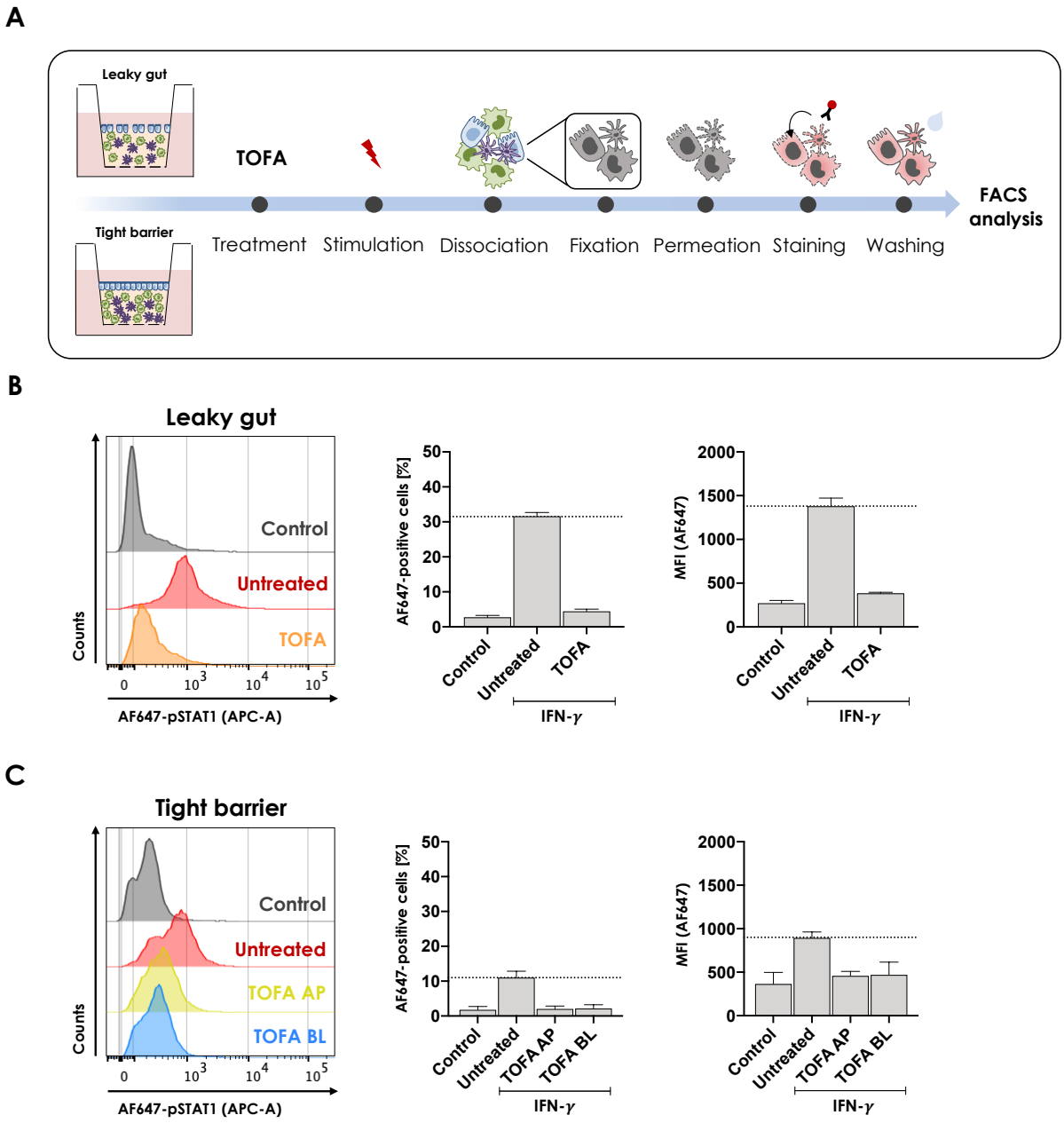


Figure 4.19 Flow cytometric analysis of STAT1 phosphorylation for JAK/STAT pathway activation and downregulation within the co-culture models. Scheme of working procedure for co-culture pre-treatment with TOFA, followed by the activation and detection of protein phosphorylation via intracellular staining (**A**). Phosphorylation profile of pSTAT1 of leaky gut model pre-treated twice on day 6/7 with 5 µM TOFA for 6 h applied to both compartments (**B**) and of tight barrier model pre-treated on day 11/12 with 5 µM TOFA for 6 h applied either to the apical (AP) or basolateral (BL) compartment (**C**). After pre-treatment, both co-cultures were stimulated with 50 ng/mL IFN-γ for 1 h and subsequently dissociated for phospho-specific STAT1 staining and FACS analysis. Phosphorylation of STAT1 is represented as histogram overlay with AF647 emission collected at APC instrument setting (APC- A) and summarized in both percentage of pSTAT1-positive cells (%) and mean fluorescence intensity (MFI). pSTAT1-positive cells are compared to unstimulated (control; grey), untreated cells (red), and TOFA pre-treatments applied to the apical (AP; yellow), basolateral (BL; violet), or both compartments (orange). Data of are means ± SD, for mono-cultures (n=3; N=1), tight model (n=9; N=3), and leaky model (n=15; N=5).

4.3.4 Efficacy testing of JAK/STAT pathway using siRNA-based nanomedicine

The investigations regarding JAK/STAT pathway activation and inhibition resulted in optimized treatment conditions and suitable control groups within the experimental design necessary to validate the effects of siRNA-based nanomedicine (4.2.7). In this line, IFN-γ stimulation and TOFA pre-treatment represented the situation without the intervention of interest (negative control) and in presence of intervention with expected effect (positive control), respectively. Within these essential components, the efficacy for JAK/STAT downregulation using unlabeled siJAK1-loaded LNPs was investigated within the leaky gut model representing distinct IBD pathophysiology.

Figure 4.20 illustrates the flow cytometry results obtained after different pre-treatment strategies applied to the leaky gut model after pre-treatment with TOFA (5 µM; orange) or siJAK1-loaded nanoplexes (N/P ratio of 8) at two different concentrations with either 45 µg or 90 µg LNPs and 135 nM (N/P 8 Low; blue) or 270 nM (N/P 8 High; green) siRNA per well, respectively. Therapeutic efficacy was compared to IFN-γ stimulated untreated control (untreated; red), whereas the unstimulated untreated control displayed the basal phosphorylation level of STAT1 (control; grey) (Fig. 4.20B). For the easier comparison of several treatment options, pSTAT1-positive cells represented as percentage were normalized to the untreated IFN-γ stimulated control (untreated cells were set to 100%). The small molecule JAKi TOFA added to both, apical and basolateral compartment, decreased JAK/STAT signaling significantly by 86.0 ± 2.1% compared to untreated control, as indicated by the quantified fluorescence signal almost back to baseline (Fig. 4.20C). Repetitive treatment with siJAK1-loaded LNPs induced a dose-dependent signal inhibition and displayed JAK/STAT downregulation by 9.6 ± 11.8% and 15.7 ± 12.1% for low and high nanoplex concentrations, respectively (Fig. 4.20C). Lower doses of nanoplexes attenuated the IFN-γ-induced phosphorylation of STAT1, however, without significant difference to the untreated cells. In contrast, higher nanoplex concentration indicated a significant inhibition of JAK/STAT activation compared to IFN-γ stimulation alone.

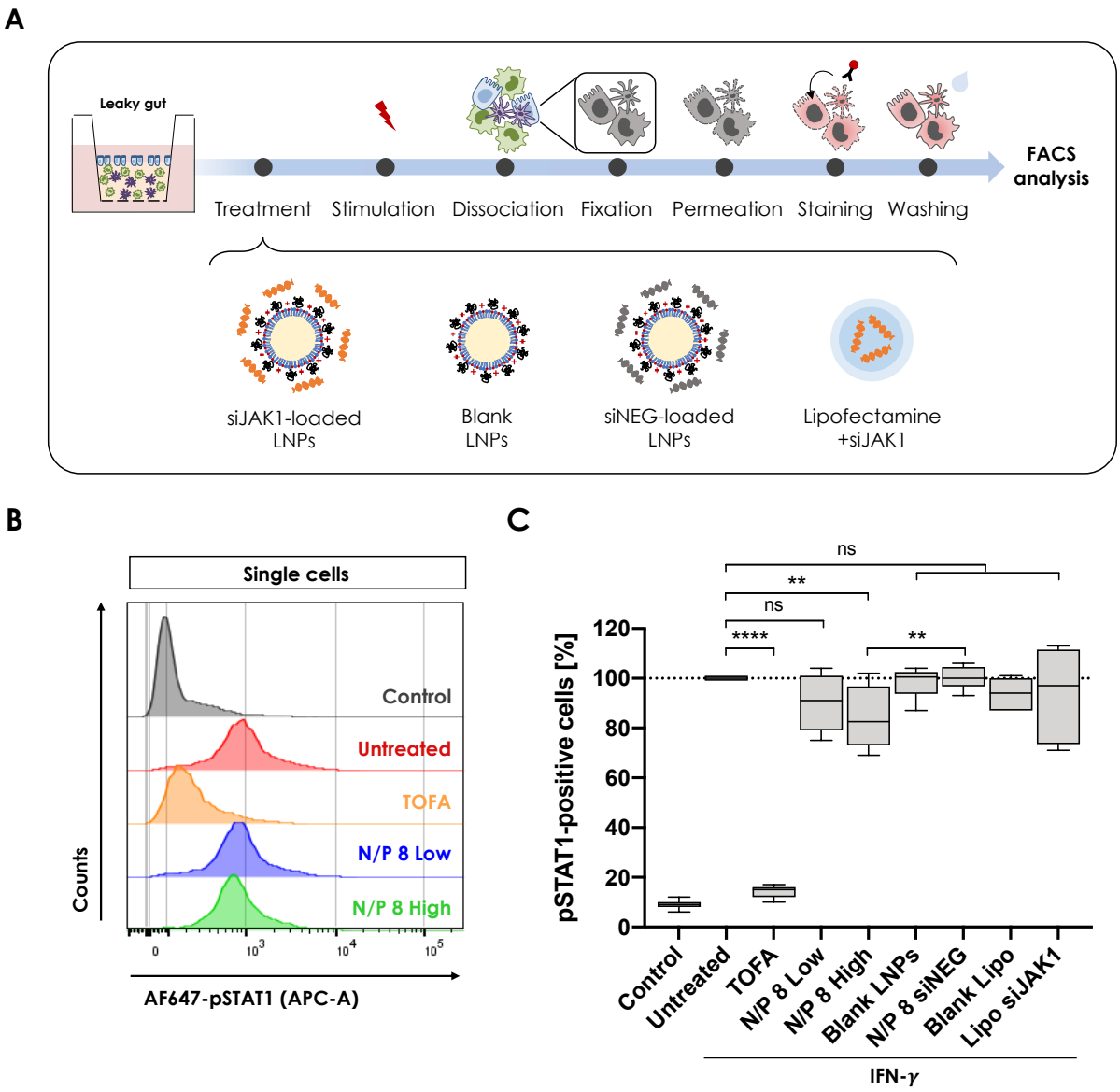


Figure 4.20 JAK/STAT pathway inhibition in leaky gut model using siRNA-based nanomedicine. Scheme of working procedure including different pre-treatments, JAK/STAT activation and dissociation of the co-culture, followed by subsequent detection of protein phosphorylation via intracellular staining (**A**). Leaky gut model was pre-treated with TOFA (5 µM) or siJAK1-loaded nanoplexes (N/P ratio of 8) at low and high concentration (45 µg or 90 µg LNPs and 135 nM or 270 nM siRNA per well, respectively). Pre-treatment was followed by IFN-γ stimulation (50 ng/mL) for 1 h. Afterwards, co-culture was dissociated, fixed and permeabilized for intracellular staining with AF647 mouse anti-phospho-STAT1 (pY701) antibody and the phosphorylation profile of STAT1 (pSTAT1) was analyzed by FACS. Histogram overlay represents the single cells of untreated unstimulated (control; grey), untreated IFN-γ-stimulated (untreated; red), pre-treated with tofacitinib as a positive control (TOFA; orange), or with nanoplexes at low (blue) and high (green) concentration (**B**). Further control treatments included un-loaded LNPs (blank LNPs; 90 µg/well); LNPs loaded with non-targeting siRNA (N/P 8 siNEG; 270 nM) and lipofectamine RNAiMAX alone (blank Lipo) or with siJAK1 (Lipo siJAK1; 270 nM). pSTAT1-positive cells are represented as percentage, normalized to the untreated cells (**C**). The box plots depict the minimum and maximum values (whiskers), the upper and lower quartiles, and the median. Significant

differences are represented as ** p< 0.01 and **** p< 0.0001 according to ANOVA; for TOFA (n= 15; N= 5), N/P 8 Low/High (n= 9; N= 3), and control treatments (n= 6; N= 2).

However, both nanoplex concentrations displayed high standard deviations with around 12% without significant changes in STAT1 phosphorylation status between the two doses (Fig. 4.20C). The observed JAK/STAT downregulation using nanoplexes was associated with the silencing efficacy of the cargo, namely siRNA targeting JAK1, since the control treatments did not affect the signal transduction. Compared to untreated cells, the application of blank LNPs (without siRNA cargo) or loaded with non-targeting siRNA (N/P 8 siNEG) at comparable concentrations displayed pSTAT1-positive cells of 98.3 ± 6.2% and 100.2 ± 4.8%, respectively (Fig. 4.20C). Similar results were obtained for control treatments using the lipid-based transfection reagent Lipofectamine (Lipo) with 93.6 ± 5.9% and 93.9 ± 17.3% for Lipo applied alone (Blank Lipo) and Lipo containing siJAK1 at high concentration (Lipo siJAK1), respectively (Fig. 4.20C).

Taken together, repetitive treatment of the leaky gut model using siJAK1-loaded LNPs resulted in a significant JAK/STAT pathway inhibition at high doses, but without achieving the almost complete signal inhibition, as observed for TOFA pre-treatment.

4.4 Discussion

Current treatment options for IBD patients are limited to unspecific immune-modulatory agents such as corticosteroids which are related to prolonged treatment, adverse effects, and inadequate or lost response [80]. In the last decade, molecular targeted therapeutics have emerged with the focus on IBD pathophysiology including biologic therapies with higher specificity [230]. However, undesired effects still arise due to systemic administration of anti-inflammatory treatment [66]. Nowadays, there is an unmet need for drug delivery strategies that preferentially target the drug to the diseased intestine [231]. Such delivery system in combination with an innovative siRNA-based therapeutic approach targeting JAK/STAT signal pathway was explored by means of the complex *in vitro* model representing the human intestine. The here described leaky gut model with IBD-related pathophysiology provided the combined investigation of intestinal barrier crossing and efficacy testing of drug and drug delivery systems.

Nanoplex trafficking and cellular interaction was explored by microscopic analysis using fluorescently-labeled nanoplexes. Corresponding cationic nanocarriers were designed for facilitated cellular uptake and supported delivery of a variety of therapeutic agents including nucleic acids [196]. This lipid-based formulations are widely investigated for oral delivery and associated with beneficial properties such as colloidal stability, biocompatibility and the possibility for scale-up production [232]. The solid lipid nanocarriers used for this study aimed for localized drug delivery into the inflamed gut without affecting the surrounding healthy tissue in IBD patients. *In vivo* data obtained from murine colitis models demonstrated a size-dependent deposition of nanoparticles in inflamed but not healthy colon with enhanced accumulation of 100 nm particles compared to microparticles [233,234]. This delivery strategy is related to the concept of passive targeting to inflamed tissue, comparable to the concept of epithelial enhanced permeation and retention effect [235,236]. Moreover, the increased permeability of nanoformulations within inflamed tissues is

interconnected with the increased number of present immune cells which mediate the pro-inflammatory environment. In the context of inflammation, a significant contribution to drug carrier accumulation is mediated by resident and infiltrating phagocytes such as macrophages, neutrophils or dendritic cells that are enriched within the inflamed mucosa [237]. The efficient uptake of siRNA-loaded LNPs was proven for epithelial- and macrophage-like cells that are present in the co-culture model. As expected, macrophages showed increased phagocytosis of blank and siRNA-loaded LNPs compared to epithelial cells which is related to the primary role of this cell type. As a part of the first-line defence, macrophages are responsible for the elimination of foreign particulates and thus, engulf more efficiently encountered nanoparticles [238]. Furthermore, nano-sized particles were found to be advantageous regarding the rapid intestinal clearance as a result of diarrhea, a common symptom of IBD [239,240]. Besides size-mediated mechanisms, charge interaction may occur for anionic nanoparticles that preferentially accumulate at the sites of inflammation with positively charged proteins deposited within injured epithelium [241,242]. However, recent studies have shown that in comparison to anionic or neutral charge, an enhanced cellular internalization and paracellular transport by enterocytes was observed for cationic nanoparticles [243,244]. Compared to liposomal formulations, present solid lipid nanoparticles offered long-term colloidal stability in aqueous buffer due to their lipid core matrix [196].

Preceding uptake studies performed in the tight barrier model showed that LPS inflammation and related barrier decrease of around 20% did not improve LNP penetration into the sub-epithelial space. Even for extended incubation (24 h), nanocarriers were not able to encounter the underlying immune cells. Any potential hindered diffusion of nanocarrier and/or siRNA through the collagen matrix was excluded by uptake studies performed without the presence of the Caco-2 cell monolayer on top of the co-culture. As a result, both LNPs and siRNA cargo were able to penetrate through the collagen layer which was followed by the uptake within the underlying immune cells.

For the tight barrier model, LNPs were co-localized together with siRNA cargo within the Caco-2 cell layer and in parts accumulated in dead or dying cells identified on the surface of the epithelium, mainly due to cell membrane leakiness. As cellular uptake is affected by the physiochemical property of the carrier, present LNP formulation was beneficial for cellular uptake due to its cationic charge and nanoscale size of 40 nm. Despite these properties may change once LNPs are subjected to biological fluids, dense polyethylene glycol (PEG) coating is related to the reduction of LNP hydrophobicity and surface charge density [245]. On the one side, PEGylation reduces particle aggregation or opsonization, but at the same time may impact efficient cellular uptake [206]. Nevertheless, qualitative and quantitative studies in epithelial- and macrophage-like cells confirmed the efficient internalization of blank and siRNA-loaded LNPs. Moreover, under physiological conditions, nanoplexes should overcome the mucus barrier before reaching the intestinal epithelium. The high density of PEGylation on LNP surface favours mucus penetration, a rather important biological barrier for nanocarriers [49]. This hydrophilic surface showed an accelerated penetration into the inflamed intestinal epithelium *ex vivo* [246].

Analysis of nanoplex trafficking in the leaky gut model displayed a divergent deposition with an accumulation of both, siRNA and LNPs, within the sub-confluent regions. This regional deposition of nanoplexes was associated with an increase of local concentration of respective siRNA therapeutics. These findings underlined the advantage of the leaky gut model which reproduced the phenomenon observed *in vivo* with nanoparticle accumulation within inflamed intestinal breaches. In addition, nanoplexes were penetrating into the leaky regions and reached the underlying the sub-epithelial compartment with facilitated uptake in present immune cells. Despite several siRNA-based therapeutics are under clinical development, to date only three siRNA drugs were approved for rare and life-threatening diseases [247]. Notwithstanding that siRNAs have an outstanding potential, these polyanionic molecules are highly instable in biological fluids, can potential cause off-target effects, and are highly depend on chemical modifications and effective delivery strategies

[248]. The importance of the drug delivery vehicle became obvious, as no fluorescence signal was detected after the application of naked siRNA which might be related to its unfavourable characteristics like its strong charge and instability. This is in agreement with previous studies, where naked siRNA was not detected within the GI tract after oral administration in mice, suggesting its fast degradation and poor cellular uptake when applied without assistance of delivery systems [249]. Electrostatic repulsion between the strong net negative charge of the naked RNA and cell membranes precludes the cellular uptake of epithelial and immune cells [250].

Flow cytometric analysis of nanoparticle uptake is a fast high throughput method to obtain the relative amount of cells that are associated with fluorescently labelled nanoparticles. The main advantage of this technique is the resolution to identify the NP load per cell of thousands of individual cells which is expressed by cell fluorescence intensity distributions [251]. However, there is no discrimination between internalized NPs (intracellular) and their association to the cellular membrane (extracellular). In combination to microscopic analysis there are valuable insights that LNPs were internalized by cells. Taken together, an increased percentage of siJAK1-positive cells was found upon complexation with LNPs, however, compared to cellular association of nanoplexes the silencing efficacy of siJAK1 provided a more important readout. The localized delivery of JAK inhibitors was investigated within the leaky gut model that combines an intestinal barrier property and immune target cells necessary to evaluate corresponding drug function. To this end, delivery efficacy and target engagement against JAK1 were quantified via downstream analysis of STAT1 protein phosphorylation (pSTAT1) after IFN-γ stimulation.

JAK/STAT inhibition was chosen within the "treat to target" paradigm for IBD and used as a functional assay to reveal therapeutic efficacy of two different pharmaceutical approaches. Transcriptional data from whole human biopsis showed an upregulation of all four JAK kinases in IBD patients suffering from UC, and JAK1 was found in myeloid and epithelial cells of the human intestine (predominantly macrophages and dendritic cells) [83]. Nevertheless, the suppression of JAK/STAT

pathway should be highly specific in order to minimize the interference with other biologically relevant processes mediated by JAK/STAT including cell differentiation, growth and survival [252]. Important considerations involve the local and selective JAK inhibition within the inflamed tissue as well as minimal systemic exposure and in preference, the restriction to one specific JAK kinase for selective immune modulation within the target cell population [83,253].

JAK/STAT pathway activation and downregulation was tested first in mono-culture setups in order to optimize the functional assay for the quantification of pSTAT1, the molecular affectors downstream of the signaling cascade. Corresponding flow cytometric analysis were transferred to the co-culture setup including IFN-γ stimulation and JAKi TOFA pre-treatment. Accordingly, the model´s suitability was verified in terms of adequate response to IFN-γ as well as efficient JAK/STAT downregulation mediated by TOFA. An elevated amount of the immunomodulator IFN-γ was obserevd during chronic inflammation and concerning JAK/STAT pathway, IFN-γ binding activated JAK kinase pair of 1/3 or JAK1/TYK2 [83,254]. The detection and quantification of phosphorylated STAT1 by flow cytometry provided the resolution down to individual cells in contrast to Western blotting [255]. Assay performance was validated by the use of appropriate staining controls including isotype control or unstained cells which defined antibody specificity. However, unstimulated cells represented a more important control necessary to identify the steady-state phosphorylation for each cell type. In this context, the highest basal phosphorylation was assigned to macrophages compared to the other cell types. This has been attributed to the PMA-mediated expression of an IFN-γ-inducible enzyme that may have lead the expression in differentiated THP-1 cells [256]. In line with previous studies, transient IFN-γ-mediated STAT1 activation of macrophages has a typical peak within 15-60 min and resolution after 2-6 hours after stimulation [257]. In addition, 3D cultivation of primary macrophages that were embedded in ECM (collagen) modulated their polarization and showed an amplified response to IFN-γ via pSTAT1 [258]. Nevertheless, STAT phosphorylation is highly dynamic and fast de-

phosphorylation required fast cell fixation [255]. Thus, the inevitable dissociation of the co-culture model right after IFN-*γ*-stimulation could have an impact on the phosphorylation state detection due to the postponed fixation step. The significant down-regulation of JAK/STAT after TOFA pre-treatment was related to the fact that the drug may have reached the majority of cells due to increased permeation into the co-culture model. TOFA as a non-specific pan-JAKi but preferentially inhibiting JAK1/3, is the first JAKi approved as a treatment for UC, and diffuses passively inside the cells and impedes downstream phosphorylation of target STATs [259,260]. Co-culture pre-treatment with TOFA was used here as a positive control for the STAT1 phosphorylation assay and repetitive dosage for 6 hours at 5µM applied to both compartments ensured saturation of the system. Longer incubation of TOFA at 5 µM concentration (48 h) showed a decreased wound healing process by *in vitro* scratch assay using Caco-2 cells [261]. As described previously, this effect is related to the panJAKi of TOFA involving JAK3 necessary for intestinal repair mechanisms [262]. A recent study used the same TOFA concentration of 5 µM and revealed a high *in vitro* permeability in Caco-2 cells with a low efflux ratio [263].

LNPs, composed of a lipid core and stabilized by a surfactant shell, were used to improve the delivery of siRNA therapeutic. Driven by electrostatic interactions, stable nanoplex formulations were prepared by complexation of negatively charged siRNA targeting human JAK1 (siJAK1) on the surface of cationic LNPs. siJAK1 duplexes aimed for silencing the gene activity of JAK1 within the leaky gut model. In comparison to TOFA, the silencing effects of siJAK1 were less pronounced, however, corresponded to the observed siRNA trafficking within the co-culture model where nanoplexes accumulated within the leaky regions. After their penetration into the sub-epithelial layer only a small portion of the underlying immune cells was reached by siRNA, as the main protagonist of pSTAT1 activation. From the microscopic analysis, the sub-confluent and still proliferative active Caco-2 cell layer displayed the internalization of siRNA-loaded LNPs to a higher extent. As previously published, transfection of differentiated epithelial cell layers was more difficult compared to less

differentiated sub-confluent cells [264]. Thus, leakiness or sub-confluency of Caco-2 cells had a beneficial effect on siRNA transfection efficacy. However, as Caco-2 cells showed a reduced response to IFN-γ stimulation, the epithelial cells contributed less to the overall phosphorylation pattern of STAT1. In this line, macrophages are in general considered as hard-to transfect cells due to evolved mechanisms to recognize foreign nucleic acid [265]. Despite dTHP-1 cells showed an increased uptake of nanoplexes compared to epithelial cells, the observations of uptake studies performed within in the mono-culture setup, however, did not correspond to the co-culture scenario. Since the exposure was different (not directly involving all cell types), merely Caco-2 cells were positive for nanoplexes and only to a smaller extent for the immune cells. Nevertheless, high specificity and efficacy profile of corresponding siJAK1 was recently proven in different cells, even for very low concentration (5 pM), and displayed low side and off-target effects [167]. A complete inhibition of IFN-γ signaling pathway was shown for Caco-2 cells and primary human macrophages after 48 h post-transfection using siJAK1 (10 nM) and Lipofectamine. However, the experimental parameters and functional assays were different from the co-culture setup including lipofection performed in 2D mono-cultures under serum-free conditions or knock down efficiencies evaluated on protein (Western blot analysis) and mRNA level (qPCR).

In summary, this data suggests that a much higher percentage of cells within the co-culture must be encountered by siRNA-loaded LNPs in order to induce higher JAK/STAT inhibition. Nevertheless, partial silencing efficiency might already ameliorate the course of disease *in vivo*. In addition, an improved resolution and understanding to what extent each cell type contributed the overall phosphorylation profile could be expanded by the combination of phospho-specific staining with cell-type specific markers (e.g. epithelial and immune cell marker).

Since the sequence specificity of the present siRNA was designed to target human JAK1, only human cell-based models can be used to confirm the transfection efficiency excluding the existing *in vivo* animal models. In this context, *in vivo* efficacy

testing of preclinical RNA therapeutics could be performed within human organoid cultures or biopsis [266].

Furthermore, as wound healing and inflammation are connected biological processes, the promotion of mucosal wound healing was chosen as an additional goal for IBD therapy [212,267]. Accordingly, the still growing epithelial cell layer of the leaky gut model could be further investigated in terms of novel targets and intestinal tissue repair mechanism.

4.5 Conclusion

In conclusion, the leaky gut model represents a complex *in vitro* model mimicking the chronically inflamed human intestinal interface and provided valuable insights for the study of anti-inflammatory drugs and nanomedicines. Severe IBD pathophysiology was introduced by the presence of a sub-confluent epithelial layer and immune system protagonists in close proximity. *In vitro* disease modelling enabled the investigation of intestinal barrier crossing of siRNA-based nanomedicine under diseased conditions. In contrast to the intact epithelium of the tight barrier, nanoplexes accumulated within the epithelial breaches of the leaky gut model and partially penetrated into the sub-epithelial zone. As a consequence, nanoplexes supported the delivery and release of the siRNA which was able to reach the target immune cells located underneath the epithelium. Besides the microscopic analysis of trafficking and penetration into the intestinal mucosa, the leaky gut model was used to evaluate the therapeutic efficacy of respective siRNA-based nanomedicine. Moreover, this human cell-based co-culture model enabled the transfection efficiency testing of siRNA designed for human specificity. Accordingly, focusing a particular target molecule, a functional assay was developed to detect JAK/STAT signal pathway activation necessary to predict reliable drug-target interaction. Thus, the leaky gut model allowed for a first selection and optimization of related drug delivery systems. In conclusion, this intestinal *in vitro*

model could be applied as a pre-clinical platform to complement *in vivo* analysis for faster translation of novel drug candidates and/or drug delivery systems into the clinic.

5 Summary and outlook

The GI tract includes multiple biological barriers to oral drug delivery. The intestinal mucosa provides several challenges for drug and delivery systems including the mucus as well as cellular barriers on which this work has focused.

Due to mucus heterogeneity, multiple interactions sites for drug and drug delivery systems are present. The combination of various *in vitro* models and techniques provided the possibility to characterize the impact of intestinal mucus on drug and drug carrier diffusion. Depending on selected model, different aspects of the mucus barrier were investigated and provided necessary insights in potential drug carrier interactions with mucus.

The herein developed leaky gut model demonstrated a higher responsiveness on inflammatory stimulation, partial access to the immune cells, and therefore improved the test system for anti-inflammatory nanomedicine targeting monocytic cells.

The leaky gut model shows the potential for further improvements towards enhanced physiological relevance by the addition of a mucus layer or by replacing the incorporated cell lines with cells from other sources. The implementation of mucus by i.a. mucus-secreting cells or artificial mucus could be beneficial to provide a complete setup of the intestinal interface. However, increased model complexity should not conflict with controlled conditions and the assignment of respective effects. The use of patient-derived cell material would improve model´s applicability for testing individual responsiveness to medication and for identification of the optimal treatment option. Furthermore, as wound healing and inflammation are highly interconnected biological mechanisms, the sub-confluent but still growing epithelial layer could lead to further investigations of epithelial healing factors and novel targets supporting barrier restoration. Further applications of the leaky gut model could be performed for GI safety assessment including drug-induced or environmental toxicity studies.

In biomedical research, *in vitro* models of the intestine are used to complement *in vivo* analysis and represent a suitable testing platform to predict reliable mucus and drug-target interaction. However, this requires an appropriate characterization of respective models with respect to their limitations, standardization and physiological resemblance.

6 References

[1] J.F. Reinus, D. Simon, Gastrointestinal anatomy and physiology: The essentials, 2014. https://doi.org/10.1002/9781118833001.

[2] A.M. Pedersen, A. Bardow, S.B. Jensen, B. Nauntofte, Saliva and gastrointestinal functions of taste, mastication, swallowing and digestion, Oral Dis. 8 (2002) 117–129. https://doi.org/10.1034/j.1601-0825.2002.02851.x.

[3] S. Hua, E. Marks, J.J. Schneider, S. Keely, Advances in Oral Drug Delivery for Regional Targeting in the Gastrointestinal Tract - Influence of Physiological, Pathophysiological and Pharmaceutical Factors, Front. Pharmacol. 11 (2020) 1–22. https://doi.org/10.3389/fphar.2020.00524.

[4] N.J. Spencer, H. Hu, Enteric nervous system: sensory transduction, neural circuits and gastrointestinal motility, Nat. Rev. Gastroenterol. Hepatol. 17 (2020) 338–351. https://doi.org/10.1038/s41575-020-0271-2.

[5] A.M. Mowat, W.W. Agace, Regional specialization within the intestinal immune system, Nat. Rev. Immunol. 14 (2014) 667–685. https://doi.org/10.1038/nri3738.

[6] H.F. Helander, L. Fändriks, Surface area of the digestive tract – revisited, Scand. J. Gastroenterol. 49 (2014) 681–689. https://doi.org/10.3109/00365521.2014.898326.

[7] S.N. Steinway, J. Saleh, B.K. Koo, D. Delacour, D.H. Kim, Human Microphysiological Models of Intestinal Tissue and Gut Microbiome, Front. Bioeng. Biotechnol. 8 (2020). https://doi.org/10.3389/fbioe.2020.00725.

[8] G. Zhu, J. Hu, R. Xi, The cellular niche for intestinal stem cells: a team effort, Cell Regen. 10 (2021) 1–16. https://doi.org/10.1186/s13619-020-00061-5.

[9] E. Martini, S.M. Krug, B. Siegmund, M.F. Neurath, C. Becker, Mend Your Fences: The Epithelial Barrier and its Relationship With Mucosal Immunity in Inflammatory Bowel Disease, Cmgh. 4 (2017) 33–46. https://doi.org/10.1016/j.jcmgh.2017.03.007.

[10] L.W. Peterson, D. Artis, Intestinal epithelial cells: Regulators of barrier function and immune homeostasis, Nat. Rev. Immunol. 14 (2014) 141–153. https://doi.org/10.1038/nri3608.

[11] S.A. Hewes, R.L. Wilson, M.K. Estes, N.F. Shroyer, S.E. Blutt, K.J. Grande-Allen, In Vitro Models of the Small Intestine: Engineering Challenges and Engineering Solutions, Tissue Eng. - Part B Rev. 26 (2020) 313–326. https://doi.org/10.1089/ten.teb.2019.0334.

[12] A. Segers, I. Depoortere, Circadian clocks in the digestive system, Nat. Rev. Gastroenterol. Hepatol. 18 (2021) 239–251. https://doi.org/10.1038/s41575-020-00401-5.

[13] J.M. Allaire, S.M. Crowley, H.T. Law, S.Y. Chang, H.J. Ko, B.A. Vallance, The Intestinal Epithelium: Central Coordinator of Mucosal Immunity, Trends Immunol. 39 (2018) 677–696. https://doi.org/10.1016/j.it.2018.04.002.

[14] A.R. Henderson, H. Choi, E. Lee, Blood and lymphatic vasculatures on-chip platforms and their applications for organ-specific in vitro modeling, Micromachines. 11 (2020). https://doi.org/10.3390/mi11020147.

[15] J.S. Alexander, V.C. Ganta, P.A. Jordan, M.H. Witte, Gastrointestinal lymphatics in health and disease, Pathophysiology. 17 (2010) 315–335. https://doi.org/10.1016/j.pathophys.2009.09.003.

[16] E.A. Eloe-Fadrosh, D.A. Rasko, The human microbiome: from symbiosis to pathogenesis, Annu. Rev. Med. 64 (2013) 145–163. https://doi.org/10.1146/annurev-med-010312-133513.

[17] C. Werlang, G. Cárcarmo-Oyarce, K. Ribbeck, Engineering mucus to study and influence the microbiome, Nat. Rev. Mater. 4 (2019) 134–145. https://doi.org/10.1038/s41578-018-0079-7.

[18] R. Sender, S. Fuchs, R. Milo, Are We Really Vastly Outnumbered? Revisiting the Ratio of Bacterial to Host Cells in Humans, Cell. 164 (2016) 337–340. https://doi.org/10.1016/j.cell.2016.01.013.

[19] J.M. Rodríguez, K. Murphy, C. Stanton, R.P. Ross, O.I. Kober, N. Juge, E. Avershina, K. Rudi, A. Narbad, M.C. Jenmalm, J.R. Marchesi, M.C. Collado, The composition of the gut microbiota throughout life, with an emphasis on early life, Microb. Ecol. Heal. Dis. 26 (2015) 1–17. https://doi.org/10.3402/mehd.v26.26050.

[20] C.C. Bain, A.M. Mowat, Macrophages in intestinal homeostasis and inflammation., Immunol. Rev. 260 (2014) 102–117. https://doi.org/10.1111/imr.12192.
[21] B.D. McDonald, B. Jabri, A. Bendelac, Diverse developmental pathways of intestinal intraepithelial lymphocytes, Nat. Rev. Immunol. 18 (2018) 1–12. https://doi.org/10.1038/s41577-018-0013-7.
[22] N. Kobayashi, D. Takahashi, S. Takano, S. Kimura, K. Hase, The Roles of Peyer's Patches and Microfold Cells in the Gut Immune System: Relevance to Autoimmune Diseases, Front. Immunol. 10 (2019) 1–15. https://doi.org/10.3389/fimmu.2019.02345.
[23] B. Ruder, C. Becker, At the Forefront of the Mucosal Barrier: The Role of Macrophages in the Intestine, Cells. 9 (2020). https://doi.org/10.3390/cells9102162.
[24] S.R. Lueschow, S.J. McElroy, The Paneth Cell: The Curator and Defender of the Immature Small Intestine, Front. Immunol. 11 (2020) 1–12. https://doi.org/10.3389/fimmu.2020.00587.
[25] H.-A. Ting, J. von Moltke, The Immune Function of Tuft Cells at Gut Mucosal Surfaces and Beyond, J. Immunol. 202 (2019) 1321–1329. https://doi.org/10.4049/jimmunol.1801069.
[26] M. Friedrich, M. Pohin, F. Powrie, Cytokine Networks in the Pathophysiology of Inflammatory Bowel Disease, Immunity. 50 (2019) 992–1006. https://doi.org/10.1016/j.immuni.2019.03.017.
[27] T. Pelaseyed, J.H. Bergström, J.K. Gustafsson, A. Ermund, G.M.H. Birchenough, A. Schütte, S. van der Post, F. Svensson, A.M. Rodríguez-Piñeiro, E.E.L. Nyström, C. Wising, M.E. V Johansson, G.C. Hansson, The mucus and mucins of the goblet cells and enterocytes provide the first defense line of the gastrointestinal tract and interact with the immune system., Immunol. Rev. 260 (2014) 8–20. https://doi.org/10.1111/imr.12182.
[28] K.R. Groschwitz, S.P. Hogan, S.P. Groschwitz, Katherine R. and Hogan, Intestinal Barrier Function: Molecular Regulation and Disease Pathogenesis, J. Allergy Clin. Immunol. 23 (2009) 3–22. https://doi.org/10.1016/j.jaci.2009.05.038.Intestinal.
[29] B.H. Bajka, N.M. Rigby, K.L. Cross, A. Macierzanka, A.R. Mackie, The influence of small intestinal mucus structure on particle transport ex vivo, Colloids Surfaces B Biointerfaces. 135 (2015) 73–80. https://doi.org/10.1016/j.colsurfb.2015.07.038.
[30] X. Murgia, B. Loretz, O. Hartwig, M. Hittinger, C.-M.M. Lehr, The role of mucus on drug transport and its potential to affect therapeutic outcomes, Adv. Drug Deliv. Rev. 124 (2018) 82–97. https://doi.org/10.1016/j.addr.2017.10.009.
[31] M.E.V. Johansson, H. Sjövall, G.C. Hansson, The gastrointestinal mucus system in health and disease, Nat. Rev. Gastroenterol. Hepatol. 10 (2013) 352–361. https://doi.org/10.1038/nrgastro.2013.35.
[32] C. Atuma, V. Strugala, A. Allen, L. Holm, The adherent gastrointestinal mucus gel layer: Thickness and physical state in vivo, Am. J. Physiol. - Gastrointest. Liver Physiol. 280 (2001) 922–929. https://doi.org/10.1152/ajpgi.2001.280.5.g922.
[33] R. Bansil, B.S. Turner, Mucin structure, aggregation, physiological functions and biomedical applications, Curr. Opin. Colloid Interface Sci. 11 (2006) 164–170. https://doi.org/10.1016/j.cocis.2005.11.001.
[34] A. Macierzanka, A.R. Mackie, B.H. Bajka, N.M. Rigby, F. Nau, D. Dupont, Transport of particles in intestinal mucus under simulated infant and adult physiological conditions: Impact of mucus structure and extracellular DNA, PLoS One. 9 (2014) 1–11. https://doi.org/10.1371/journal.pone.0095274.
[35] L. Sardelli, D.P. Pacheco, A. Ziccarelli, M. Tunesi, O. Caspani, A. Fusari, F. Briatico Vangosa, C. Giordano, P. Petrini, Towards bioinspired: In vitro models of intestinal mucus, RSC Adv. 9 (2019) 15887–15899. https://doi.org/10.1039/c9ra02368b.
[36] R. Bansil, B.S. Turner, The biology of mucus: Composition, synthesis and organization, Adv. Drug Deliv. Rev. 124 (2018) 3–15. https://doi.org/10.1016/j.addr.2017.09.023.
[37] M.E.V. Johansson, J.M. Holmén Larsson, G.C. Hansson, The two mucus layers of colon are organized by the MUC2 mucin, whereas the outer layer is a legislator of host-microbial interactions, Proc. Natl. Acad. Sci. U. S. A. 108 (2011) 4659–4665. https://doi.org/10.1073/pnas.1006451107.

[38] J. Fang, H. Wang, Y. Zhou, H. Zhang, H. Zhou, X. Zhang, Slimy partners: the mucus barrier and gut microbiome in ulcerative colitis, Exp. Mol. Med. 53 (2021) 772–787. https://doi.org/10.1038/s12276-021-00617-8.
[39] O. Lieleg, K. Ribbeck, Biological hydrogels as selective diffusion barriers, Trends Cell Biol. 21 (2011) 543–551. https://doi.org/https://doi.org/10.1016/j.tcb.2011.06.002.
[40] P. Paone, P.D. Cani, Mucus barrier, mucins and gut microbiota: the expected slimy partners?, Gut. 69 (2020) 2232 LP – 2243. https://doi.org/10.1136/gutjnl-2020-322260.
[41] J.-F. Sicard, G. Le Bihan, P. Vogeleer, M. Jacques, J. Harel, Interactions of Intestinal Bacteria with Components of the Intestinal Mucus, Front. Cell. Infect. Microbiol. 7 (2017) 387. https://doi.org/10.3389/fcimb.2017.00387.
[42] D. Boltin, T.T. Perets, A. Vilkin, Y. Niv, Mucin function in inflammatory bowel disease: an update., J. Clin. Gastroenterol. 47 (2013) 106–111. https://doi.org/10.1097/MCG.0b013e3182688e73.
[43] M.E.V. Johansson, Mucus layers in inflammatory bowel disease, Inflamm. Bowel Dis. 20 (2014) 2124–2131. https://doi.org/10.1097/MIB.0000000000000117.
[44] C.T. Capaldo, D.N. Powell, D. Kalman, Layered defense: how mucus and tight junctions seal the intestinal barrier, J. Mol. Med. 95 (2017) 927–934. https://doi.org/10.1007/s00109-017-1557-x.
[45] G.C. Hansson, Role of mucus layers in gut infection and inflammation, Curr. Opin. Microbiol. 15 (2012) 57–62. https://doi.org/10.1016/j.mib.2011.11.002.
[46] E.A. Eloe-Fadrosh, D.A. Rasko, The human microbiome: from symbiosis to pathogenesis, Annu. Rev. Med. 64 (2013) 145–163. https://doi.org/10.1146/annurev-med-010312-133513.
[47] T.L. Carlson, J.Y. Lock, R.L. Carrier, Engineering the Mucus Barrier, Annu. Rev. Biomed. Eng. 20 (2018) 197–220. https://doi.org/10.1146/annurev-bioeng-062117-121156.
[48] J. Kirch, A. Schneider, B. Abou, A. Hopf, U.F. Schaefer, M. Schneider, C. Schall, C. Wagner, C.M. Lehr, Optical tweezers reveal relationship between microstructure and nanoparticle penetration of pulmonary mucus, Proc. Natl. Acad. Sci. U. S. A. 109 (2012) 18355–18360. https://doi.org/10.1073/pnas.1214066109.
[49] X. Murgia, P. Pawelzyk, U.F. Schaefer, C. Wagner, N. Willenbacher, C.M. Lehr, Size-Limited Penetration of Nanoparticles into Porcine Respiratory Mucus after Aerosol Deposition, Biomacromolecules. 17 (2016) 1536–1542. https://doi.org/10.1021/acs.biomac.6b00164.
[50] R.A. Cone, Barrier properties of mucus, Adv. Drug Deliv. Rev. 61 (2009) 75–85. https://doi.org/10.1016/j.addr.2008.09.008.
[51] J.Y. Lock, T.L. Carlson, C.M. Wang, A. Chen, R.L. Carrier, Acute Exposure to Commonly Ingested Emulsifiers Alters Intestinal Mucus Structure and Transport Properties, Sci. Rep. 8 (2018) 1–14. https://doi.org/10.1038/s41598-018-27957-2.
[52] O. Lieleg, I. Vladescu, K. Ribbeck, Characterization of particle translocation through mucin hydrogels, Biophys. J. 98 (2010) 1782–1789. https://doi.org/10.1016/j.bpj.2010.01.012.
[53] R. Okumura, K. Takeda, Roles of intestinal epithelial cells in the maintenance of gut homeostasis, Exp. Mol. Med. 49 (2017) e338-8. https://doi.org/10.1038/emm.2017.20.
[54] J.Y. Lee, V.C. Wasinger, Y.Y. Yau, E. Chuang, V. Yajnik, R.W.L. Leong, Molecular pathophysiology of epithelial barrier dysfunction in inflammatory bowel diseases, Proteomes. 6 (2018) 1–17. https://doi.org/10.3390/PROTEOMES6020017.
[55] T. Oshima, H. Miwa, Gastrointestinal mucosal barrier function and diseases, J. Gastroenterol. 51 (2016) 768–778. https://doi.org/10.1007/s00535-016-1207-z.
[56] A.C. Luissint, C.A. Parkos, A. Nusrat, Inflammation and the Intestinal Barrier: Leukocyte–Epithelial Cell Interactions, Cell Junction Remodeling, and Mucosal Repair, Gastroenterology. 151 (2016) 616–632. https://doi.org/10.1053/j.gastro.2016.07.008.
[57] S. Guo, R. Al-Sadi, H.M. Said, T.Y. Ma, Lipopolysaccharide causes an increase in intestinal tight junction permeability in vitro and in vivo by inducing enterocyte membrane expression and localization of TLR-4 and CD14, Am. J. Pathol. 182 (2013) 375–387. https://doi.org/10.1016/j.ajpath.2012.10.014.
[58] R. Curciarello, K.E. Canziani, G.H. Docena, C.I. Muglia, Contribution of non-immune cells to activation and modulation of the intestinal inflammation, Front. Immunol. 10 (2019) 1–10.

https://doi.org/10.3389/fimmu.2019.00647.
[59] J.F. Burgueño, M.T. Abreu, Epithelial Toll-like receptors and their role in gut homeostasis and disease, Nat. Rev. Gastroenterol. Hepatol. 17 (2020) 263–278. https://doi.org/10.1038/s41575-019-0261-4.
[60] M.T. Abreu, Toll-like receptor signalling in the intestinal epithelium: How bacterial recognition shapes intestinal function, Nat. Rev. Immunol. 10 (2010) 131–143. https://doi.org/10.1038/nri2707.
[61] R. Okumura, K. Takeda, Maintenance of intestinal homeostasis by mucosal barriers, Inflamm. Regen. 38 (2018) 1–8. https://doi.org/10.1186/s41232-018-0063-z.
[62] G.G. Kaplan, J.W. Windsor, The four epidemiological stages in the global evolution of inflammatory bowel disease, Nat. Rev. Gastroenterol. Hepatol. (2020). https://doi.org/10.1038/s41575-020-00360-x.
[63] R.B. Sartor, Mechanisms of disease: Pathogenesis of Crohn's disease and ulcerative colitis, Nat. Clin. Pract. Gastroenterol. Hepatol. 3 (2006) 390–407. https://doi.org/10.1038/ncpgasthep0528.
[64] A.N. Ananthakrishnan, Epidemiology and risk factors for IBD, Nat. Rev. Gastroenterol. Hepatol. 12 (2015) 205–217. https://doi.org/10.1038/nrgastro.2015.34.
[65] L. Petagna, A. Antonelli, C. Ganini, V. Bellato, M. Campanelli, A. Divizia, C. Efrati, M. Franceschilli, A.M. Guida, S. Ingallinella, F. Montagnese, B. Sensi, L. Siragusa, G.S. Sica, Pathophysiology of Crohn's disease inflammation and recurrence, Biol. Direct. 15 (2020) 1–10. https://doi.org/10.1186/s13062-020-00280-5.
[66] S. Hua, E. Marks, J.J. Schneider, S. Keely, Advances in oral nano-delivery systems for colon targeted drug delivery in inflammatory bowel disease: Selective targeting to diseased versus healthy tissue, Nanomedicine Nanotechnology, Biol. Med. 11 (2015) 1117–1132. https://doi.org/10.1016/j.nano.2015.02.018.
[67] D.C. Baumgart, W.J. Sandborn, Crohn ' s disease, Lancet. 380 (2013) 1590–1605. https://doi.org/10.1016/S0140-6736(12)60026-9.
[68] I. Ordás, L. Eckmann, M. Talamini, D.C. Baumgart, W.J. Sandborn, Ulcerative colitis., Lancet. 380 (2012) 1606–1619. https://doi.org/10.1016/S0140-6736(12)60150-0.
[69] S. Carding, K. Verbeke, D.T. Vipond, B.M. Corfe, L.J. Owen, Dysbiosis of the gut microbiota in disease, Microb. Ecol. Health Dis. 26 (2015) 26191. https://doi.org/10.3402/mehd.v26.26191.
[70] F. Cordes, D. Foell, J.N. Ding, G. Varga, D. Bettenworth, Differential regulation of JAK/STAT-signaling in patients with ulcerative colitis and Crohn's disease, World J. Gastroenterol. 26 (2020) 4055–4075. https://doi.org/10.3748/wjg.v26.i28.4055.
[71] M.F. Peters, A.L. Choy, C. Pin, D.J. Leishman, A. Moisan, L. Ewart, P.J. Guzzie-Peck, R. Sura, D.A. Keller, C.W. Scott, K.L. Kolaja, Developing: In vitro assays to transform gastrointestinal safety assessment: Potential for microphysiological systems, Lab Chip. 20 (2020) 1177–1190. https://doi.org/10.1039/c9lc01107b.
[72] Y.Z. Zhang, Y.Y. Li, Inflammatory bowel disease: Pathogenesis, World J. Gastroenterol. 20 (2014) 91–99. https://doi.org/10.3748/wjg.v20.i1.91.
[73] R.B. Sartor, Genetics and environmental interactions shape the intestinal microbiome to promote inflammatory bowel disease versus mucosal homeostasis, Gastroenterology. 139 (2010) 1816–1819. https://doi.org/10.1053/j.gastro.2010.10.036.
[74] M.F. Viola, G. Boeckxstaens, Intestinal resident macrophages: Multitaskers of the gut, Neurogastroenterol. Motil. 32 (2020) 1–12. https://doi.org/10.1111/nmo.13843.
[75] M. Zaeem Cader, A. Kaser, Recent advances in inflammatory bowel disease: Mucosal immune cells in intestinal inflammation, Gut. 62 (2013) 1653–1664. https://doi.org/10.1136/gutjnl-2012-303955.
[76] A. Geremia, P. Biancheri, P. Allan, G.R. Corazza, A. Di Sabatino, Innate and adaptive immunity in inflammatory bowel disease, Autoimmun. Rev. 13 (2014) 3–10. https://doi.org/https://doi.org/10.1016/j.autrev.2013.06.004.
[77] K.L. Wallace, L.-B. Zheng, Y. Kanazawa, D.Q. Shih, Immunopathology of inflammatory bowel

disease., World J. Gastroenterol. 20 (2014) 6–21. https://doi.org/10.3748/wjg.v20.i1.6.
[78] M. Leppkes, M.F. Neurath, Cytokines in inflammatory bowel diseases – Update 2020, Pharmacol. Res. 158 (2020). https://doi.org/10.1016/j.phrs.2020.104835.
[79] M.F. Neurath, New targets for mucosal healing and therapy in inflammatory bowel diseases, Mucosal Immunol. 7 (2014) 6–19. https://doi.org/10.1038/mi.2013.73.
[80] M.F. Neurath, Current and emerging therapeutic targets for IBD, Nat. Rev. Gastroenterol. Hepatol. 14 (2017) 269–278. https://doi.org/10.1038/nrgastro.2016.208.
[81] S.C. Park, Y.T. Jeen, Anti-integrin therapy for inflammatory bowel disease, World J. Gastroenterol. 24 (2018) 1868–1880. https://doi.org/10.3748/wjg.v24.i17.1868.
[82] H.C.-H. Chan, S.C. Ng, Emerging biologics in inflammatory bowel disease, J. Gastroenterol. 52 (2017) 141–150. https://doi.org/10.1007/s00535-016-1283-0.
[83] A. Salas, C. Hernandez-Rocha, M. Duijvestein, W. Faubion, D. McGovern, S. Vermeire, S. Vetrano, N. Vande Casteele, JAK–STAT pathway targeting for the treatment of inflammatory bowel disease, Nat. Rev. Gastroenterol. Hepatol. 17 (2020) 323–337. https://doi.org/10.1038/s41575-020-0273-0.
[84] D.M. Schwartz, Y. Kanno, A. Villarino, M. Ward, M. Gadina, J.J. O'Shea, JAK inhibition as a therapeutic strategy for immune and inflammatory diseases, Nat. Rev. Drug Discov. 16 (2017) 843–862. https://doi.org/10.1038/nrd.2017.201.
[85] S. Danese, M. Argollo, C. Le Berre, L. Peyrin-Biroulet, JAK selectivity for inflammatory bowel disease treatment: Does it clinically matter?, Gut. 68 (2019) 1893–1899. https://doi.org/10.1136/gutjnl-2019-318448.
[86] A.A. Date, J. Hanes, L.M. Ensign, Nanoparticles for oral delivery: Design, evaluation and state-of-the-art, J. Control. Release. 240 (2016) 504–526. https://doi.org/10.1016/j.jconrel.2016.06.016.
[87] M.P. Desai, V. Labhasetwar, G.L. Amidon, R.J. Levy, Gastrointestinal uptake of biodegradable microparticles: effect of particle size, Pharm. Res. 13 (1996) 1838–1845. https://doi.org/10.1023/a:1016085108889.
[88] C.-M. Lehr, F.G.J. Poelma, H.E. Junginger, J.J. Tukker, An estimate of turnover time of intestinal mucus gel layer in the rat in situ loop, Int. J. Pharm. 70 (1991) 235–240. https://doi.org/10.1016/0378-5173(91)90287-X.
[89] S. Zhu, M. Zeng, G. Feng, H. Wu, Platinum Nanoparticles As A Therapeutic Agent Against Dextran Sodium Sulfate-Induced Colitis In Mice., Int. J. Nanomedicine. 14 (2019) 8361–8378. https://doi.org/10.2147/IJN.S210655.
[90] A. Lamprecht, Nanomedicines in gastroenterology and hepatology, Nat. Rev. Gastroenterol. Hepatol. 12 (2015) 195–204. https://doi.org/10.1038/nrgastro.2015.37.
[91] M. Lopez-Yrigoyen, L. Cassetta, J.W. Pollard, Macrophage targeting in cancer, Ann. N. Y. Acad. Sci. (2020) 1–24. https://doi.org/10.1111/nyas.14377.
[92] C. Schmidt, C. Lautenschlaeger, E.M. Collnot, M. Schumann, C. Bojarski, J.D. Schulzke, C.M. Lehr, A. Stallmach, Nano- and microscaled particles for drug targeting to inflamed intestinal mucosa - A first in vivo study in human patients, J. Control. Release. 165 (2013) 139–145. https://doi.org/10.1016/j.jconrel.2012.10.019.
[93] J.A. Jiminez, T.C. Uwiera, G.D. Inglis, R.R.E. Uwiera, Animal models to study acute and chronic intestinal inflammation in mammals, Gut Pathog. 7 (2015) 1–31. https://doi.org/10.1186/s13099-015-0076-y.
[94] V. Valatas, G. Bamias, G. Kolios, Experimental colitis models: Insights into the pathogenesis of inflammatory bowel disease and translational issues, Eur. J. Pharmacol. 759 (2015) 253–264. https://doi.org/10.1016/j.ejphar.2015.03.017.
[95] D. Low, D.D. Nguyen, E. Mizoguchi, Animal models of ulcerative colitis and their application in drug research, Drug Des. Devel. Ther. 7 (2013) 1341–1356. https://doi.org/10.2147/DDDT.S40107.
[96] S. Wirtz, V. Popp, M. Kindermann, K. Gerlach, B. Weigmann, S. Fichtner-Feigl, M.F. Neurath, Chemically induced mouse models of acute and chronic intestinal inflammation, Nat. Protoc. 12

(2017) 1295–1309. https://doi.org/10.1038/nprot.2017.044.
[97] D.L. Gibbons, J. Spencer, Mouse and human intestinal immunity: Same ballpark, different players; Different rules, same score, Mucosal Immunol. 4 (2011) 148–157. https://doi.org/10.1038/mi.2010.85.
[98] V. Valatas, M. Vakas, G. Kolios, The value of experimental models of colitis in predicting efficacy of biological therapies for inflammatory bowel diseases, Am. J. Physiol. - Gastrointest. Liver Physiol. 305 (2013). https://doi.org/10.1152/ajpgi.00004.2013.
[99] A. Nishida, C.W. Lau, M. Zhang, A. Andoh, H.N. Shi, E. Mizoguchi, A. Mizoguchi, The membrane-bound mucin Muc1 regulates T helper 17-cell responses and colitis in mice., Gastroenterology. 142 (2012) 865-874.e2. https://doi.org/10.1053/j.gastro.2011.12.036.
[100] M. Van der Sluis, B.A.E. De Koning, A.C.J.M. De Bruijn, A. Velcich, J.P.P. Meijerink, J.B. Van Goudoever, H.A. Büller, J. Dekker, I. Van Seuningen, I.B. Renes, A.W.C. Einerhand, Muc2-deficient mice spontaneously develop colitis, indicating that MUC2 is critical for colonic protection., Gastroenterology. 131 (2006) 117–129. https://doi.org/10.1053/j.gastro.2006.04.020.
[101] E. Mizoguchi, D. Low, Y. Ezaki, T. Okada, Recent updates on the basic mechanisms and pathogenesis of inflammatory bowel diseases in experimental animal models, Intest. Res. 18 (2020) 151–167. https://doi.org/10.5217/IR.2019.09154.
[102] L.E. Wagar, R.M. Difazio, M.M. Davis, Advanced model systems and tools for basic and translational human immunology, Genome Med. 10 (2018) 1–14. https://doi.org/10.1186/s13073-018-0584-8.
[103] M.K. Jonsson, T.A. an Veen, J. Synnergren, B. Becker, Towards Creating the Perfect in Vitro Cell Model, Stem Cells Int. 2016 (2016) 3459730. https://doi.org/10.1155/2016/3459730.
[104] F. Hugenholtz, W.M. de Vos, Mouse models for human intestinal microbiota research: a critical evaluation, Cell. Mol. Life Sci. 75 (2018) 149–160. https://doi.org/10.1007/s00018-017-2693-8.
[105] J. Kim, B.K. Koo, J.A. Knoblich, Human organoids: model systems for human biology and medicine, Nat. Rev. Mol. Cell Biol. 21 (2020) 571–584. https://doi.org/10.1038/s41580-020-0259-3.
[106] K.D. Swanson, E. Theodorou, E. Kokkotou, P. Drug, E. Unit, B. Israel, D. Medical, Reproducing the human mucosal environment ex vivo: inflammatory bowel disease as a paradigm, Curr. Opin. Gastroenterol. 34 (2018) 384–391. https://doi.org/10.1097/MOG.0000000000000485.
[107] A. Jarry, F. Malard, C. Bou-hanna, G. Meurette, M. Mohty, J. Mosnier, C.L. Laboisse, C. Bossard, Interferon-Alpha Promotes Th1 Response and Epithelial Apoptosis via Inflammasome Activation in Human Intestinal Mucosa, Cell. Mol. Gastroenterol. Hepatol. 3 (2017) 72–81. https://doi.org/10.1016/j.jcmgh.2016.09.007.
[108] D.E. Lefebvre, K. Venema, L. Gombau, L.G. Valerio, J. Raju, G.S. Bondy, H. Bouwmeester, R.P. Singh, A.J. Clippinger, E.M. Collnot, R. Mehta, V. Stone, Utility of models of the gastrointestinal tract for assessment of the digestion and absorption of engineered nanomaterials released from food matrices, Nanotoxicology. 9 (2015) 523–542. https://doi.org/10.3109/17435390.2014.948091.
[109] O. Hartwig, M.A. Shetab Boushehri, K.S. Shalaby, B. Loretz, A. Lamprecht, C.-M. Lehr, Drug delivery to the inflamed intestinal mucosa - targeting technologies and human cell culture models for better therapies of IBD, Adv. Drug Deliv. Rev. (2021) 113828. https://doi.org/10.1016/j.addr.2021.113828.
[110] S. Batista Leite, M. Cipriano, D. Carpi, S. Coecke, M. Holloway, R. Corvi, A. Worth, J. Barroso, M. Whelan, Establishing the scientific validity of complex in vitro models: Results of a EURL ECVAM survey, Publ. Off. Eur. Union. (2021) 1–28. https://doi.org/10.2760/376171.
[111] I.J. Hidalgo, T.J. Raub, R.T. Borchardt, Characterization of the Human Colon Carcinoma Cell Line (Caco-2) as a Model System for Intestinal Epithelial Permeability, Gastroenterology. 96 (1989) 736–749. https://doi.org/10.1016/S0016-5085(89)80072-1.
[112] F. Antunes, F. Andrade, F. Araújo, D. Ferreira, B. Sarmento, Establishment of a triple co-culture in vitro cell models to study intestinal absorption of peptide drugs, Eur. J. Pharm. Biopharm. 83

(2013) 427–435. https://doi.org/10.1016/j.ejpb.2012.10.003.
[113] S. Devriese, L. Van den Bossche, S. Van Welden, T. Holvoet, I. Pinheiro, P. Hindryckx, M. De Vos, D. Laukens, T84 monolayers are superior to Caco-2 as a model system of colonocytes, Histochem. Cell Biol. 148 (2017) 85–93. https://doi.org/10.1007/s00418-017-1539-7.
[114] L. Schulte, M. Hohwieler, M. Müller, J. Klaus, Intestinal organoids as a novel complementary model to dissect inflammatory bowel disease, Stem Cells Int. 2019 (2019). https://doi.org/10.1155/2019/8010645.
[115] S.E. Blutt, S.E. Crawford, S. Ramani, W.Y. Zou, M.K. Estes, Engineered Human Gastrointestinal Cultures to Study the Microbiome and Infectious Diseases, Cmgh. 5 (2018) 241–251. https://doi.org/10.1016/j.jcmgh.2017.12.001.
[116] I. Schoultz, Å. Keita, Cellular and Molecular Therapeutic Targets in Inflammatory Bowel Disease—Focusing on Intestinal Barrier Function, Cells. 8 (2019) 193. https://doi.org/10.3390/cells8020193.
[117] A. Wikman-Larhed, P. Artursson, Co-cultures of human intestinal goblet (HT29-H) and absorptive (Caco-2) cells for studies of drug and peptide absorption, Eur. J. Pharm. Sci. 3 (1995) 171–183. https://doi.org/https://doi.org/10.1016/0928-0987(95)00007-Z.
[118] G.J. Mahler, M.L. Shuler, R.P. Glahn, Characterization of Caco-2 and HT29-MTX cocultures in an in vitro digestion/cell culture model used to predict iron bioavailability, J. Nutr. Biochem. 20 (2009) 494–502. https://doi.org/10.1016/j.jnutbio.2008.05.006.
[119] C. Hilgendorf, H. Spahn-Langguth, C.G. Regårdh, E. Lipka, G.L. Amidon, P. Langguth, Caco-2 versus Caco-2/HT29-MTX co-cultured cell lines: Permeabilities via diffusion, inside- and outside-directed carrier-mediated transport, J. Pharm. Sci. 89 (2000) 63–75. https://doi.org/10.1002/(SICI)1520-6017(200001)89:1<63::AID-JPS7>3.0.CO;2-6.
[120] M. Boegh, S.G. Baldursdóttir, A. Müllertz, H.M. Nielsen, Property profiling of biosimilar mucus in a novel mucus-containing in vitro model for assessment of intestinal drug absorption, Eur. J. Pharm. Biopharm. 87 (2014) 227–235. https://doi.org/10.1016/j.ejpb.2014.01.001.
[121] N.A. Mabbott, D.S. Donaldson, H. Ohno, I.R. Williams, A. Mahajan, Microfold (M) cells: Important immunosurveillance posts in the intestinal epithelium, Mucosal Immunol. 6 (2013) 666–677. https://doi.org/10.1038/mi.2013.30.
[122] A. des Rieux, V. Fievez, I. Théate, J. Mast, V. Préat, Y.-J. Schneider, An improved in vitro model of human intestinal follicle-associated epithelium to study nanoparticle transport by M cells, Eur. J. Pharm. Sci. 30 (2007) 380–391. https://doi.org/https://doi.org/10.1016/j.ejps.2006.12.006.
[123] C. Schimpel, B. Teubl, M. Absenger, C. Meindl, E. Fröhlich, G. Leitinger, A. Zimmer, E. Roblegg, Development of an advanced intestinal in vitro triple culture permeability model to study transport of nanoparticles, Mol. Pharm. 11 (2014) 808–818. https://doi.org/10.1021/mp400507g.
[124] A. des Rieux, V. Fievez, M. Garinot, Y.J. Schneider, V. Préat, Nanoparticles as potential oral delivery systems of proteins and vaccines: A mechanistic approach, J. Control. Release. 116 (2006) 1–27. https://doi.org/10.1016/j.jconrel.2006.08.013.
[125] S. Hua, Advances in Oral Drug Delivery for Regional Targeting in the Gastrointestinal Tract - Influence of Physiological, Pathophysiological and Pharmaceutical Factors, Front. Pharmacol. 11 (2020) 1–22. https://doi.org/10.3389/fphar.2020.00524.
[126] G.R. Jones, C.C. Bain, T.M. Fenton, A. Kelly, S.L. Brown, A.C. Ivens, M.A. Travis, P.C. Cook, A.S. MacDonald, Dynamics of colon monocyte and macrophage activation during colitis, Front. Immunol. 9 (2018). https://doi.org/10.3389/fimmu.2018.02764.
[127] A.L. Hart, H.O. Al-Hassi, R.J. Rigby, S.J. Bell, A. V. Emmanuel, S.C. Knight, M.A. Kamm, A.J. Stagg, Characteristics of intestinal dendritic cells in inflammatory bowel diseases, Gastroenterology. 129 (2005) 50–65. https://doi.org/10.1053/j.gastro.2005.05.013.
[128] F. Pan, L. Han, Y. Zhang, Y. Yu, J. Liu, Optimization of Caco-2 and HT29 co-culture in vitro cell models for permeability studies, Int. J. Food Sci. Nutr. 66 (2015) 680–685. https://doi.org/10.3109/09637486.2015.1077792.
[129] A.A.M. Kämpfer, P. Urbán, S. Gioria, N. Kanase, V. Stone, A. Kinsner-Ovaskainen, Development

of an in vitro co-culture model to mimic the human intestine in healthy and diseased state, Toxicol. Vitr. 45 (2017) 31–43. https://doi.org/10.1016/j.tiv.2017.08.011.
[130] A.A.M. Kämpfer, P. Urbán, R. La, I. Ojea, N. Kanase, Toxicology in Vitro Ongoing in fl ammation enhances the toxicity of engineered nanomaterials : Application of an in vitro co-culture model of the healthy and in fl amed intestine, 63 (2020). https://doi.org/10.1016/j.tiv.2019.104738.
[131] L.G. Griffith, M.A. Swartz, Capturing complex 3D tissue physiology in vitro, 7 (2006) 211–224. https://doi.org/10.1038/nrm1858.
[132] C. Pereira, F. Araújo, C.C. Barrias, P.L. Granja, B. Sarmento, Dissecting stromal-epithelial interactions in a 3D in vitro cellularized intestinal model for permeability studies, Biomaterials. 56 (2015) 36–45. https://doi.org/https://doi.org/10.1016/j.biomaterials.2015.03.054.
[133] B. Yi, K.Y. Shim, S.K. Ha, J. Han, H.H. Hoang, I. Choi, S. Park, J.H. Sung, Three-dimensional in vitro gut model on a villi-shaped collagen scaffold, Biochip J. 11 (2017) 219–231. https://doi.org/10.1007/s13206-017-1307-8.
[134] J. Costa, A. Ahluwalia, Advances and Current Challenges in Intestinal in vitro Model Engineering: A Digest, Front. Bioeng. Biotechnol. 7 (2019) 1–14. https://doi.org/10.3389/fbioe.2019.00144.
[135] Z. Huang, Z. Wang, S. Long, H. Jiang, J. Chen, J. Zhang, L. Dong, A 3-D artificial colon tissue mimic for the evaluation of nanoparticle-based drug delivery system, Mol. Pharm. 11 (2014) 2051–2061. https://doi.org/10.1021/mp400723j.
[136] N. Li, D. Wang, Z. Sui, X. Qi, L. Ji, X. Wang, L. Yang, Development of an improved three-dimensional in vitro intestinal mucosa model for drug absorption evaluation, Tissue Eng. - Part C Methods. 19 (2013) 708–719. https://doi.org/10.1089/ten.tec.2012.0463.
[137] S.C. Papadakis GZ, Millo C, J. Yu, S. Peng, D. Luo, J.C. March, In vitro 3D human small intestinal villous model for drug permeability determination, Physiol. Behav. 176 (2011) 2173–2178. https://doi.org/10.1002/bit.24518.
[138] A. des Rieux, E.G.E. Ragnarsson, E. Gullberg, V. Préat, Y.-J. Schneider, P. Artursson, Transport of nanoparticles across an in vitro model of the human intestinal follicle associated epithelium, Eur. J. Pharm. Sci. 25 (2005) 455–465. https://doi.org/https://doi.org/10.1016/j.ejps.2005.04.015.
[139] Y. Chen, Y. Lin, K.M. Davis, Q. Wang, J. Rnjak-Kovacina, C. Li, R.R. Isberg, C.A. Kumamoto, J. Mecsas, D.L. Kaplan, Robust bioengineered 3D functional human intestinal epithelium, Sci. Rep. 5 (2015) 1–11. https://doi.org/10.1038/srep13708.
[140] R.H. Dosh, N. Jordan-Mahy, C. Sammon, C.L. Le Maitre, Long-term in vitro 3D hydrogel co-culture model of inflammatory bowel disease, Sci. Rep. 9 (2019) 1–15. https://doi.org/10.1038/s41598-019-38524-8.
[141] A.A.M. Kämpfer, M. Busch, R.P.F. Schins, Advanced in vitro testing strategies and models of the intestine for nanosafety research, Chem. Res. Toxicol. 33 (2020) 1163–1178. https://doi.org/10.1021/acs.chemrestox.0c00079.
[142] J.S. Dutton, S.S. Hinman, R. Kim, Y. Wang, N.L. Allbritton, Primary Cell-Derived Intestinal Models: Recapitulating Physiology, Trends Biotechnol. 37 (2019) 744–760. https://doi.org/10.1016/j.tibtech.2018.12.001.
[143] A. Ranga, N. Gjorevski, M.P. Lutolf, Drug discovery through stem cell-based organoid models, Adv. Drug Deliv. Rev. 69–70 (2014) 19–28. https://doi.org/10.1016/j.addr.2014.02.006.
[144] A. Fatehullah, S.H. Tan, N. Barker, Organoids as an in vitro model of human development and disease, Nat. Cell Biol. 18 (2016) 246–254. https://doi.org/10.1038/ncb3312.
[145] H.C.K. Angus, A.G. Butt, M. Schultz, R.A. Kemp, Intestinal Organoids as a Tool for Inflammatory Bowel Disease Research, Front. Med. 6 (2020) 1–9. https://doi.org/10.3389/fmed.2019.00334.
[146] M. Li, I.A.M. De Graaf, G.M.M. Groothuis, Precision-cut intestinal slices: Alternative model for drug transport, metabolism, and toxicology research, Expert Opin. Drug Metab. Toxicol. 12 (2016) 175–190. https://doi.org/10.1517/17425255.2016.1125882.
[147] L.C. Delon, Z. Guo, A. Oszmiana, C.C. Chien, R. Gibson, C. Prestidge, B. Thierry, A systematic investigation of the effect of the fluid shear stress on Caco-2 cells towards the optimization of

epithelial organ-on-chip models, Biomaterials. 225 (2019) 119521. https://doi.org/10.1016/j.biomaterials.2019.119521.
[148] H.J. Kim, D.E. Ingber, Gut-on-a-Chip microenvironment induces human intestinal cells to undergo villus differentiation., Integr. Biol. (Camb). 5 (2013) 1130–1140. https://doi.org/10.1039/c3ib40126j.
[149] H.J. Kim, H. Li, J.J. Collins, D.E. Ingber, Contributions of microbiome and mechanical deformation to intestinal bacterial overgrowth and inflammation in a human gut-on-a-chip, Proc. Natl. Acad. Sci. U. S. A. 113 (2016) E7–E15. https://doi.org/10.1073/pnas.1522193112.
[150] C. Beaurivage, E. Naumovska, Y.X. Chang, E.D. Elstak, A. Nicolas, H. Wouters, G. van Moolenbroek, H.L. Lanz, S.J. Trietsch, J. Joore, P. Vulto, R.A.J. Janssen, K.S. Erdmann, J. Stallen, D. Kurek, Development of a gut-on-a-chip model for high throughput disease modeling and drug discovery, Int. J. Mol. Sci. 20 (2019). https://doi.org/10.3390/ijms20225661.
[151] Q. Ramadan, L. Jing, Characterization of tight junction disruption and immune response modulation in a miniaturized Caco-2/U937 coculture-based in vitro model of the human intestinal barrier., Biomed. Microdevices. 18 (2016) 11. https://doi.org/10.1007/s10544-016-0035-5.
[152] L. Gijzen, D. Marescotti, E. Raineri, A. Nicolas, H.L. Lanz, D. Guerrera, R. van Vught, J. Joore, P. Vulto, M.C. Peitsch, J. Hoeng, G. Lo Sasso, D. Kurek, An Intestine-on-a-Chip Model of Plug-and-Play Modularity to Study Inflammatory Processes, SLAS Technol. 25 (2020) 585–597. https://doi.org/10.1177/2472630320924999.
[153] J.M. Donkers, H. Eslami Amirabadi, E. van de Steeg, Intestine-on-a-chip: Next level in vitro research model of the human intestine, Curr. Opin. Toxicol. 25 (2021) 6–14. https://doi.org/10.1016/j.cotox.2020.11.002.
[154] M. Noben, W. Vanhove, K. Arnauts, A.S. Ramalho, G. Van Assche, C. Verfaillie, M. Ferrante, A. Santo Ramalho, G. Van Assche, S. Vermeire, C. Verfaillie, M. Ferrante, Human intestinal epithelium in a dish: Current models for research into gastrointestinal pathophysiology, United Eur. Gastroenterol. J. 5 (2017) 1073–1081. https://doi.org/10.1177/2050640617722903.
[155] F. Leonard, E.M. Collnot, C.M. Lehr, A three-dimensional coculture of enterocytes, monocytes and dendritic cells to model inflamed intestinal mucosa in vitro, Mol. Pharm. 7 (2010) 2103–2119. https://doi.org/10.1021/mp1000795.
[156] F. Leonard, H. Ali, E.M. Collnot, B.J. Crielaard, T. Lammers, G. Storm, C.M. Lehr, Screening of budesonide nanoformulations for treatment of inflammatory bowel disease in an inflamed 3D cell-culture model, ALTEX. 29 (2012) 275–285. https://doi.org/10.14573/altex.2012.3.275.
[157] J. Susewind, C. De Souza Carvalho-Wodarz, U. Repnik, E.M. Collnot, N. Schneider-Daum, G.W. Griffiths, C.M. Lehr, A 3D co-culture of three human cell lines to model the inflamed intestinal mucosa for safety testing of nanomaterials, Nanotoxicology. 10 (2016) 53–62. https://doi.org/10.3109/17435390.2015.1008065.
[158] K. Khanvilkar, M.D. Donovan, D.R. Flanagan, Drug transfer through mucus, Adv. Drug Deliv. Rev. 48 (2001) 173–193. https://doi.org/10.1016/S0169-409X(01)00115-6.
[159] A.C. Groo, F. Lagarce, Mucus models to evaluate nanomedicines for diffusion, Drug Discov. Today. 19 (2014) 1097–1108. https://doi.org/10.1016/j.drudis.2014.01.011.
[160] M. Boegh, H.M. Nielsen, Mucus as a barrier to drug delivery - Understanding and mimicking the barrier properties, Basic Clin. Pharmacol. Toxicol. 116 (2015) 179–186. https://doi.org/10.1111/bcpt.12342.
[161] A. Lechanteur, J. das Neves, B. Sarmento, The role of mucus in cell-based models used to screen mucosal drug delivery, Adv. Drug Deliv. Rev. 124 (2018) 50–63. https://doi.org/10.1016/j.addr.2017.07.019.
[162] J.Y. Lock, T.L. Carlson, R.L. Carrier, Mucus models to evaluate the diffusion of drugs and particles, Adv. Drug Deliv. Rev. 124 (2018) 34–49. https://doi.org/10.1016/j.addr.2017.11.001.
[163] A.P. Walczak, E. Kramer, P.J.M. Hendriksen, R. Helsdingen, M. Van Der Zande, I.M.C.M. Rietjens, H. Bouwmeester, In vitro gastrointestinal digestion increases the translocation of polystyrene nanoparticles in an in vitro intestinal co-culture model, Nanotoxicology. 9 (2015)

886–894. https://doi.org/10.3109/17435390.2014.988664.
[164] T. Delmas, A. Fraichard, P.-A. Bayle, I. Texier, M. Bardet, J. Baudry, J. Bibette, A.-C. Couffin, Encapsulation and Release Behavior from Lipid Nanoparticles: Model Study with Nile Red Fluorophore, J. Colloid Sci. Biotechnol. 1 (2012) 16–25. https://doi.org/10.1166/jcsb.2012.1010.
[165] I. Texier, M. Goutayer, A. Da Silva, L. Guyon, N. Djaker, V. Josserand, E. Neumann, J. Bibette, F. Vinet, Cyanine-loaded lipid nanoparticles for improved in vivo fluorescence imaging, J. Biomed. Opt. 14 (2009) 054005. https://doi.org/10.1117/1.3213606.
[166] J.J. Gravier, F.P.N.Y. Garcia, T. Delmas, F. Mittler, A.-C. Couffin, F. Vinet, I. Texier-Nogues, Lipidots: competitive organic alternative to quantum dots for *in vivo* fluorescence imaging, J. Biomed. Opt. 16 (2011) 1–11. https://doi.org/10.1117/1.3625405.
[167] F. Clément, A. Nougarède, S. Combe, F. Kermarrec, A.K. Dey, P. Obeid, F.P. Navarro, P.N. Marche, E. Sulpice, X. Gidrol, Therapeutic siRNAs targeting JAK/STAT signalling pathway in inflammatory bowel diseases., J. Crohns. Colitis. (2021). https://doi.org/10.1093/ecco-jcc/jjab129.
[168] D.K. Ho, S. Frisch, A. Biehl, E. Terriac, C. De Rossi, K. Schwarzkopf, F. Lautenschläger, B. Loretz, X. Murgia, C.M. Lehr, Farnesylated Glycol Chitosan as a Platform for Drug Delivery: Synthesis, Characterization, and Investigation of Mucus-Particle Interactions, Biomacromolecules. 19 (2018) 3489–3501. https://doi.org/10.1021/acs.biomac.8b00795.
[169] I.F. Sbalzarini, P. Koumoutsakos, Feature point tracking and trajectory analysis for video imaging in cell biology, J. Struct. Biol. 151 (2005) 182–195. https://doi.org/https://doi.org/10.1016/j.jsb.2005.06.002.
[170] M. Kilcoyne, J.Q. Gerlach, M.P. Farrell, V.P. Bhavanandan, L. Joshi, Periodic acid–Schiff's reagent assay for carbohydrates in a microtiter plate format, Anal. Biochem. 416 (2011) 18–26. https://doi.org/10.1016/j.ab.2011.05.006.
[171] X. Murgia, H. Yasar, C. Carvalho-Wodarz, B. Loretz, S. Gordon, K. Schwarzkopf, U. Schaefer, C.-M. Lehr, Modelling the bronchial barrier in pulmonary drug delivery: A human bronchial epithelial cell line supplemented with human tracheal mucus, Eur. J. Pharm. Biopharm. 118 (2017) 79–88. https://doi.org/https://doi.org/10.1016/j.ejpb.2017.03.020.
[172] D.K. Ho, R. Christmann, X. Murgia, C. De Rossi, S. Frisch, M. Koch, U.F. Schaefer, B. Loretz, D. Desmaele, P. Couvreur, C.M. Lehr, Synthesis and Biopharmaceutical Characterization of Amphiphilic Squalenyl Derivative Based Versatile Drug Delivery Platform, Front. Chem. 8 (2020) 1–14. https://doi.org/10.3389/fchem.2020.584242.
[173] M. Boegh, S.G. Baldursdottir, M.H. Nielsen, A. Müllertz, H.M. Nielsen, Development and Rheological Profiling of Biosimilar Mucus, Annu. Trans. Nord. Rheol. Soc. 21 (2013) 233–240.
[174] B.C. Huck, O. Hartwig, A. Biehl, K. Schwarzkopf, C. Wagner, B. Loretz, X. Murgia, C.-M. Lehr, Macro- and Microrheological Properties of Mucus Surrogates in Comparison to Native Intestinal and Pulmonary Mucus, Biomacromolecules. 20 (2019) 3504–3512. https://doi.org/10.1021/acs.biomac.9b00780.
[175] S.K. Lai, Y.Y. Wang, D. Wirtz, J. Hanes, Micro- and macrorheology of mucus, Adv. Drug Deliv. Rev. 61 (2009) 86–100. https://doi.org/10.1016/j.addr.2008.09.012.
[176] M.J. Saxton, K. Jacobson, Single-particle tracking: applications to membrane dynamics., Annu. Rev. Biophys. Biomol. Struct. 26 (1997) 373–399. https://doi.org/10.1146/annurev.biophys.26.1.373.
[177] J. Grießinger, S. Dünnhaupt, B. Cattoz, P. Griffiths, S. Oh, S.B.I. Gómez, M. Wilcox, J. Pearson, M. Gumbleton, M. Abdulkarim, I. Pereira De Sousa, A. Bernkop-Schnürch, Methods to determine the interactions of micro- and nanoparticles with mucus, Eur. J. Pharm. Biopharm. 96 (2015) 464–476. https://doi.org/10.1016/j.ejpb.2015.01.005.
[178] M. Boegh, M. García-Díaz, A. Müllertz, H.M. Nielsen, Steric and interactive barrier properties of intestinal mucus elucidated by particle diffusion and peptide permeation, Eur. J. Pharm. Biopharm. 95 (2015) 136–143. https://doi.org/10.1016/j.ejpb.2015.01.014.
[179] A.W. Larhed, P. Artursson, J. Gråsjö, E. Björk, Diffusion of drugs in native and purified

gastrointestinal mucus, J. Pharm. Sci. 86 (1997) 660–665. https://doi.org/10.1021/js960503w.
[180] J. Suh, M. Dawson, J. Hanes, Real-time multiple-particle tracking: applications to drug and gene delivery, Adv. Drug Deliv. Rev. 57 (2005) 63–78. https://doi.org/https://doi.org/10.1016/j.addr.2004.06.001.
[181] B.S. Schuster, L.M. Ensign, D.B. Allan, J.S. Suk, J. Hanes, Particle tracking in drug and gene delivery research: State-of-the-art applications and methods, Adv. Drug Deliv. Rev. 91 (2015) 70–91. https://doi.org/10.1016/j.addr.2015.03.017.
[182] S.K. Lai, D.E. O'Hanlon, S. Harrold, S.T. Man, Y.Y. Wang, R. Cone, J. Hanes, Rapid transport of large polymeric nanoparticles in fresh undiluted human mucus, Proc. Natl. Acad. Sci. U. S. A. 104 (2007) 1482–1487. https://doi.org/10.1073/pnas.0608611104.
[183] B.C. Tang, M. Dawson, S.K. Lai, Y.Y. Wang, J.S. Suk, M. Yang, P. Zeitlin, M.P. Boyle, J. Fu, J. Hanes, Biodegradable polymer nanoparticles that rapidly penetrate the human mucus barrier, Proc. Natl. Acad. Sci. U. S. A. 106 (2009) 19268–19273. https://doi.org/10.1073/pnas.0905998106.
[184] B.S. Schuster, J.S. Suk, G.F. Woodworth, J. Hanes, Nanoparticle diffusion in respiratory mucus from humans without lung disease, Biomaterials. 34 (2013) 3439–3446. https://doi.org/10.1016/j.biomaterials.2013.01.064.
[185] J.S. Crater, R.L. Carrier, Barrier Properties of Gastrointestinal Mucus to Nanoparticle Transport, Macromol. Biosci. 10 (2010) 1473–1483. https://doi.org/10.1002/mabi.201000137.
[186] H.M. Yildiz, L. Speciner, C. Ozdemir, D.E. Cohen, R.L. Carrier, Food-associated stimuli enhance barrier properties of gastrointestinal mucus, Biomaterials. 54 (2015) 1–8. https://doi.org/10.1016/j.biomaterials.2015.02.118.
[187] L. Krupa, B. Bajka, R. Staroń, D. Dupont, H. Singh, K. Gutkowski, A. Macierzanka, Comparing the permeability of human and porcine small intestinal mucus for particle transport studies, Sci. Rep. 10 (2020) 1–12. https://doi.org/10.1038/s41598-020-77129-4.
[188] A.N. Round, N.M. Rigby, A. Garcia De La Torre, A. Maclerzanka, E.N.C. Mills, A.R. MacKie, Lamellar structures of MUC2-rich mucin: A potential role in governing the barrier and lubricating functions of intestinal mucus, Biomacromolecules. 13 (2012) 3253–3261. https://doi.org/10.1021/bm301024x.
[189] H.M. Yildiz, C.A. McKelvey, P.J. Marsac, R.L. Carrier, Size selectivity of intestinal mucus to diffusing particulates is dependent on surface chemistry and exposure to lipids, J. Drug Target. 23 (2015) 768–774. https://doi.org/10.3109/1061186X.2015.1086359.
[190] S.L. McGill, H.D.C. Smyth, Disruption of the mucus barrier by topically applied exogenous particles., Mol. Pharm. 7 (2010) 2280–2288. https://doi.org/10.1021/mp100242r.
[191] S.S. Olmsted, J.L. Padgett, A.I. Yudin, K.J. Whaley, T.R. Moench, R.A. Cone, Diffusion of macromolecules and virus-like particles in human cervical mucus, Biophys. J. 81 (2001) 1930–1937. https://doi.org/10.1016/S0006-3495(01)75844-4.
[192] J.K. Gustafsson, A. Ermund, M.E. V Johansson, A. Schütte, G.C. Hansson, H. Sjövall, An ex vivo method for studying mucus formation, properties, and thickness in human colonic biopsies and mouse small and large intestinal explants, Am. J. Physiol. Gastrointest. Liver Physiol. 302 (2012) G430–G438. https://doi.org/10.1152/ajpgi.00405.2011.
[193] L. Szentkuti, K. Lorenz, The thickness of the mucus layer in different segments of the rat intestine, Histochem. J. 27 (1995) 466–472. https://doi.org/10.1007/BF02388803.
[194] V. Strugala, P.W. Dettmar, J.P. Pearson, Thickness and continuity of the adherent colonic mucus barrier in active and quiescent ulcerative colitis and Crohn's disease, Int. J. Clin. Pract. 62 (2008) 762–769. https://doi.org/10.1111/j.1742-1241.2007.01665.x.
[195] J. Bruniaux, E. Sulpice, F. Mittler, I. Texier, X. Gidrol, F.P. Navarro, Cationic lipid nanoemulsions for RNAi screening, Tech. Proc. 2013 NSTI Nanotechnol. Conf. Expo, NSTI-Nanotech 2013. 3 (2013) 323–326.
[196] A.-C. Couffin, J. Bruniaux, T. Courant, A. Fournier, A. Hoang, J. Mérian, C. Martin, A. Fournier, I. Texier, E. Sulpice, X. Gidrol, R. Auzély-Velty, F. Navarro, Nanoemulsion with tuneable lipid shell dedicated to targeted delivery of small and biomacro- molecules, in: TechConnect Briefs,

2014: pp. 267–270.
[197] A.K. Blakney, P.F. McKay, B.I. Yus, Y. Aldon, R.J. Shattock, Inside out: optimization of lipid nanoparticle formulations for exterior complexation and in vivo delivery of saRNA, Gene Ther. 26 (2019) 363–372. https://doi.org/10.1038/s41434-019-0095-2.
[198] P. Lundquist, P. Artursson, Oral absorption of peptides and nanoparticles across the human intestine: Opportunities, limitations and studies in human tissues, Adv. Drug Deliv. Rev. 106 (2016) 256–276. https://doi.org/10.1016/j.addr.2016.07.007.
[199] I. Behrens, P. Stenberg, P. Artursson, T. Kissel, Transport of lipophilic drug molecules in a new mucus-secreting cell culture model based on HT29-MTX cells, Pharm. Res. 18 (2001) 1138–1145. https://doi.org/10.1023/A:1010974909998.
[200] N. Navabi, M.A. McGuckin, S.K. Lindén, Gastrointestinal Cell Lines Form Polarized Epithelia with an Adherent Mucus Layer when Cultured in Semi-Wet Interfaces with Mechanical Stimulation, PLoS One. 8 (2013). https://doi.org/10.1371/journal.pone.0068761.
[201] Y. Wu, L. Tang, B. Wang, Q. Sun, P. Zhao, W. Li, The role of autophagy in maintaining intestinal mucosal barrier, J. Cell. Physiol. 234 (2019) 19406–19419. https://doi.org/10.1002/jcp.28722.
[202] A. Wikman, J. Karlsson, I. Carlstedt, P. Artursson, A Drug Absorption Model Based on the Mucus Layer Producing Human Intestinal Goblet Cell Line HT29-H, Pharm. Res. An Off. J. Am. Assoc. Pharm. Sci. 10 (1993) 843–852. https://doi.org/10.1023/A:1018905109971.
[203] L.M. Ensign, R. Cone, J. Hanes, Oral drug delivery with polymeric nanoparticles: The gastrointestinal mucus barriers, Adv. Drug Deliv. Rev. 64 (2012) 557–570. https://doi.org/10.1016/j.addr.2011.12.009.
[204] S.K. Lai, Y.Y. Wang, J. Hanes, Mucus-penetrating nanoparticles for drug and gene delivery to mucosal tissues, Adv. Drug Deliv. Rev. 61 (2009) 158–171. https://doi.org/10.1016/j.addr.2008.11.002.
[205] I. Behrens, A.I.V. Pena, M.J. Alonso, T. Kissel, Comparative uptake studies of bioadhesive and non-bioadhesive nanoparticles in human intestinal cell lines and rats: the effect of mucus on particle adsorption and transport., Pharm. Res. 19 (2002) 1185–1193. https://doi.org/10.1023/a:1019854327540.
[206] J.S. Suk, Q. Xu, N. Kim, J. Hanes, L.M. Ensign, PEGylation as a strategy for improving nanoparticle-based drug and gene delivery, Adv. Drug Deliv. Rev. 99 (2016) 28–51. https://doi.org/10.1016/j.addr.2015.09.012.
[207] A.M. Bannunah, D. Vllasaliu, J. Lord, S. Stolnik, Mechanisms of Nanoparticle Internalization and Transport Across an Intestinal Epithelial Cell Model: Effect of Size and Surface Charge, Mol. Pharm. 11 (2014) 4363–4373. https://doi.org/10.1021/mp500439c.
[208] S. Guo, Y. Liang, L. Liu, M. Yin, A. Wang, K. Sun, Y. Li, Y. Shi, Research on the fate of polymeric nanoparticles in the process of the intestinal absorption based on model nanoparticles with various characteristics: size, surface charge and pro-hydrophobics, J. Nanobiotechnology. 19 (2021) 1–21. https://doi.org/10.1186/s12951-021-00770-2.
[209] I. Koboziev, F. Karlsson, S. Zhang, M.B. Grisham, Pharmacological intervention studies using mouse models of the inflammatory bowel diseases: Translating preclinical data into new drug therapies, Inflamm. Bowel Dis. 17 (2011) 1229–1245. https://doi.org/10.1002/ibd.21557.
[210] R. Ahmad, M.F. Sorrell, S.K. Batra, P. Dhawan, A.B. Singh, Gut permeability and mucosal inflammation: Bad, good or context dependent, Mucosal Immunol. 10 (2017) 307–317. https://doi.org/10.1038/mi.2016.128.
[211] A. Parker, L. Vaux, A.M. Patterson, A. Modasia, D. Muraro, A.G. Fletcher, H.M. Byrne, P.K. Maini, A.J.M. Watson, C. Pin, Elevated apoptosis impairs epithelial cell turnover and shortens villi in TNF-driven intestinal inflammation, Cell Death Dis. 10 (2019). https://doi.org/10.1038/s41419-018-1275-5.
[212] L. Thoo, M. Noti, P. Krebs, Keep calm: the intestinal barrier at the interface of peace and war, Cell Death Dis. 10 (2019). https://doi.org/10.1038/s41419-019-2086-z.
[213] J.R. Turner, Intestinal mucosal barrier function in health and disease, Nat. Rev. Immunol. 9 (2009) 799–809. https://doi.org/10.1038/nri2653.

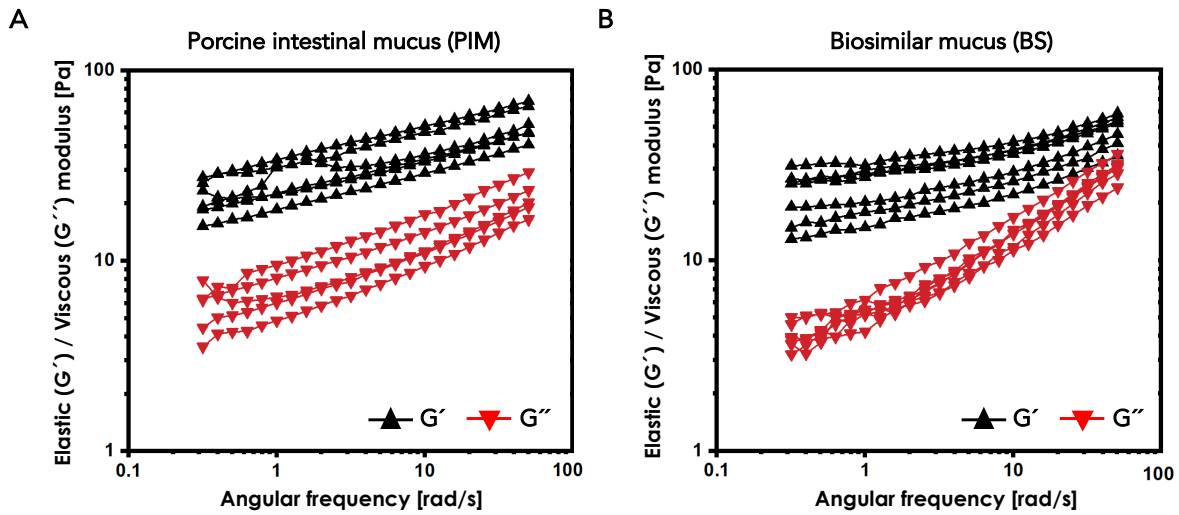
[214] J. V. Patankar, C. Becker, Cell death in the gut epithelium and implications for chronic inflammation, Nat. Rev. Gastroenterol. Hepatol. 17 (2020) 543–556. https://doi.org/10.1038/s41575-020-0326-4.
[215] A. Fasano, Leaky gut and autoimmune diseases, Clin. Rev. Allergy Immunol. 42 (2012) 71–78. https://doi.org/10.1007/s12016-011-8291-x.
[216] M. Camilleri, C. Enteric, N. Translational, M. Clinic, The Leaky Gut: Mechanisms, Measurement and Clinical Implications in Humans, 68 (2020) 1516–1526. https://doi.org/10.1136/gutjnl-2019-318427.The.
[217] J.J. Liu, K. Wong, A.L. Thiesen, S.J. Mah, L.A. Dieleman, B. Claggett, J.R. Saltzman, R.N. Fedorak, Increased epithelial gaps in the small intestines of patients with inflammatory bowel disease: Density matters, Gastrointest. Endosc. 73 (2011) 1174–1180. https://doi.org/10.1016/j.gie.2011.01.018.
[218] R. Kiesslich, C.A. Duckworth, D. Moussata, A. Gloeckner, L.G. Lim, M. Goetz, D.M. Pritchard, P.R. Galle, M.F. Neurath, A.J.M. Watson, Local barrier dysfunction identified by confocal laser endomicroscopy predicts relapse in inflammatory bowel disease, Gut. 61 (2012) 1146–1153. https://doi.org/10.1136/gutjnl-2011-300695.
[219] J. Yeste, X. Illa, M. Alvarez, R. Villa, Engineering and monitoring cellular barrier models, J. Biol. Eng. 12 (2018) 1–19. https://doi.org/10.1186/s13036-018-0108-5.
[220] D. Fleisher, Biological Transport Phenomena in the Gastrointestinal Tract: Cellular Mechanisms, in: 1999.
[221] J. Susewind, A cell line-based co-culture model of the inflamed intestinal mucosa and its application for safety and efficacy testing of nanomaterials, 2015.
[222] Y. Sambuy, I. De Angelis, G. Ranaldi, M.L. Scarino, A. Stammati, F. Zucco, The Caco-2 cell line as a model of the intestinal barrier: Influence of cell and culture-related factors on Caco-2 cell functional characteristics, Cell Biol. Toxicol. 21 (2005) 1–26. https://doi.org/10.1007/s10565-005-0085-6.
[223] E. Van Goethem, R. Guiet, S. Balor, G.M. Charrière, R. Poincloux, A. Labrousse, I. Maridonneau-Parini, V. Le Cabec, Macrophage podosomes go 3D., Eur. J. Cell Biol. 90 (2011) 224–236. https://doi.org/10.1016/j.ejcb.2010.07.011.
[224] M.E. Lund, J. To, B.A. O'Brien, S. Donnelly, The choice of phorbol 12-myristate 13-acetate differentiation protocol influences the response of THP-1 macrophages to a pro-inflammatory stimulus, J. Immunol. Methods. 430 (2016) 64–70. https://doi.org/10.1016/j.jim.2016.01.012.
[225] A. Spano, S. Barni, L. Sciola, PMA withdrawal in PMA-treated monocytic THP-1 cells and subsequent retinoic acid stimulation, modulate induction of apoptosis and appearance of dendritic cells, Cell Prolif. 46 (2013) 328–347. https://doi.org/10.1111/cpr.12030.
[226] E.K. Park, H.S. Jung, H.I. Yang, M.C. Yoo, C. Kim, K.S. Kim, Optimized THP-1 differentiation is required for the detection of responses to weak stimuli, Inflamm. Res. 56 (2007) 45–50. https://doi.org/10.1007/s00011-007-6115-5.
[227] H. Bosshart, M. Heinzelmann, THP-1 cells as a model for human monocytes, Ann. Transl. Med. 4 (2016) 4–7. https://doi.org/10.21037/atm.2016.08.53.
[228] M. Guerville, G. Boudry, Gastrointestinal and hepatic mechanisms limiting entry and dissemination of lipopolysaccharide into the systemic circulation, Am. J. Physiol. - Gastrointest. Liver Physiol. 311 (2016) G1–G15. https://doi.org/10.1152/ajpgi.00098.2016.
[229] F. Koohestani, A.G. Braundmeier, A. Mahdian, J. Seo, J.J. Bi, R.A. Nowak, Extracellular matrix collagen alters cell proliferation and cell cycle progression of human uterine leiomyoma smooth muscle cells, PLoS One. 8 (2013) 1–15. https://doi.org/10.1371/journal.pone.0075844.
[230] R. Weisshof, K. El Jurdi, N. Zmeter, D.T. Rubin, Emerging Therapies for Inflammatory Bowel Disease, Adv. Ther. 35 (2018) 1746–1762. https://doi.org/10.1007/s12325-018-0795-9.
[231] C. Yang, D. Merlin, Nanoparticle-mediated drug delivery systems for the treatment of IBD: Current perspectives, Int. J. Nanomedicine. 14 (2019) 8875–8889. https://doi.org/10.2147/IJN.S210315.
[232] L. Wu, M. Liu, W. Shan, Y. Cui, Z. Zhang, Y. Huang, Lipid nanovehicles with adjustable surface

properties for overcoming multiple barriers simultaneously in oral administration, Int. J. Pharm. 520 (2017) 216–227. https://doi.org/10.1016/j.ijpharm.2017.02.015.
[233] A. Lamprecht, U. Schäfer, C.-M. Lehr, Size-Dependent Bioadhesion of Micro- and Nanoparticulate Carriers to the Inflamed Colonic Mucosa, Pharm. Res. 18 (2001) 788–793. https://doi.org/10.1023/A:1011032328064.
[234] A. Lamprecht, H. Yamamoto, H. Takeuchi, Y. Kawashima, Nanoparticles enhance therapeutic efficiency by selectively increased local drug dose in experimental colitis in rats, J. Pharmacol. Exp. Ther. 315 (2005) 196–202. https://doi.org/10.1124/jpet.105.088146.
[235] B. Xiao, D. Merlin, Oral colon-specific therapeutic approaches toward treatment of inflammatory bowel disease, Expert Opin. Drug Deliv. 9 (2012) 1393–1407. https://doi.org/10.1517/17425247.2012.730517.
[236] J. Mérian, J. Gravier, F. Navarro, I. Texier, Fluorescent nanoprobes dedicated to in vivo imaging: From preclinical validations to clinical translation, Molecules. 17 (2012) 5564–5591. https://doi.org/10.3390/molecules17055564.
[237] H. Ali, E.M. Collnot, M. Windbergs, C.M. Lehr, Nanomedicines for the treatment of inflammatory bowel diseases, Eur. J. Nanomedicine. 5 (2013) 23–38. https://doi.org/10.1515/ejnm-2013-0004.
[238] P.D. Smith, L.E. Smythies, R. Shen, T. Greenwell-Wild, M. Gliozzi, S.M. Wahl, Intestinal macrophages and response to microbial encroachment, Mucosal Immunol. 4 (2011) 31–42. https://doi.org/10.1038/mi.2010.66.
[239] H. Laroui, D.S. Wilson, G. Dalmasso, K. Salaita, N. Murthy, S. V. Sitaraman, D. Merlin, Nanomedicine in GI, Am. J. Physiol. - Gastrointest. Liver Physiol. 300 (2011) 371–383. https://doi.org/10.1152/ajpgi.00466.2010.
[240] A. Beloqui, R. Coco, M. Alhouayek, M.Á. Solinís, A. Rodríguez-Gascón, G.G. Muccioli, V. Préat, Budesonide-loaded nanostructured lipid carriers reduce inflammation in murine DSS-induced colitis., Int. J. Pharm. 454 (2013) 775–783. https://doi.org/10.1016/j.ijpharm.2013.05.017.
[241] B. Tirosh, N. Khatib, Y. Barenholz, A. Nissan, A. Rubinstein, Transferrin as a luminal target for negatively charged liposomes in the inflamed colonic mucosa., Mol. Pharm. 6 (2009) 1083–1091. https://doi.org/10.1021/mp9000926.
[242] I. Schoultz, Å. V. Keita, The Intestinal Barrier and Current Techniques for the Assessment of Gut Permeability, Cells. 9 (2020) 1–30. https://doi.org/10.3390/cells9081909.
[243] A.M. Bannunah, D. Vllasaliu, J. Lord, S. Stolnik, Mechanisms of nanoparticle internalization and transport across an intestinal epithelial cell model: Effect of size and surface charge, Mol. Pharm. 11 (2014) 4363–4373. https://doi.org/10.1021/mp500439c.
[244] X.-J. Du, J.-L. Wang, S. Iqbal, H.-J. Li, Z.-T. Cao, Y.-C. Wang, J.-Z. Du, J. Wang, The effect of surface charge on oral absorption of polymeric nanoparticles, Biomater. Sci. 6 (2018) 642–650. https://doi.org/10.1039/C7BM01096F.
[245] J.T. Huckaby, S.K. Lai, PEGylation for enhancing nanoparticle diffusion in mucus, Adv. Drug Deliv. Rev. 124 (2018) 125–139. https://doi.org/10.1016/j.addr.2017.08.010.
[246] C. Lautenschläger, C. Schmidt, C.-M. Lehr, D. Fischer, A. Stallmach, PEG-functionalized microparticles selectively target inflamed mucosa in inflammatory bowel disease, Eur. J. Pharm. Biopharm. 85 (2013) 578–586. https://doi.org/https://doi.org/10.1016/j.ejpb.2013.09.016.
[247] M.M. Zhang, R. Bahal, T.P. Rasmussen, J.E. Manautou, X. Zhong, The growth of siRNA-based therapeutics: Updated clinical studies, Biochem. Pharmacol. 189 (2021) 114432. https://doi.org/https://doi.org/10.1016/j.bcp.2021.114432.
[248] I. V. Chernikov, V. V. Vlassov, E.L. Chernolovskaya, Current development of siRNA bioconjugates: From research to the clinic, Front. Pharmacol. (2019). https://doi.org/10.3389/fphar.2019.00444.
[249] R.L. Ball, P. Bajaj, K.A. Whitehead, Oral delivery of siRNA lipid nanoparticles: Fate in the GI tract, Sci. Rep. 8 (2018) 1–12. https://doi.org/10.1038/s41598-018-20632-6.
[250] J. Guo, X. Jiang, S. Gui, RNA interference-based nanosystems for inflammatory bowel disease therapy, Int. J. Nanomedicine. 11 (2016) 5287–5310. https://doi.org/10.2147/IJN.S116902.

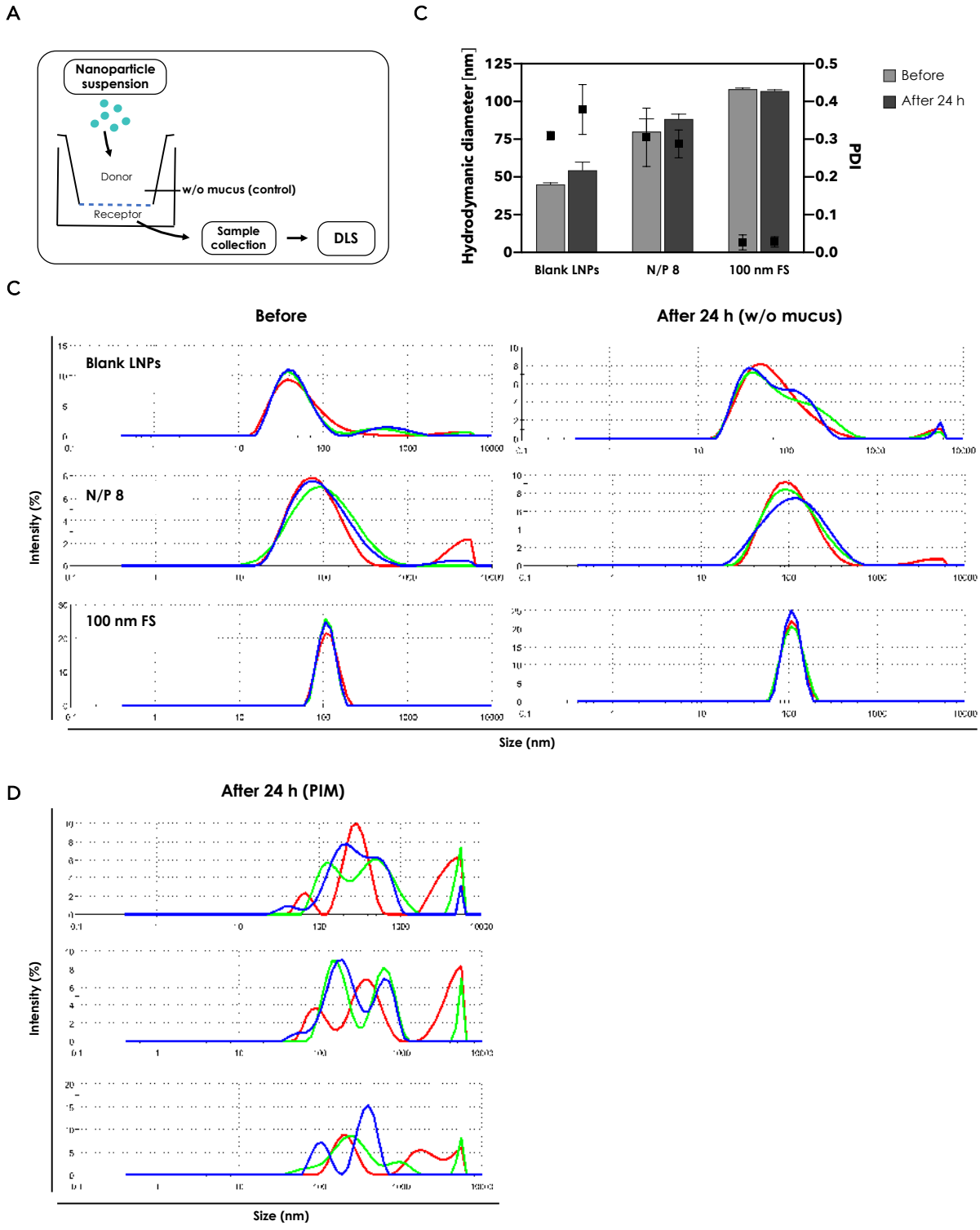
[251] B. Drasler, D. Vanhecke, L. Rodriguez-Lorenzo, A. Petri-Fink, B. Rothen-Rutishauser, Quantifying nanoparticle cellular uptake: Which method is best?, Nanomedicine. 12 (2017) 1095–1099. https://doi.org/10.2217/nnm-2017-0071.
[252] S. Danese, M. Grisham, J. Hodge, J.-B. Telliez, JAK inhibition using tofacitinib for inflammatory bowel disease treatment: a hub for multiple inflammatory cytokines, Am. J. Physiol. Gastrointest. Liver Physiol. 310 (2016) G155–G162. https://doi.org/10.1152/ajpgi.00311.2015.
[253] D.T. Beattie, M.T. Pulido-Rios, F. Shen, M. Ho, E. Situ, P.R. Tsuruda, P. Brassil, M. Kleinschek, S. Hegde, Intestinally-restricted Janus Kinase inhibition: A potential approach to maximize the therapeutic index in inflammatory bowel disease therapy, J. Inflamm. (United Kingdom). 14 (2017) 1–11. https://doi.org/10.1186/s12950-017-0175-2.
[254] L. Camoglio, A.A. Te Velde, A.J. Tigges, P.K. Das, S.J.H. Van Deventer, Altered expression of interferon-**γ** and interleukin-4 in inflammatory bowel disease, Inflamm. Bowel Dis. 4 (1998) 285–290. https://doi.org/10.1002/ibd.3780040406.
[255] P.O. Krutzik, G.P. Nolan, Intracellular Phospho-protein Staining Techniques for Flow Cytometry: Monitoring Single Cell Signaling Events, Cytom. Part A. 55 (2003) 61–70. https://doi.org/10.1002/cyto.a.10072.
[256] S. Cohen, S. Dovrat, R. Sarid, E. Huberman, S. Salzberg, JAK–STAT signaling involved in phorbol 12-myristate 13-acetate- and dimethyl sulfoxide-induced 2′-5′ oligoadenylate synthetase expression in human HL-60 leukemia cells, Leuk. Res. 29 (2005) 923–931. https://doi.org/https://doi.org/10.1016/j.leukres.2005.01.015.
[257] L.B. Ivashkiv, IFN**γ**: signalling, epigenetics and roles in immunity, metabolism, disease and cancer immunotherapy, Nat. Rev. Immunol. 18 (2018) 545–558. https://doi.org/10.1038/s41577-018-0029-z.
[258] M. Court, M. Malier, A. Millet, 3D type I collagen environment leads up to a reassessment of the classification of human macrophage polarizations, 2019. https://doi.org/10.1016/j.biomaterials.2019.04.018.
[259] A. T. Virtanen, T. Haikarainen, J. Raivola, O. Silvennoinen, Selective JAKinibs: Prospects in Inflammatory and Autoimmune Diseases, BioDrugs. 33 (2019) 15–32. https://doi.org/10.1007/s40259-019-00333-w.
[260] J.A. Hodge, T.T. Kawabata, S. Krishnaswami, J.D. Clark, J.B. Telliez, M.E. Dowty, S. Menon, M. Lamba, S. Zwillich, The mechanism of action of tofacitinib - an oral Janus kinase inhibitor for the treatment of rheumatoid arthritis, Clin. Exp. Rheumatol. 34 (2016) 318–328.
[261] K. Gerlach, K. Lechner, V. Popp, L. Offensperger, S. Zundler, M. Wiendl, E. Becker, R. Atreya, T. Rath, M.F. Neurath, B. Weigmann, The JAK1/3 Inhibitor to Tofacitinib Suppresses T Cell Homing and Activation in Chronic Intestinal Inflammation, J. Crohn's Colitis. (2020) 244–257. https://doi.org/10.1093/ecco-jcc/jjaa162.
[262] N. Kumar, J. Mishra, V.S. Narang, C.M. Waters, Janus kinase 3 regulates interleukin 2-induced mucosal wound repair through tyrosine phosphorylation of villin, J. Biol. Chem. 282 (2007) 30341–30345. https://doi.org/10.1074/jbc.C600319200.
[263] W.J. Sandborn, D.D. Nguyen, D.T. Beattie, P. Brassil, W. Krey, J. Woo, E. Situ, R. Sana, E. Sandvik, M.T. Pulido-Rios, R. Bhandari, J.A. Leighton, R. Ganeshappa, D.L. Boyle, B. Abhyankar, M.A. Kleinschek, R.A. Graham, J. Panes, Development of gut-selective pan-janus kinase inhibitor TD-1473 for ulcerative colitis: A translational medicine programme, J. Crohn's Colitis. 14 (2020) 1202–1213. https://doi.org/10.1093/ecco-jcc/jjaa049.
[264] E. Rybakovsky, M.C. Valenzano, K.M. Diguilio, N.B. Buleza, D. V. Moskalenko, R.N. Harty, J.M. Mullin, Improving transient transfection efficiency in a differentiated, polar epithelial cell layer, J. Biomol. Tech. 30 (2019) 19–24. https://doi.org/10.7171/jbt.19-3002-001.
[265] A.-A. Keller, M.B. Maeß, M. Schnoor, B. Scheiding, S. Lorkowski, Transfecting Macrophages., Methods Mol. Biol. 1784 (2018) 187–195. https://doi.org/10.1007/978-1-4939-7837-3_18.
[266] B. Laperrousaz, S. Porte, S. Gerbaud, V. Härmä, F. Kermarrec, V. Hourtane, F. Bottausci, X. Gidrol, N. Picollet-D'hahan, Direct transfection of clonal organoids in Matrigel microbeads: a promising approach toward organoid-based genetic screens, Nucleic Acids Res. 46 (2018) e70–

e70. https://doi.org/10.1093/nar/gky030.
[267] S. Danese, M. Grisham, J. Hodge, J.B. Telliez, JAK inhibition using tofacitinib for inflammatory bowel disease treatment: A hub for multiple inflammatory cytokines, Am. J. Physiol. - Gastrointest. Liver Physiol. 310 (2016) G155–G162. https://doi.org/10.1152/ajpgi.00311.2015.

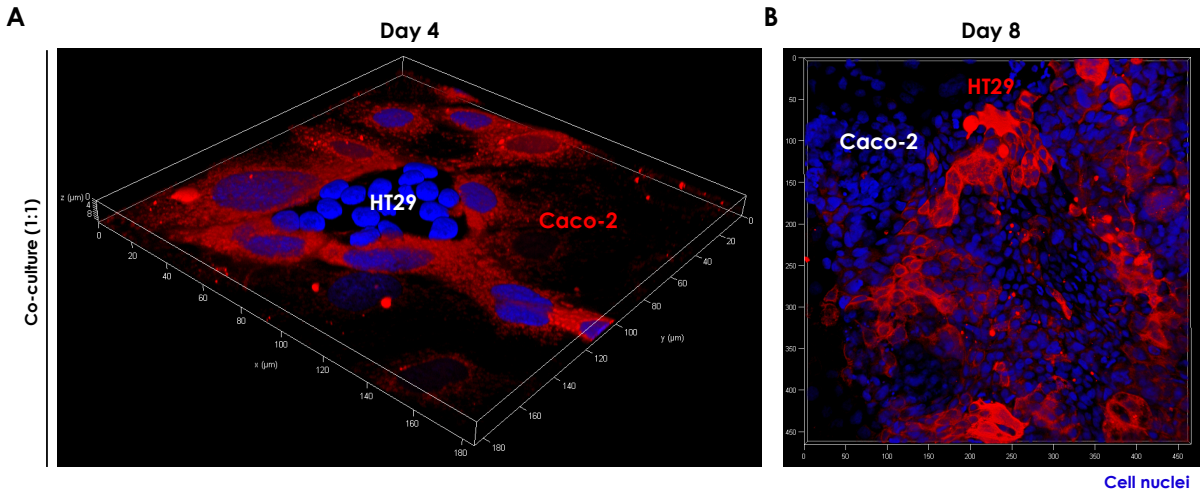
7 Appendix



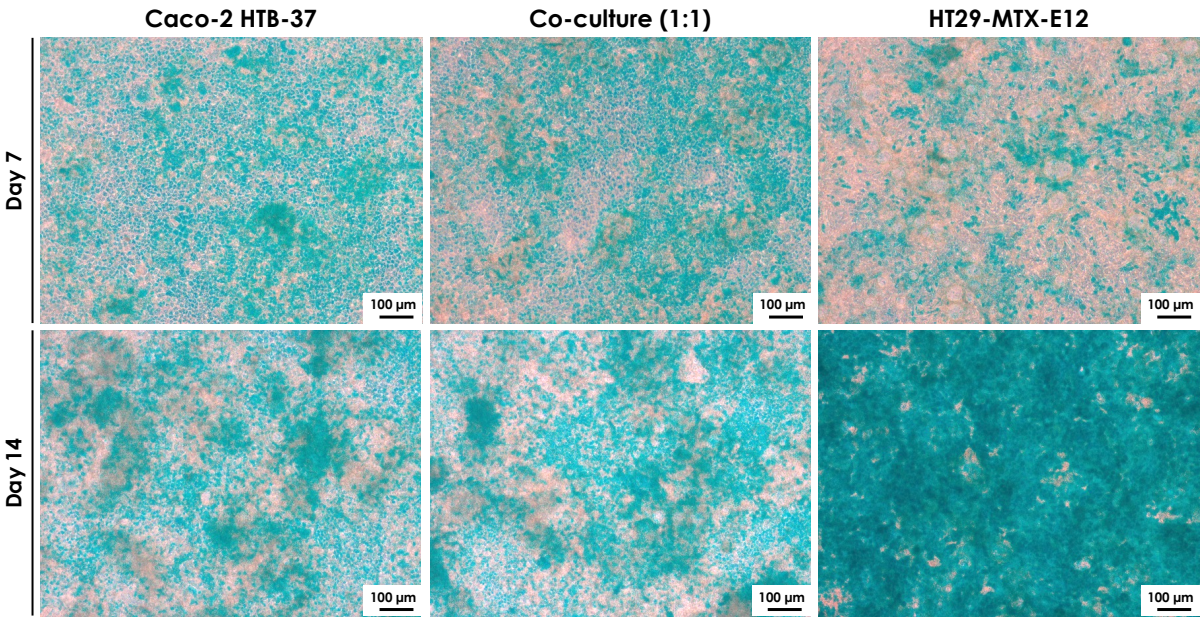
SI Figure 1 Inter- and intra-animal variations of isolated porcine intestinal mucus (PIM) from 3 pigs (**A**) and batch-to-batch variations of biosimilar mucus from 3 preparations (BS; **B**). Oscillatory measurements of PIM and BS displaying storage (elastic; G') and loss (viscous; G'') moduli with frequency-dependency in a frequency range of 0.3 – 50 rad/s. All measurements were performed at a strain-amplitude of 1%, within the linear viscoelastic region.



SI Figure 2 Particle integrity check after transport study. Schematic illustration of particle integrity verification after completed transport study through the empty Transwell® insert without mucus sample (control; 24h) (**A**). Particle diameter and polydisperse index (PDI) of blank LNPs, siJAK1-loaded LNPs (nanoplexes; N/P 8), and tracer particles (100 nm FS) were measured via DLS (**B**). Representative graphs obtained from DLS measurements with intensity distributions of collected samples before and after 24 h (transport performed w/o mucus) (**C**). Representative graphs obtained from DLS measurements with intensity distributions of collected samples after 24 h (transport performed through porcine intestinal mucus; PIM) (**D**). Data is represented as mean ± SD of three wells.



SI Figure 3 Confocal microscopic images of co-culture consisting of (enterocyte-like) Caco-2 HTB-37 and (goblet cell-like) HT29-MTX-E12 cells (ratio of 1:1). Before seeding, cells were pre-stained using CellTrace™ staining (indicated in red). Co-culture at day 4 with pre-stained Caco-2 HTB-37 cells (red) and unstained HT29-MTX-E12 (white) (**A**). Co-culture at day 8 with pre-stained HT29-MTX-E12 cells (red) and unstained Caco-2 HTB-37 (white). After fixation, cell nuclei were stained additionally with DAPI (blue) (**B**).



SI Figure 4 Light microscopic images of Caco-2 HTB-37, HT29-MTX-E12 cells, and co-culture of both cell types (ratio of 1:1) stained with Alcian blue for acidic mucins (day 7 *versus* 14).

8 Scientific output

8.1 Publications

Research papers:

Hartwig O, Loretz B, Nougarede A, Jary D, Sulpice E, Gidrol X, Navarro NF, Lehr CM. Leaky gut model of the human intestinal mucosa for testing siRNA-based nanomedicine targeting JAK1. (*Journal of Controlled Release*; manuscript under revision).

Heinrich E, **Hartwig O**, Walt C, Loretz B, Lehr CM, Müller R, Kiemer AK, Koch M, Hermann J, Fuhrmann G. A biogenic carrier against GI infections: loading extracellular vesicles with ciprofloxacin to treat *Shigella flexneri*. (*Manuscript under revision*).

Arrua EC, **Hartwig O**, Ho DK, Loretz B, Murgia X, Salomon CJ, Lehr CM. Surfactant-Free Glibenclamide Nanoparticles: Formulation, Characterization and Evaluation of Interactions with Biological Barriers. Pharm Res. 2021 Jun;38(6):1081-1092. doi: 10.1007/s11095-021-03056-2.

Lee S, Nasr S, **Hartwig O**, Kayab C, Boese A, Koch M, Loretz B, Buhler E, Hirsch A KH and Lehr CM. Dynaplexes, a new class of pH-responsive dynamic proteoid nanoparticles for safe and efficient mRNA transfection. (*Manuscript under revision*)

Huck BC*, **Hartwig O***, Biehl A, Schwarzkopf K, Wagner C, Loretz B, Murgia X, Lehr CM. Macro- and Microrheological Properties of Mucus Surrogates in Comparison to Native Intestinal and Pulmonary Mucus. *Biomacromolecules* 20(9):3504-3512. doi: 10.1021/acs.biomac.9b00780. (* equal author contribution)

Review papers:

Hartwig O*, Shetab Boushehri MA*, Shalaby KS, Loretz B, Lamprecht A, Lehr CM. Drug delivery to the inflamed intestinal mucosa - targeting technologies and human cell culture models for better therapies of IBD. *Advanced Drug Delivery Reviews* (2021) Aug; 175:113828. doi: 10.1016/j.addr.2021.113828. (* equal author contribution)

Murgia X, Loretz B, **Hartwig O**, Hittinger M, Lehr CM. The role of mucus on drug transport and its potential to affect therapeutic outcome. *Advanced Drug Delivery Reviews* 124:82-97. doi: 10.1016/j.addr.2017.10.009.

Savla R, **Hartwig O**, Lim Chin WW, Loretz B, Lehr CM (2018) Oral delivery of macromolecules. *Pharmaceutical Technology Europe* 30(7), pp. 22–26.

8.2 Oral presentations

Regular progress reporting and scientific exchange - Presentation at Consortium Meetings of EU-project "NewDeal" (11/12 July 2017 Paris, France; 21-23 February 2018 Brussels, Belgium; 12/13 September 2018 Barcelona, Spain; 27/28 March 2019 London, UK; 24/25 September 2019 Vigo, Spain; 21/22 September 2020 Virtual Meeting)

"**New siRNA nanotherapy for inflammatory bowel disease targeting Janus kinase 1/3**" – Helmholtz Institute for Pharmaceutical Research Saarland (HIPS) Project Presentation (17 September 2019) Saarbrücken, Germany.

"**In vitro models for the investigation of intestinal mucosa with a special focus on inflamed condition**" - Controlled Release Society (CRS) Local Chapter "Functional biomaterials and release of nucleic acid drugs" (7/8 March 2019) Leipzig, Germany.

8.3 Poster presentations

"**Cell culture model of the inflamed human intestinal mucosa for investigating nanomedicine against IBD**" - Controlled Release Society (CRS) Global Meeting (21-24 July 2019), Valencia, Spain.

"**Advanced co-culture model mimicking the inflammation of the human intestinal mucosa**" - Workshop "Interactions between nanomaterials & the immune system" (9/10 July 2018), Milan, Italy.

"**Advanced co-culture model mimicking the inflammation of the human intestinal mucosa**" - Doktorandentag (2018), Universität des Saarlandes, Saarbrücken, Germany.

9 Acknowledgements

First and foremost, I would like to thank my ´Doktorvater´ Prof. Dr. Claus-Michael Lehr for providing me this fascinating and challenging doctoral research project within the Drug Delivery department. I would like to thank for his trust in me, his convincing encouragement and valuable guidance throughout my PhD. I would like to extend my sincerely gratitude to my supervisor Dr. Brigitta Loretz and her indispensable assistance during the whole course of my PhD. I am very grateful for her daily guidance and invaluable efforts to foster my scientific formation.

Particularly, I would like to thank Prof. Dr. Alexandra K. Kiemer for supporting the development of my PhD project, for the fruitful discussions during our thesis advisory committee meetings and for reviewing my PhD thesis. Moreover, I would like to thank Prof. Dr. Ulrich Schäfer for the proof-reading as well as for the highly appreciated comments to improve the quality of the PhD thesis.

I gratefully acknowledge the invaluable experience within the EU-project NEW DEAL with exciting and instructive scientific exchange with all the consortium members.

Special thanks to all my co-authors for the excellent collaboration and their contribution to original research papers as well as review articles. In this context, I would like to thank Prof. Dr. Matthias Laschke from the Institute for Clinical and Experimental Surgery for the pleasant collaboration.

Importantly, I wish to thank all the members of the DDEL department including the BION group for the great working atmosphere as well as the pleasant time we spent together after work. I am particularly thankful for the everlasting support of the technicians and office management. I am deeply grateful to have met many wonderful persons during this time, but especially my office roommates Rebekka and Benedikt.

Finally, I would like to thank my family and friends, and especially my husband Amerigo who pushed me consistently through my PhD with persistent motivation, infinite patience and love.